Oil & Natural Gas Technology

DOE Award No.: DE-FG26-02NT15451

Final Report

Multicomponent Seismic Analysis and Calibration to Improve Recovery from Algal Mounds: Application to the Roadrunner/Towaoc Area of the Paradox Basin, Ute Mountain Ute Reservation, Colorado

Submitted by:
Golder Associates Inc.
18300 NE Union Hill Road, Suite 200
Redmond, WA 98052

Prepared for:
United States Department of Energy
National Energy Technology Laboratory

December 17, 2007

Office of Fossil Energy

MULTICOMPONENT SEISMIC ANALYSIS AND CALIBRATION TO IMPROVE RECOVERY FROM ALGAL MOUNDS: APPLICATION TO THE ROADRUNNER/TOWAOC AREA OF THE PARADOX BASIN, UTE MOUNTAIN UTE RESERVATION, COLORADO

Final Technical Report – September 23, 2002 through September 30, 2007

Paul La Pointe[1]
Claudia Rebne[2]
Steve Dobbs[3]
Colby VanDenberg[3]
Jim Gaiser[4]

Rich Van Dok[4]
Robert Benson[5]
Tom Davis[5]
Zhiqiang Gu[6]
Milind Deo[6]

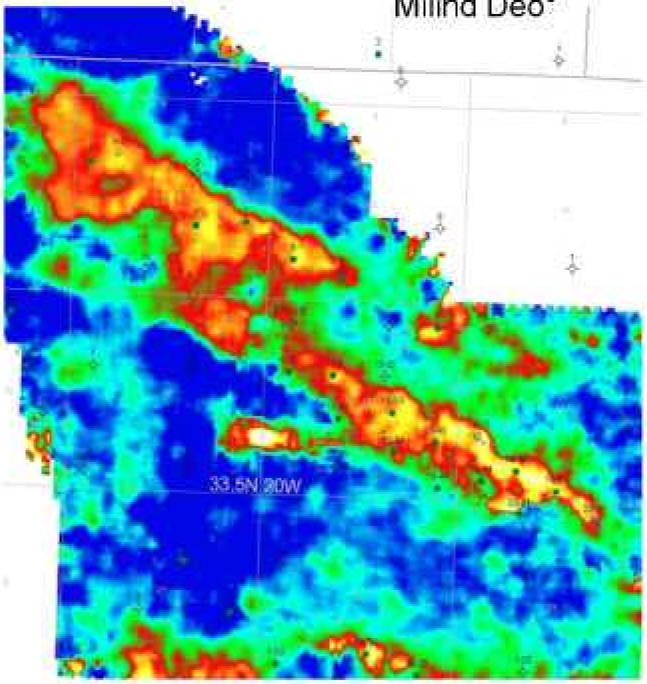

Report Date: September 30, 2007

DOE Award Number: DE-FG26-02NT15451

[1]Golder Associates Inc.
18300 NE Union Hill Road, Suite 200
Redmond, WA 98052

[2]Legacy Energy Corporation
P. O. Box 480272
Denver, CO 80248

[3]Red Willow Production Company
P.O. Box 737
Ignacio, Colorado 81137

[4]WesternGeco
1625 Broadway, Suite 1300
Denver, CO 80202

[5]Department of Geophysics
Colorado School of Mines
Golden, CO 80401

University of Utah
Department of Chemical Engineering
72 South Central Campus Drive,
University of Utah
Salt Lake City, Utah 84112

DISCLAIMERS

The following disclaimer applies to this report and any interpretation provided by Golder Associates Inc.:

> Any interpretation, engineering design work, research, analysis, or recommendation furnished with the services or otherwise communicated by Golder Associates Incorporated (hereinafter also referred to as "GAI") at any time in connection with the services are opinions based on inferences from measurements and empirical relationships and assumptions, which inferences and assumptions are not infallible, and with respect to which professionals in the industry may differ. Accordingly, GAI cannot and does not warrant the accuracy, correctness or completeness of any such interpretation or description. Customer acknowledges that it is accepting the services "as is", that GAI makes no representation or warranty, express or implied, of any kind or description in respect thereto, and that such services are delivered with the explicit understanding and agreement that any action customer may take based on the services received shall be at its own risk and responsibility and customer shall have no claim against GAI as a consequence thereof.
>
> Customer confirms that GAI has made no promise or statement regarding the services that is inconsistent with these terms, or that has created or amounted to a warranty that the services would conform to any such promise or statement, and GAI disclaims any and all warranties regarding the same.

ABSTRACT

This report describes the final project results made in fulfillment of contract DE-FG26-02NT15451, "Multicomponent Seismic Analysis and Calibration to Improve Recovery from Algal Mounds: Application to the Roadrunner/Towaoc Area of the Paradox Basin, Ute Mountain Ute Reservation, Colorado".

The goals of this project were:

1. To enhance recovery of oil contained within algal mounds on the Ute Mountain Ute tribal lands.
2. To promote the use of advanced technology and expand the technical capability of the Native American Oil production corporations by direct assistance in the current project and dissemination of technology to other Tribes.
3. To develop an understanding of multicomponent seismic data as it relates to the variations in permeability and porosity of algal mounds, as well as lateral facies variations, for use in both reservoir development and exploration.
4. To identify any undiscovered algal mounds for field-extension within the area of seismic coverage.
5. To evaluate the potential for applying CO2 floods, steam floods, water floods or other secondary or tertiary recovery processes to increase production.

The technical work scope was carried out by:

1. Acquiring multicomponent seismic data over the project area;
2. Processing and reprocessing the multicomponent data to extract as much geological and engineering data as possible within the budget and time-frame of the project;
3. Preparing maps and data volumes of geological and engineering data based on the multicomponent seismic and well data;
4. Selecting drilling targets if warranted by the seismic interpretation;
5. Constructing a static reservoir model of the project area; and
6. Constructing a dynamic history-matched simulation model from the static model.

Transfer of technical information was accomplished through several means:

1. Red Willow Production Company, a wholly-owned company of the Southern Ute Tribe, was a major partner and co-funder of this project. Red Willow's staff was intimately involved with all aspects of the seismic acquisition, processing and interpretation of the multicomponent seismic data, and was also responsible for drilling targets derived from the interpreted seismic data;
2. Project results were made available to Ute Mountain Ute Tribe through their oil & gas consultants who mange the development of oil & gas resources on Ute Mountain Ute tribal lands;
3. Several presentations on aspects of the project were made at professional conferences; and

4. A project web site was established and used to make reports, background information, and selected data available to the general oil & gas community

The original project scope covered a 6 mi^2 (15.6 km^2) area encompassing two algal mound fields (Towaoc and Roadrunner). 3D3C seismic data was to acquired over this area to delineate mound complexes and image internal reservoir properties such as porosity and fluid saturations. After the project began, the Red Willow Production Company, a project partner and fully-owned company of the Southern Ute Tribe, contributed additional money to upgrade the survey to a nine-component (3D9C) survey. The purpose of this upgrade to nine components was to provide additional shear wave component data that might prove useful in delineating internal mound reservoir attributes. Also, Red Willow extended the P-wave portion of the survey to the northwest of the original 6 mi^2 (15.6 km^2) 3D9C area in order to extend coverage further to the northwest to the Marble Wash area.

In order to accomplish this scope of work, 3D9C seismic data set covering two known reservoirs was acquired and processed. Three-dimensional, zero-offset vertical seismic profile (VSP) data was acquired to determine the shear wave velocities for processing the sh3Dseismic data. Anisotropic velocity, and azimuthal AVO processing was carried out in addition to the conventional 3D P-wave data processing. All P-, PS- and S-wave volumes of the seismic data were interpreted to map the seismic response. The interpretation consisted of conventional cross-plots of seismic attributes vs. geological and reservoir engineering data, as well as multivariate and neural net analyses to assess whether additional resolution on exploration and engineering parameters could be achieved through the combined use of several seismic variables. Engineering data in the two reservoirs was used to develop a combined lithology, structure and permeability map.

On the basis of the seismic data, a well was drilled into the northern mound trend in the project area. This well, Roadrunner #9-2, was brought into production in late April 2006 and continues to produce modest amounts of oil and gas. As of the end of August 2007, the well has produced approximately 12,000 barrels of oil and 32,000 mcf of gas.

A static reservoir model was created from the seismic data interpretations and well data. The seismic data was tied to various markers identified in the well logs, which in turn were related to lithostratigraphy. The tops and thicknesses of the various units were extrapolated from well control based upon the seismic data that was calibrated to the well picks. The reservoir engineering properties were available from a number of wells in the project area. Multivariate regressions of seismic attributes versus engineering parameters, such as porosity, were then used to guide interpolation away from well control. These formed the basis for dynamic reservoir simulations. The simulations were used to assess the potential for additional reservoir development, and to provide insight as to how well the multivariate approach worked for assigning more realistic values of internal mound reservoir properties.

Technology transfer was accomplished through several approaches, the most prominent through the partnering with Red Willow Production Company, a wholly-owned petroleum exploration company of the Southern Ute Tribe. Red Willow played a key role in all aspects of the seismic permitting, acquisition and interpretation; as Red Willow had never before undertaken a 3D9C survey, this project provided a substantial growth in the company's understanding of the application and usefulness of this emerging technology in oil exploration and development. Other methods in which knowledge gained in this project have been presentation of results to Ute Mountain Ute Tribe engineers employed by the Tribe to manage their resources; presentations of aspects of the project at National and International Technical conferences; and maintenance of a project website.

Delays in the project were caused by the company originally selected to acquire the 3D data choosing to leave the North American market prior to the contracts being signed. This led to a re-bid of the seismic data acquisition, which was further delayed by missing a season for carrying out the environmental survey required for permitting. As a result, the project requested and was granted no-cost extensions that extended the duration of the project to five years.

Table of Contents

List of Figures

List of Tables

1 INTRODUCTION

1.1 Undiscovered Oil Potential in the Ismay Algal Mounds

The U. S. Geological Survey reported in their most recent national assessment of undiscovered petroleum resources in the Paradox Basin (Gautier and others, 1996) that the mean estimate of recoverable undiscovered oil in the Porous Carbonate Buildup Play (Figure 1-1) in the Paradox Basin (Play No. 2102), of which the Ismay is the major established reservoir, is approximately 153 MMBO. They also estimate that there is a 5% probability that an undiscovered field will contain 40 MMBO, and that there would be a minimum of 10 undiscovered fields, a median of 20 undiscovered fields, and a maximum of about 50 undiscovered fields. The play is an oil and gas play. Discoveries are typically in the 1 MMBO to 10 MMBO, although the Aneth Field may contain an order of magnitude more oil in these facies

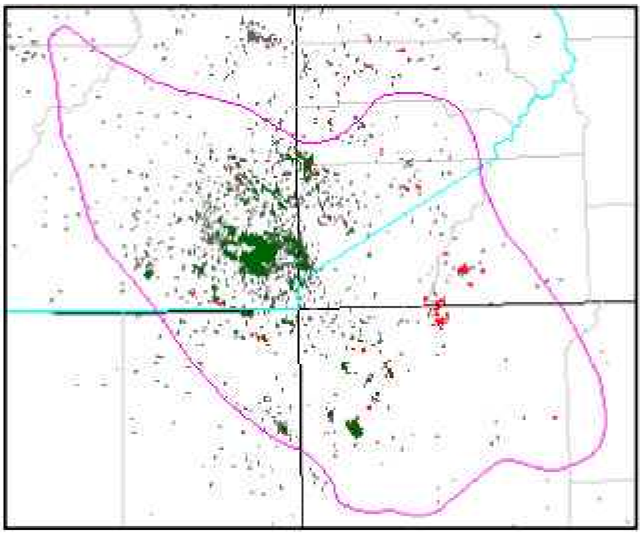

Figure 1-1 (above). Location of USGS's Carbonate Buildup Play (purple outline) and locations where wells have produced oil (green squares) and gas (red squares) from this play (Gautier and others, 1996).

Figure 1-2 (right). Stratigraphic column for the prospective region (Gautier and others, 1996).

AGE		FORMATION OR GROUP
CRETACEOUS		Mesaverde Group (Ferron Ss. Member)
		Mancos Shale
		Dakota Sandstone Burro Canyon Formation Morrison Formation
JURASSIC		San Rafael Group
		Glen Canyon Group
TRIASSIC		Chinle Formation Shinarump Member
		Moenkopi Formation Timpoweap Member
PERMIAN	Cutler Formation	Kaibab Ls. / White Rim Ss. / De Chelley Ss.
		Organ Rock Tongue
		Cedar Mesa Sandstone
		Halgaito Tongue
PENNSYLVANIAN	Hermosa Group	Honaker Trail Formation
		Paradox Formation Ismay "Zone" Desert Creek "Zone"
		Pinkerton Trail Formation
		Molas Formation
MISSISSIPPIAN		Leadville Limestone
DEVONIAN		Ouray Limestone
		Elbert Formation McCracken Member
		Aneth Formation
SILURIAN		
ORDOVICIAN		
CAMBRIAN		Lynch Dolomite
		Muav Limestone
		Bright Angel Shale
		Tapeats Sandstone / Ignacio Quartzite
ARCHEAN		Igneous and metamorphic rocks

Figure 1-1 shows the outline of this play, along with the locations of discovered oil and gas accumulations. Figure 1-2 shows a simplified stratigraphic column. The Ute Mountain Ute Tribe reservation (Figure 1-3) includes the southwestern Colorado portion of the play that has discovered accumulations of oil. The reservoirs are typically mounds of algal (*sp. Ivanovia*) limestone associated with organic-rich black dolomitic shale and mudstone rimming evaporite sequences of the Paradox Formation of the Hermosa Group (Figure 1-4). Net pay is on the order of 3 m – 15 m but occasionally reaches a net thickness of 30 m. Porosities typically vary from 5% to 20%. The traps are sourced by interbedded organic-rich dolomitic shales and mudstones. Oil generation occurred from the Late Cretaceous to the Paleocene. After expulsion, oil moved updip or migrated locally. There are a variety of seals, including overlying evaporites and interbedded shale. Most production ranges in depth from 1500 m to 2000 m.

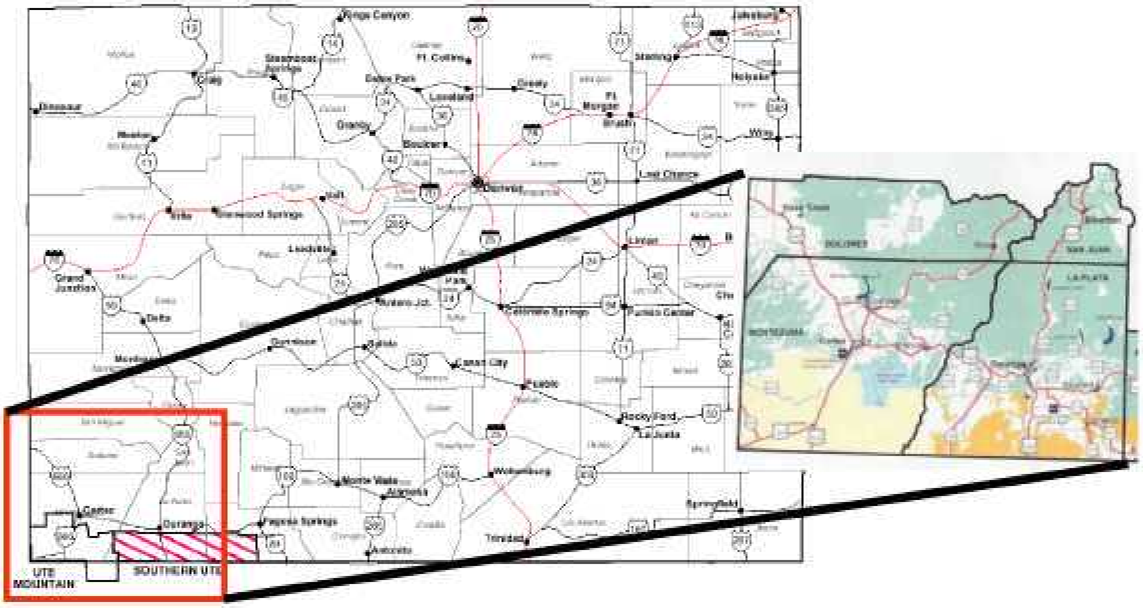

Figure 1-3. Location map for project. The Ute Mountain Ute reservation occupies the southwestern corner of the state of Colorado (unshaded region), adjacent to the Southern Ute reservation (red cross-hatching) to the east.

1.2 Exploration and Production Challenges

The goal of this project was to reliably delineate stratigraphic features that are on the order of 200 to 1000 acres. These features have little structural expression. The mounds are surrounded and overlain by massive anhydrite. The reservoir properties of these mounds are not homogeneous. From the standpoint of reservoir development of an existing algal mound field, the critical factors lie in predicting the porosity, permeability, internal mound geometries and fluid content of the mounds. While well information and production data are useful in understanding some of these variations, they cannot alone be used to make more accurate descriptions of the salient reservoir parameters between well control. This requires the use of some tool that provides at least an indirect indication of these properties away from well control. For this purpose, seismic data is the most appropriate technology available.

The usefulness of seismic technology has been exemplified by industry's improved exploration success in the algal mound play in the Paradox Basin (Figure 1-5). 2D seismic was first applied in the early 1980's. Success rates for exploration wells were around 10%. This increased to about 25% in the mid-1990's as conventional 3D seismic data was acquired for use in delineating exploration targets. Advanced multicomponent technology, such as 3D3C and 3D9C, could improve success rates in exploration even more and also provide better static reservoir models for existing fields. The key to developing a better image of the reservoir's internal geometry and flow properties is to utilize fluid saturations and azimuthal processing that can directly respond to oriented heterogeneities and changes in fluid saturations. Thus, acquisition of shear-wave data and advanced azimuthal processing or both shear- and compressional-wave data will potentially provide a much higher resolution of internal mound geometry and, from a reservoir engineering standpoint, a better model of the distribution of reservoir porosity and permeability

Improving exploration success and optimizing development of highly heterogeneous stratigraphic reservoirs where porosity and permeability vary in unpredictable ways due to facies variations is a challenging problem but one for which a solution will provide many benefits. An important example of this is in the algal mounds of the Lower and Upper Ismay reservoirs of the Paradox Basin in Utah and Colorado (Figure 1-4 and Figure 1-5). Production varies dramatically over short distances at mound edges. Even within mound complexes, production rates, saturations and cumulative production by well can vary significantly. If it were possible to more sharply delineate mound boundaries, and to delineate regions of better reservoir development, exploration success and field development could be improved through a better delineation of regions of good or bad reservoir permeability and porosity between existing well control.

Recent advances in seismic acquisition and processing offer new ways to see smaller features with more confidence and to characterize the internal structure of reservoirs such as algal mounds (Table 1-1). However, these methods have been relatively untested in the field.

As with any indirect means of detection, such as seismic data, the multicomponent seismic attribute data needs to be calibrated; a connection needs to be made between the indirect data and the parameters of interest, in this case, formation tops, thicknesses facies and their reservoir properties. The relations between 3D9C data and reservoir properties like porosity, permeability, internal mound geometry and fluid content of the mounds have not yet been established through field development experience or through laboratory studies. Calibration studies are necessary to support the establishment of these links. Therefore, this project required calibration of the various seismic attributes to geological and engineering data measured in wells.

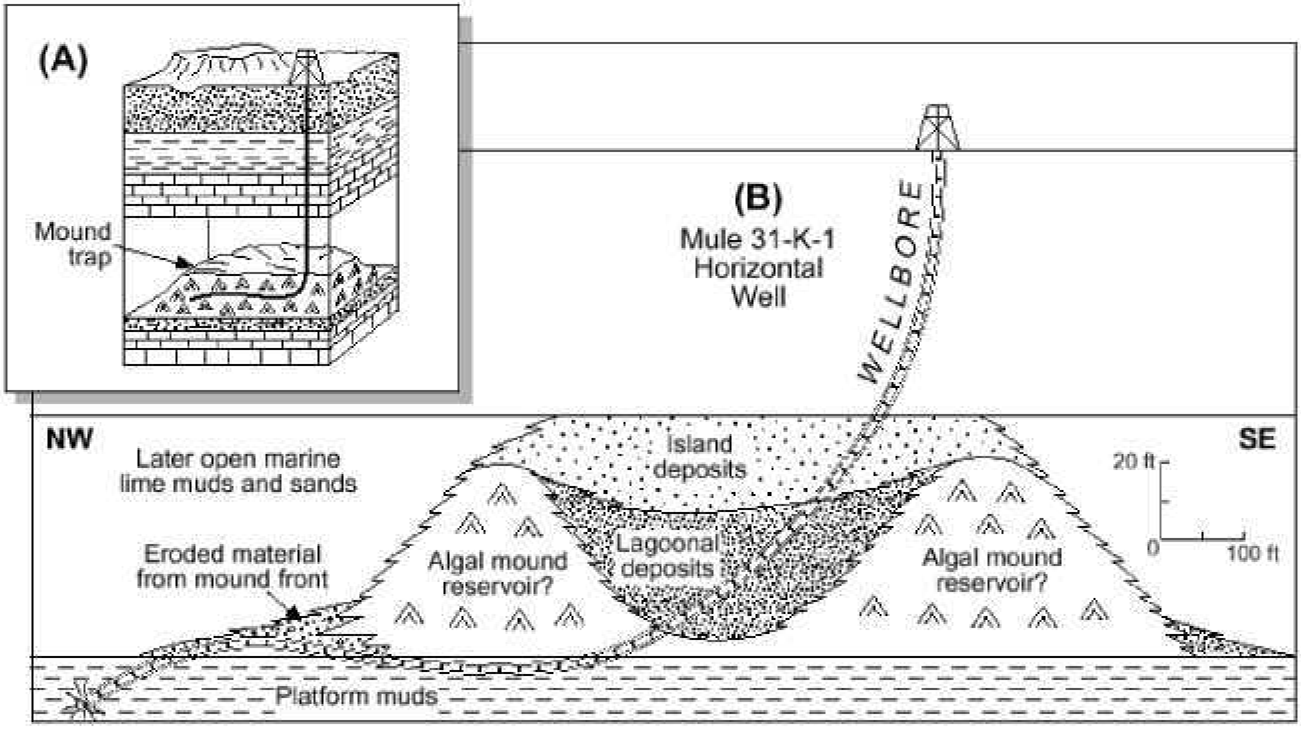

Figure 1-4. Hypothetical cross-section through an algal mound (from Chidsey and others, 2004).

Reservoir Property	Wavefield	Attribute
Porosity	P, S, PS	Amplitude, shear wave splitting
Permeability	P, S	Energy flow[1], shear wave splitting direction
Saturation	S	Shear wave splitting
Viscosity	S	Frequency and attenuation[2]
Density	P, S, PS	Amplitude variation with offset (AVO)[3]
Structure	P	Travel-time

[1] product of P- and S-wave amplitude at zero offset
[2] e.g. Duranti (2001) and Michaud (2001)
[3] Amaral (2001)

Table 1-1. Relationship between reservoir properties and multicomponent attributes. Table prepared by Tom Davis, Colorado School of Mines, Phase IX Proposal, Reservoir Characterization Project (http://www.mines.edu/academic/geophysics/rcp/)

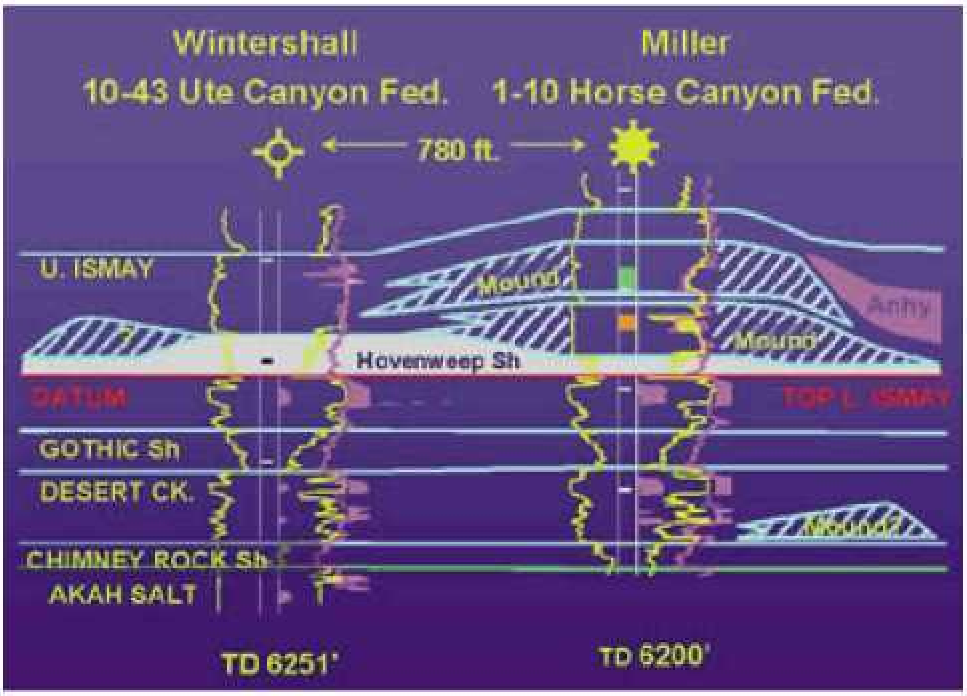

Figure 1-5. Cross section of two wells, one drilled on 2D seismic, the other on conventional 3D seismic. **The Horse Canyon Federal # I - I 0 well was drilled just south of the Blanding Prospect Area by Miller Energy in 1998. This well location was based on 3D seismic data, and is only 700 feet away from a dry hole drilled in the 1980s based on 2D seismic data. The well IP'd for 960 BOPD and 3 MMCFGPD. This is a good case history illustrating that the older 2D seismic data did reliably detect a mound, but the 3D seismic data was required to image the productive portion of the mound and resulted in a prolific new discovery. From Louden and others (2002).**

1.3 Technical Approach

1.3.1 MAIN PROJECT PHASES

The main steps in the project are outlined below:

1. Acquire a 3D9C over existing algal mound production as well as off-mound area (Towaoc & Roadrunner Fields), and additional 3D p-wave only survey over the Marble Wash area to the northwest
2. Acquire a 3D VSP (vertical seismic profile) in a well to provide velocity control for processing the 3D9C data
3. Process 3D data for P-wave, S-wave, P-S wave, AVO and anisotropic velocity attributes
4. Calibrate processed seismic data against core and well log interpretations
5. Select drilling locations
6. Calibrate processed seismic data against reservoir engineering data
7. Develop static reservoir model
8. Develop dynamic history-matched reservoir simulation model

The seismic data was acquired over portions of three existing fields, Towaoc, Roadrunner and Marble Wash (Figure 1-6), as well as non-productive acreage in between the three fields.

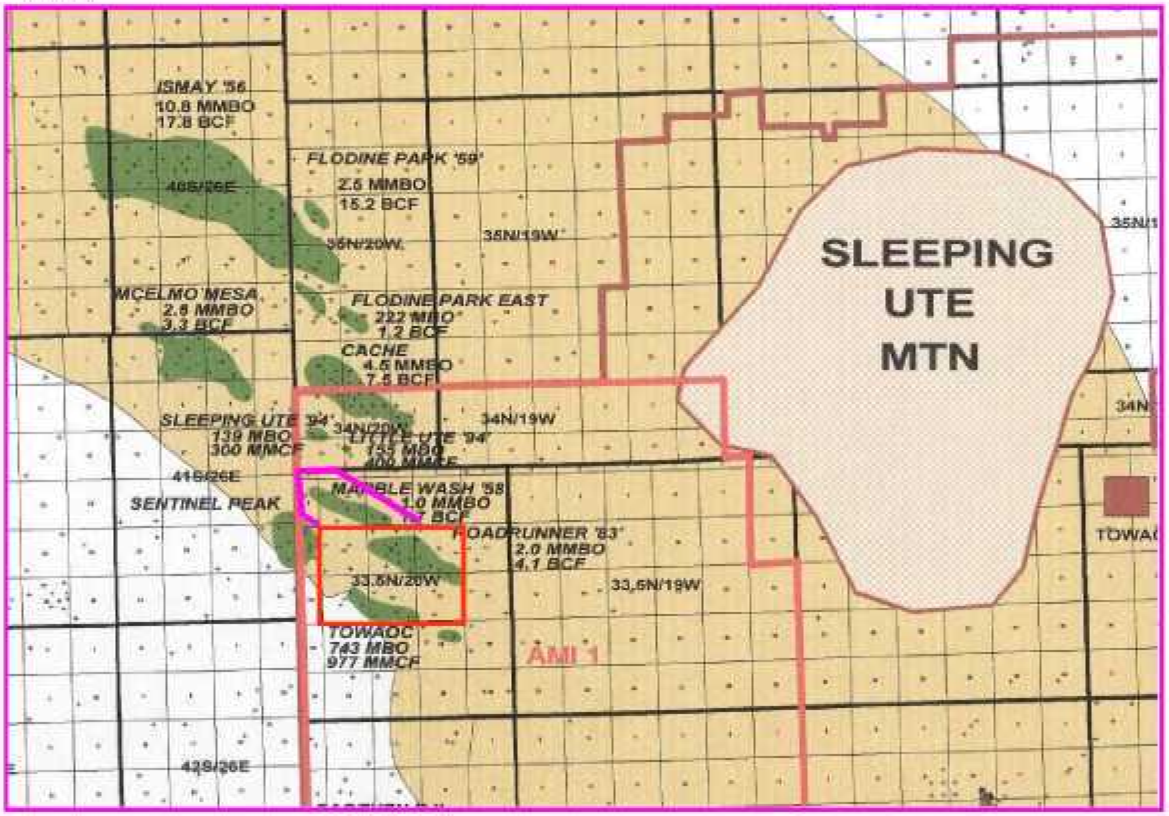

Figure 1-6. Location of the 6 square mile area (outlined by red rectangle) where 3D9C seismic data was obtained. Also shown are the outlines of existing algal mound fields (Gautier and others, 1996). The survey was later extended to the northwest to acquire P-wave data over the Marble Wash Field (purple outlined area).

1.4 Project Team

The project team pooled the resources and talents of a number of organizations and individuals. Substantial funding came from the U.S. Department of Energy ($736,696) and Red Willow (20% cost-share, increased substantially during the project through an upgrade of the 3D3C survey to a 3D9C survey, and expansion of the P-wave survey approximately 50% over the original project footprint). The project was managed by Golder Associates Inc., Redmond, WA with Paul La Pointe serving as Project Manager. The 3D9C seismic data was acquired by SolidState, headed up by Trent Middleton. The 3D Zero-offset VSP was acquired by Baker-Atlas and processed by their subsidiary, VSFusion, under the direction of Mark Miller. Tom Davis of the Colorado School of Mines provided significant survey design advice for the acquisition survey. Processing of the seismic data was carried out by AXIS Geophysics (now a part of ION corporation) by Aaron Pearson, and Rich Van Dok and Jim Gaiser of WesternGeco also processed the P-wave , PS-wave and S-wave data. Interpretation of the P-wave data was led by Claudia Rebne of Legacy Energy and Colby VanDenberg of the Southern Ute Tribe's Red Willow Production Company. Additional P-wave interpretation and interpretation of the multicomponent data was led by Robert Benson of the Colorado School of Mines. Steve Dobbs of Red Willow served as overall project manager for Red Willow's interests for the project, and played the lead role in selecting drilling locations. Multivariate analysis of the seismic data and the construction of the static reservoir model were carried out by Golder Associates' staff in Redmond, WA, under the direction of Paul La Pointe. Golder Associates' also developed and maintained the project website. Dynamic reservoir simulation was carried out by Milind Deo and Zhiqiang Gu at the University of Utah. Gerry Simon, a petroleum engineering consultant who represents Ute Mountain Ute tribal oil & gas interests, assisted the project in supplying petroleum engineering data that was needed. Virginia Wayland served as Project Manager for the U.S. Dept of Energy, National Energy Technology Laboratory. There were many unexpected hurdles to overcome in the successful execution of this project, and it is a credit to the many team members and their persistence and ingenuity that all technical, logistical and contractual obstacles were successfully overcome.

1.5 Report Outline

The remainder of this report describes the technical work completed in this project. An Executive Summary may be found in Section 2. Section 3 describes the experimental methods used to date, including the data used. Section 4 describes the project results. Section 5 describes conclusions regarding the primary project objectives. References cited are listed in Section 6, while Section 7 lists and describes the many acronyms and abbreviations used throughout this report.

2 EXECUTIVE SUMMARY

The project, "Multicomponent Seismic Analysis and Calibration to Improve Recovery from Algal Mounds: Application To The Roadrunner/Towaoc Area of the Paradox Basin, Ute Mountain Ute Reservation, Colorado", carried out under DOE Award Number: DE-FG26-02NT15451, achieved its stated goals:

1. To enhance recovery of oil contained within algal mounds on the Ute Mountain Ute tribal lands.
2. To promote the use of advanced technology and expand the technical capability of the Native American Oil production corporations by direct assistance in the current project and dissemination of technology to other Tribes.
3. To develop an understanding of multicomponent seismic data as it relates to the variations in permeability and porosity of algal mounds, as well as lateral facies variations, for use in both reservoir development and exploration.
4. To identify any undiscovered algal mounds for field-extension within the area of seismic coverage.
5. To evaluate the potential for applying CO2 floods, steam floods, water floods or other secondary or tertiary recovery processes to increase production.

Recovery has already been enhanced by the drilling and completion of the Marble Wash #9-2 well on tribal lands in the project area. This well was drilled based upon seismic data acquired, processed and interpreted by the project team, and has led to the production and sale of more than 12,000 barrels of oil and 7,000 mcf of gas. The well still continues to produce. Comparing the production rates and characteristics thus far to other vertical wells drilled into the mound complexes in the project area, the Marble Wash #9-2 could produce many tens of thousands of additional barrels of oil. Currently most of the gas is being flared, but it could become more attractive to sell the gas in the future.

The significant involvement of the technical staff of the Red Willow Energy company, a wholly-owned company of the Southern Ute Tribe, and their direct contribution of cash to the project has promoted the use of advanced multicomponent seismic technology in terms of its costs, acquisition design, processing workflows, interpretation techniques and usefulness in enhancing exploration and development. This project has greatly expanded their technical capability to undertake similar projects in the future. Additional promotion among Native American oil companies and the industry in general was carried out through presentations at conferences and industry meetings within the geophysical, geological and engineering communities.

This project is the first time that a 3D9C survey has been acquired, processed, interpreted and used for exploration and production for algal mounds. Extensive analyses evaluating various techniques were carried out to determine the relation between the multicomponent attributes and reservoir engineering parameters internal to the mounds. These internal reservoir parameters included porosity, water saturation, net to gross, permeability, and a variety of other parameters important for engineering and field development. It was found that the multicomponent data provides credible estimates of porosity-related parameters such as OOIP. Estimates of fluid saturations were less certain, although there may be several ways to improve these estimate as well, for example, using a different processing workflow to improved the frequency content of the shear wave data , or to make some adjustments to the regression equations.

Once the initial maps of gross mound thickness, gross reservoir thickness, and other reservoir stratigraphic tops and isopachs had been created from the project data, they were used to site new wells. In the project area, the mounds trend WNW. The internal thickness variation of these complexes is not smooth; there can be buildups and areas of little or no mound facies separated by very short lateral distances. Three well locations were selected and permitted in the main mound complex is areas that appeared to have thick gross reservoir and mound structure. The first well, Marble Wash #9-2, was drilled into a portion of the mound that appeared to have a good reservoir potential and at a distance from existing and historical wells. The #9-2 closely matched the pre-drill estimates of various gross thicknesses, although the drilling got stuck for over two weeks while a nearby water injector probably flushed some of the oil. There are many additional possible locations for drilling consideration that appear to be located in areas of mound thicks where there appears to be a low probability of drainage by previous wells.

A final goal of this project was to assess the potential for applying secondary or tertiary recovery methods to enhance production. The project evaluated this potential through dynamic simulation. A static model was constructed from the seismic data and well penetrations. Reservoir properties such as matrix porosity, water saturation, net-to-gross and permeability were assigned solely on the basis of the seismic attributes. The static model was used to construct a dynamic flow model that was then history-matched to ten wells in the project area. The dynamic simulations indicated that the reservoir, as modeled, contains a significant amount of oil, which is essentially locked due to lack of reservoir energy. Providing this energy in the form of water or gas drive could re-energize the reservoir and reactivate production. Indeed, analyses of secondary and tertiary recovery strategies for other algal mound fields in the Paradox Basin (Chidsey, 2003) indicate that the use of CO_2 might boost recoveries to as much as 70%. If the 4 million barrels EUR represents about a 17% primary recovery, that would suggest that an additional 12 million barrels might be recoverable through secondary or tertiary recovery.

In addition, this project has generated data that will become available to academic and government researchers and industry practitioners to use to evaluate other processing workflows or interpretation techniques. The Colorado School of Mines has already considered re-processing the data in new ways to enhance the frequency content of the shear wave data for their own objectives and at their own expense.

3 EXPERIMENTAL METHODS

3.1 3D9C Seismic Acquisition

In the fall of 2002 just prior to signing the contracts with the US Dept of Energy to initiate the project, WesternGeco, the project's intended seismic acquisition contractor, decided to discontinue this service in North America. The contract was opened to re-bid among those companies able to acquire this type of data, and SolidState, a division of Grant Geophysical was selected based on cost and crew availability. The need to find a new acquisition contractor and re-bid the contract, coupled with weather issues, caused a delay of approximately 16 months in the acquisition schedule. During the re-bid process, however, Red Willow contributed additional funds to upgrade the seismic survey from 3D3C to 3D9C, and to extend the P-wave survey to additional area to the northwest of the original project footprint (Figure 3-1). The difference between these two surveys is that the 3D9C survey uses orthogonal shear wave sources, as well as records the seismic waves using orthogonal horizontal geophones. Shear wave sources are oriented inline and crossline to the receiver lines, as are the horizontal geophones. Additional information concerning 3D9C surveys, acquisition and processing can be found in Simmons and Backus (2001).

The permits for the survey were issued in the fall of 2003 after a Finding of No Significant Impact. Due to winter weather conditions, acquisition was delayed until the spring of 2004; acquisition in the field took place between April 1, 2004 and April 22, 2004. Figure 3-2 is an image from Google Earth© of the project area and surrounding landscape. This image also shows the location of the Marble Wash #9-2 well drilled during the project whose location was based on the seismic data acquired for the project.

Figure 3-3 shows the geometry of the sources and receivers. The S-wave source direction was parallel and perpendicular to source lines (NE/SW and NW/SE) while the horizontal geophones are aligned with the receiver line direction (E/W and N/S). This required an additional rotation of the sensors to get all of them into the same frame of reference. Table 3-1 summarizes additional details of the acquisition program. Figures 3-4 through 3-13 are photos taken by project team member Claudia Rebne of Legacy Energy during the field acquisition.

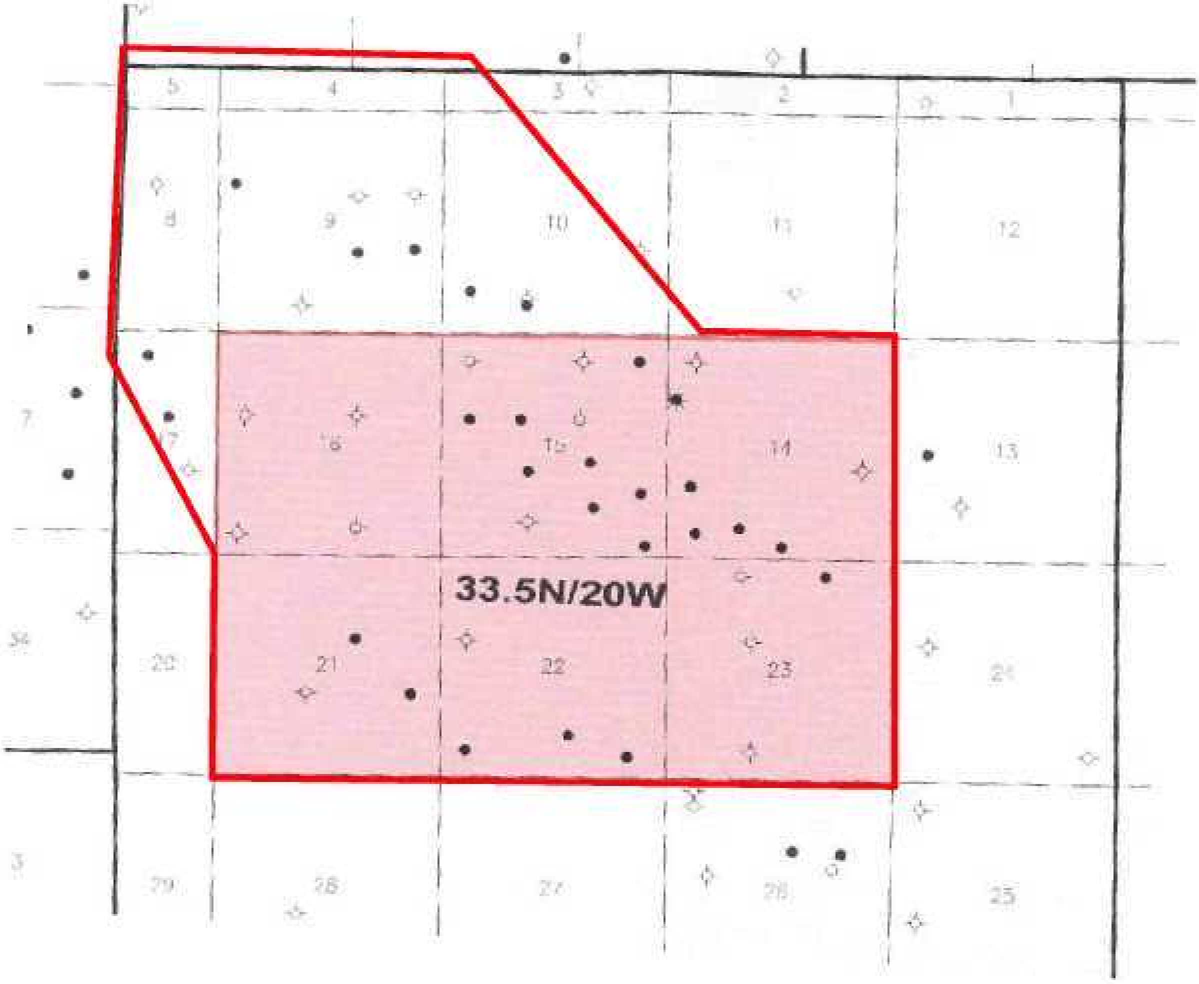

Figure 3-1. Close-up view of the 6 square mile area over which 3D9C seismic data was acquired for the project. Also shown are wells within the immediate project area. The area enclosed by the solid red line not shaded pink is the northwest extension of the P-wave survey.

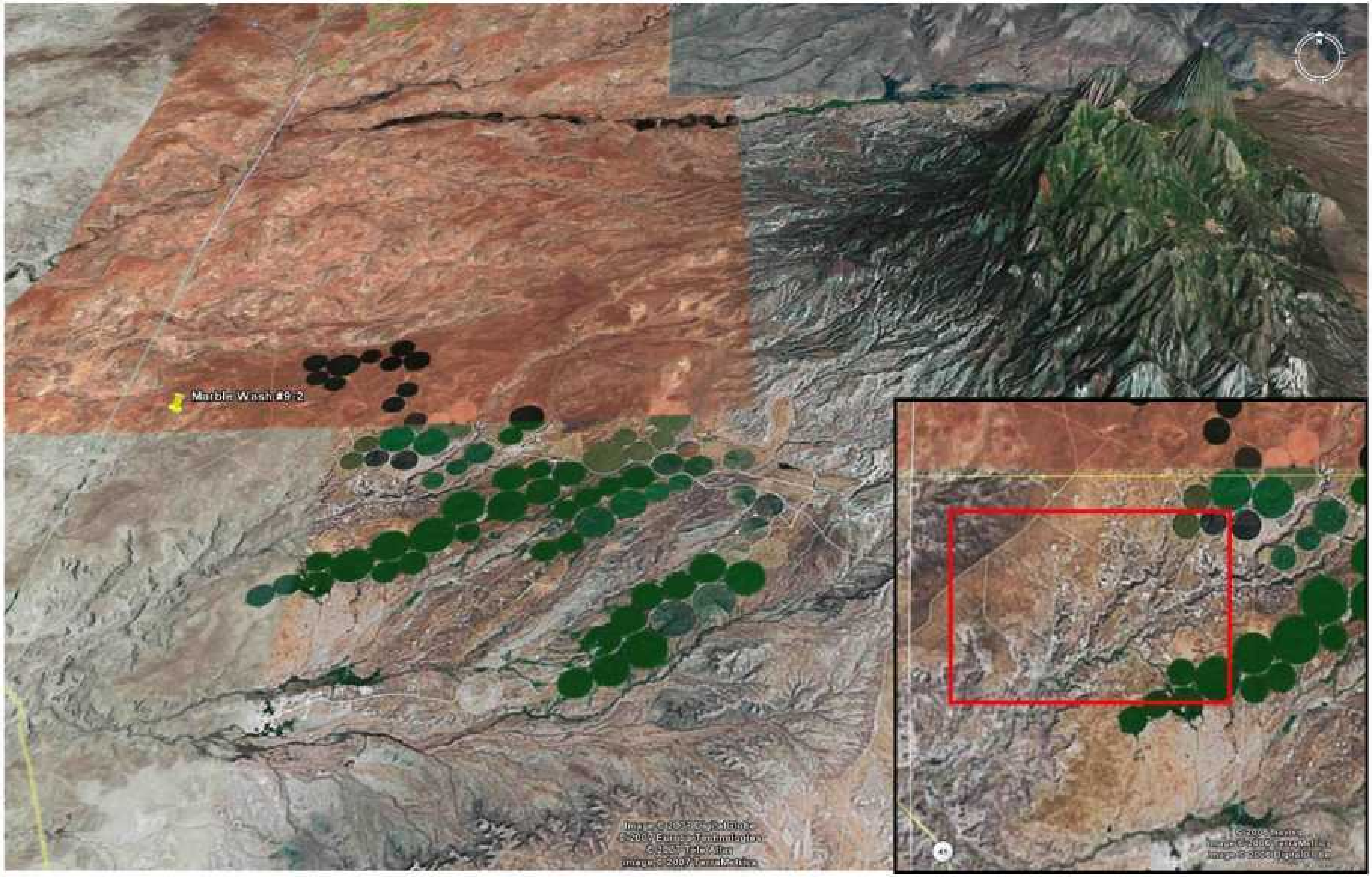

Figure 3-2. Satellite photo view of the project area. The Marble Wash #9-2 well, drilled based on the seismic data acquired for the project is shown. The drainage immediately to the south of the well location is Marble Wash. Sleeping Ute Mountain rises to the east of the project area. Inset photo shows extent of 3D9C survey. Image from GoogleEarth ©

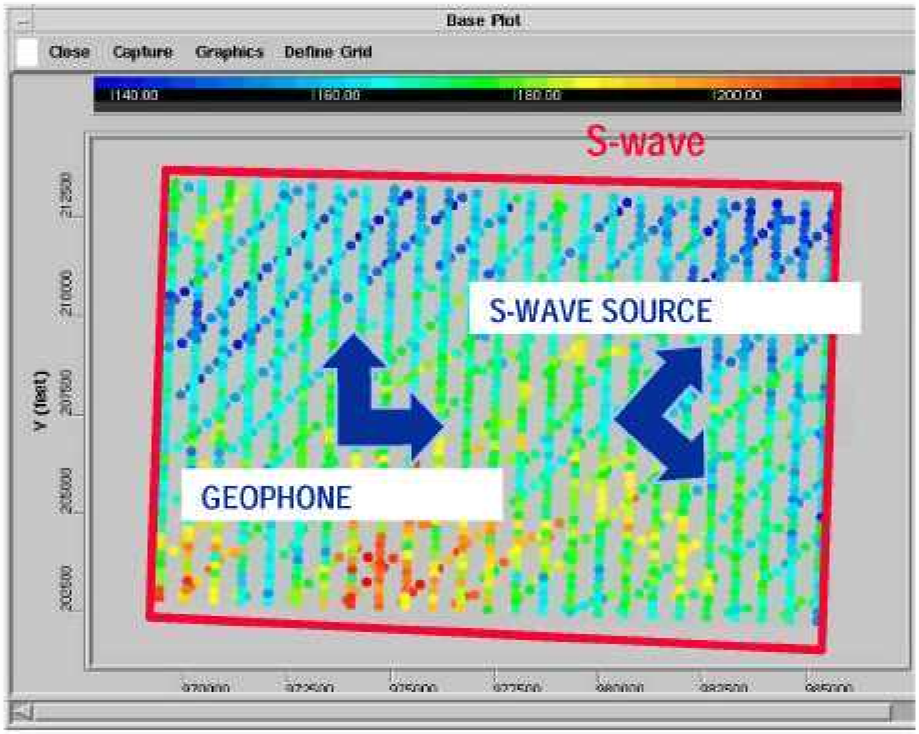

Figure 3-3. Acquisition geometry for multicomponent seismic survey.

Program Size: 6.0 square miles

Line Parameters
Receiver point interval: 220 ft
Source point interval: 220 ft
Total receiver points: 1784
Total source points: 848

Source Type for programs
P Waves: 4 sweeps x 10 seconds
Shear 1: 4 sweeps x 10 seconds
Shear 2: 4 sweeps x 10 seconds

Recording Parameters
Record Length: 6 seconds
Geophone array: 6 over 45 ft
Live patch: 14 lines X 60 channels
Roll on / roll off: Yes
Sample Rate: 2 ms

Table 3-1. Description of multicomponent acquisition program.

The following section shows photos of the 3D9C seismic acquisition. All photos were taken by Claudia Rebne, Legacy Energy.

Figure 3-4. View of Ute Mountain.

Figure 3-5. The Roadrunner Field.

Figure 3-6. Equipment staging for 3D9C acquisition

Figure 3-7. Geophones and other seismic gear being readied.

Figure 3-8. Helicopter moving equipment into sensitive areas to avoid environmental harm.

Figure 3-9. Moving trucks into position.

Figure 3-10. One of the trucks used to generate the seismic source energy.

Figure 3-11. A multicomponent geophone.


04/08/2004

Figure 3-12. Recording truck.


04/09/2004

Figure 3-13. Data recording in progress.

3.2 VSP Acquisition

The following information has been excerpted from the complete report prepared by VSFusion/Baker-Atlas. The complete report may be viewed on the project website, http://utemountain.golder.com.

3.2.1 ACQUISITION METHODS

On April 20 and 21, 2004, Baker Atlas conducted a 9-C Zero Offset and a far offset VSP Survey (Figure 3-14) in the Mountain Tribal #23-31 well (Figure 3-15), located in Montezuma, Colorado. The survey was run using a three component, one-level 6204 tool from 1000 ft to 5710 ft (305 m to 1740 m) measured depth below KB. Baker Atlas provided the wireline. Data were recorded as SEG-Y files. At the time of the survey, the well had been drilled and cased to a total depth of 6067 ft (1849 m) measured depth below KB. All measured depths were referenced to the Kelly Bushing (KB) at an elevation of 5078 ft 1547.8 m) above MSL (Mean Sea Level). The ground elevation at the wellhead was 5064 ft (1543.5 m) above MSL (Figure 3-14). The energy source was a Pelton Advance II Version 5E vibrator which had a sweep length of 10 seconds and a frequency rangy of 6 to 120 Hz for P-wave excitation. For shear wave excitation, the frequency range was 5-60 Hz.

Four (4) VSP surveys were conducted for this project. These surveys are: two (2) zero offset shear wave VSP (offset 1 and offset 2 in the field engineer's report), one (1) zero offset P-wave VSP (offset 3), and one (1) far offset P-wave VSP (offset 4). One of the shear wave source vibrator was facing NW at 309 degrees (offset 1), and the other shear wave source vibrator was facing SW at 220 degrees (offset 2).

For the zero offset surveys, the source location was 390 ft (118.9 m) away from the wellhead at an azimuth of 360 degrees. The ground elevation at the near offset source location was 5064 ft (1543.5 m) above mean sea level.

For the far offset, the P-wave source was located at 1430 ft (435.9 m) from the wellhead with an azimuth of 230 degrees from North. The ground elevation at the far offset source location was also 5064 ft (1543.5 m) above the mean sea level. The survey configuration display was shown in Figure 3-16. A map view of the zero offset and far offset source locations as well as the shear wave source directions are shown in Figure 3-17.

At the start of the survey, the wireline depth sensor was zeroed at the Kelly Bushing (KB) elevation. The geophone receiver tool was lowered down the well to 5710 ft (274 m) measured depth below KB. During downtrip, the geophone was stopped at a number of depths to check the equipment performance. Recording proceeded as the geophone was raised to the station depth of 1000 ft (305 m) measured depth below KB. At each downhole station, the wireline cable was stopped, the geophone firmly clamped to the borehole wall by means of the remote control locking arm of the tool and data recorded.

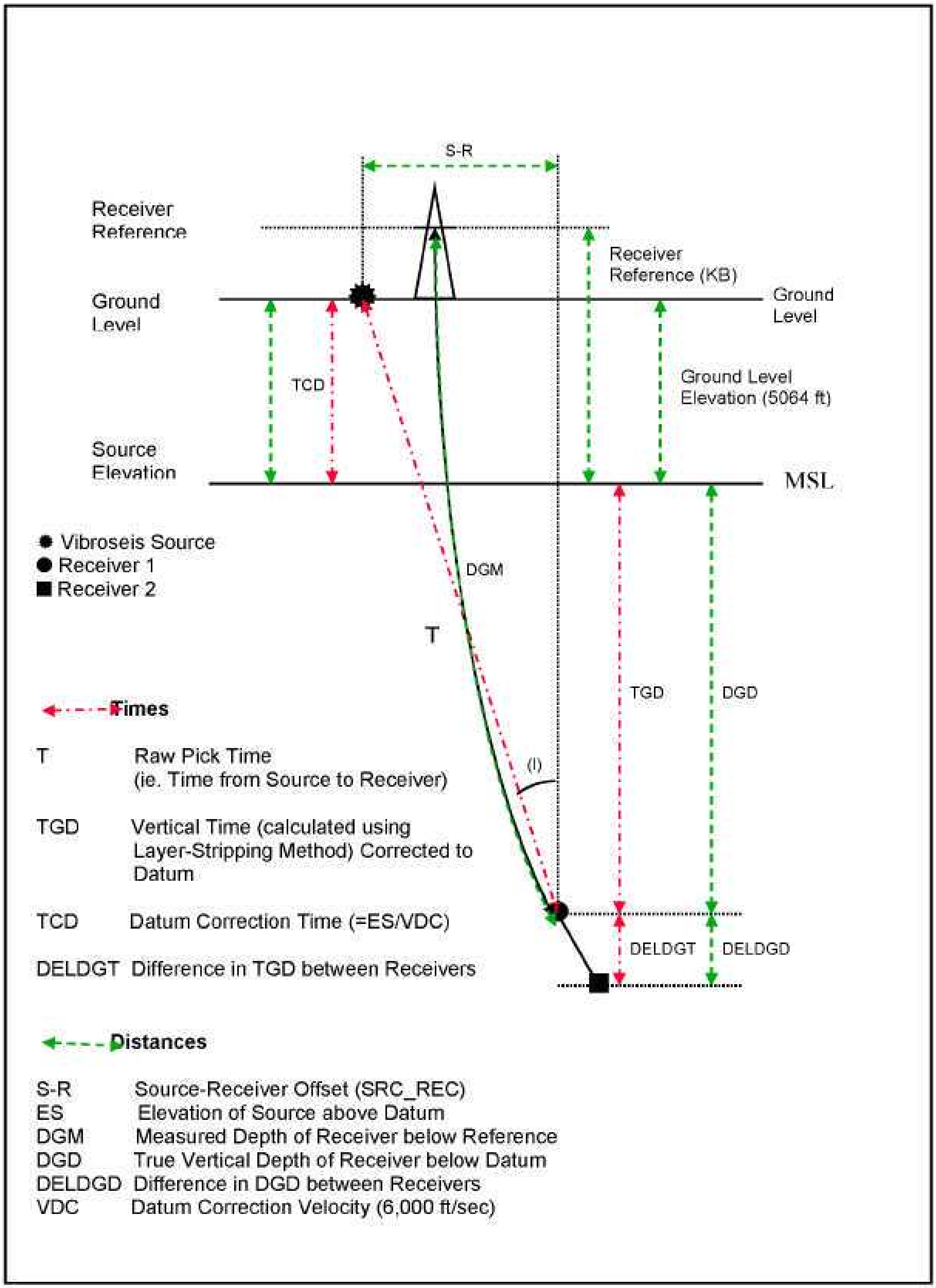

Figure 3-14. VSP Acquisition Schematic.

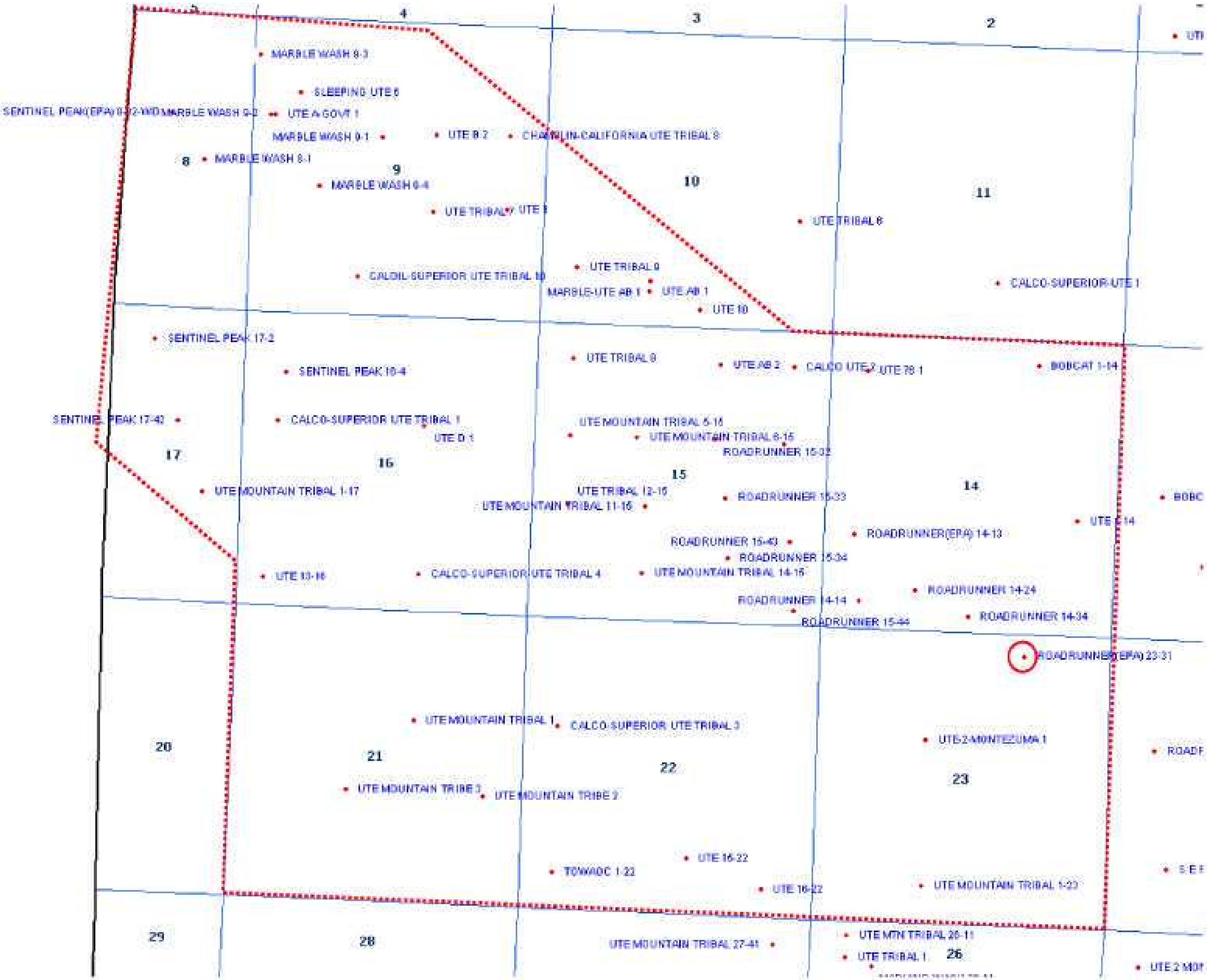

Figure 3-15. Location of wells in project area. VSP well indicated by red circle. Approximate project boundaries shown by red dashed line.

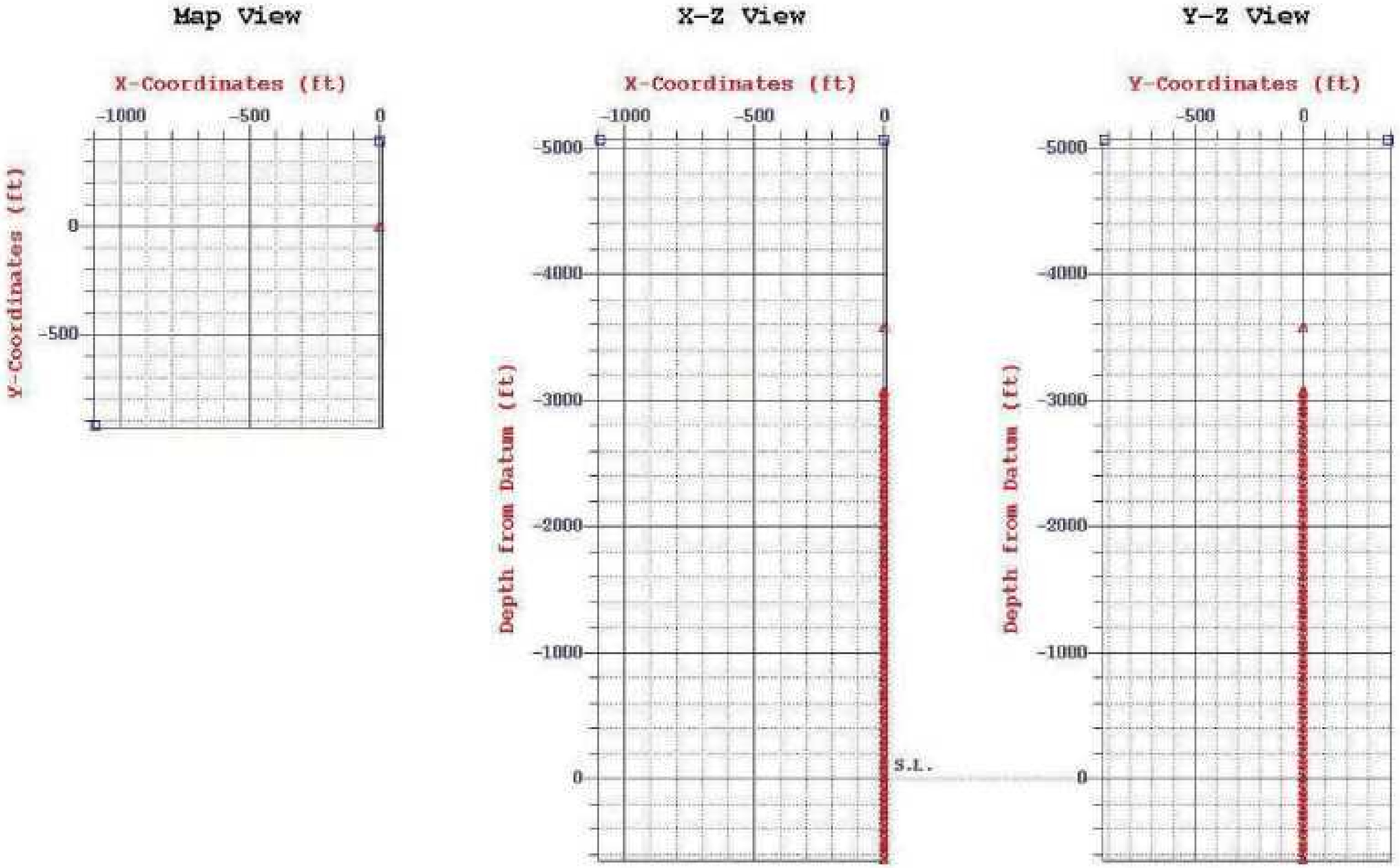

Figure 3-16. Survey geometry display.

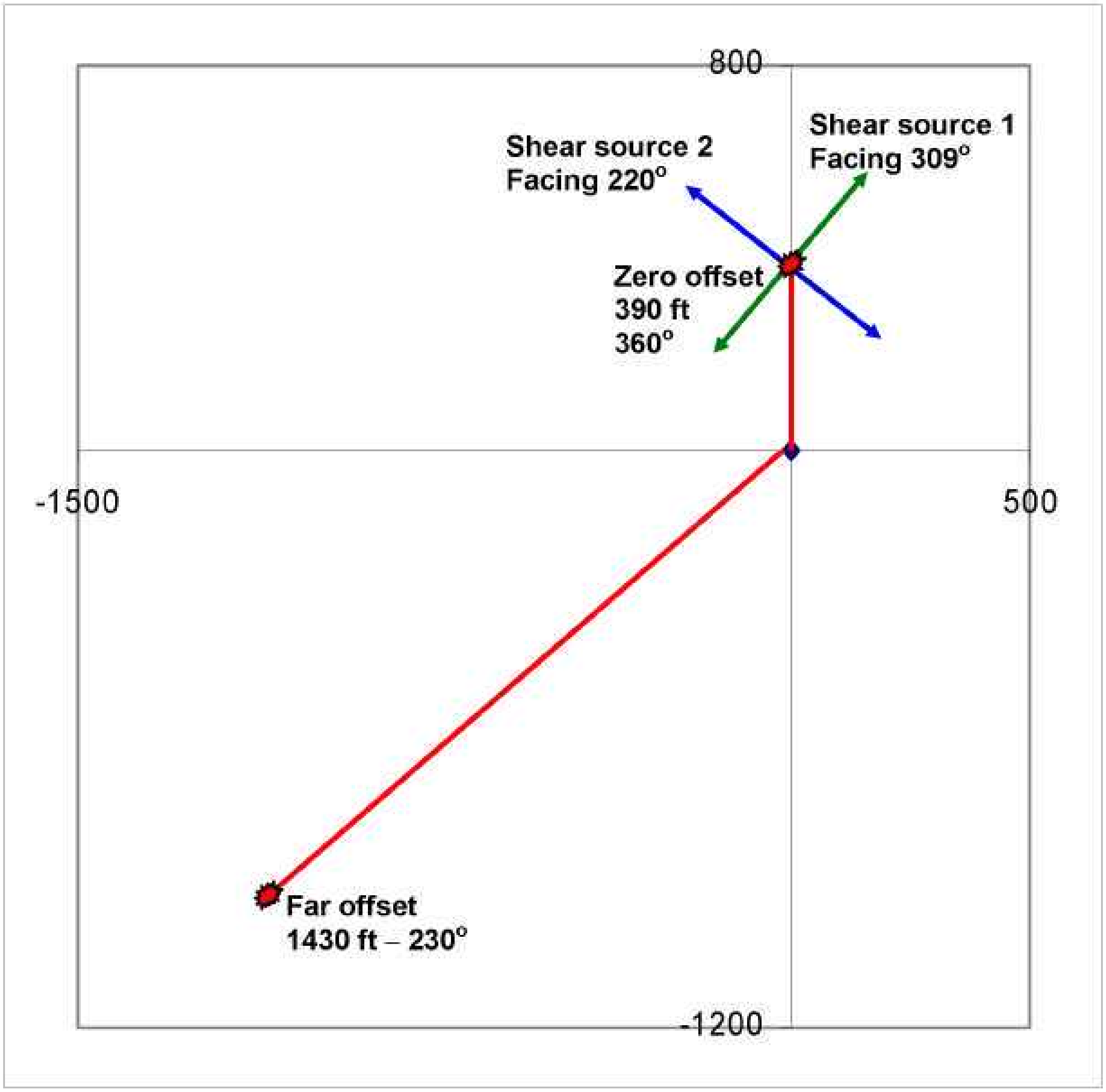

Figure 3-17. Map of the source locations and shear source directions.

When necessary, the cable was slackened after the tool was locked in position to minimize cable-induced noise. The data were recorded for 6 seconds at 2 msec sampling interval. Table 3-2 lists the acquisition survey details, while Table 3-3 lists the raw data details of the entire survey data set. Figures 3-18 through 3-20, taken by project team member Claudia Rebne of Legacy Energy, show the field acquisition of the VSP data.

Well Data:
Casing : 5.5" from 0 to 6067 ft MDKB
TD : 5721 ft MDKB

Elevations:
Kelly Bushing (KB) : 5078 ft above MSL
Ground Elevation : 5064 ft below MSL
Seismic Datum (SRD) : 0.0 ft (MSL)

Recording System:
Type : 6204
Data Format : SEGY
Sample Interval : 2 msec
Record Length : 6 seconds

Geophone:
Geophone Type : LRS1011 HT
Number of Levels Occupied : 78 levels
Shallowest Geophone Level : 1000 ft (K.B.)
Deepest Geophone Level : 5710 ft (K.B.)
Quality of Geophone Breaks: : Fair

Source:
Type : Pelton Advance II Version SE Vibrators
Zero Offset : 390 ft
Zero Offset Azimuth : 360 Degrees
Far Offset : 1430 ft
Far Offset Azimuth : 230 Degrees
Source Elevation : 5064 ft above MSL

Table 3-2. Acquisition parameters.

Survey Type	Covered Depth	Number of Traces
ZVSP P-wave (Offset 3)	1500 – 5710 ft	3031
ZVSP NW S-wave (Offset 1)	1000 – 5710 ft	3073
ZVSP SW S-wave (Offset 2)	1000 – 5710 ft	2891
OVSP P-wave (Offset 4)	1500 – 5660 ft	2856

Table 3-3. Raw data details of the data.


04/19/2004

Figure 3-18. Assembling equipment for the VSP.


04/19/2004

04/19/2004

Figure 3-19. Rig for acquisition of the VSP data.

Figure 3-20. Acquiring the VSP data.

3.3 Seismic Processing

The seismic data processing was carried out by WesternGeco and by AXIS (now part of the ION network of companies). Each company has specialized processing workstreams to extract attributes from multicomponent data; as such, both companies independently applied their technologies to the acquired seismic data. A description of the processing carried out by Western Geco is described in Section 3.3.1; the processing carried out by AXIS is described in Section 3.3.2.

3.3.1 WESTERNGECO PROCESSING

3.3.1.1 Compressional Wave Processing

The following 14 steps describe the compressional wave processing:

1. Pre-processing, consisting of
    - data transfer
    - display of shot records and deletion of bad traces
    - define geometry, compute field static corrections
    - spherical divergence compensation and trace balance
    - grid data in appropriate surface bins
2. Noise attenuation
    - f-x Coherent Noise Suppression
    - Adaptive Noise Cancellation
    - f-k Filter
3. Signal processing
    - Surface-consistent or trace-by-trace deconvolution
    - Model-based wavelet processing
    - Time variant spectral whitening
4. Preliminary stack
    - Stack with signal processing and regional velocity
5. 3D refraction statics
    - First-break picking of all records
    - Offset and weathering velocity testing
    - Stack with signal processing and refraction statics
6. 3D velocity analysis
7. Surface-consistent 3D residual reflection statics
8. NMO and trim statistics, if appropriate
9. EQ DMO and stack
10. Spectral whitening
11. Random noise attenuation (f-xy deconvolution)
12. Time-variant filter and scaling
13. Time migration
14. Spectral whitening

3.3.1.2 Shear Wave Processing

1. Pre-processing
    - Data transfer
    - Display shot records and delete bad traces
    - Define geometry – compute field static corrections
    - Extract S-wave components
    - Spherical divergence compensation and/or trace balance
    - Grid data
2. Noise attenuation
    - f-x Coherent Noise Suppression
    - Adaptive Noise Cancellation
    - f-k filter
3. Signal processing
    - Determine S1/S2 orientation of the overburden and rotate to S1/S2 coordinate system
    - Surface-consistent amplitude compensation
    - Surface-consistent deconvolution
    - Model-based wavelet procession
    - Model-based Q compensation
    - Time-variant spectral whitening
4. Preliminary stack
    - Stack with signal processing and regional velocity
5. 3D refraction statics
    - First-break picking of all records
    - Offset and weathering velocity testing
    - 3D refraction tomography
    - Use PS detector statics or hand statics as applicable
6. 3D velocity analysis
    - Azimuth limited as needed
7. Surface-consistent 3D residual reflection statics
8. 3D velocity analysis
    - Azimuth limited as needed
9. Surface-consistent 3D residual reflection statics
10. NMO and mute
11. EQ DMO and stack
12. Spectral whitening, as needed
13. Random noise attenuation (f-xy deconvolution)
14. Time-variant filter and scaling
15. Time migration
    - Full wavefield Extended Stolt
    - Modified residual method

3.3.1.3 P to S Converted Wave

1. Pre-processing
    - Data transfer
    - Display shot records and delete bad traces
    - Define geometry – compute field static corrections
    - Spherical divergence compensation and/or trace balance
    - Grid data
    - Verify orientation of H1 and H2
2. Noise attenuation)
    - f-x Coherent Noise Suppression
    - f-k filter
3. Receiver rotation to radial and transverse
4. Determine S1 and S2 from supergathers and restrict azimuths (if appropriate)
    - Receiver rotation to S1 and S2 (if appropriate)
    - Proceed with limited-azimuth volumes for statics, CCP binning and velocities
5. Signal Processing
    - Surface-consistent deconvolution
    - Model-based wavelet procession
    - Time-variant spectral whitening
6. Preliminary stack
    - Estimate preliminary γ_o
    - Stack with signal processing and regional velocity
7. P-wave source statics application
8. 3D velocity analysis
9. Receiver statics computed from common-receiver gathers/stacks
10. Surface-consistent 3D residual reflection statics
11. P-S common conversion point (CCP) binning
    - Depth-dependent correction
    - Measure γ_o from P-wave stack and preliminary PS-wave stack
    - Compute CCP locations using γ_o and γ_{eff}
12. 3D velocity analysis
13. Surface-consistent 3D residual reflection statics
14. Multi-window P-S common conversion point (CCP) binning
    - Depth-dependent correction
    - Measure γ_o from P-wave stack and preliminary PS-wave stack
    - Compute CCP locations using γ_o and γ_{eff}
15. 3D velocity analysis
16. Iterate steps 13-15 as needed
17. Higher order moveout (if necessary)
18. 3D velocity analysis
19. Final CCP bin
20. P-S DMO (if necessary)
21. Stack
22. Random noise attenuation (f-xy deconvolution)

23. Time-variant filter and scaling
24. P-S migration
25. Process transverse (or S2) component using parameters from radial (or S1)

3.3.1.4 Azimuthal Anisotropy Analysis (S-wave only)

1. 2Cx2C Alford rotation of volumes to S1/S2 and two off-diagonal components
2. Rotation and layer stripping analysis at horizons of interest

3.3.1.5 Azimuthal Anisotropy Analysis (PS-wave only)

1. Receiver rotation to radial and transverse
2. Azimuth limit radial and transverse volumes to 8 azimuth sectors (0-360 x 45 degrees); 16 total volumes
3. NMO and stack
4. Random noise attenuation (f-xy deconvolution)
5. Time-variant filtering and scaling
6. P-S time migration
7. 2C x 2C Alford rotation of volumes to S1/S2 and two off-diagonal components
8. Combine all azimuth volumes into one 2C by 2C set
9. Rotation and layer stripping analysis at horizons of interest

3.3.1.6 Summary of Data Deliverables from Processing

1. Final PP DMO stack and migration volumes – P-wave
2. Final ShSh DMO stack and migration volumes – S-wave
3. Final SvSv DMO stack and migration volumes – S-wave
4. Final ShSv DMO stack and migration volumes – Off-diagonal S-wave
5. Final SvSh DMO stack and migration volumes – Off-diagonal S-wave
6. Final PS CCP stack and migration volumes – mode-converted wave (radial component or S1)
7. Final PS CCP stack and migration volumes – mode-converted wave (transverse component or S2)
8. Fold map – CMP binning
9. Fold map – CCP binning at target horizon)
10. Vp stacking velocity field
11. Vsh stacking velocity field
12. Vsv stacking velocity field
13. Vps stacking velocity field
14. Vp/Vs voloume from PS CCP binning run
15. Detailed processing report

3.3.2 AXIS PROCESSING

3.3.2.1 Azimuthal Processing Approach

AXIS processed the 3D9C seismic data to further extract attributes, and to account for possibly azimuthal variations in velocity which has been encountered elsewhere in the Rocky Mountains. The neglect of azimuthal variations in the processing if the rock possesses azimuthally-varying velocity can lead to the following problems:

- Affects processing quality and resolution
- Requires high-resolution velocity analysis
- Causes a regional velocity overprint
- Causes mis-stacking near faults
- Affects 2D and narrow azimuth 3D data
- Causes acquisition footprint when uncorrected
- Affects time-lapse 3D comparisons
- Makes AVO analysis impossible
- Bleeds into azimuthal AVO analysis

On the other hand, when the azimuthal velocity is properly taken into account during processing, the resulting data has much greater utility for a variety of exploration and production uses. In particular, the data can be used to provide much more reliable data on:

- Fracturing below isotropic seals
- Analysis for water coning
- Analysis for water and CO2 floods
- Drilling hazard analysis and horizontal well planning
- Analysis for tight gas sweet spots
- Correct velocities for depth conversion and pressure/gas saturation prediction
- Subtle structure depth conversion
- Less 3D footprint
- Better data quality because of higher useful fold
- Better frequency content because of proper stacking
- Better surface consistent statics solutions
- Zero offset well ties

AXIS utilized three of their proprietary processing workflows to account for the possibly azimuthal velocity effects: WAVO™, AWAVO™ and the AZIM™ processing algorithms.

WAVO™ is a wavelet-based AVO method. By calculating the AVO gradient over a short time window that is proportional to the dominant frequency, incorrect values at zero crossings due to NMO stretch and tuning effects are mitigated. These potentially lead to more diagnostic crossplots and better resolution of layers.

AWAVO™ computes the AVO gradient on azimuthally sorted gathers (Figure 4-50 through Figure 4-51). The processing produces several parameters that potentially can delineate interfaces with high resolution. Parameters include:

- difference between the maximum and minimum gradients;
- direction of maximum gradient; and
- calculated error.

AZIM™ measures and corrects azimuthally varying time shifts related to azimuthally varying anisotropy (Figure 4-52 through Figure 4-55). This correction often leads to improved stack volumes. Moreover, their measurement and subsequent inversion yields velocity volumes related to the magnitude and azimuth of anisotropy as it varies both temporally and spatially.

There are a large number of attributes derived from pre- and post-stack seismic and velocities. The initial inspection shows an anomaly(ies) west and north of the 06406 well at the reservoir level. The anomaly is especially consistent between the isotropic WAVO™ and AZIM™ Vfast azimuth volumes.

3.3.2.2 Data Processing Steps & Resulting Data Sets

The processing can be separated into three portions: azimuthal velocity analysis, isotropic AVO, and azimuthal AVO.

During the azimuthal velocity analysis every 3x3 CDP was analyzed. This resulted in seven data volumes:

- RMS Vfast (RMS velocity of fast propagation direction)
- RMS Vfast minus Vslow (RMS velocity magnitude difference)
- RMS Error (Estimated error in RMS Vfast)
- RMS Azimuthal Direction (Direction of Vfast)
- Interval Vfast (Interval velocity of fast propagation direction)
- Interval Vfast minus Vslow (Interval velocity magnitude difference)
- Interval Vfast Azimuthal Direction

The isotropic AVO analysis employed a three-term fit for all angles. This produced:

- Migrated intercept
- Migrated gradient
- Migrated Third Term
- Damped Migrated Third Term in high confidence areas

The final stage of processing, azimuthal AVO, produced an additional three data sets:

- Migrated G1-G2 (High minus low gradient)
- Migrated G1 Azimuthal Direction
- Migrated G1-G2 Error

Some of these data volumes produced during processing were used to develop the calibration for detecting algal mounds and delineating their internal geological and fluid geometries. Other data volumes serve the role as quality checks, so that the areas where a particular data volume may be less reliable could be assessed and identified.

3.4 3D VSP Processing

First, the digital data was format-converted and displayed. The true reference signal traces were examined, their onset arrival times were picked at the first peaks and each downhole geophone trace was subsequently shifted by the first-break arrival time value of the corresponding true reference trace. At each depth level, an average of 6 shots was performed. The data of all shots at a depth level were edited and summed to produce a stacked 3-C digital record for this depth level. Then the stacked data were arranged according to increasing depth. Source-receiver geometry was applied. First arrival times on each depth level were picked in order to compute a time/depth curve.

The accuracy of the depth sensor was checked by comparing first arrival times of the same depth station occupied during the down and up trips. The agreement was found to be good, as shown in Table 3-4.

Measured Depth	**Time Descending**	**Time Ascending**
	Initial Picks (ms)	**Initial Picks (ms)**
5010 ft (1523 m)	451.1 (P-ZVSP)	451.0 (P-ZVSP)
5010 ft (1523 m)	466.8 (P-OVSP)	466.9 (P-OVSP)

Table 3-4. Depth sensor accuracy.

The raw 3-component data of the four VSP surveys are shown in Figure 3-21. As can be seen on the plot, the P-wave arrivals on the zero offset and far offset P-wave data were fairly good on the vertical component. However, the shear wave arrivals on the two shear source data were not consistent (peaks on some depth levels and troughs on the others) because of the geophone orientations varying from level to level down in the borehole. Higher resolution views of the displays may be viewed on the project website.

Three-component rotation was needed to get consistent shear wave arrivals for different depth levels. Theoretically, the geophone tool orientation information is needed to perform the shear wave 3-C rotation. Since this information is not available for this survey, the far offset P-wave data was first rotated to determine the geophone orientations at each depth level down in the borehole. Horizontal rotation of the far offset P-wave data at a depth level gives the orientation angle of the two horizontal geophone components at that level. This orientation angle was used to rotate the shear wave data.

Figure 3-22 displays the rotated data of the far offset P-wave VSP and the two zero offset S-wave VSP. The shear wave arrivals on the 2 shear source VSPs are very clear and consistent after rotation. Zero offset P-wave VSP data were also included Figure 3-22 with first breaks marked.

Figure 3-23 is the far offset P-wave VSP horizontal rotation hodograms display.

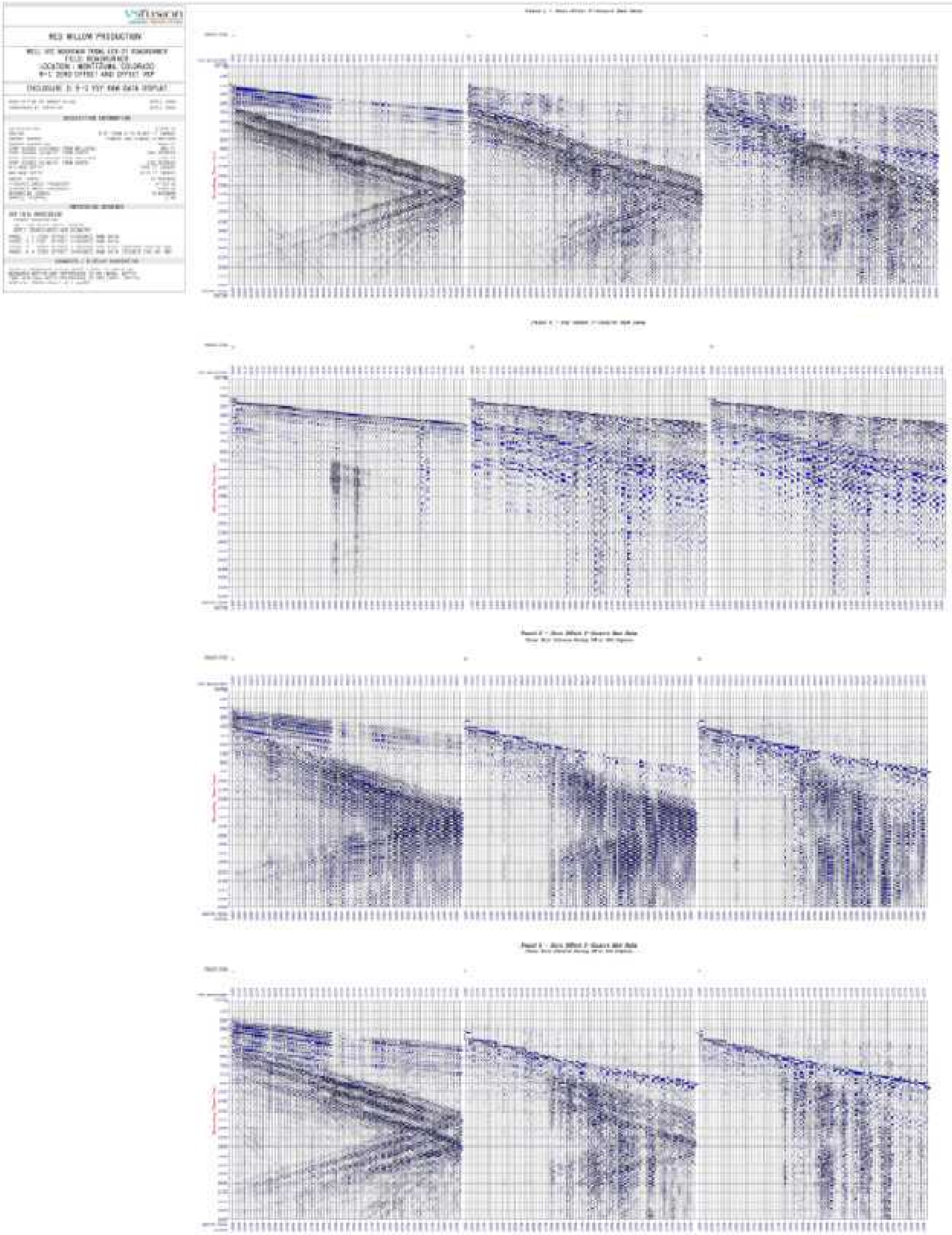

Figure 3-21. 9C VSP raw data display.

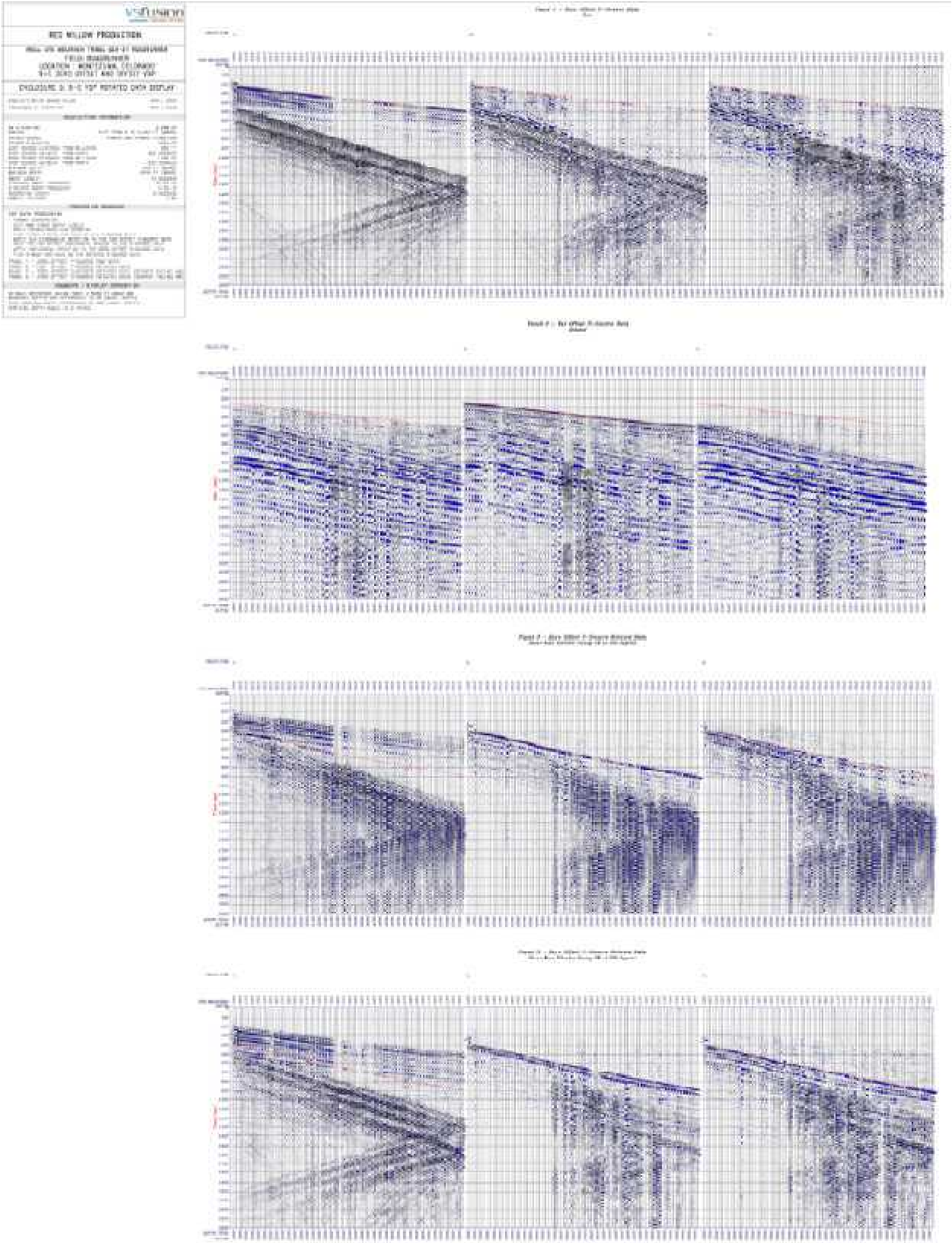

Figure 3-22. Rotated 9C VSP data display.

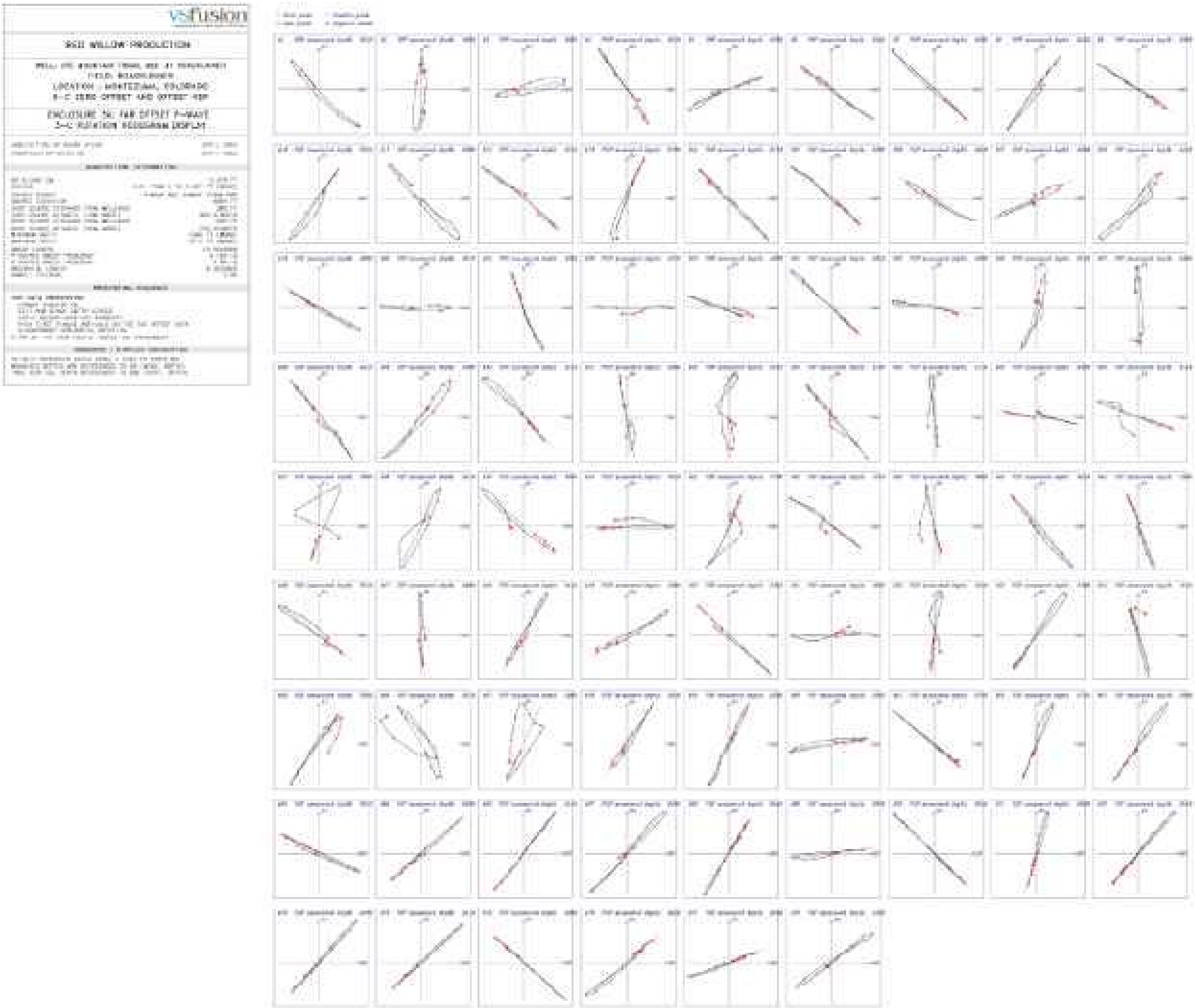

Figure 3-23. Far-offset P-wave 3C rotation hodogram display.

3.4.1 VELOCITY COMPUTATIONS

3.4.1.1 Zero offset P-wave Data (Offset 3)

The vertical component of the zero offset P-wave data was used for P-wave velocity analysis. The observed first arrival times at each depth were converted to vertical times using the bend ray method and then referenced to the datum of Mean Sea Level (MSL), using a correction velocity of 10,000 ft/sec. These time-depth pairs were then used as input for the final velocity survey computations. The average, RMS, and interval velocities were calculated.

3.4.1.2 Zero offset S-wave Data (Offset 1 and Offset 2)

The radial component of the shear wave data (after 3C rotation) was used for S-wave velocity analysis. The reference S-wave velocity at MSL was 5405 ft/sec which was calculated from the P-wave reference velocity (10,000 ft/sec) using a Vp/Vs ratio of 1.85. The average, RMS, and interval velocities were for the shear source facing NW at 309 degrees (offset 1) and for the shear source facing SW at 220 degrees (offset 2).

3.4.1.3 Vp/Vs, Vs/Vs, and Poisson Ratios

The P-wave velocity from the zero offset P-wave source and shear wave velocities from the two shear sources (NW facing and SW facing) were used to calculate dynamic Vp/Vs, Vs/Vs, and Poisson ratios.

3.4.2 VSP PROCESSING

The zero offset P-wave, far offset P-wave, and the 2 zero offset S-wave data were processed individually to get the P-wave and S-wave corridor stacks and CDP transforms.

3.4.2.1 Zero offset P-wave data

3.4.2.1.1 Total Wavefield

The summed, vertical component trace data (76 traces) were sorted by depth and used for VSP processing. A compensation for amplitude decay due to spherical divergence was applied using an exponential gain function of T**1.8 (where T is recorded time). Trace balancing was applied to the wavefield.

There was a strong tube wave package in the data. Several methods were tested to suppress the tube waves without damage the down and up going P-wave signals. None of them were very successful. An end mute was selected to cut off the tube waves before further processing.

3.4.2.1.2 Downgoing Wavefield

The direct arrivals of the wavefield data were cross-correlated with a selected reference trace, shifted in time to ensure maximum coherency of the compressional downgoing wavefield, and then aligned at 200 msec. A 9-point median filter in pass-mode was then applied to separate out the downgoing wavefield, followed by a zero phase 3/8 – 80/120 Hz bandpass.

3.4.2.1.3 Deconvolved Downgoing Wavefield

The VSP is unique in that it records the downgoing reverberant wavefield as well as the upgoing wavefield. The downgoing information can be used to design an operator that can provide effective deconvolution of the upgoing ray paths. This deconvolution is performed by using a deterministic process and is normally applied on a trace-by-trace basis.

The deterministic process provides source shaping as well as multiple suppression capabilities. The downgoing wavefield was carefully examined to determine the length of the deconvolution operator to apply to the data. The waveform is reasonably consistent over the 600 ms of live data after which it tends to vary with depth. A 600 ms trace by trace deconvolution operator was computed and then applied to the downgoing wavefield traces with 6% white noise followed by a zero phase 3/8 – 80/120 Hz bandpass filter. The application of the deconvolution operator collapses the first 600 ms of the wavefield into a spike.

3.4.2.1.4 Upgoing Wavefield

A 9-point median separation filter was applied to the wavefield on the vertical component to separate the upgoing wavefield, followed by a zero phase 3/8 – 80/120 Hz bandpass filter. The upgoing wavefield data were then shifted to two-way time in order to align the coherent upgoing wavefield and a source-to-datum correction was applied to reference the vertical time to datum, using a correction velocity of 10,000 ft/sec.

3.4.2.1.5 Deconvolved Upgoing Wavefield

Trace-by-trace deterministic deconvolution operators of 600 ms long were computed from the downgoing wavefield and were applied to the upgoing wavefield followed by a zero phase 3/8 – 80/120 Hz bandpass filter. The white noise applied was 6%. A 3-point dip median filter was applied to the deconvolved upgoing wavefield.

3.4.2.1.6 Corridor Window and Corridor Stack

A corridor of data was interactively designed using a time varying mute pattern following the first break trends to include only primary events. The resultant muted traces were median summed to one trace. This one trace was displayed repeatedly 16 times for clarity.

3.4.2.1.7 VSP-CDP Transform

A depth model was generated using velocity information calculated from zero offset P-wave velocity analysis. The model and the final upwaves were input to the VSP-CDP transform program. After specifying the survey geometry, ray tracing was performed on the input depth model to map the direct arrival times. The arrival times were then compared to the recorded first arrival times in order to update the velocities of the different layers in the model. After the model velocities had been corrected, ray tracing was done to determine the arrival time curves from the reflecting interfaces defined in the model. The model-generated arrival time curves were compared to the arrival time curves exhibited by the recorded VSP data in order to establish the accuracy of the structural model. In case of a mismatch, the VSP data was transformed to the offset and depth (x, y) space to update the model.

Starting with the shallowest velocity layer and this process was repeated for each reflecting horizon in the model. The drift between the model derived first arrival times and the recorded times were constantly monitored after each update to ensure the accuracy of the layer velocities. A 25 ft trace spacing was used to bin the data. A 3-point median enhancement filter was then applied.

3.4.2.2 Zero offset S-wave data (NW facing source, offset 1)

3.4.2.2.1 Total Wavefield

The radial component of the 3-C rotated data was used for VSP processing. A compensation for amplitude decay due to spherical divergence was applied using an exponential gain function of T**1.5 (where T is recorded time). Trace balancing was applied to the wavefield.

There were some very noisy/ringing traces in the data. A spectral analysis was carried out and it was noticed that a big spike occurred at around 36 Hz in those traces. A 36 Hz notch filter was applied to the data.

3.4.2.2.2 Downgoing Wavefield and Downwave Deconvolution

The radial component data was then processed to separate the down and up going wavefields. The shear wave arrivals of the wavefield were cross-correlated with a selected reference trace, shifted in time to ensure maximum coherency of the shear downgoing wavefield, and then aligned at 200 msec. A 13-point median filter in pass-mode was then applied to separate out the downgoing wavefield, followed by a zero phase 3/8 – 80/120 Hz bandpass filter.

Deterministic downwave deconvolution was performed using 200 ms window from shear wave arrivals with 6% white noise followed by a zero phase 3/8 – 80/120 Hz bandpass filter. The application of the deconvolution operator collapses the first 200 ms of the wavefield into a spike.

3.4.2.2.3 Upgoing Wavefield and Upwave Deconvolution

A 13-point median separation filter was applied to the radial component to separate the upgoing wavefield, followed by a zero phase 3/8 – 80/120 Hz bandpass filter.

The upgoing wavefield data were then shifted to two-way time in order to align the coherent upgoing wavefield and a source-to-datum correction was applied to reference the vertical time to datum, using a correction velocity of 5,405 ft/sec.

Another notch filter of 39 Hz was applied to the upwaves followed by a 3-point dip median filter to enhance the upwaves.

Trace-by-trace deterministic deconvolution operators of 200 ms long were computed from the downgoing wavefield and were applied to the upgoing wavefield followed by a zero phase 3/8 – 80/120 Hz bandpass filter. The white noise applied was 6. A 5-point dip median filter was applied to the deconvolved upgoing wavefield.

3.4.2.2.4 Corridor Window and Corridor Stack

A corridor of data was interactively designed using a time varying mute pattern following the first break trends to include only primary events. The resultant muted traces were median summed to one trace. This one trace was displayed repeatedly 16 times for clarity.

3.4.2.2.5 Shear Wave VSP-CDP Transform

For Shear Wave VSP-CDP transform, the depth model was generated using velocity information calculated from zero offset S-wave velocity analysis. The model and the final upwaves were input to the VSP-CDP transform program. After specifying the survey geometry, ray tracing was performed on the input depth model to map the direct arrival times. The arrival times were then compared to the recorded first arrival times in order to update the velocities of the different layers in the model. After the model velocities had been corrected, ray tracing was done to determine the arrival time curves from the reflecting interfaces defined in the model. The model-generated arrival time curves were compared to the arrival time curves exhibited by the recorded VSP data in order to establish the accuracy of the structural model. In case of a mismatch, the VSP data was transformed to the offset and depth (x,y) space to update the model.

Starting with the shallowest velocity layer and this process was repeated for each reflecting horizon in the model. The drift between the model derived first arrival times and the recorded times were constantly monitored after each update to ensure the accuracy of the layer velocities.

A 25 ft trace spacing was used to bin the data. A 3-point median enhancement filter was then applied.

3.4.2.3 Zero offset S-wave data (SW facing source, offset 2)

The procedure to process this data set is similar to that stated in Section 3.4.2.2. The radial component of the 3-C rotated data was used for VSP processing. A compensation for amplitude decay due to spherical divergence was applied using an exponential gain function of T**1.5 (where T is recorded time). Trace balancing was applied to the wavefield.

A 45 Hz notch filter was first applied to the data. Then a 13-point median filter in pass-mode was then applied to separate out the down and upgoing wavefields, followed by a zero phase 3/8 – 80/120 Hz bandpass filter.

A 38 Hz notch filter and a 3-point dip median filter were applied to the upgoing wavefield. Deterministic downwave deconvolution was performed using 200 ms window from shear wave arrivals with 6% white noise followed by a zero phase 3/8 – 80/120 Hz bandpass filter. A 5-point dip median filter was applied to the deconvolved upgoing wavefield.

A corridor of data was interactively designed using a time varying mute pattern following the first break trends to include only primary events. The resultant muted traces were median summed to one trace. This one trace was displayed repeatedly 16 times for clarity.

3.4.2.4 Far offset P-wave data

After 3-C rotation, the downgoing P-wave energy was maximized on the radial component, while the upgoing P-wave energy was maximum on the perpendicular component for the far offset P-wave data. Therefore, the radial component was used to separate downgoing wavefield using a 9-point median filter, and the perpendicular component was used to separate the upgoing wavefield. T**1.5 spherical divergence gain correction was applied before wavefield separation.

A 13-point dip median filter was applied to the upwaves to suppress the downgoing tube waves and a 15-point dip median filter was applied to remove the upgoing shear energy. A 3-point dip median filter was used to enhance the upgoing P-waves. 3/8 – 80/20 Hz zero phase bandpass filter was used following the median/dip median filters.

Deterministic downwave deconvolution was performed using 350 ms window from the first P-wave arrivals with 6% white noise followed by a zero phase 3/8 – 80/120 Hz bandpass filter. The far offset data processing sequence is shown in Figure 3-24.

VSP-CDP transform of the far offset P-wave VSP data was generated using the final upgoing wavefield and P-wave velocity model from zero offset P-wave data. The diagnostic plot together with the velocity model, the survey geometry, the input upwaves, and the drift curves are shown in Figure 3-25

3.4.3 VSP IMAGE CORRELATION DISPLAYS

3.4.3.1 Zero offset and Far offset P-wave data

For comparison, the corridor stack and VSP-CDP transform of the zero offset P-wave survey and the CDP transform of the far offset P-wave survey were combined. Following zero phase bandpass filters were then applied:

3/8 – 80/120 Hz
3/8 – 70/105 Hz
3/8 – 60/90 Hz
3/8 – 50/75 Hz

3/8 – 40/60 Hz
3/8 – 30/45 Hz

3.4.3.2 Zero offset S-wave data

The corridor stacks of the two zero offset S-wave surveys and the CDP transforms were merged into one file. The following zero phase bandpass filters were applied:

3/8 – 60/90 Hz
3/8 - 50/75 Hz
3/8 – 40/60 Hz
3/8 – 30/45 Hz
3/8 - 20/30 Hz

For data after deconvolution, normal polarity shows an increase in Acoustic Impedance (a positive reflection coefficient) as a trough.

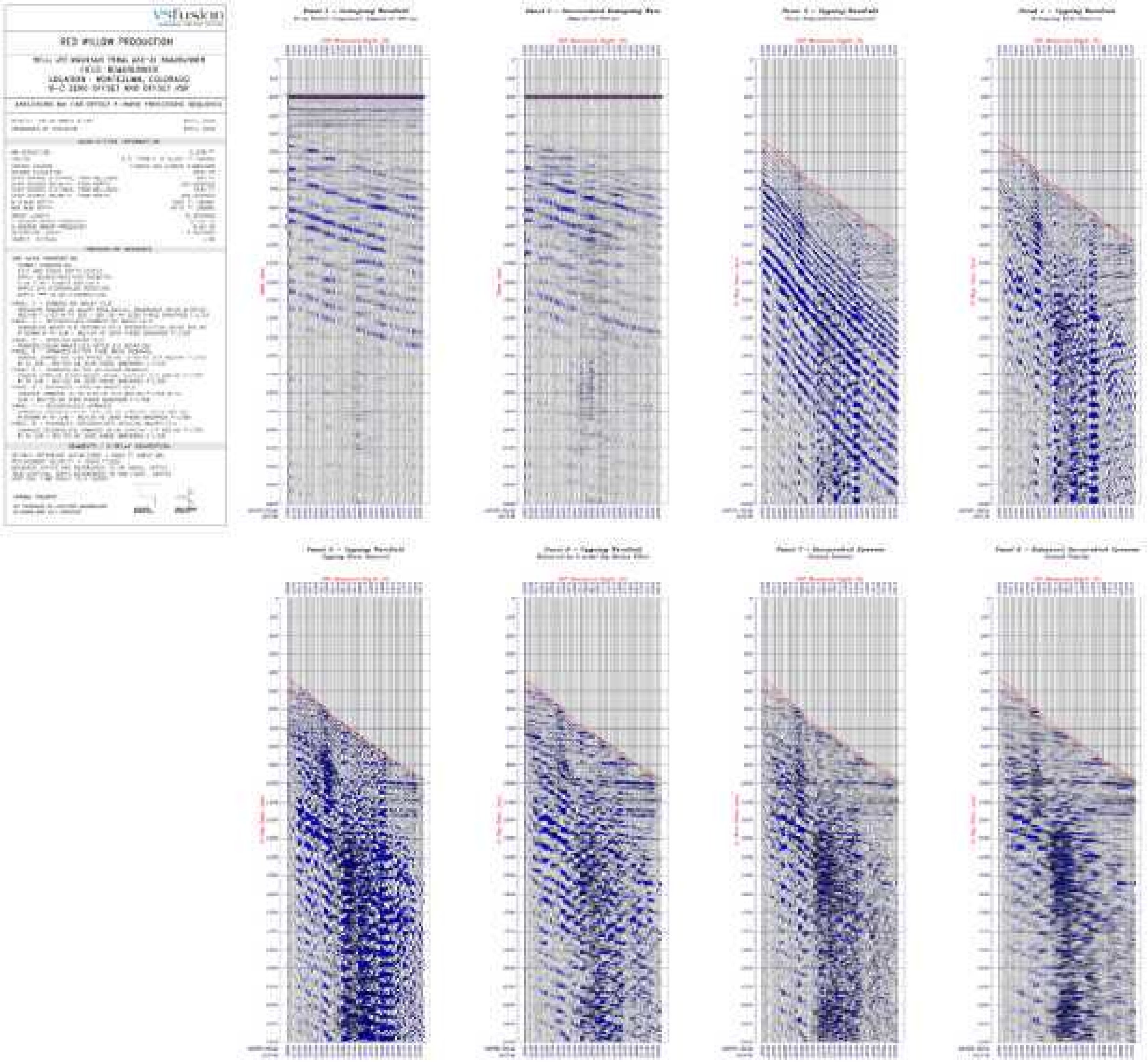

Figure 3-24. Far-offset P-wave processing sequence.

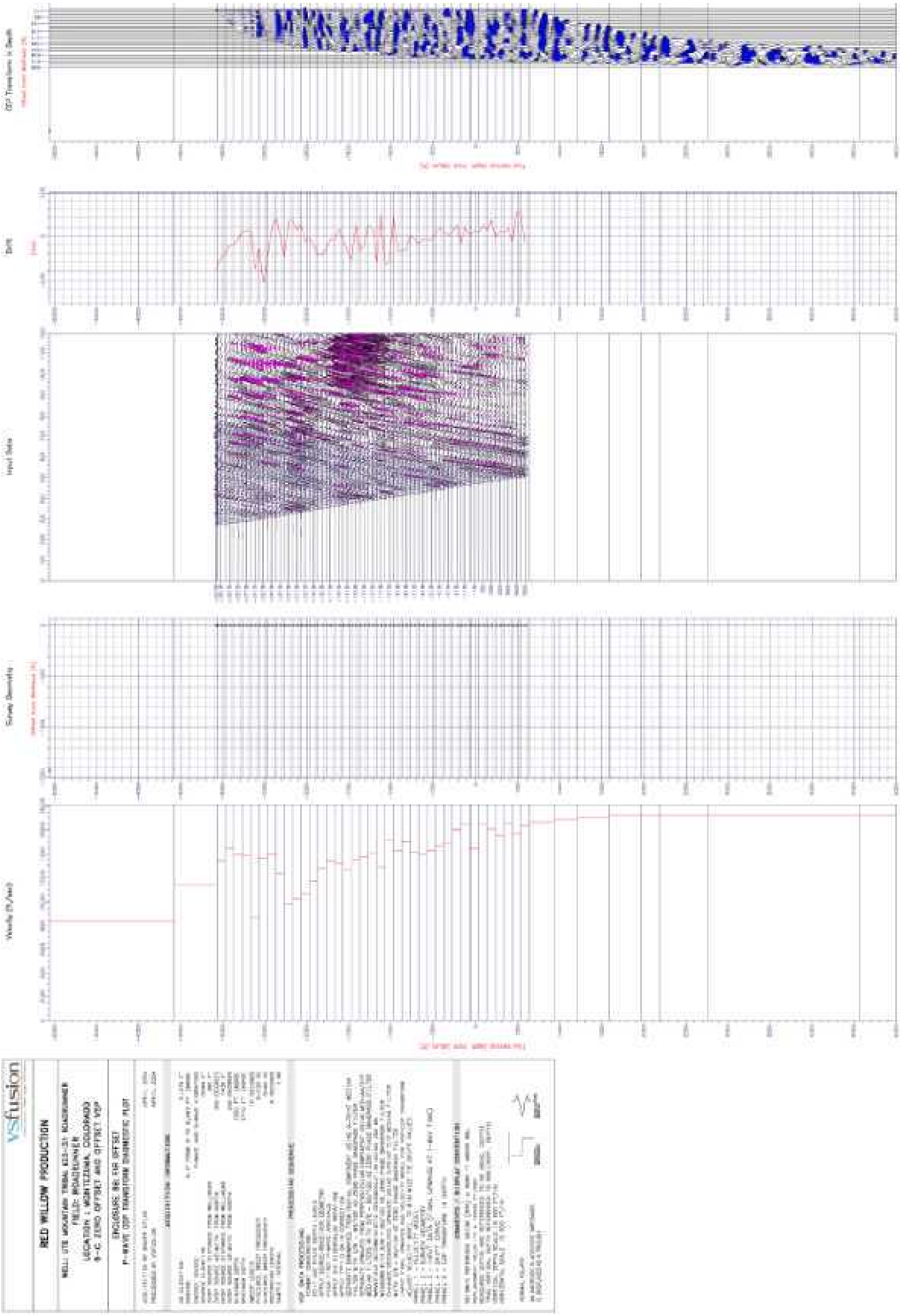

Figure 3-25. P-wave CDP diagnostic transform plot.

3.5 Development of Static Reservoir Model

3.5.1 MULTIVARIATE ANALYSIS OF P-, PS- AND S-WAVE ATTRIBUTES VS. RESERVOIR PROPERTIES

One of the goals of this project was to assess whether multicomponent seismic could provide additional constraints on the reservoir properties of the algal mound complexes, in addition to improving the geometrical resolution of the mounds. Conventional 3D P-wave data can provide good delineation of the external mound geometry and some indication of reservoir properties. Shear wave data, because of its greater sensitivity to void space and fluids, offers greater potential for characterizing reservoir properties.

Table 3-5 shows the relations that have been published among the P-, PS-, (or C-) and S-wave data attributes and reservoir properties.

Reservoir Property	**Wavefield**	**Attribute**
Porosity	P, S, PS	Amplitude, shear wave splitting
Permeability	P, S	Energy flow[1], shear wave splitting direction
Saturation	S	Shear wave splitting
Viscosity	S	Frequency and attenuation[2]
Density	P, S, PS	Amplitude variation with offset (AVO)[3]
Structure	P	Travel-time

[1] product of P- and S-wave amplitude at zero offset

[2] e.g. Duranti (2001) and Michaud (2001)

[3] Amaral (2001)

Table 3-5. Possible relationships between reservoir properties and multicomponent attributes. Table prepared by Tom Davis, Colorado School of Mines, Phase IX Proposal, Reservoir Characterization Project (http://www.mines.edu/academic/geophysics/rcp/)

The experimental method for evaluating whether seismic attributes could be used to constrain reservoir properties was motivated by the presumption that no single seismic attribute was likely to be a sufficient predictor of a reservoir attribute. Net pay, porosity and other target reservoir property in the Ismay horizons are likely to be functions of multiple geological processes, and together with the coarseness of the frequency response of the converted and shear wave data, it was thought unlikely that any single seismic attribute would have the resolution or have sufficient direct correlation with the reservoir property of interest to be able to predict the reservoir parameters. Therefore, a multivariate analysis methodology was adopted. The advantage of this approach is that the full suites of P-, C- and S-wave attributes were used jointly. The combined use of multiple variables helped to overcome the limitations of resolution, and made it possible to incorporate multiple factors for prediction.

The seismic variables used in the analysis are shown in Table 3-6 . A reference diagram illustrating the correspondence between the seismic markers and the stratigraphy is shown in Figure 3-26.

Seismic Volume	**Parameters**	**Variable Acronym**
P-wave	Top Ismay	UI
	Top Upper Ismay Carbonate	UIC
	Top Lower Ismay	LI
	Top Desert Creek	DC
	Isopach of Top Ismay to Top Upper Ismay Carbonate	UI-UIC
	Isopach of Top Upper Ismay Carbonate to Top Lower Ismay	UI-DC
	Isopach of Top Lower Ismay to Top Desert Creek	LI-DC
	Akah Salt Amplitude	PAkah_Amp
	Cutler Amplitude	PCutl_Amp
	Lower Ismay Amplitude	PLI_Amp
	Lower Ismay RMS Amplitude	PLI_RMS_Amp
	Waveform Class	WClass
	Upper Desert Creek Amplitude	PUDC_Amp
PS- (or C-) wave	Akah Amplitude	CAkah_Amp
	Gothic Shale amplitude	CGthc_Amp
	Lower Ismay Amplitude	CLI Amp
	Upper Ismay Amplitude	CUI_Amp
	Vp/Vs ratio for Gothic to Upper Ismay interval	CVpVs_Gthc-UI
S-wave	Upper Ismay Carbonate RMS Amplitude	SUIC_RMS_Amp
	Upper Ismay to Upper Ismay Carbonate RMS Amplitude	SUIC_UI_UIC_RMS_Amp
	Vp/Vs ratio for Akah Salt to Upper Ismay Interval	SVpVs_Akah-UI

Table 3-6. Variables and their acronyms used in the multivariate analyses.

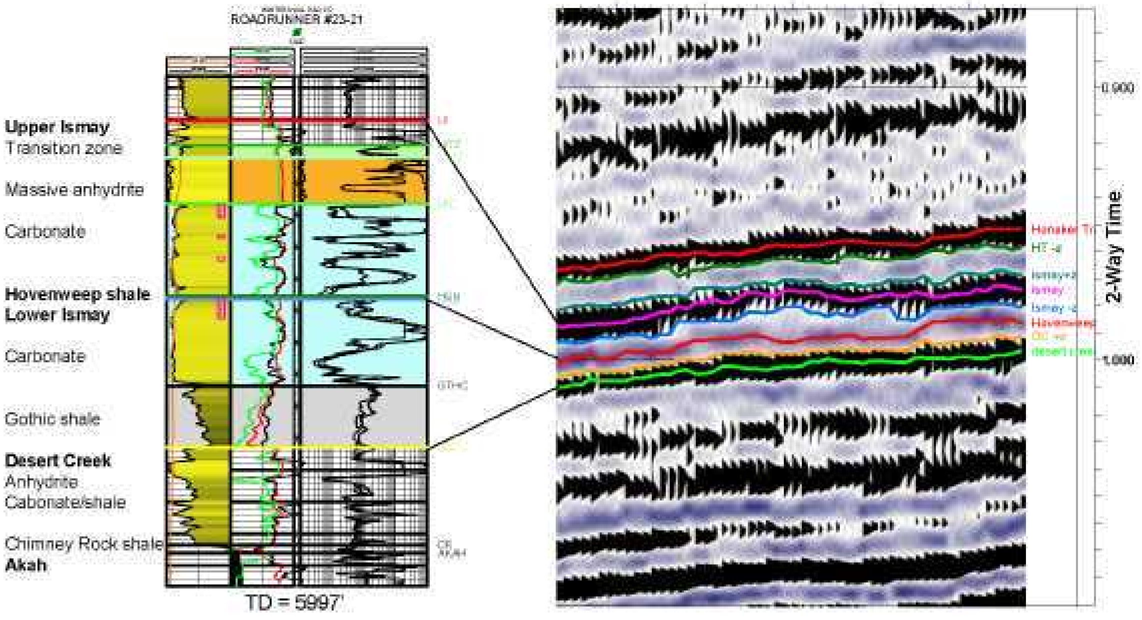

Figure 3-26. Correlation of lithostratigraphic boundaries with processed P-wave data.

Not all significant stratigraphic markers have a clear seismic expression, as shown in Figure 3-26. As a result, the surfaces corresponding to the stratigraphic tops that are poorly expressed in the seismic data were constructed though a combination of multivariate statistical analyses and geologically-based stratigraphic interpolation. Production information was aggregated at a coarser interval than the stratigraphic into five main divisions. Table 3-7 shows the wells and these divisions, which were subsequently used for multivariate analysis of production and engineering data with the seismic data.

Well Name	API Number	Zone Name
UTE MTN TRIBAL #3	5083050910000	UPPER ISMAY (Top Ismay)
	5083050910000	UI1 (Top UIC)
	5083050910000	UI2 (Internal UIC)
	5083050910000	LI1 (Top LI)
	5083050910000	LI2 (Internal LI)
UTE MOUNTAIN TRIBAL #2	5083050920000	UPPER ISMAY
	5083050920000	UI1
	5083050920000	UI2
	5083050920000	LI1
	5083050920000	LI2
UTE MTN TRIBAL #1	5083050940000	UPPER ISMAY
	5083050940000	UI1
UTE TRIBAL #1	5083051020000	UPPER ISMAY
	5083051020000	UI1
	5083051020000	UI2
	5083051020000	LI1
	5083051020000	LI2
CAL OIL-SUPERIOR #10	5083051110000	UPPER ISMAY
	5083051110000	UI1
	5083051110000	UI2
	5083051110000	LI1
	5083051110000	LI2
UTE TRIBAL-GOVT #7	5083051370000	UPPER ISMAY
	5083051370000	UI1
UTE A-GOVT #1	5083053770000	UPPER ISMAY
	5083053770000	UI1
	5083053770000	UI2
	5083053770000	LI1
	5083053770000	LI2
UTE TRIBAL #9	5083060050000	UPPER ISMAY
	5083060050000	UI1
	5083060050000	UI2
	5083060050000	LI1
	5083060050000	LI2

Well Name	API Number	Zone Name
ROADRUNNER #15-33	5083064100000	UPPER ISMAY
	5083064100000	UI1
	5083064100000	UI2
	5083064100000	LI1
	5083064100000	LI2
ROADRUNNER UTE MTN #23-31	5083064190000	UPPER ISMAY
	5083064190000	UI1
	5083064190000	UI2
	5083064190000	LI1
	5083064190000	LI2
UTE TRIBAL #8-15	5083064200000	UPPER ISMAY
	5083064200000	UI1
	5083064200000	UI2
	5083064200000	LI1
	5083064200000	LI2
UTE TRIBAL #11-15	5083064210000	UPPER ISMAY
	5083064210000	UI1
	5083064210000	UI2
	5083064210000	LI1
	5083064210000	LI2
UTE TRIBAL #5-15	5083064240000	UPPER ISMAY
	5083064240000	UI1
	5083064240000	UI2
	5083064240000	LI1
	5083064240000	LI2
SENTINEL PEAK #17-2	5083064410000	UPPER ISMAY
	5083064410000	UI1
	5083064410000	UI2
	5083064410000	LI1
	5083064410000	LI2
ROAD RUNNER #16-34	5083064450000	UPPER ISMAY
	5083064450000	UI1
	5083064450000	UI2
	5083064450000	LI1
	5083064450000	LI2

Well Name	API Number	Zone Name
UTE-AB #1	5083060080000	UPPER ISMAY
	5083060080000	UI1
	5083060080000	UI2
	5083060080000	LI1
	5083060080000	LI2
SENTINEL PEAK #17-42	5083063310000	UPPER ISMAY
	5083063310000	UI1
	5083063310000	UI2
	5083063310000	LI1
	5083063310000	LI2
SENTINEL PEAK #8-32	5083063320000	UPPER ISMAY
	5083063320000	UI1
	5083063320000	UI2
	5083063320000	LI1
	5083063320000	LI2
TOWAOC #1-22	5083063570000	UPPER ISMAY
	5083063570000	UI1
	5083063570000	UI2
	5083063570000	LI1
	5083063570000	LI2
UTE MOUNTAIN #14-13	5083063990000	UPPER ISMAY
	5083063990000	UI1
	5083063990000	UI2
	5083063990000	LI1
	5083063990000	LI2
UTE MTN UTE TRIBAL #14-24	5083064050000	UPPER ISMAY
	5083064050000	UI1
	5083064050000	UI2
	5083064050000	LI1
	5083064050000	LI2
UTE MTN UTE TRIBAL #15-43	5083064060000	UPPER ISMAY
	5083064060000	UI1
	5083064060000	UI2
	5083064060000	LI1
	5083064060000	LI2

Well Name	API Number	Zone Name
ROADRUNNER #14-14	5083064670000	UPPER ISMAY
	5083064670000	UI1
	5083064670000	UI2
	5083064670000	LI1
	5083064670000	LI2
ROADRUNNER #14-34	5083064690000	UPPER ISMAY
	5083064690000	UI1
	5083064690000	UI2
	5083064690000	LI1
	5083064690000	LI2
ROADRUNNER #15-44	5083064710000	UPPER ISMAY
	5083064710000	UI1
	5083064710000	UI2
	5083064710000	LI1
	5083064710000	LI2
ROADRUNNER #23-21	5083064810000	UPPER ISMAY
	5083064810000	UI1
	5083064810000	UI2
	5083064810000	LI1
	5083064810000	LI2
UTE #16-22	5083064900000	UPPER ISMAY
	5083064900000	UI1
	5083064900000	UI2
	5083064900000	LI1
	5083064900000	LI2
UTE #15-22	5083065010000	UPPER ISMAY
	5083065010000	UI1
	5083065010000	UI2
	5083065010000	LI1
	5083065010000	LI2
MCLISH-UTE TRIBAL #1-23	5083070010000	UPPER ISMAY
	5083070010000	UI1
	5083070010000	UI2
	5083070010000	LI1
	5083070010000	LI2

Table 3-7. List of wells and intervals with reservoir property information.

The reservoir variables considered in the analyses and their acronyms are shown in Table 3-8.

Gross Interval	Net Pay Int (TVD)	Avg Phi (Pay)
Avg Net Sw (Pay)	Avg VClay (Pay)	Pay/Gross Ratio
HPVH (Pay)	PHIH (Pay)	Net Res Int (TVD)
Avg Phi (Res)	Avg VClay (Res)	Res/Gross (Res)

Table 3-8. Reservoir variables used in multivariate analyses.

The first step in the analysis was to compute the Spearman correlation coefficients (Spearman, 1904) among the variables. Spearman coefficients were selected instead of the more familiar Pearson coefficients (which require that the variables are normally-distributed) because they are a non-parametric measure of correlation, and the probability distribution of the variables could not be ascertained given the relatively small amount of data available for analyses. The reason why correlation coefficients were calculated was to gain knowledge about the mathematical structure of the data; this knowledge was then used to guide the construction of the multivariate models.

The next step in the multivariate analysis workflow was to construct a series of multivariate regression models for each reservoir variable as a function of the seismic variables. The steps adopted for the multivariate regression are listed below:

1. Select a reservoir variable of interest from Table 3-8 as the dependent variable;
2. Select all seismic variables listed in Table 3-6;
3. Run a stepwise regression using an F-entry probability of 0.05 and an F- removal probability of 0.10 (Snedecor and Cochran, 1980);
4. Assess co-linearities among the remaining "independent" variables using the Variance Inflation Factor (VIF) and tolerance statistics (Woolridge, 2000). Remove "independent" variables such that remaining variables have VIF's greater than 15, using the correlation matrix as a guide.
5. Evaluate overall regression in terms of F-statistic and display results visually.
6. Accept any regression that is statistically significant in terms of individual coefficients ($\alpha = 0.05$), VIF (all predictor variables < 15) and regression variance as expressed by the statistical significance of the F-statistic (< 0.05).

All calculations were carried out using SPSS 13.0 (SPSS, 2004).

The results of these four calculations:

1. Address the project goal of determining whether multicomponent data can provide additional constraints on reservoir properties in algal mounds, and
2. Provide quantitative models to constrain one or more reservoir properties in the static model of the project area.

3.6 Construction of 3D Static Reservoir Model in Petrel

The construction of a 3D static reservoir model formed the basis for a dynamic siulation of the mound complex. The steps to create this model were as follows:

1. Import all of the seismically-determined reservoir tops, which consist of the Top of the Ismay, the Top of the Upper Ismay Carbonate, the Top of the Lower Ismay, and the Top of the Desert Creek. These were the only horizons that could be seismically delineated with sufficient confidence.
2. Add additional internal horizons based upon well penetrations and conformal or erosional interpolations.
3. Add properties to the layers in between the horizons based on the results of the multivariate regressions
4. Prepare an Eclipse™ reservoir simulation grid based on the results.

The model was constructed with Petrel^{TM} version 2005 (Schlumberger, 2005).

3.7 Development of Dynamic Reservoir model

The dynamic reservoir model was based upon the 3D static model for material properties and discretization geometry. In addition, well histories and other dynamic information was used to establish initial and boundary conditions, and to carry out the flow simulation over the algal mound complexes.

The creation of the static and dynamic reservoir models, and the field simulation, were carried out using Petrel^{TM} 2005 and Eclipse^{TM} 2006.2. The first step in this workflow was to create a dynamic simulation grid from the static model. The corner point geometry was considered to be a good method to grid the complex reservoir volume, since this scheme permitted the cells to have any physically valid shapes and was based on the notion of the co-ordinate lines and corner depths. In the model that was created, the z-coordinate lines were vertical, so the (X, Y) locations of points for each layer were the same. The basic mesh information is provided below:

Grid: 150*100*7
Grid block size: 100*100*depth (m)

There were seven layers in the reservoir (Upper Ismay, UI1, UI2, Hovenweep Shale, LI1, LI2 and UDC). The seismic data was available on a prescribed grid. The required reservoir properties were generated from the seismic data, and distributed on the reservoir model grid by using the seismic correlations with interpolations when necessary. A general computer program in C++ was written to transform the seismic data to Eclipse™ grid data.

The multicomponent seismic data was used to generate the reservoir properties using the multivariate approach for each cell. The seismic attributes (P-wave, PS-wave and S-wave), depth and gross data on the observation grid were used to calculate the reservoir properties (porosity, net to gross and water saturation). The correlations used were for "Reservoir" since the correlations for "Pay" were less statistically robust. Absolute permeability of each cell was obtained from the correlation of porosity and permeability as:

$$\log P_{absolute} = \log(\phi * 100)/\log 2 + 1.0 - 1/\log 2 \qquad \textbf{Equation 3-1}$$

The same porosity to permeability correlation was used for all the layers, which may not be an accurate representation of the permeability structure in the reservoir. Three of the layers (Upper Ismay, Hovenweep shale and UDC) do not contain any oil, and therefore are not considered to be part of the reservoir.

4 RESULTS AND DISCUSSION

4.1 Zero-Offset VSP

The velocities and variables calculated from them are shown in Figure 4-1, Figure 4-2 and Table 4-1. The first figure presents the velocities, while the second shows velocity ratios and the dynamic value of Poisson's ratio calculated from the velocities.

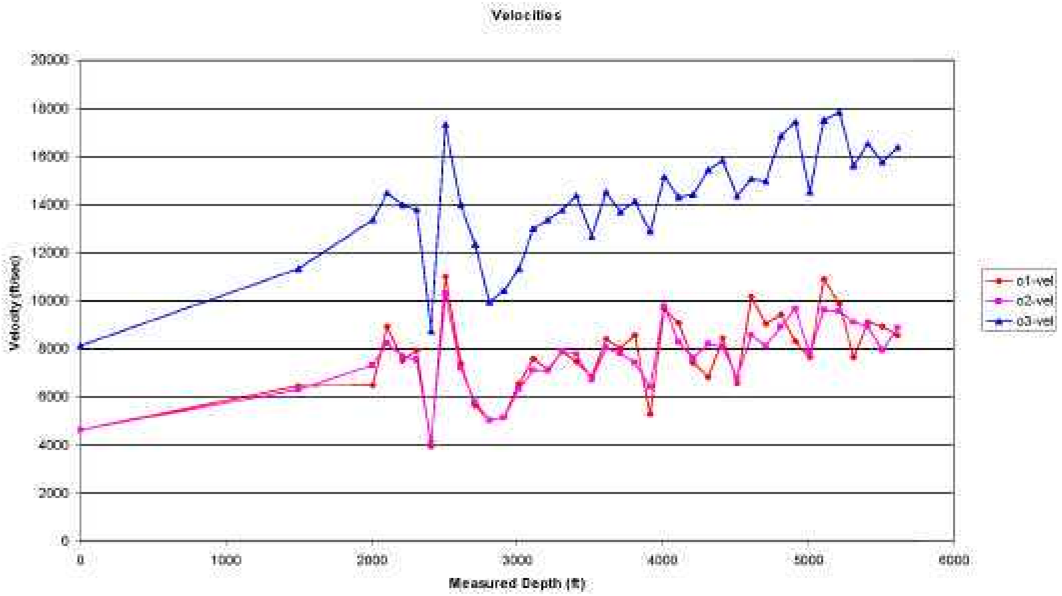

Figure 4-1. Zero offset VSP velocities (o3 – zero offset P-wave; o1 – zero offset NW facing source S-wave; o2 – zero offset SW facing source S-wave)

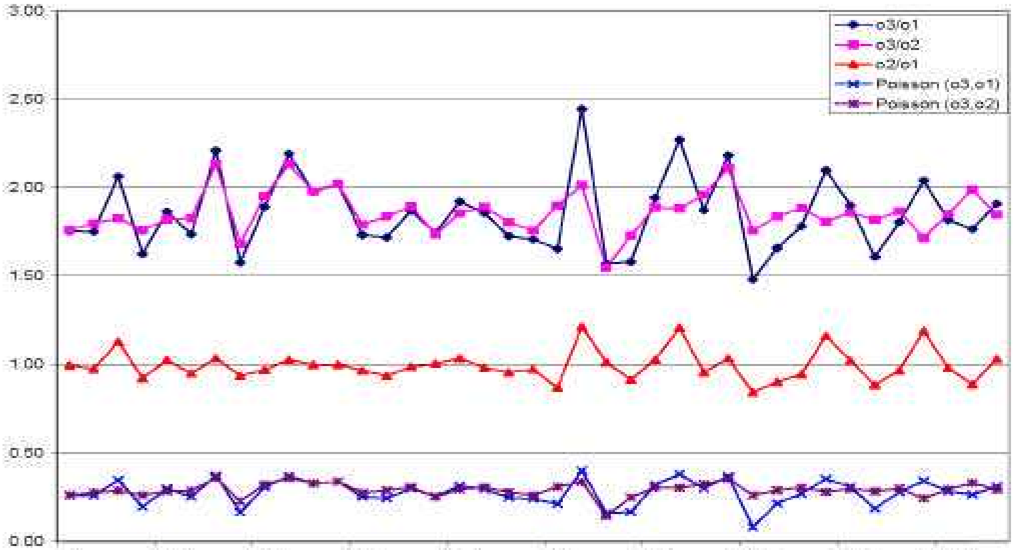

Figure 4-2. Vp/Vs, Vs/Vs, Poisson Ratio (o3 – zero offset P-wave; o1 – zero offset NW facing source S-wave; o2 – zero offset SW facing source S-wave)

MD (ft)	o1-vel	o2-vel	o3-vel	o3/o1	o3/o2	o2/o1	pois(o1)	pois(o2)
0	4630	4612.7	8124.7	1.75	1.76	1.00	0.26	0.26
1500	6451.1	6288.1	11303.2	1.75	1.80	0.97	0.26	0.28
2010	6464.9	7298.7	13351	2.07	1.83	1.13	0.35	0.29
2110	8897	8224.3	14478.1	1.63	1.76	0.92	0.20	0.26
2210	7483.1	7666.4	13966.5	1.87	1.82	1.02	0.30	0.28
2310	7936	7543.9	13794.8	1.74	1.83	0.95	0.25	0.29
2410	3945	4082	8720	2.21	2.14	1.03	0.37	0.36
2510	10980.7	10287.9	17321.2	1.58	1.68	0.94	0.16	0.23
2610	7377.1	7149	13960	1.89	1.95	0.97	0.31	0.32
2710	5619.3	5773.6	12320	2.19	2.13	1.03	0.37	0.36
2810	5020.3	5009.4	9920	1.98	1.98	1.00	0.33	0.33
2910	5141	5141.4	10406	2.02	2.02	1.00	0.34	0.34
3010	6532.7	6316.3	11324.2	1.73	1.79	0.97	0.25	0.27
3110	7557.2	7077.9	13000	1.72	1.84	0.94	0.24	0.29
3210	7139.7	7043.5	13347.1	1.87	1.89	0.99	0.30	0.31
3310	7869.5	7907.3	13727.8	1.74	1.74	1.00	0.26	0.25
3410	7470.6	7734.5	14360	1.92	1.86	1.04	0.31	0.30
3510	6802.8	6683.3	12640	1.86	1.89	0.98	0.30	0.31
3610	8397.4	8030.3	14505.5	1.73	1.81	0.96	0.25	0.28
3710	8005.7	7782.6	13680	1.71	1.76	0.97	0.24	0.26
3810	8533.2	7430.2	14115.9	1.65	1.90	0.87	0.21	0.31
3910	5266.7	6390.4	12880	2.45	2.02	1.21	0.40	0.34
4010	9626.4	9757	15120	1.57	1.55	1.01	0.16	0.14
4110	9047.6	8272.7	14303.2	1.58	1.73	0.91	0.17	0.25
4210	7408.9	7617.4	14400	1.94	1.89	1.03	0.32	0.31
4310	6791.9	8198.9	15431.5	2.27	1.88	1.21	0.38	0.30
4410	8436.9	8064.4	15812.8	1.87	1.96	0.96	0.30	0.32
4510	6557.6	6779.4	14314.2	2.18	2.11	1.03	0.37	0.36
4610	10153.8	8563.4	15044.7	1.48	1.76	0.84	0.08	0.26
4710	9006.4	8124.5	14938.5	1.66	1.84	0.90	0.21	0.29
4810	9434.9	8925.7	16829.8	1.78	1.89	0.95	0.27	0.30
4910	8293.1	9626.2	17413.9	2.10	1.81	1.16	0.35	0.28
5010	7624.9	7793.8	14501.7	1.90	1.86	1.02	0.31	0.30
5110	10860.8	9610.5	17482	1.61	1.82	0.88	0.19	0.28
5210	9864.8	9544.1	17819.7	1.81	1.87	0.97	0.28	0.30
5310	7630.3	9077	15582.6	2.04	1.72	1.19	0.34	0.24
5410	9077.4	8913	16510.8	1.82	1.85	0.98	0.28	0.29
5510	8918.1	7921.1	15760	1.77	1.99	0.89	0.26	0.33
5610	8563.2	8839.5	16355.3	1.91	1.85	1.03	0.31	0.29
5860								
Average				1.86	1.86	1.00	0.28	0.29

Table 4-1. Velocities and values of dynamic Poisson's ratio calculated from them.

The data files used to create these two figures and summary table can be viewed on and downloaded in ASCII format from the project web site.

4.1.1 CORRIDOR STACKS

Figure 4-3 and Figure 4-4 respectively show the Far- and Near-offset P-wave and Zero-offset S-Wave corridor stacks and CDP transform correlation displays. Higher quality CGM and PDF formats of these figures can be found on the project web site. For data after deconvolution, normal polarity shows an increase in Acoustic Impedance (a positive reflection coefficient) as a trough.

4.1.1.1.1 Zero-offset and Far-offset P-wave data

For comparison, the corridor stack and VSP-CDP transform of the zero-offset P-wave survey and the CDP transform of the far offset P-wave survey were combined. The following zero phase bandpass filters were then applied:

- 3/8 – 80/120 Hz
- 3/8 – 70/105 Hz
- 3/8 – 60/90 Hz
- 3/8 – 50/75 Hz
- 3/8 – 40/60 Hz
- 3/8 – 30/45 Hz

The filtered data were displayed in Figure 4-3 for both normal and reversed polarities.

4.1.1.1.2 Zer- offset S-wave data

The corridor stacks of the two zero offset S-wave surveys and the CDP transforms were merged into one file and displayed in Figure 4-4. The following zero phase bandpass filters were applied:

- 3/8 – 60/90 Hz
- 3/8 – 50/75 Hz
- 3/8 – 40/60 Hz
- 3/8 – 30/45 Hz
- 3/8 – 20/30 Hz

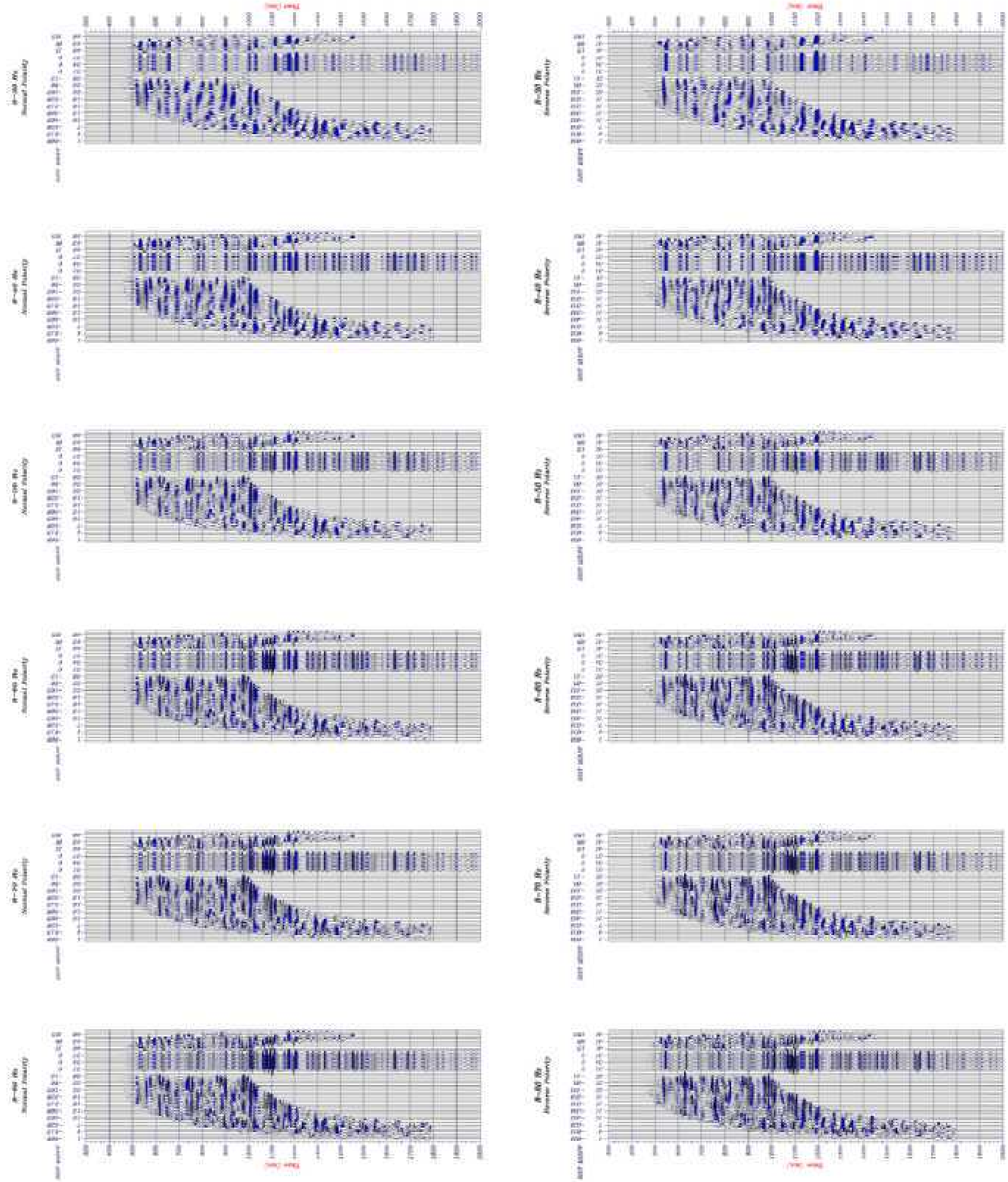

Figure 4-3. Far and Near Offset P-wave corridor stack and CDP transform correlation display.

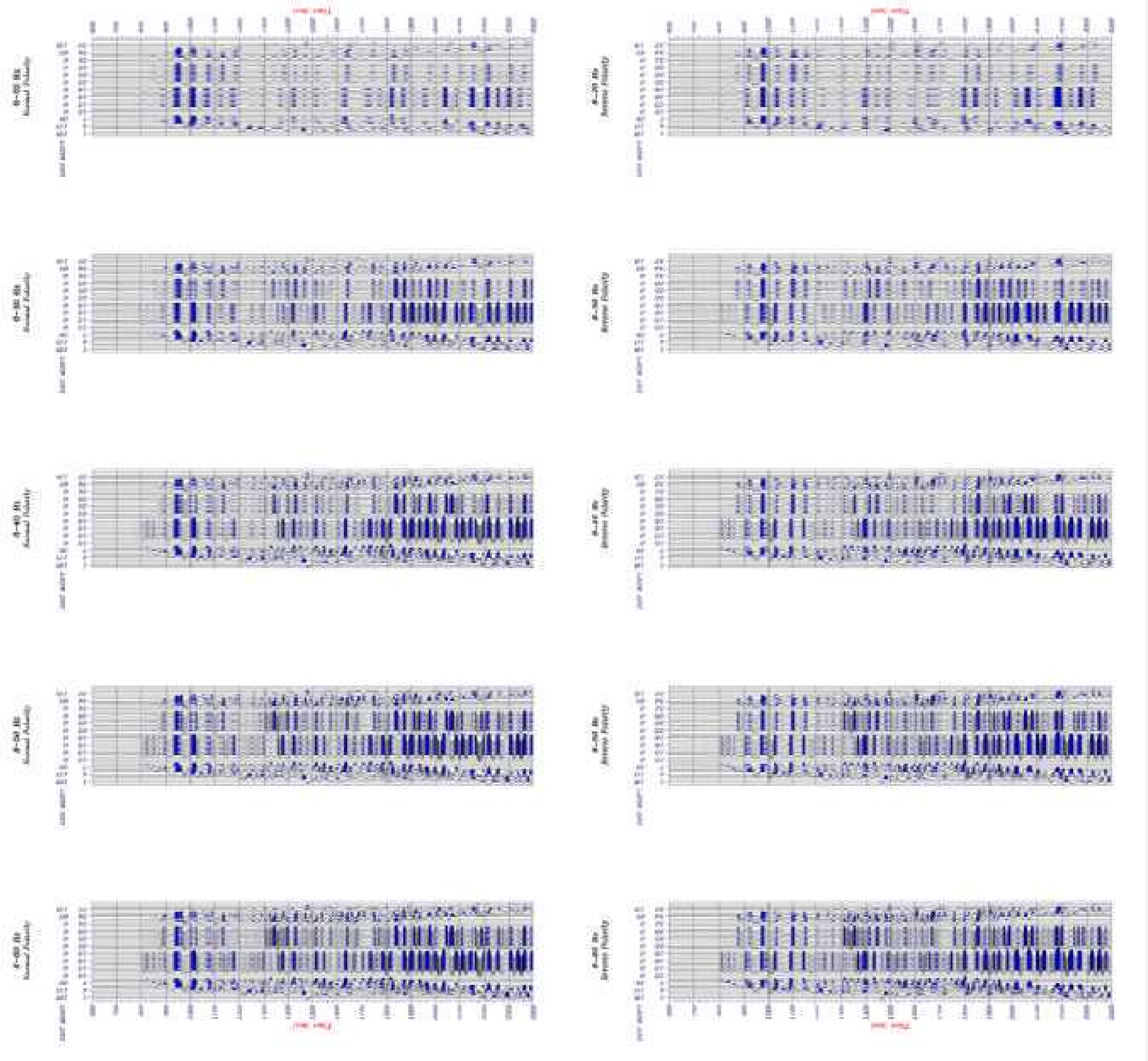

Figure 4-4. Zero Offset S-wave corridor stack and CDP transform correlation display.

4.2 Processing Results – WesternGeco

The following figures show the results of the processing workflows described in Section 3. Figure 4-5 through Figure 4-13 show typical shot records for the P-, S1- and S2-waves. Recall that there was an oblique relation between the sources and receivers (Figure 3-3), which made it is difficult to draw conclusions from these shot records. The following processing steps were performed:

- P-wave processing
    - 3D DMO, stack, 3D Random Noise Attenuation (RNA) and FK Stolt migration

- PS-wave processing
    - CCP binning/post-stack time migration
    - Limited-azimuth volumes
    - Azimuthal anisotropy (splitting) analysis

- SS-wave processing
    - Sh-Sh for statics and velocity
    - Azimuthal anisotropy (splitting) analysis

The PS-wave processing included CCP binning to correct for the movement of the reflection point from the midpoint. This was followed by a Kirchhoff post-stack time migration flow using the appropriate PS-wave velocity field. P-wave processing

4.2.1 P-WAVE PROCESSING

Figure 4-14 through Figure 4-21 show the progression of the P-wave data through the processing sequence. Figure 4-14 shows a brute stack, which is the raw data processed using the regional velocity function and elevation statics. Figure 4-15 is an example of a refraction stack, which incorporates the refractions statics. Figure 4-16 shows the SCD stack, which is the refraction stack incorporating the Surface-Consistent Deconvolution. Figure 4-17 is the SCD stack but with Time-Variant Spectral Whitening to broaden the bandwidth. Figure 4-18 contains Zone-Anomaly Processing to reduce noise bursts and anomalous spikes. Figure 4-19 is the reflection stack. Figure 4-20 is a DMO stack, which is the reflection stack with a 3D common-offset DMO. Figure 4-21 shows the final result after the DMO stack has had the FK extended Stolt migration.

4.2.2 PS – WAVE PROCESSING

Figure 4-23 and Figure 4-24 show the raw radial and transverse component shot records for the P-source. Figure 4-25 through Figure 4-30 illustrate the results of the PS-wave processing. Figure 4-25 is the brute stack for the radial component with the regional velocity function, P-wave source statics and elevation detector statics. Figure 4-26 shows the brute stack with detector hand statics to match the P-wave time structure. Figure 4-27 shows the SCD/TVSW/ZAP stack, which is essentially the same as the corresponding P-wave stack (Figure 4-18) with adjusted time windows. Figure 4-28 is the final CCP (Common-Conversion Point) stack with a time-varying correction of the reflection point. Figure 4-29 is the CCP stack with Kirchhoff post-stack time migration using the PS-wave velocities. Figure 4-30 is the final migration with 3D random noise attenuation (FXY deconvolution).

Figure 4-31 is a comparison of the PP and PS sections. The blue arrow shows the target. There is a reasonably good alignment of events.

4.2.3 AZIMUTHAL ANALYSIS

Figure 4-32 describes the azimuth sectors used to limit the PS data for azimuthal analysis. Both the radial and transverse components were used for this analysis. The transverse component data was processed using the parameters determined from the radial component.

Figure 4-33 shows one line from the survey (IL 1094) extracted for each of the 8 limited-azimuth sectors for both radial and transverse components. Note that the sectors ranged from 0 to 360 degrees in 10 degree increments. The purple arrows on the right show the analysis windows used. Layer 1 is considered the overburden and Layer 2 includes the reservoir.

Figure 4-34 shows the result of the 2C x 2C Alford rotation and layer stripping procedure performed on the data in Figure 4-33. Note that the values are in percentage anisotropy and are relatively small (<2%). Also note that there seems to be a pattern that correlates roughly the weaker anisotropy with the isochron interpretation. It is not clear why this association might occur in the case of the overburden.

Figure 4-35 shows the results from the second layer which includes the reservoir. The overall level of anisotropy is smaller and less organized. It is possible, however, to see hints of a similar NW/SE feature of weaker anisotropy.

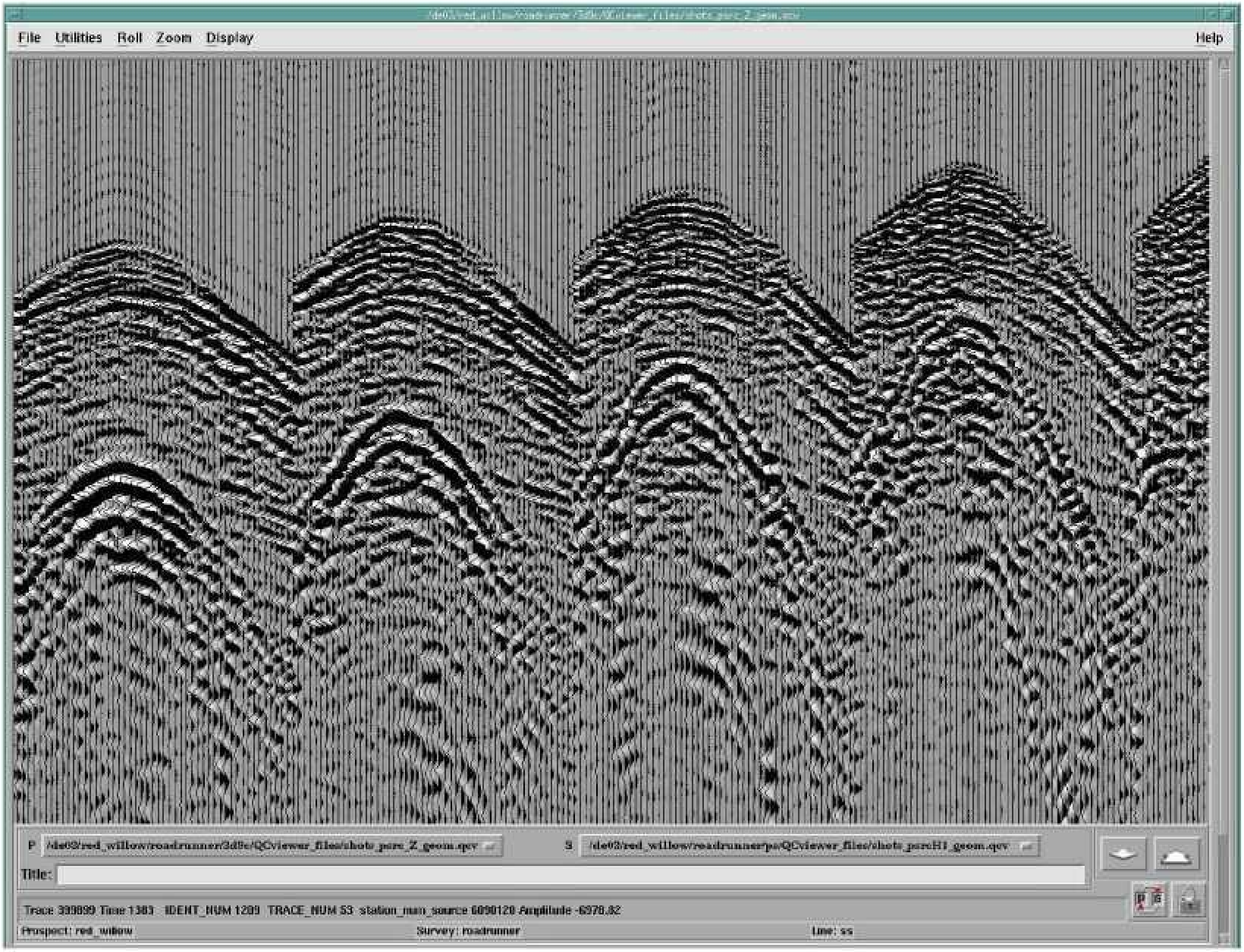

P /de03/red_willow/roadrunner/3d9c/QCviewer_files/shots_pzrc_Z_geom.qcv

S /de03/red_willow/roadrunner/ps/QCviewer_files/shots_pzrcH1_geom.qcv

Title:

Trace 399899 Time 1383 IDENT_NUM 1209 TRACE_NUM 53 station_num_source 6090120 Amplitude -6978.82

Prospect: red_willow Survey: roadrunner Line: ss

Figure 4-5. Typical Shot Record: P source – Z detector.

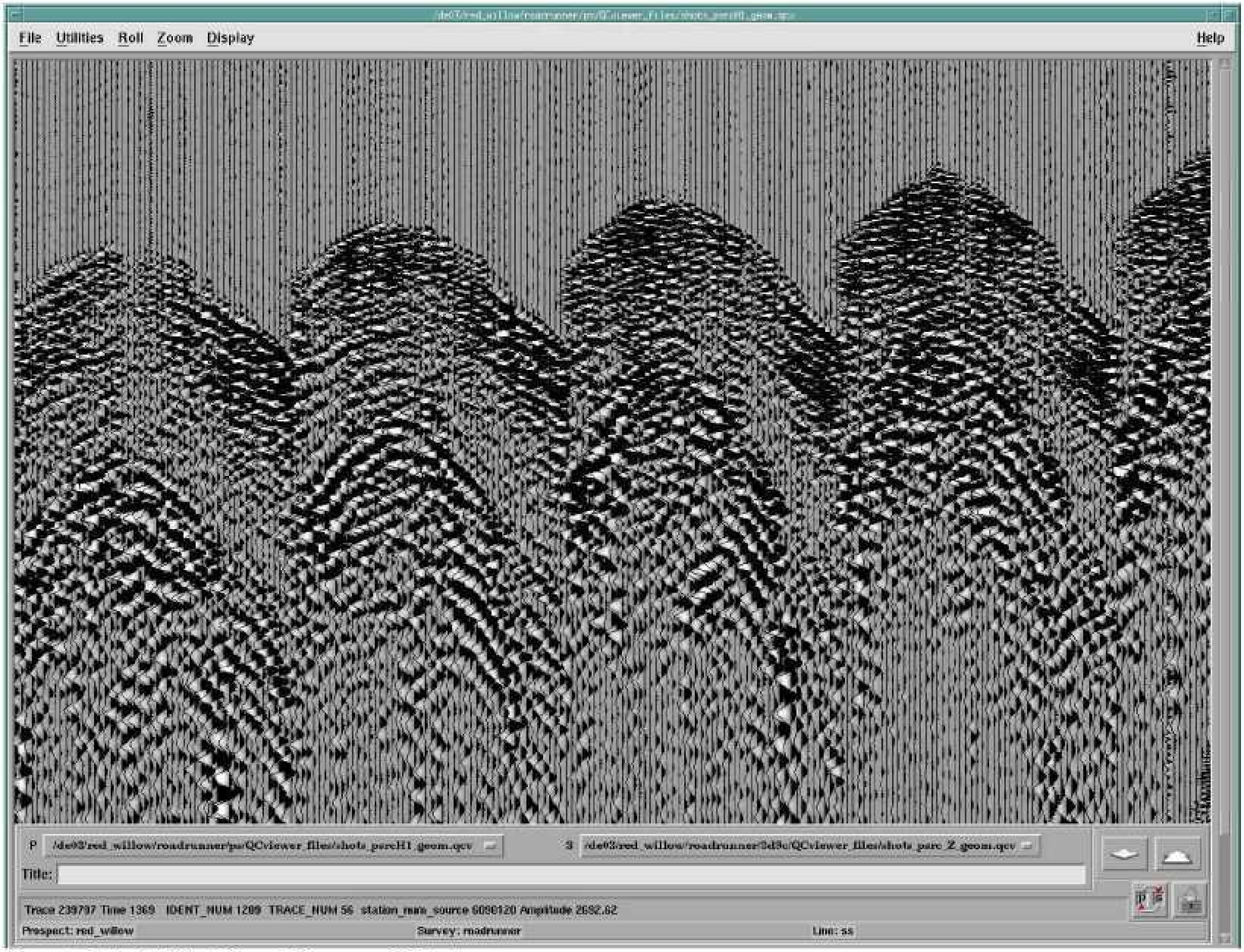

P /de02/red_willow/roadrunner/ps/QCviewer_files/shots_percH1_geom.qcv

S /de02/red_willow/roadrunner/3d3c/QCviewer_files/shots_parc_Z_geom.qcv

Title:

Trace 239797 Time 1369 IDENT_NUM 1209 TRACE_NUM 56 station_num_source 6090120 Amplitude 2692.62

Prospect: red_willow Survey: roadrunner Line: ss

Figure 4-6. Typical Shot Record: P source – X detector.

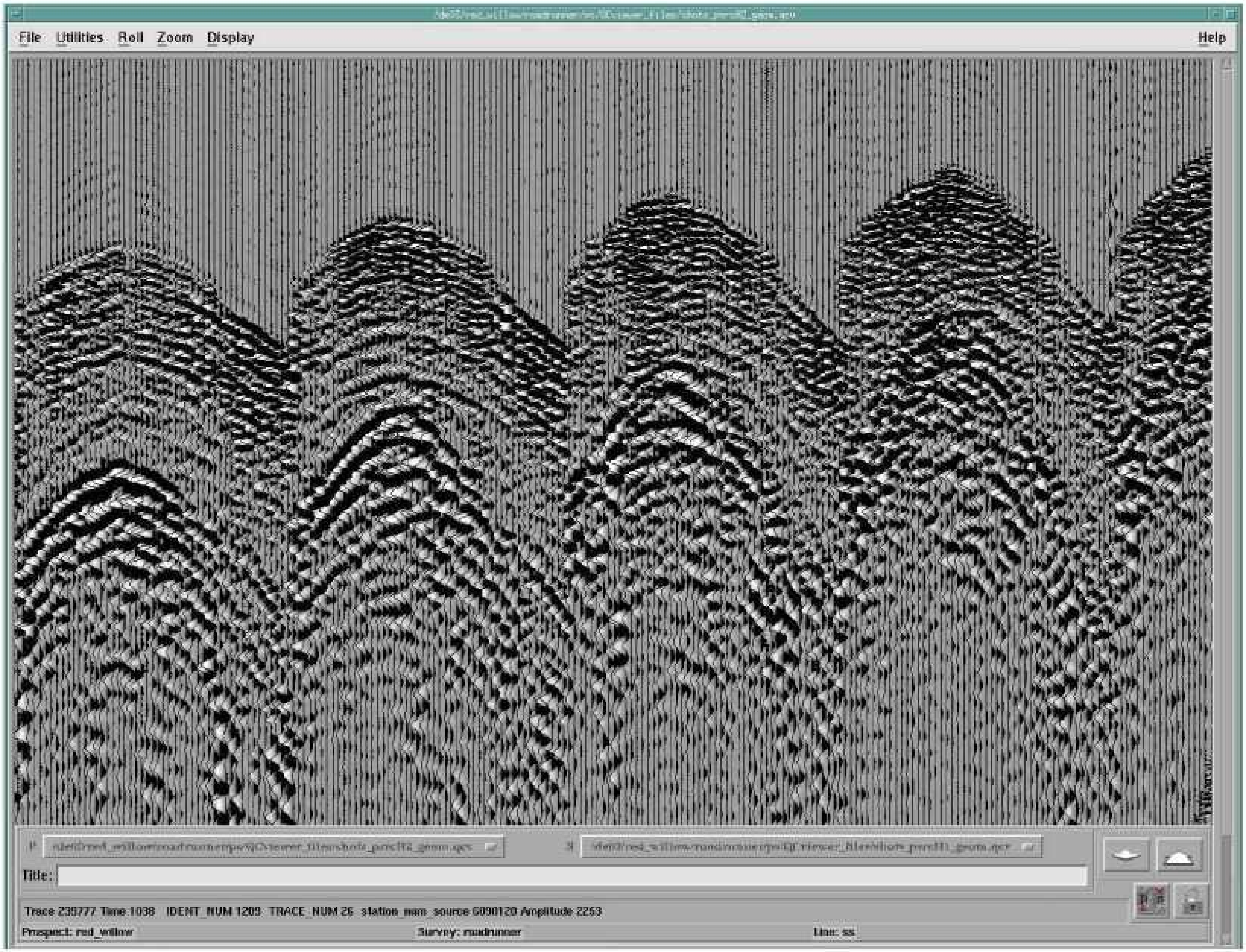

Trace 235777 Time 1038 IDENT_NUM 1209 TRACE_NUM 26 station_num source 6090120 Amplitude 2253

Prospect: red_willow

Survey: roadrunner

Line: ss

Figure 4-7. Typical Shot Record: P source – Y detector.

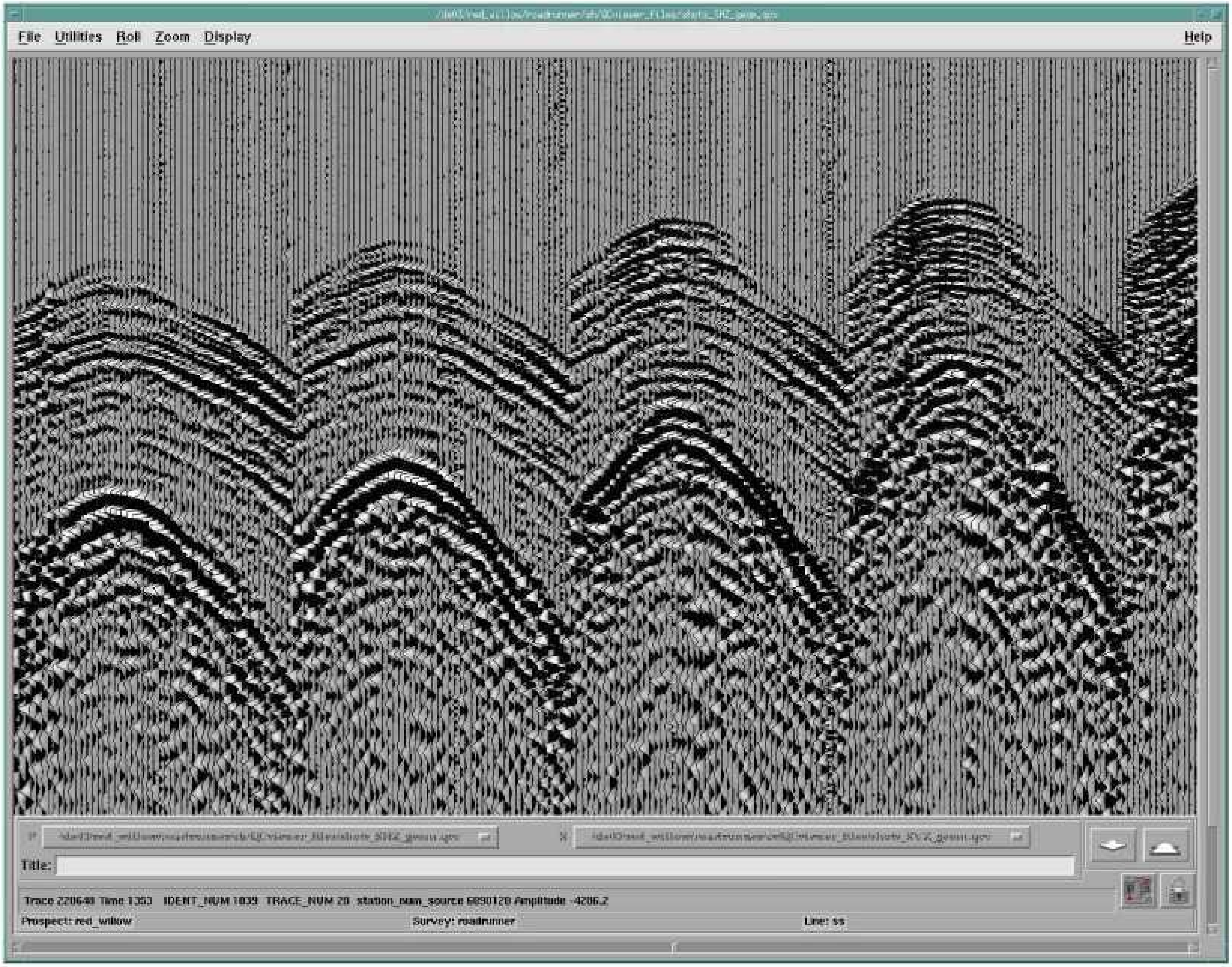

```
Trace 220648 Time 1353   IDENT_NUM 1039  TRACE_NUM 20  station_num_source 6890120 Amplitude -4206.2
Prospect: red_willow                    Survey: roadrunner                    Line: ss
```

Figure 4-8. Typical Shot Record: S1 source – Z detector.

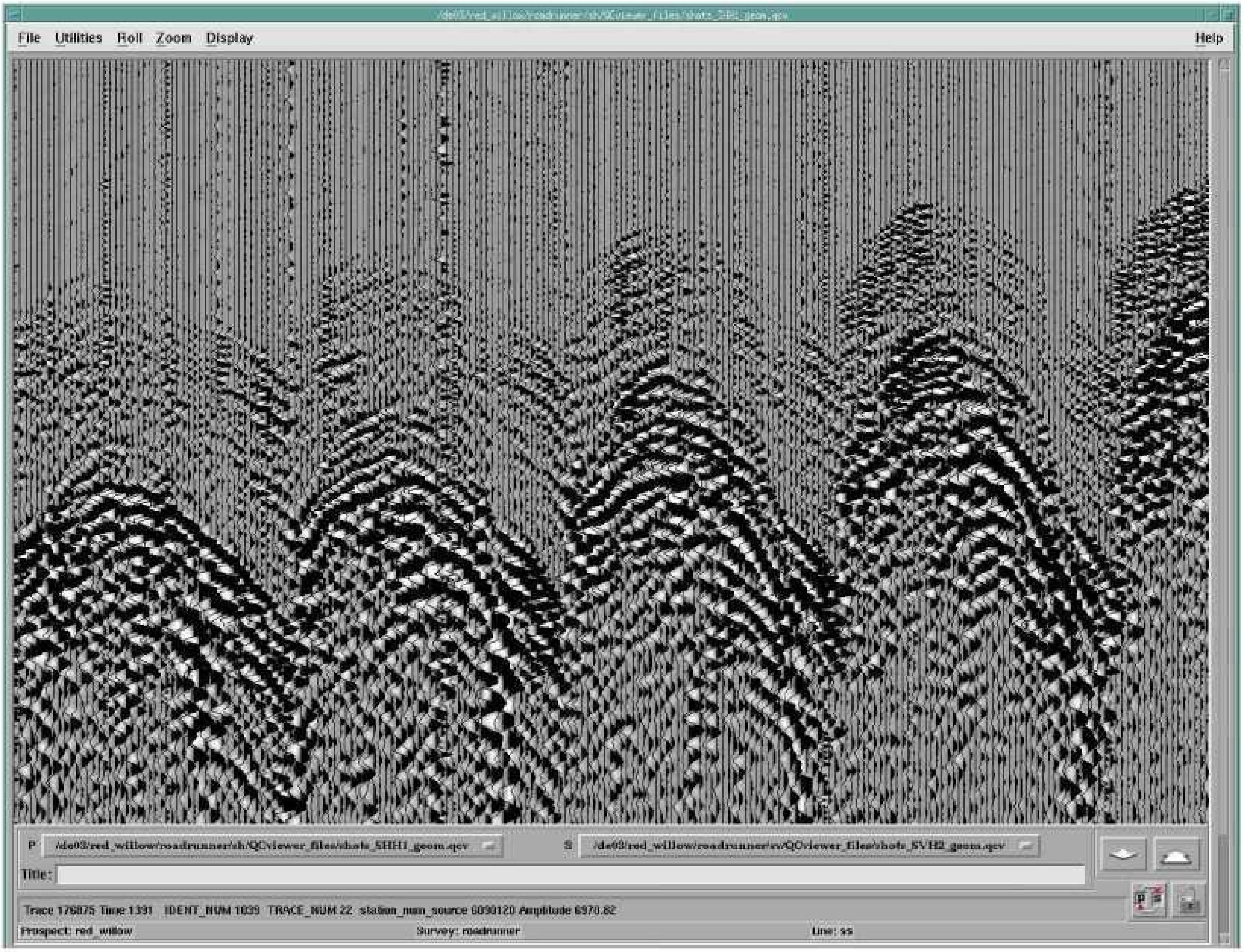

P /de03/red_willow/roadrunner/sh/QCviewer_files/shots_SHH1_geom.qcv

S /de03/red_willow/roadrunner/sv/QCviewer_files/shots_SVH2_geom.qcv

Title:

Trace 176875 Time 1391 IDENT_NUM 1039 TRACE_NUM 22 station_num_source 6090120 Amplitude 6970.82

Prospect: red_willow Survey: roadrunner Line: ss

Figure 4-9. Typical Shot Record: S1 source – X detector.

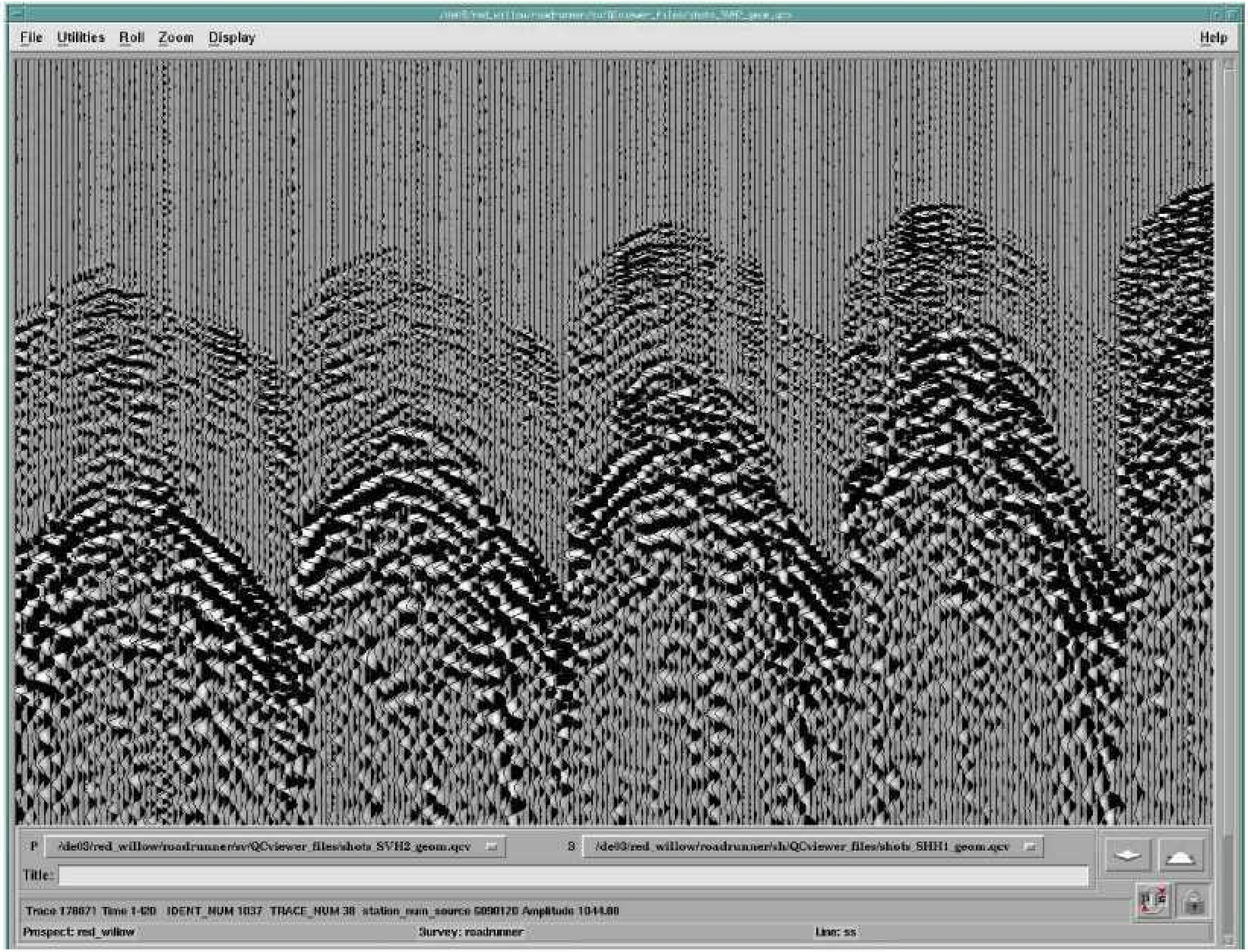

P /de03/red_willow/roadrunner/sv/QCviewer_files/shots_SVH2_geom.qcv

S /de03/red_willow/roadrunner/sh/QCviewer_files/shots_SHH1_geom.qcv

Title:

Trace 178871 Time 1420 IDENT_NUM 1037 TRACE_NUM 38 station_num_source 5090120 Amplitude 1044.80

Prospect: red_willow Survey: roadrunner Line: ss

Figure 4-10. Typical Shot Record: S1 source – Y detector.

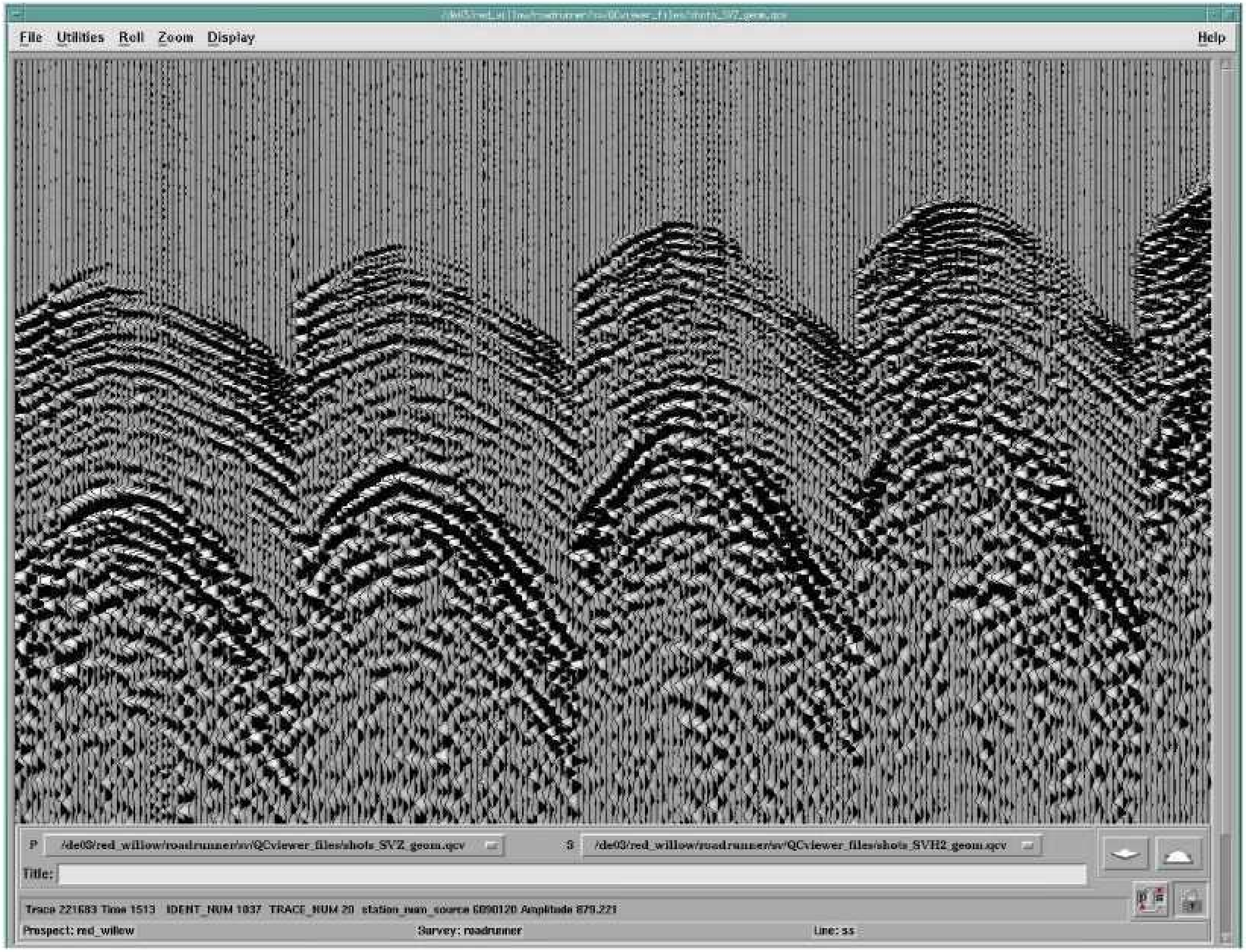

P /de03/red_willow/roadrunner/sv/QCviewer_files/shots_SVZ_geom.qcv

S /de03/red_willow/roadrunner/sv/QCviewer_files/shots_SVH2_geom.qcv

Title:

Trace 221683 Time 1513 IDENT_NUM 1037 TRACE_NUM 20 station_num_source 6090120 Amplitude 879.221

Prospect: red_willow

Survey: roadrunner

Line: ss

Figure 4-11. Typical Shot Record: S2 source – Z detector.

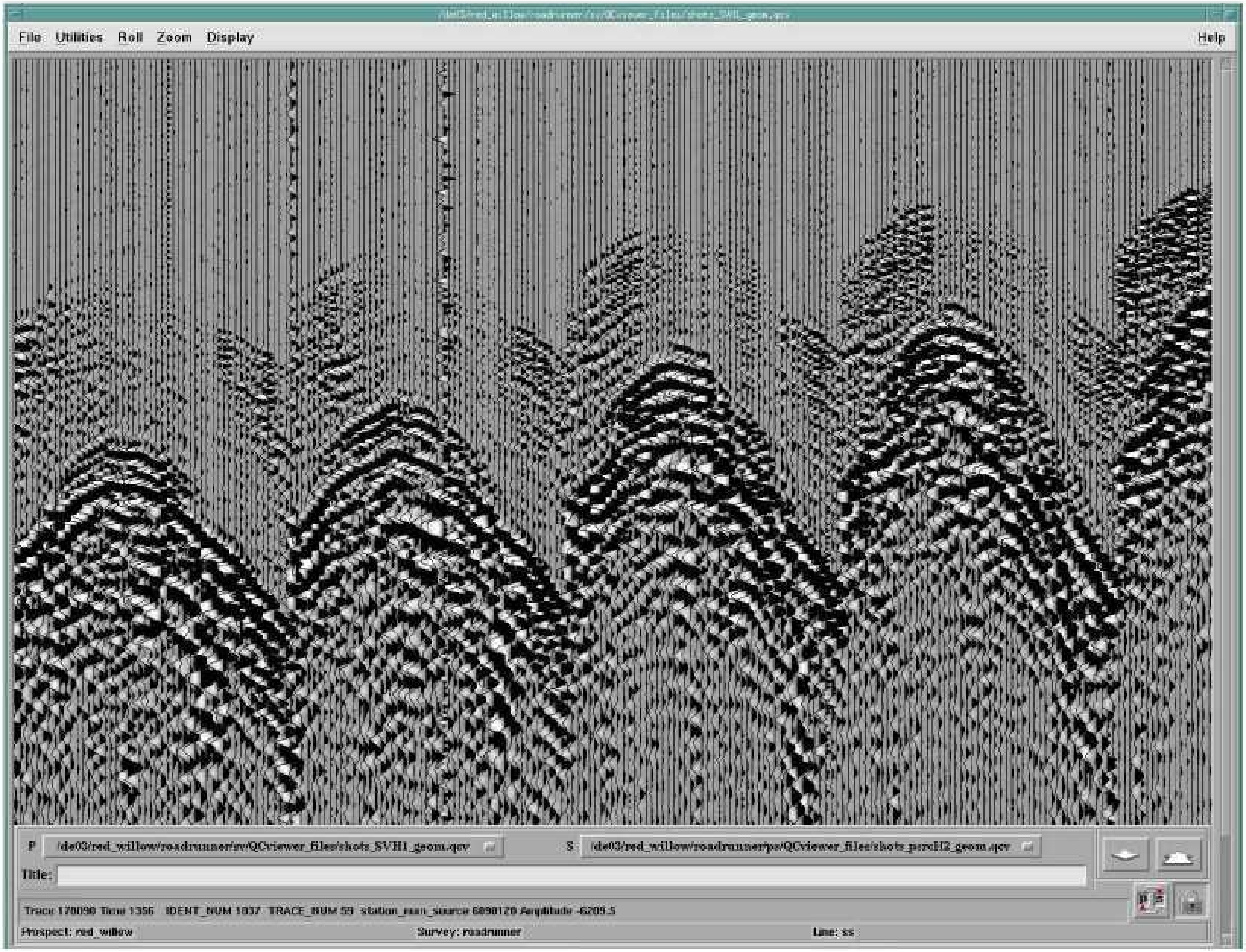

P /de03/red_willow/roadrunner/sv/QCviewer_files/shots_SVH1_geom.qcv

S /de03/red_willow/roadrunner/ps/QCviewer_files/shots_prcH2_geom.qcv

Title:

Trace 170090 Time 1356 IDENT_NUM 1037 TRACE_NUM 59 station_num_source 6090120 Amplitude -6209.5

Prospect: red_willow

Survey: roadrunner

Line: ss

Figure 4-12. Typical Shot Record: S2 source – X detector.

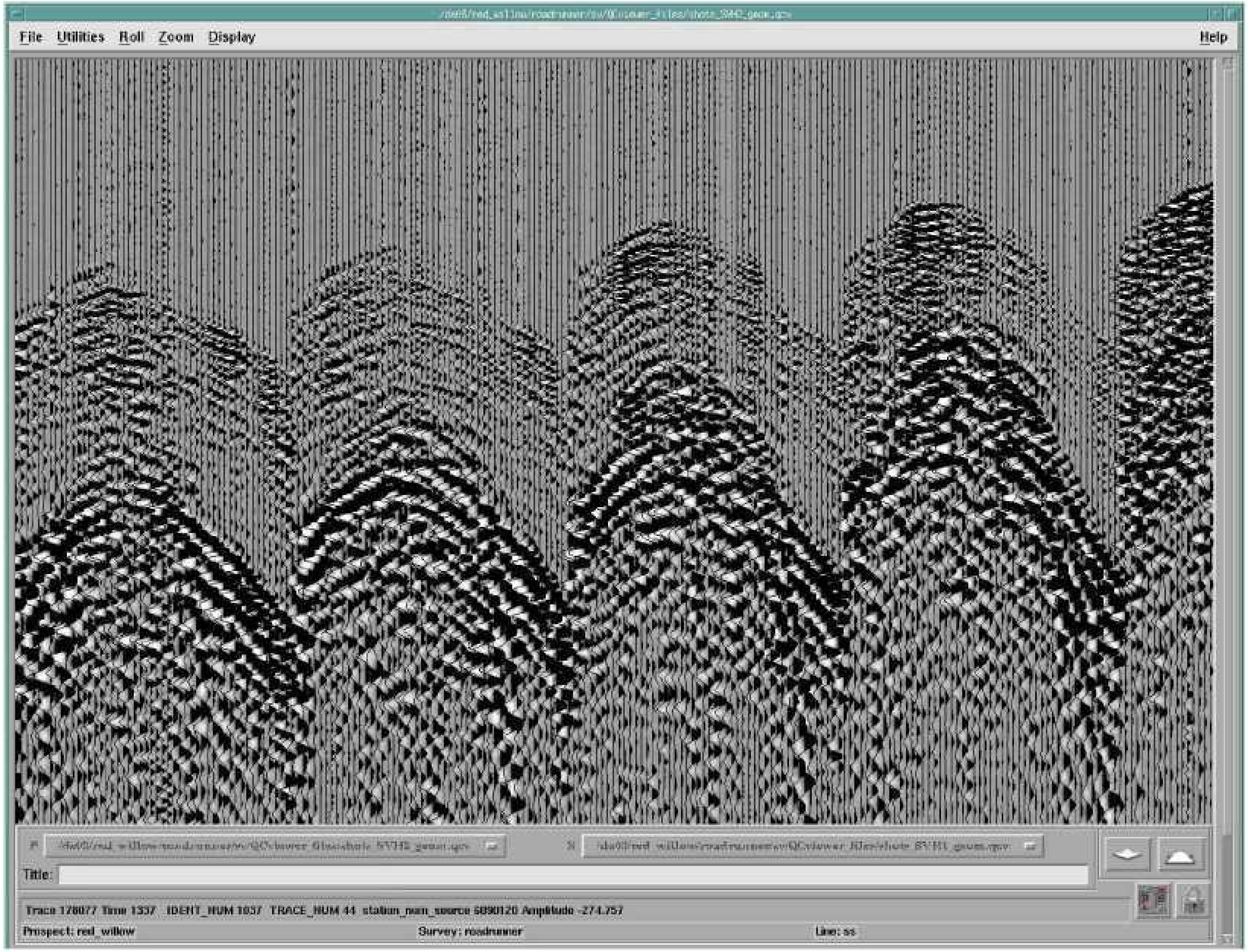

```
Trace 178077 Time 1337   IDENT_NUM 1037  TRACE_NUM 44  station_num_source 6890120 Amplitude -274.757
Prospect: red_willow                    Survey: roadrunner                    Line: ss
```

Figure 4-13 Typical Shot Record: S2 source – Y detector.

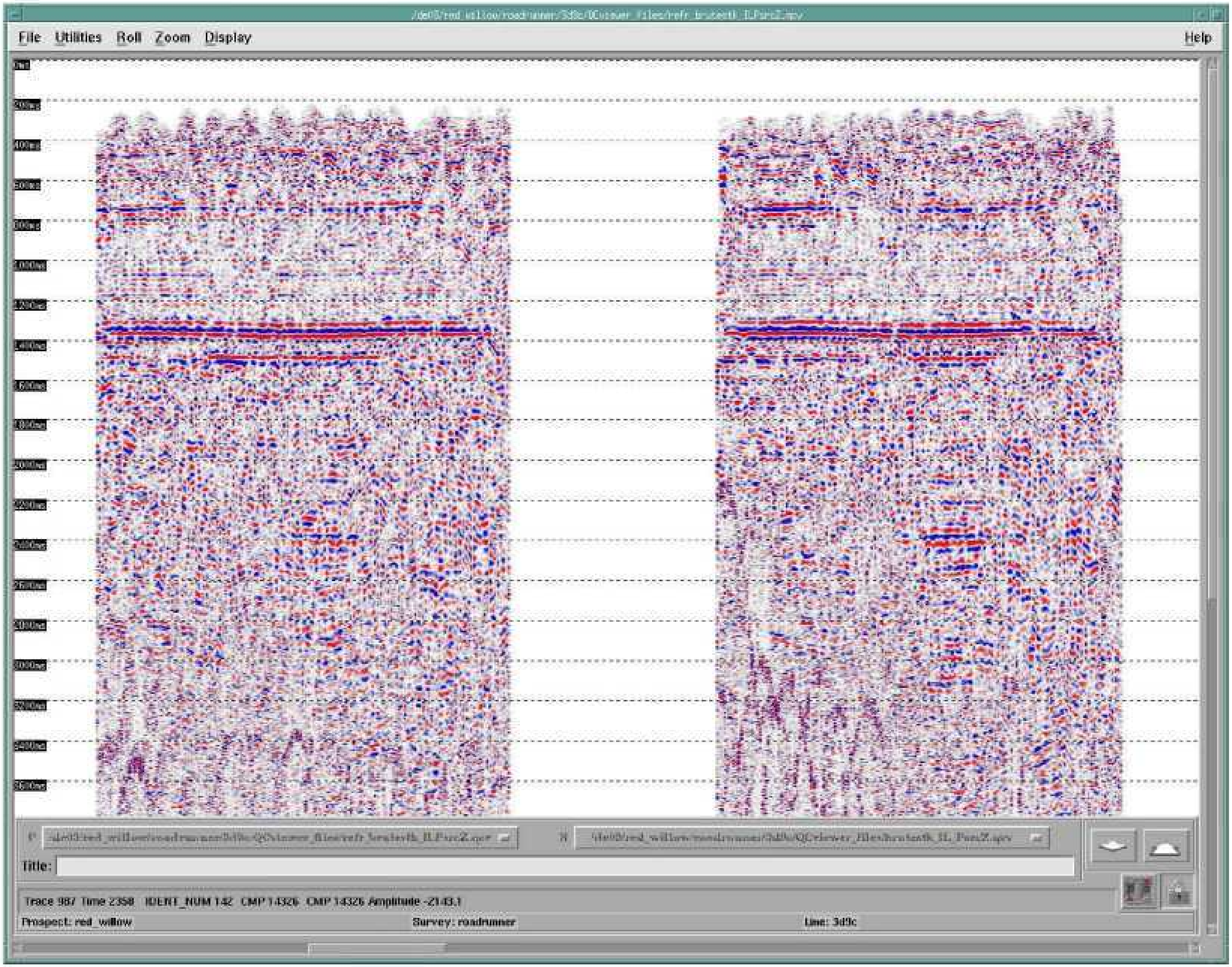

Title:

Trace 987 Time 2358 IDENT_NUM 142 CMP 14326 CMP 14326 Amplitude -2143.1

Prospect: red_willow

Survey: roadrunner

Line: 3d9c

Figure 4-14. Brute Stack: P source – Vertical component.

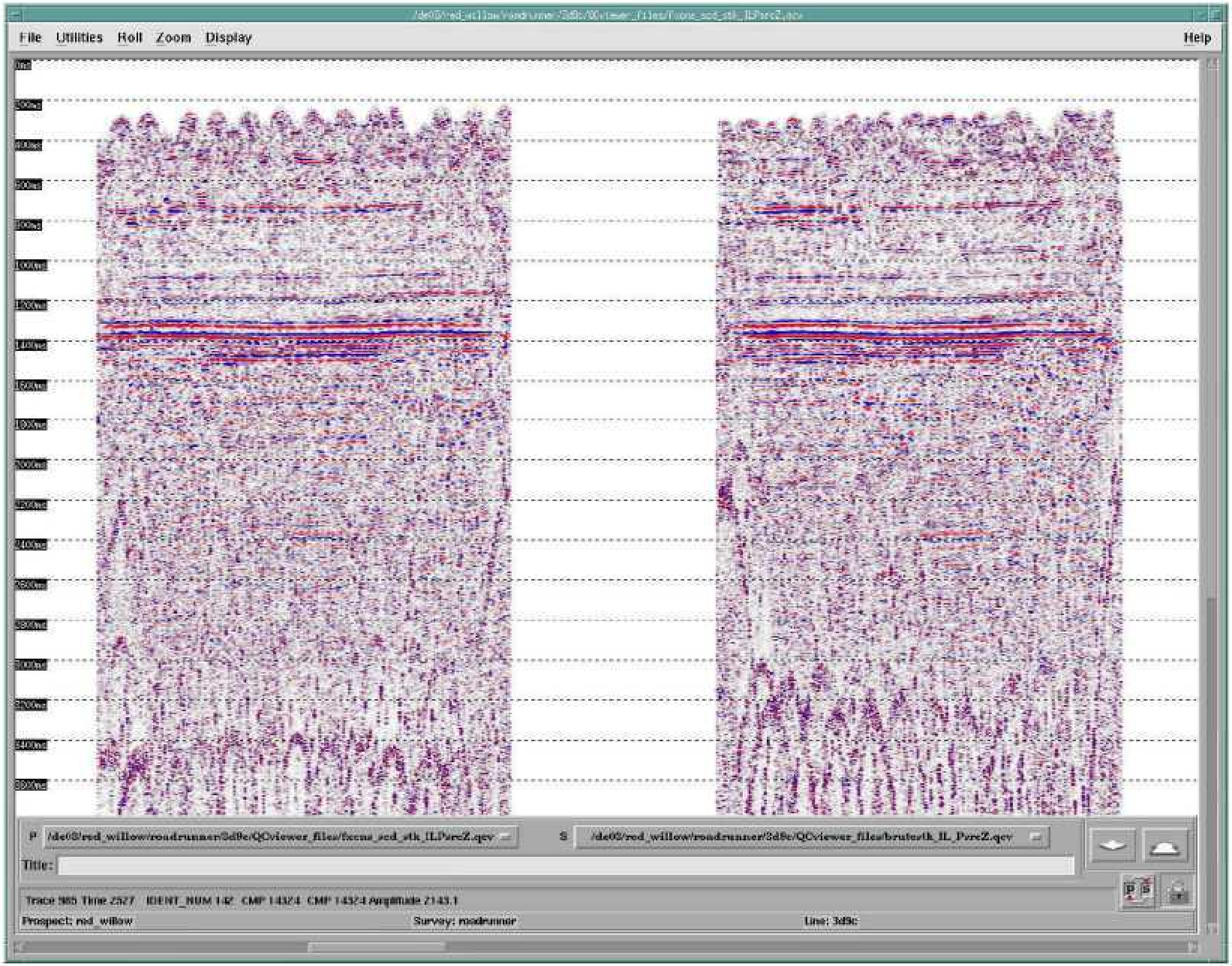

P /de03/red_willow/roadrunner/3d9c/QCviewer_files/fxcmu_scd_stk_ILPsrcZ.qcv

S /de03/red_willow/roadrunner/3d9c/QCviewer_files/brutestk_IL_PsrcZ.qcv

Trace 985 Time 2527 IDENT_NUM 142 CMP 14324 CMP 14324 Amplitude 2143.1

Prospect: red_willow Survey: roadrunner Line: 3d9c

Figure 4-15. Refraction Stack: P source – Vertical component.

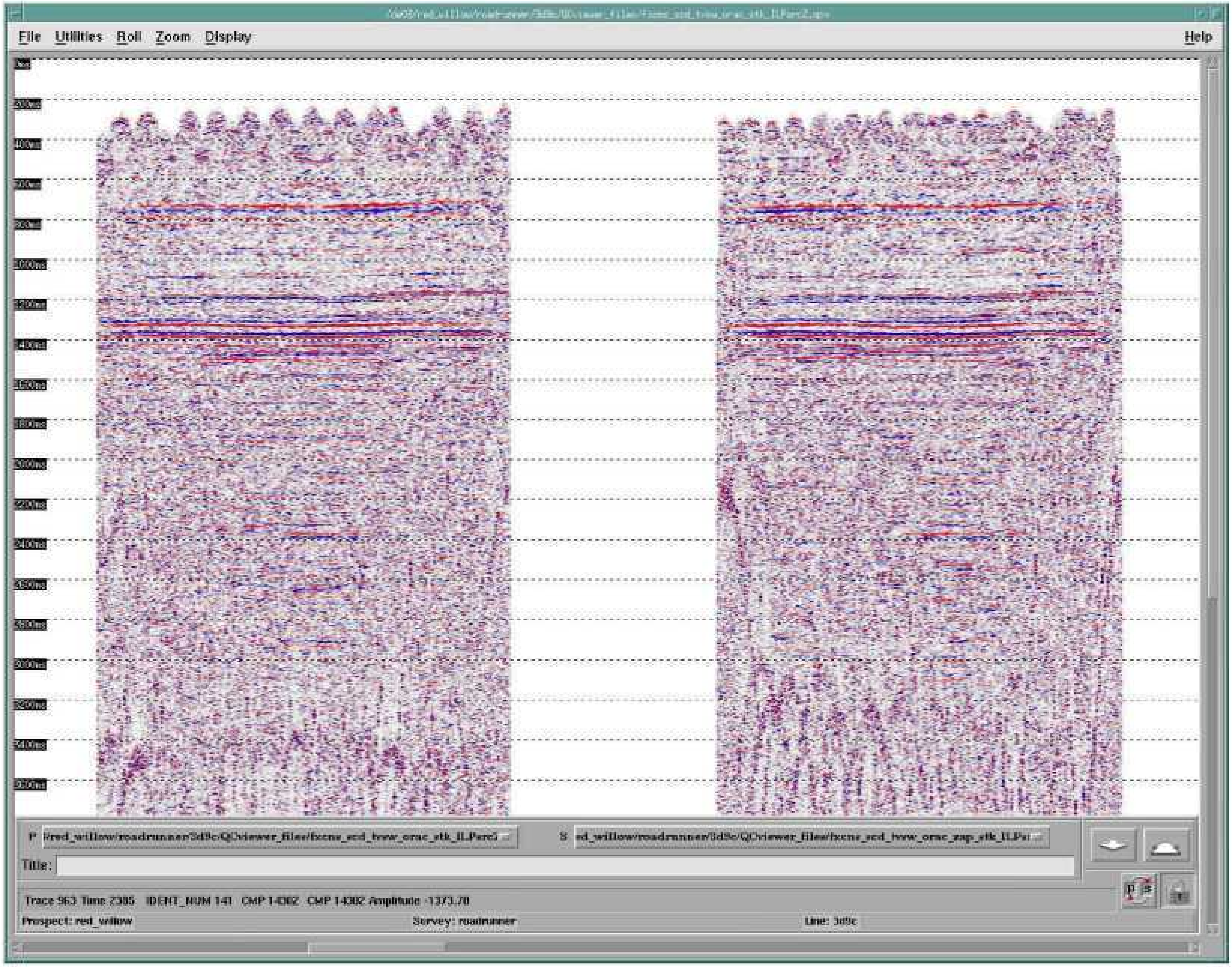

P /red_willow/roadrunner/3d9c/QCviewer_files/fxcns_scd_fvrw_orac_stk_ILPerc5

S ed_willow/roadrunner/3d9c/QCviewer_files/fxcns_scd_fvrw_orac_zap_stk_ILPs

Title:

Trace 963 Time 2385 IDENT_NUM 141 CMP 14302 CMP 14302 Amplitude -1373.70

Prospect: red_willow Survey: roadrunner Line: 3d9c

Figure 4-16. SCD Stack: P source – Vertical component.

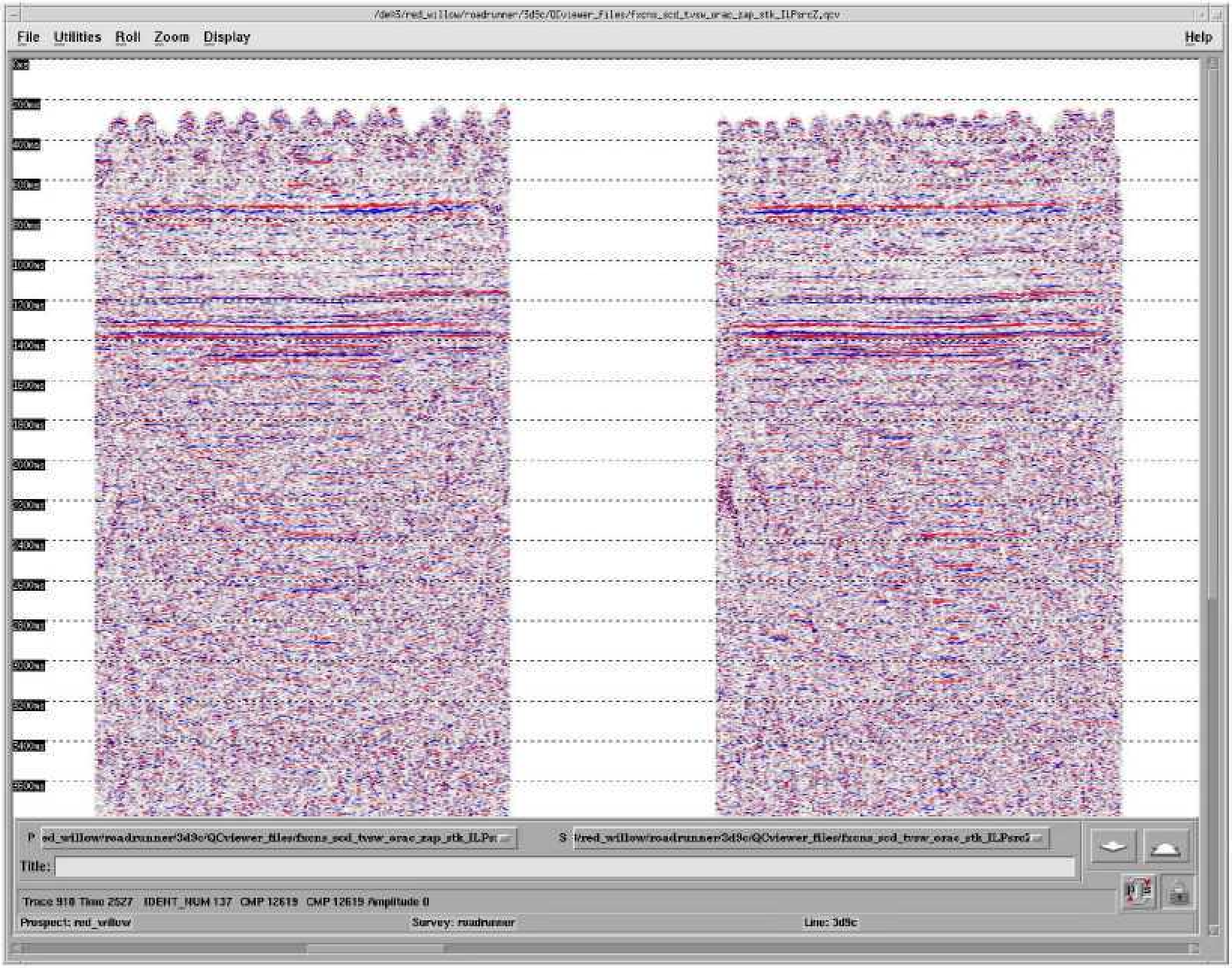

P ed_willow/roadrunner/3d9c/QCviewer_files/fxcns_scd_tvsw_orac_zap_stk_ILPs

S l/red_willow/roadrunner/3d9c/QCviewer_files/fxcns_scd_tvsw_orac_stk_ILPsrcZ

Title:

Trace 918 Time 2527 IDENT_NUM 137 CMP 12619 CMP 12619 Amplitude 0

Prospect: red_willow Survey: roadrunner Line: 3d9c

Figure 4-17. SCD/TVSW Stack: P source – Vertical component.

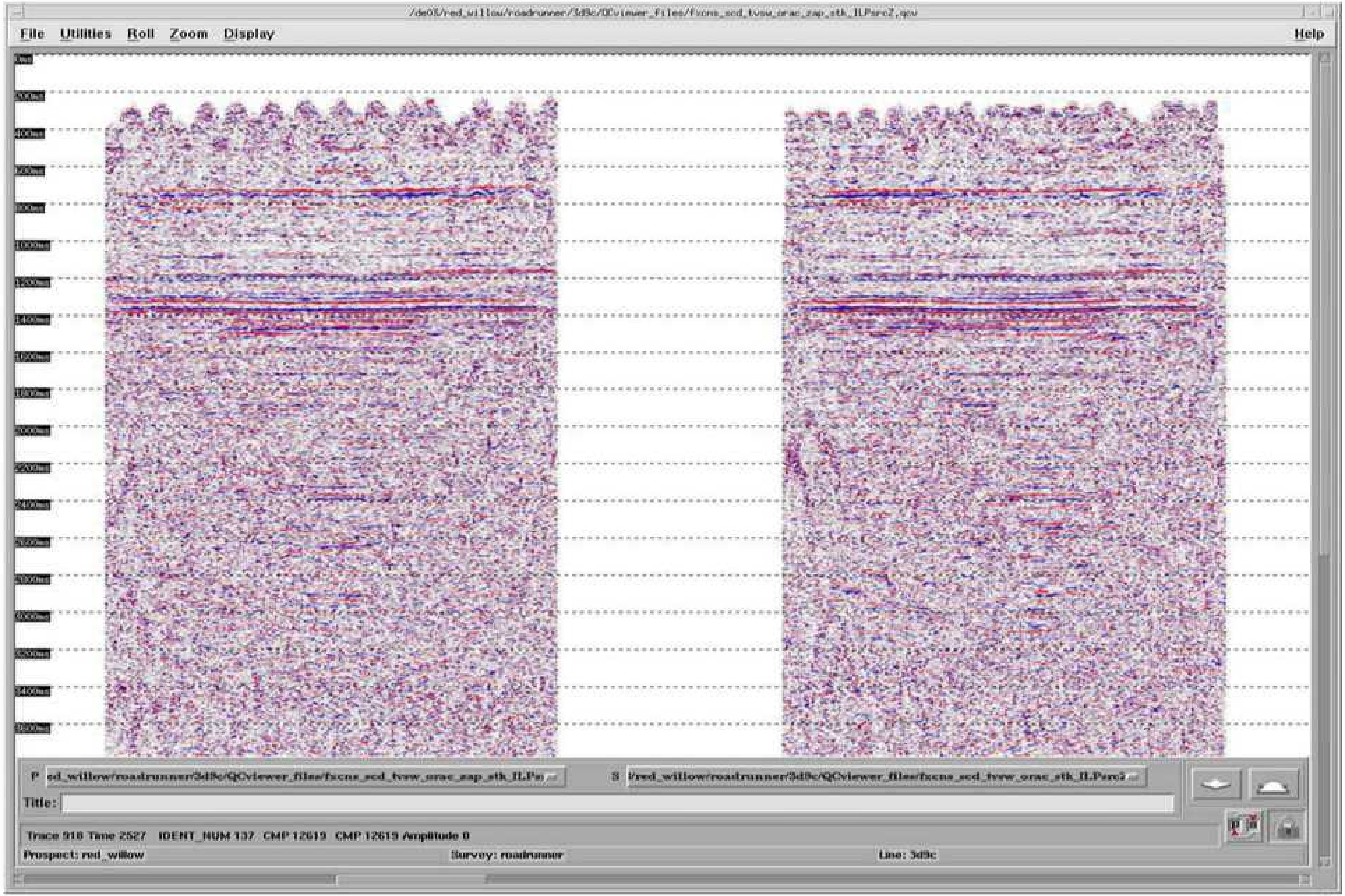

P ed_willow/roadrunner/3d9c/QCviewer_files/fxcns_scd_tvsw_orac_zap_stk_ILPs

S /red_willow/roadrunner/3d9c/QCviewer_files/fxcns_scd_tvsw_orac_stk_ILPsrcZ

Trace 918 Time 2527 IDENT_NUM 137 CMP 12619 CMP 12619 Amplitude 0

Prospect: red_willow

Survey: roadrunner

Line: 3d9c

Figure 4-18. SCD/TVSW/ZAP Stack: P source – Vertical component.

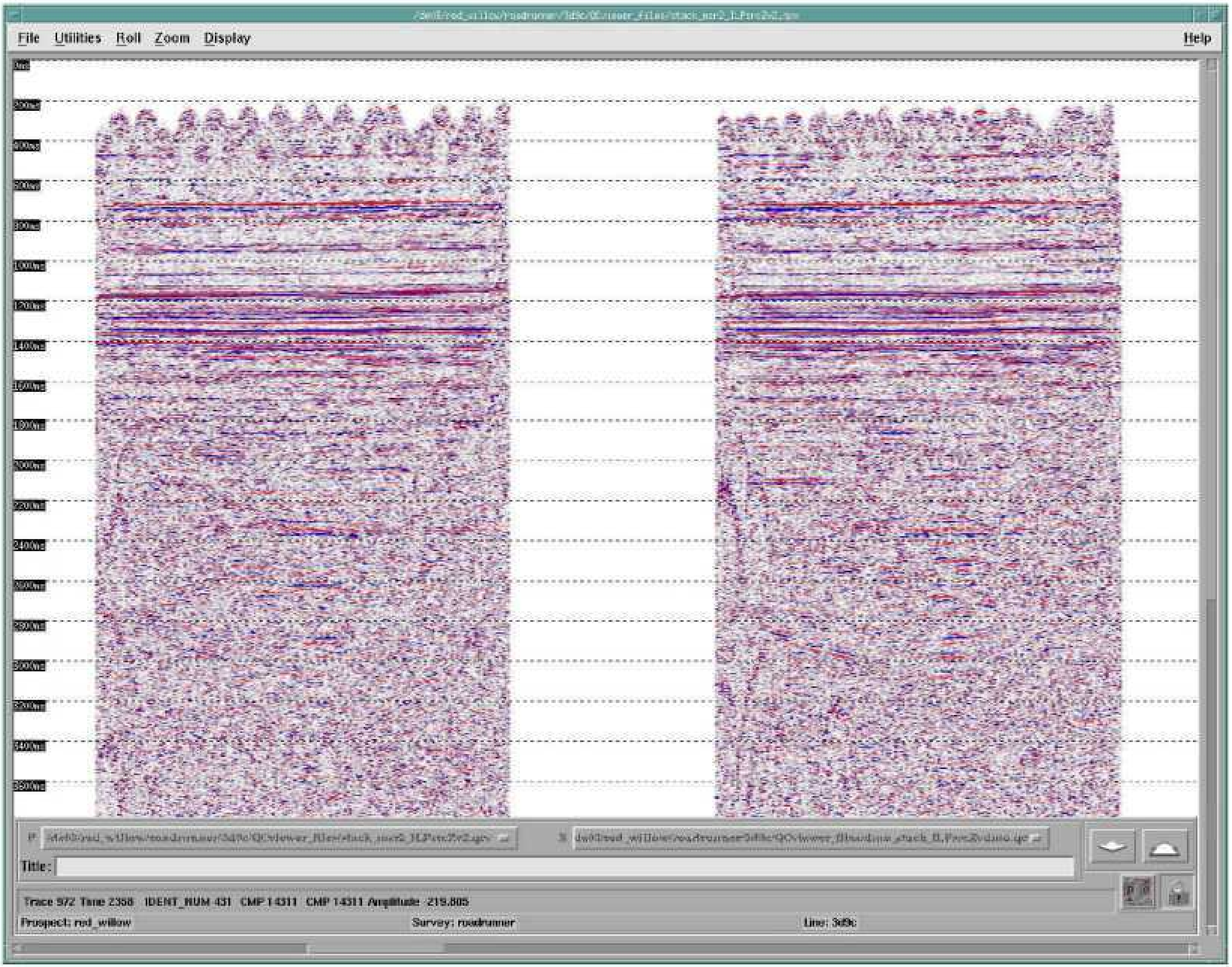

Title:

Trace 972 Time 2358 IDENT_NUM 431 CMP 14311 CMP 14311 Amplitude -219.805

Prospect: red_willow

Survey: roadrunner

Line: 3d9c

Figure 4-19. Reflection Statics Stack: P source – Vertical component

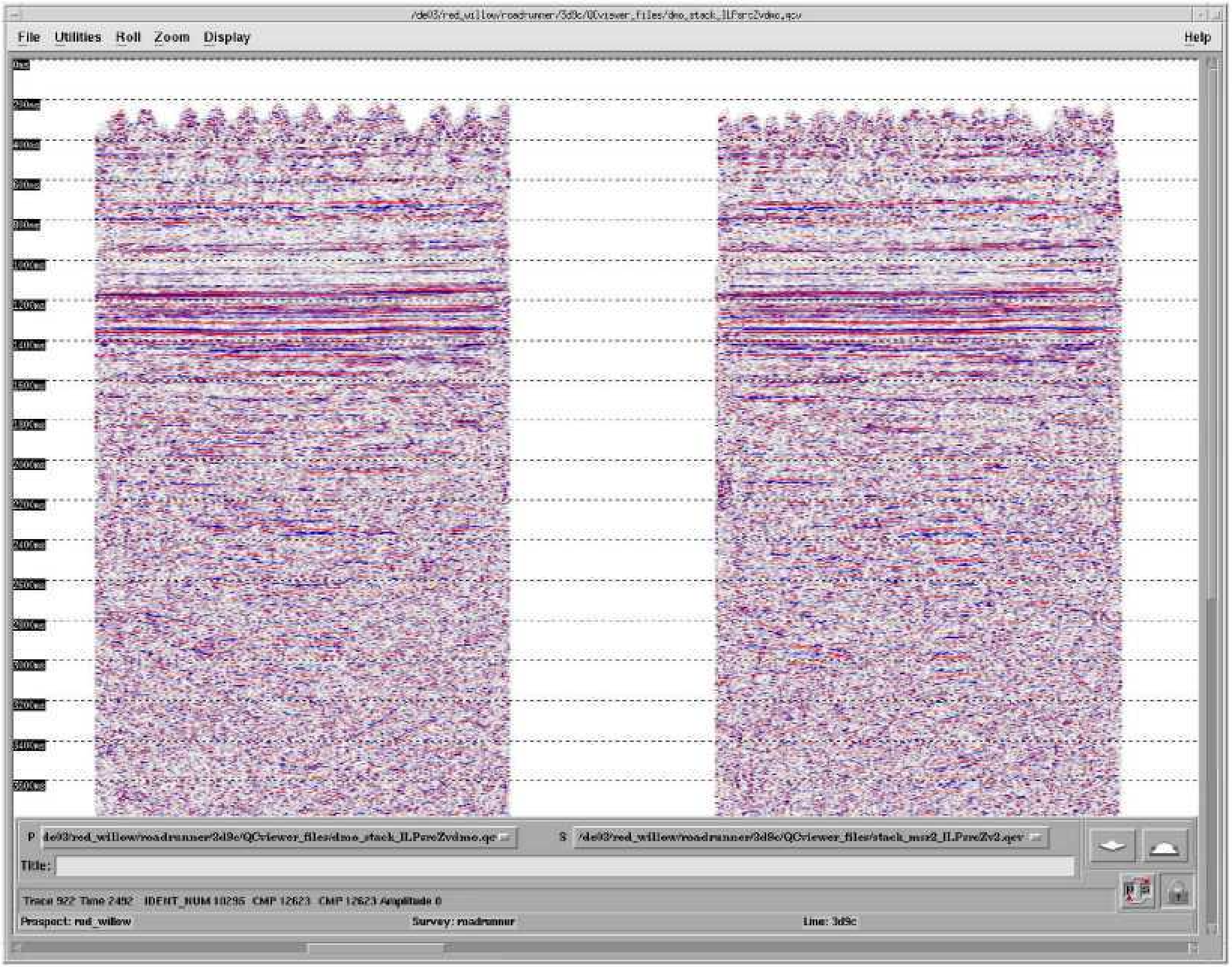

P de03/red_willow/roadrunner/3d9c/QCviewer_files/dmo_stack_ILPsrcZvdmo.qc

S /de03/red_willow/roadrunner/3d9c/QCviewer_files/stack_mx2_ILPsrcZv2.qcv

Title:

Trace 922 Time 2492 IDENT_NUM 10295 CMP 12623 CMP 12623 Amplitude 0

Prospect: red_willow Survey: roadrunner Line: 3d9c

Figure 4-20. DMO Stack: P source – Vertical component.

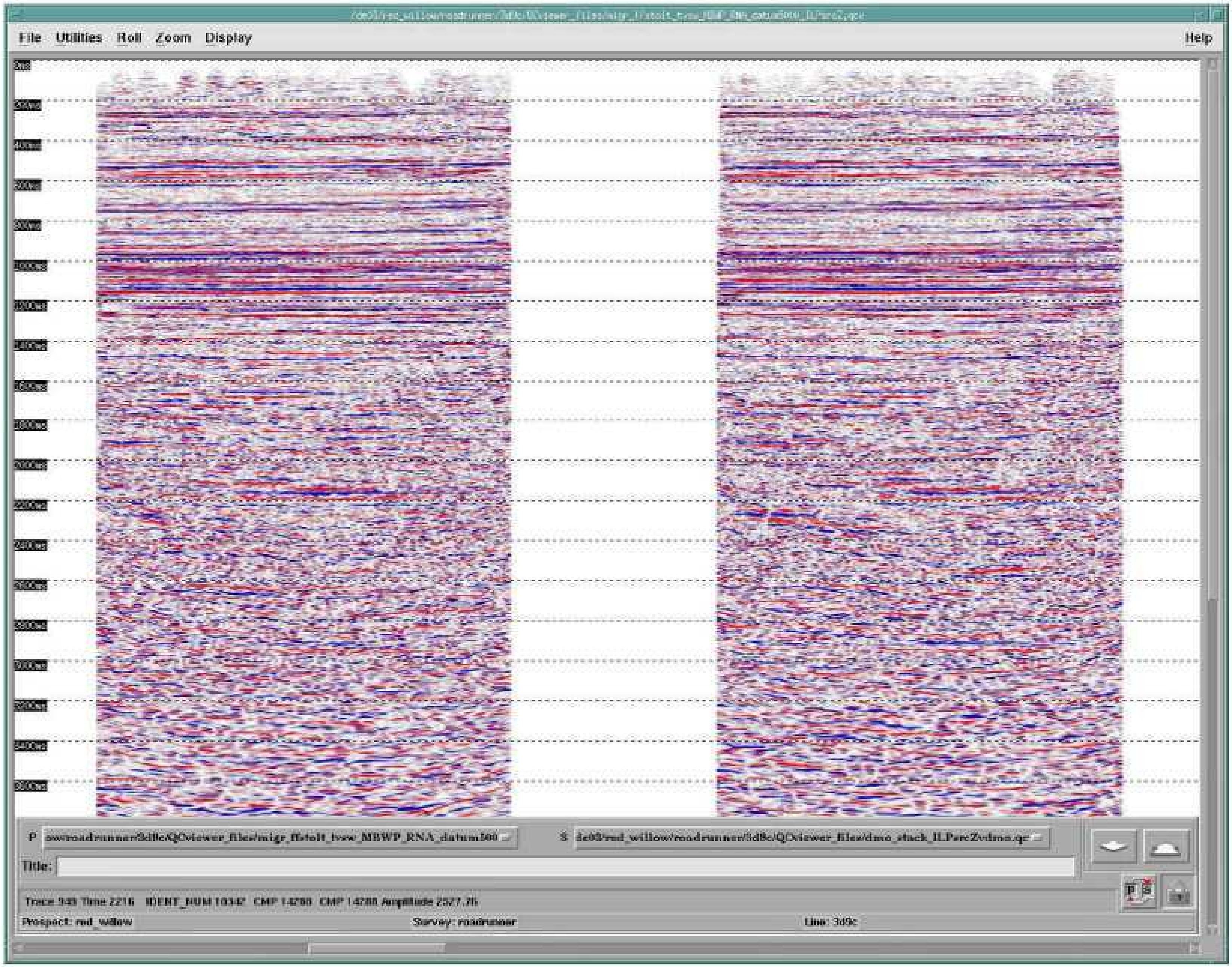

P: ow/roadrunner/3d9c/QCviewer_files/migr_ffstolt_tvsw_MBWP_RNA_datum500

S: de03/red_willow/roadrunner/3d9c/QCviewer_files/dmo_stack_ILPareZvdmo.qc

Trace 949 Time 2216 IDENT_NUM 10342 CMP 14288 CMP 14288 Amplitude 2527.76

Prospect: red_willow
Survey: roadrunner
Line: 3d9c

Figure 4-21. Final Migration: P source – Vertical component.

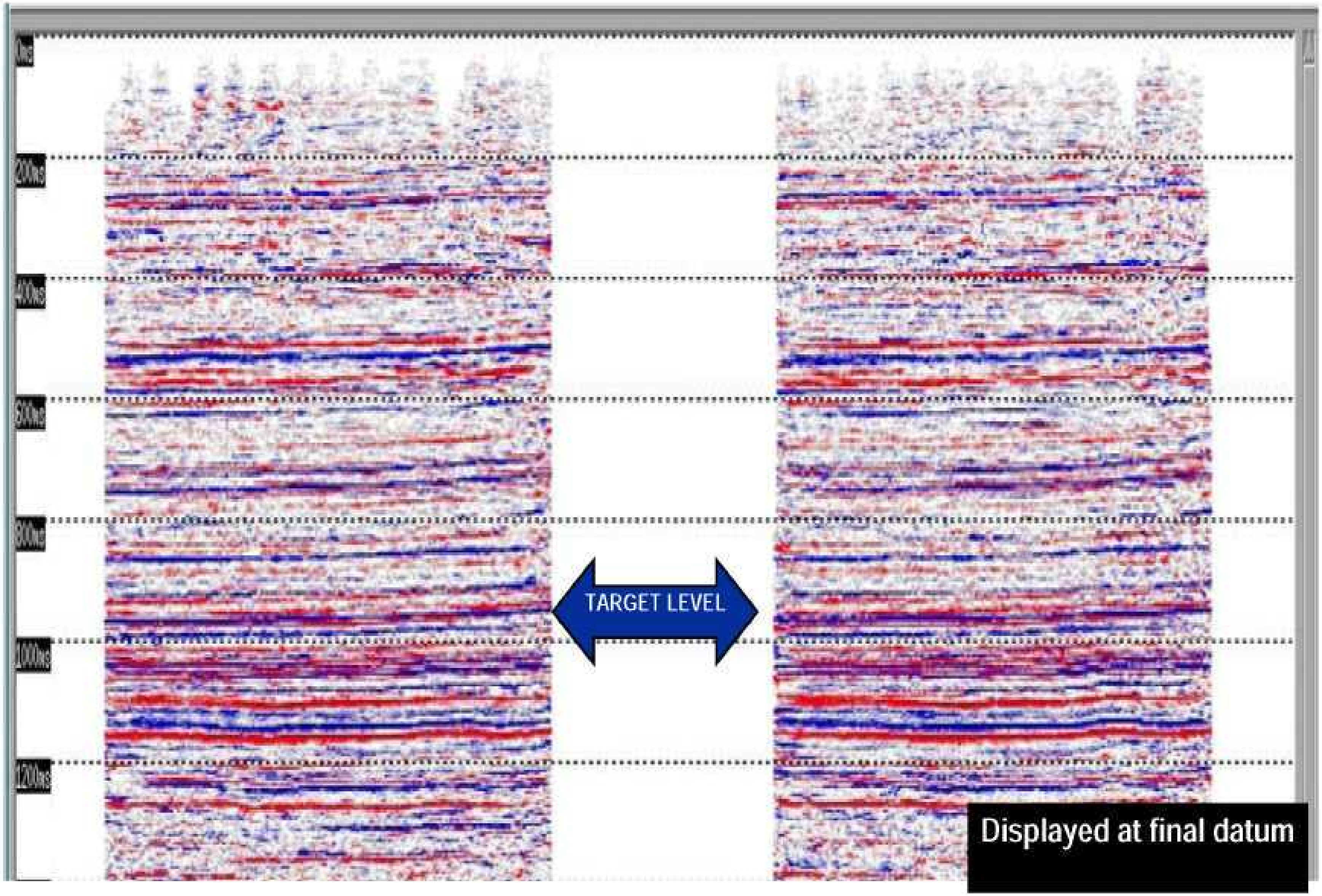

Figure 4-22. Close-up of the two examples of the Final PP Migration: P Source – Vertical component

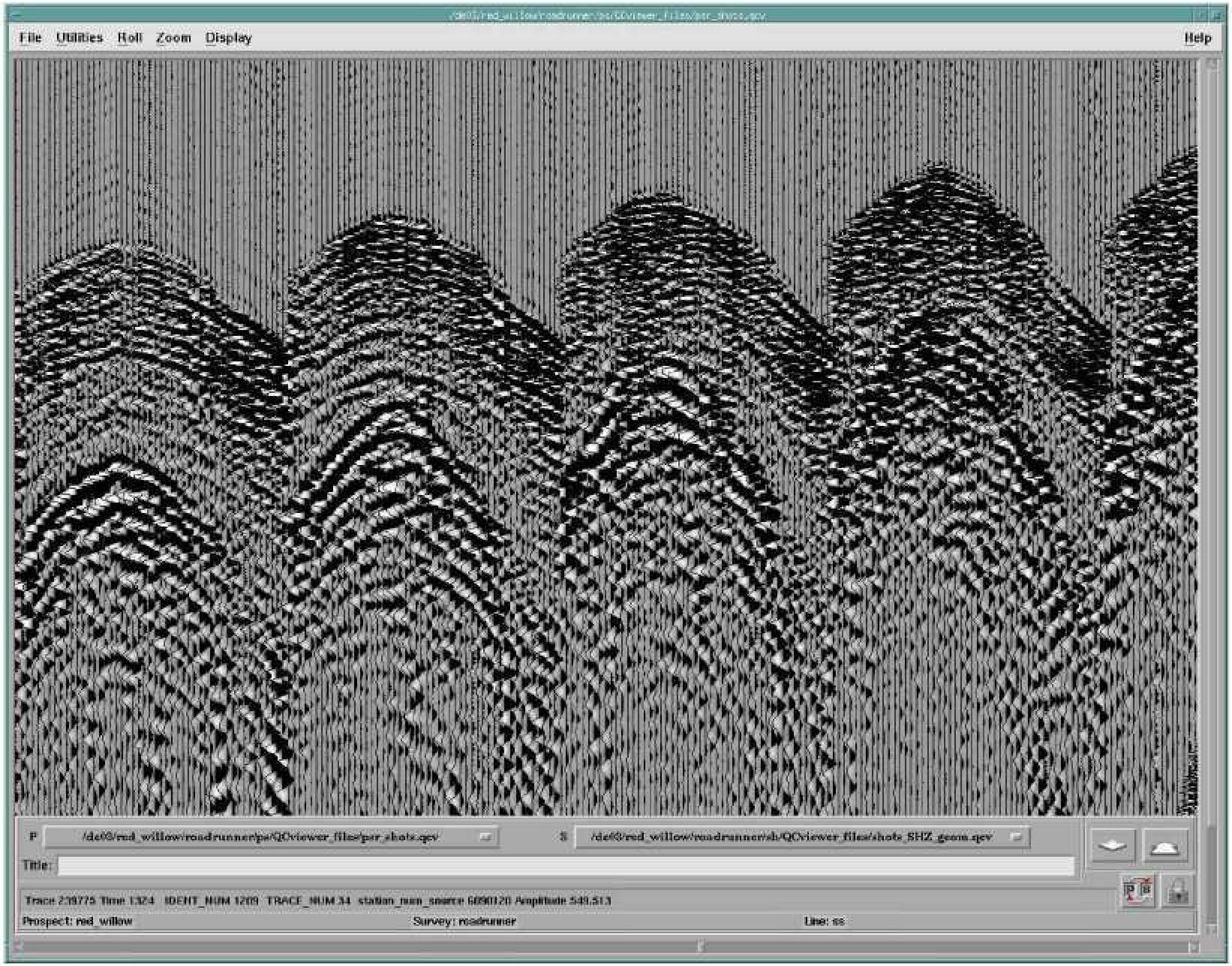

P /de03/red_willow/roadrunner/ps/QCviewer_files/psr_shots.qcv

S /de03/red_willow/roadrunner/sh/QCviewer_files/shots_SHZ_geom.qcv

Title:

Trace 239775 Time 1324 IDENT_NUM 1209 TRACE_NUM 34 station_num_source 6090120 Amplitude 549.513

Prospect: red_willow Survey: roadrunner Line: ss

Figure 4-23. Typical Shot Record: P source – Radial component.

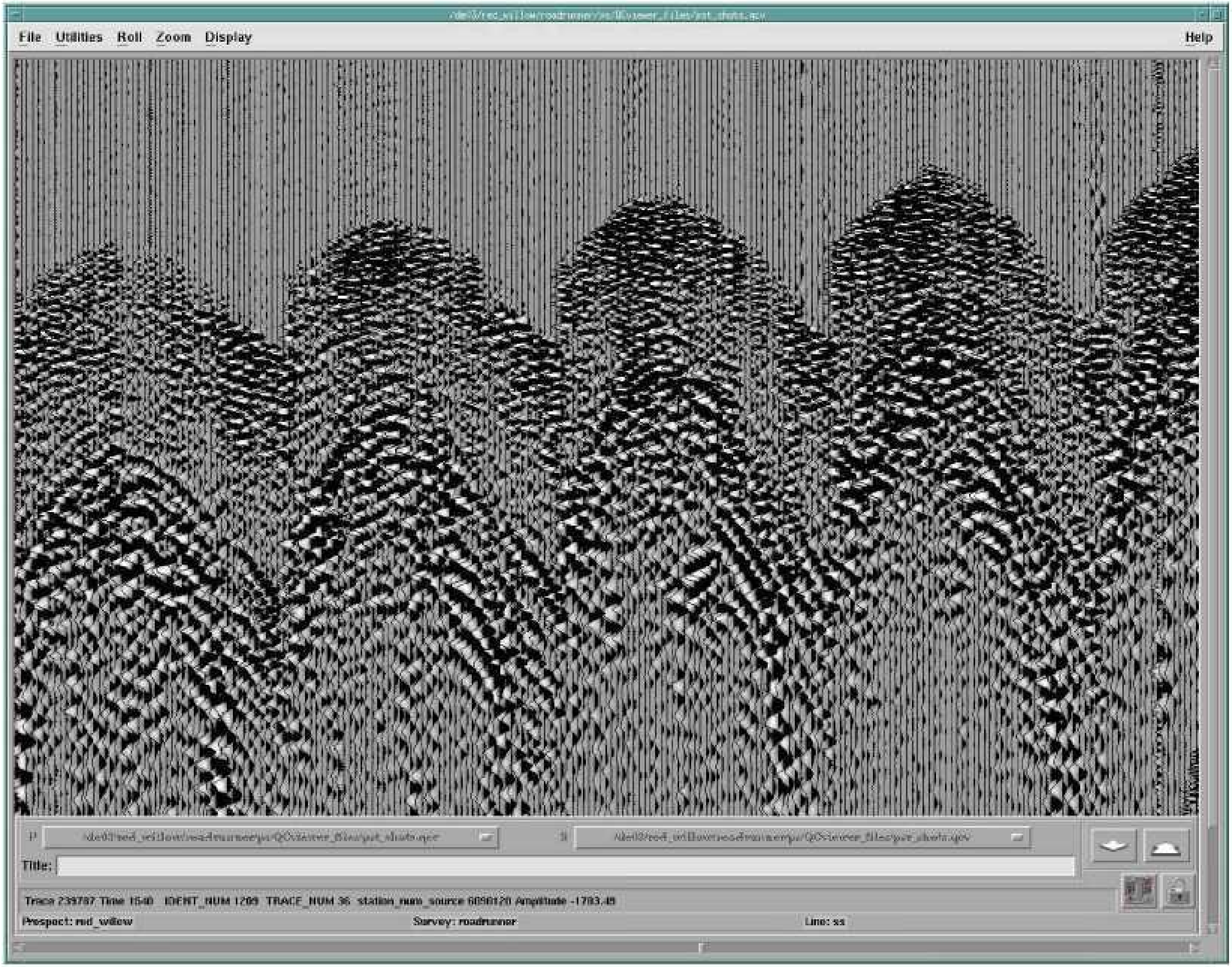

```
Trace 239787 Time 1540  IDENT_NUM 1209  TRACE_NUM 36  station_num_source 6090120 Amplitude -1783.49
Prospect: red_willow                    Survey: roadrunner                    Line: ss
```

Figure 4-24. Typical Shot Record: P source – Transverse component.

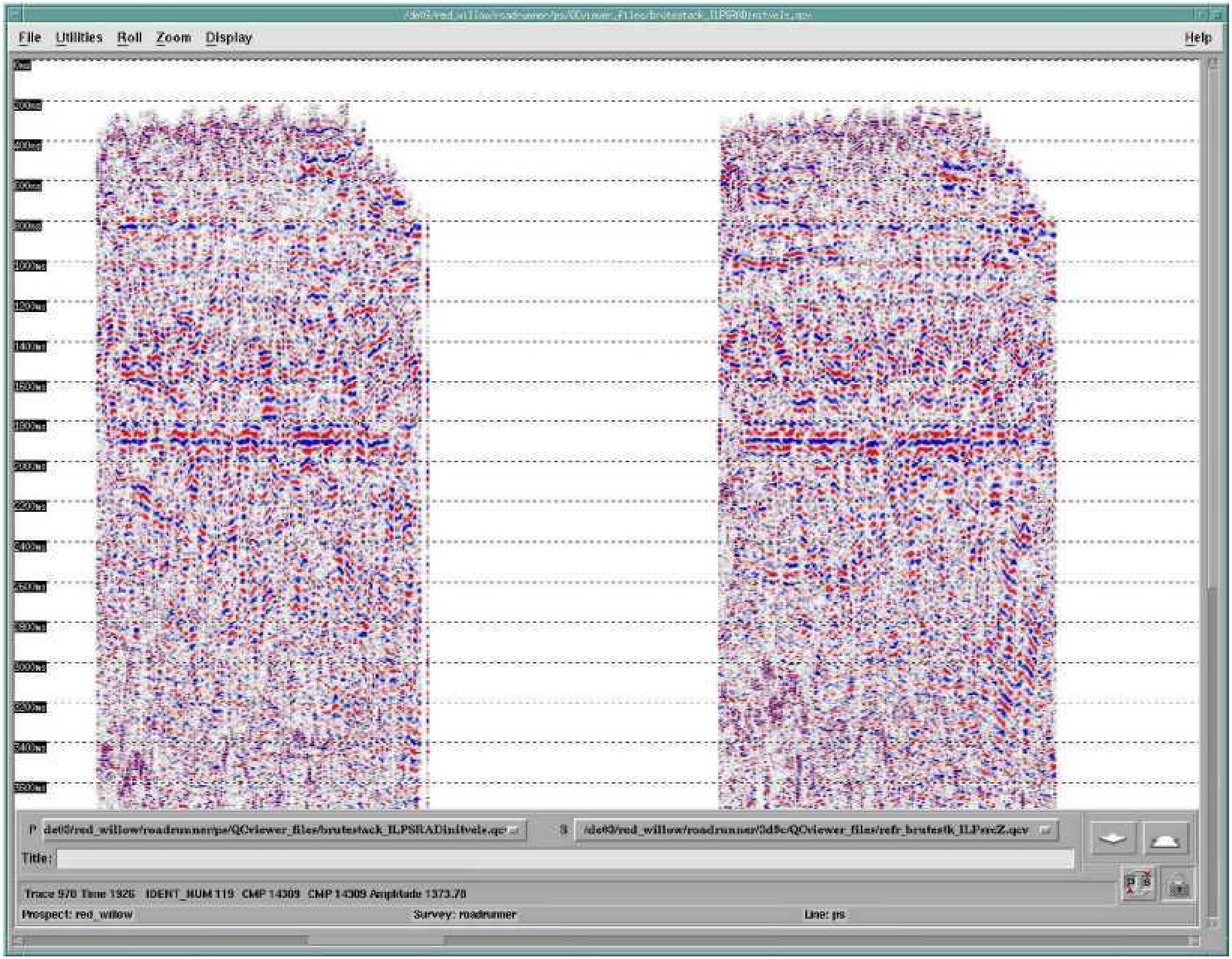

P de05/red_willow/roadrunner/ps/QCviewer_files/brutestack_ILPSRADinitvels.qc

S /de03/red_willow/roadrunner/3d9c/QCviewer_files/refr_brutestk_ILPsrcZ.qcv

Title:

Trace 970 Time 1926 IDENT_NUM 119 CMP 14309 CMP 14309 Amplitude 1373.78

Prospect: red_willow Survey: roadrunner Line: ps

Figure 4-25. Brute Stack: P source – Radial component.

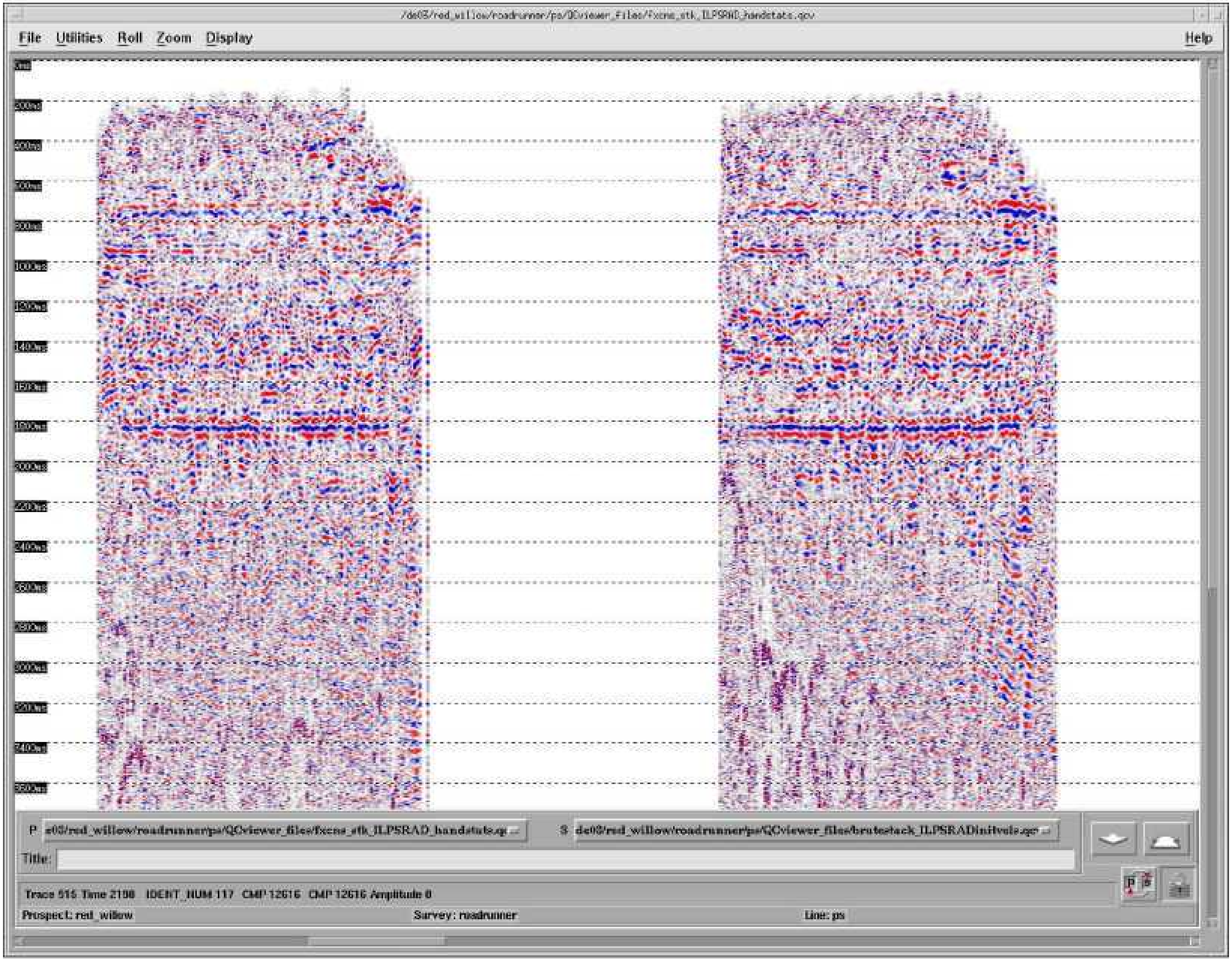

P e03/red_willow/roadrunner/ps/QCviewer_files/fxcns_stk_ILPSRAD_handstats.q

S de03/red_willow/roadrunner/ps/QCviewer_files/brutestack_ILPSRADinitvels.qc

Trace 515 Time 2198 IDENT_NUM 117 CMP 12616 CMP 12616 Amplitude 0

Prospect: red_willow Survey: roadrunner Line: ps

Figure 4-26. Preliminary Statics Stack: P source – Radial component.

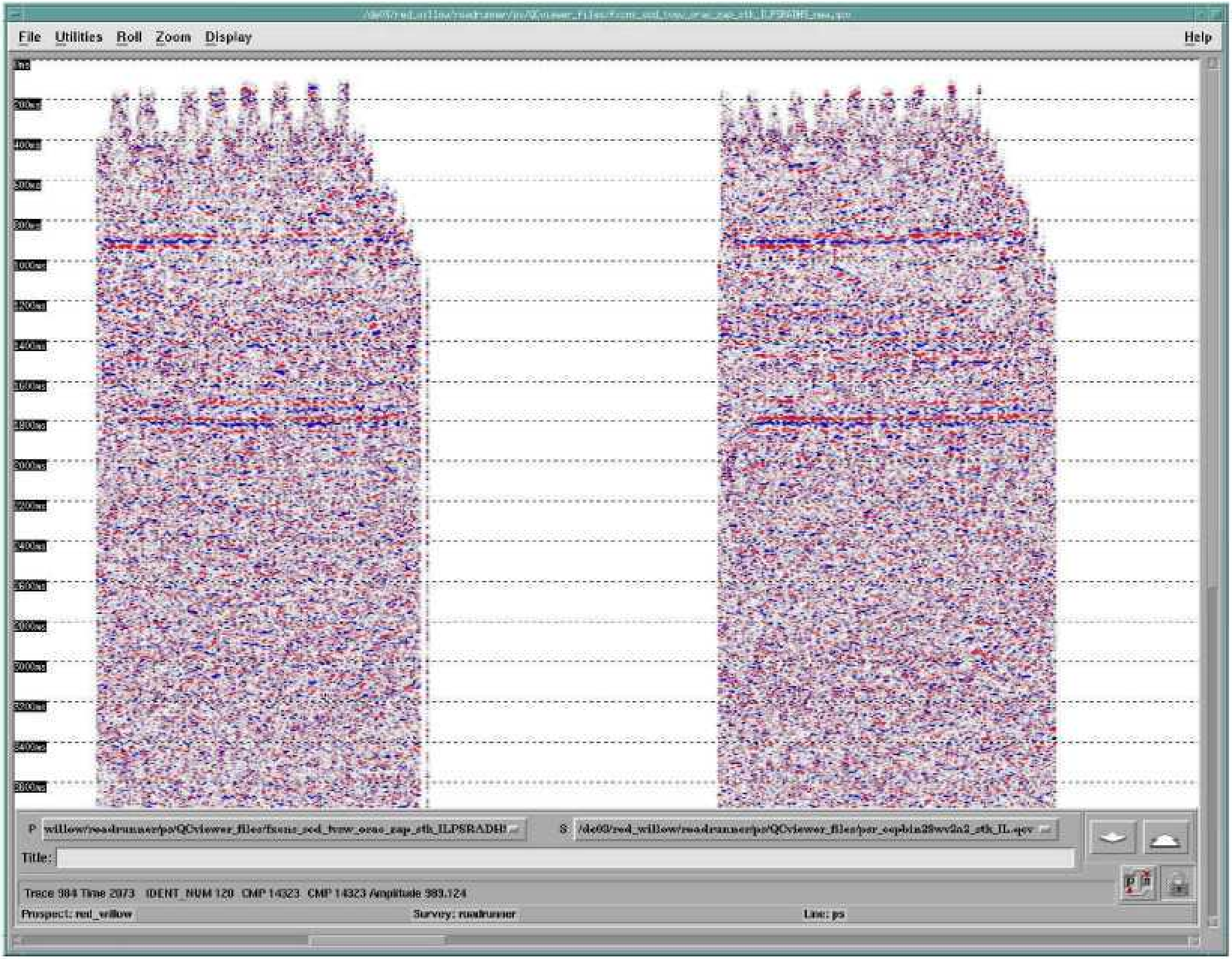

P willow/roadrunner/ps/QCviewer_files/fxsus_scd_tvsw_ornc_zap_stk_ILPSRADH!

S /de03/red_willow/roadrunner/ps/QCviewer_files/psr_copbin28wv2n2_stk_IL.qcv

Title:

Trace 984 Time 2073 IDENT_NUM 120 CMP 14323 CMP 14323 Amplitude 983.124

Prospect: red_willow Survey: roadrunner Line: ps

Figure 4-27. SCD/TVSW/ZAP Stack: P source – Radial component.

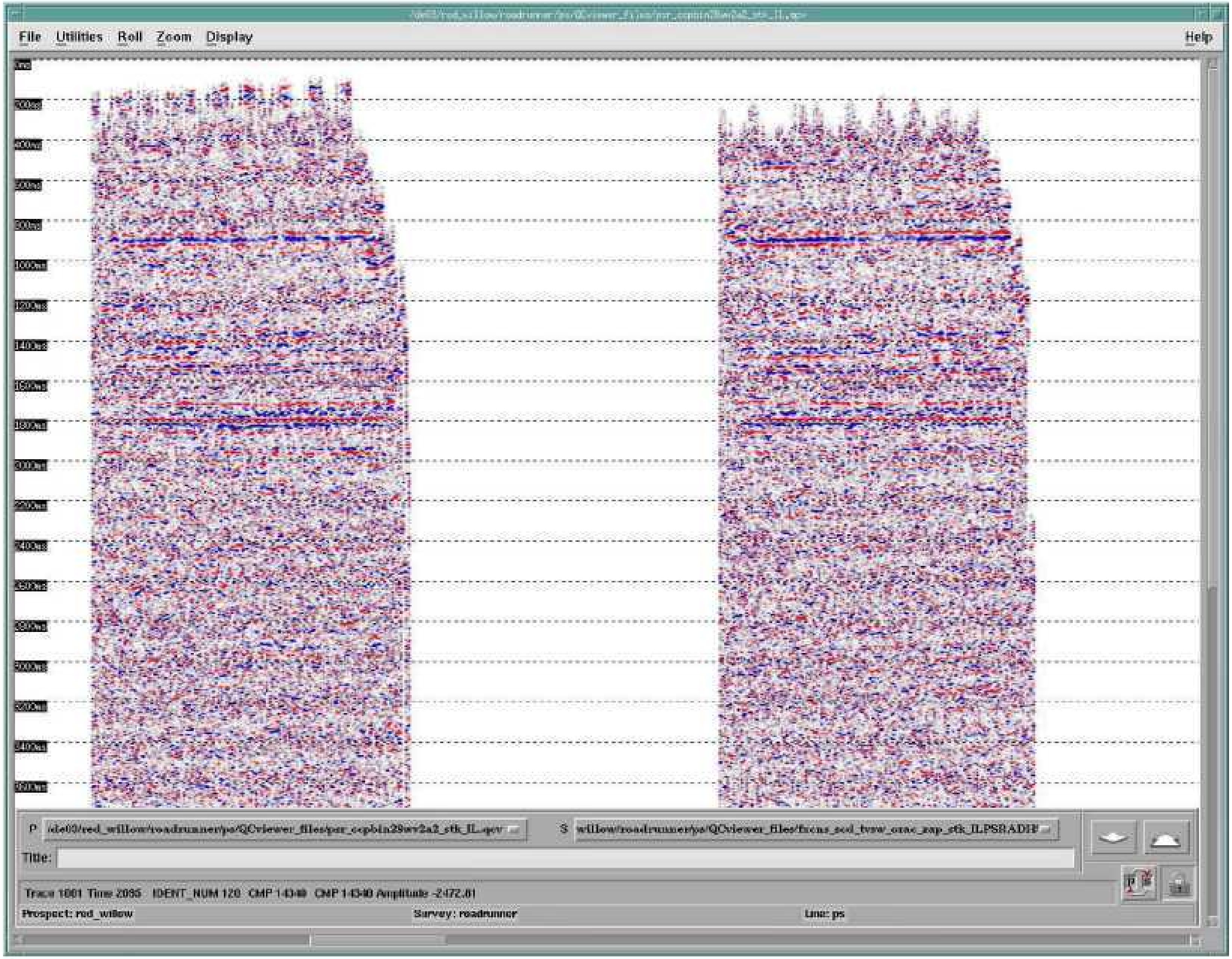

P /de03/red_willow/roadrunner/ps/QCviewer_files/psr_ccpbin29wv2a2_stk_IL.qcv

S willow/roadrunner/ps/QCviewer_files/fxcns_scd_tvsw_ozac_zap_stk_ILPSRADIF

Title:

Trace 1001 Time 2085 IDENT_NUM 120 CMP 14340 CMP 14340 Amplitude -2472.81

Prospect: red_willow Survey: roadrunner Line: ps

Figure 4-28. Final CCP Stack: P source – Radial component.

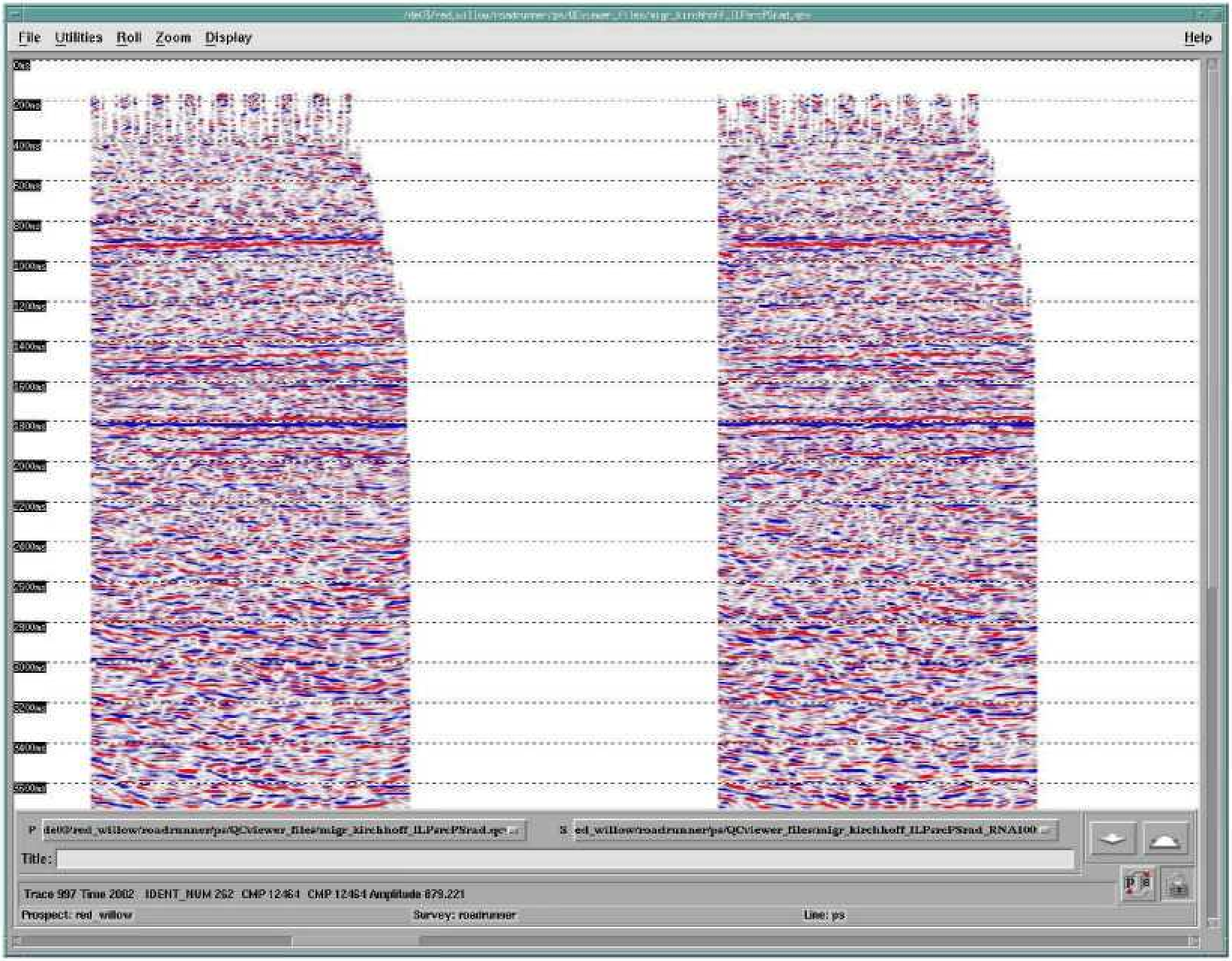

P de03/red_willow/roadrunner/ps/QCviewer_files/migr_kirchhoff_ILPrecPSrad.qc

S ed_willow/roadrunner/ps/QCviewer_files/migr_kirchhoff_ILPrecPSrad_RNA100

Title:

Trace 997 Time 2002 IDENT_NUM 262 CMP 12464 CMP 12464 Amplitude 879.221

Prospect: red_willow Survey: roadrunner Line: ps

Figure 4-29. Final Migration: P source – Radial component.

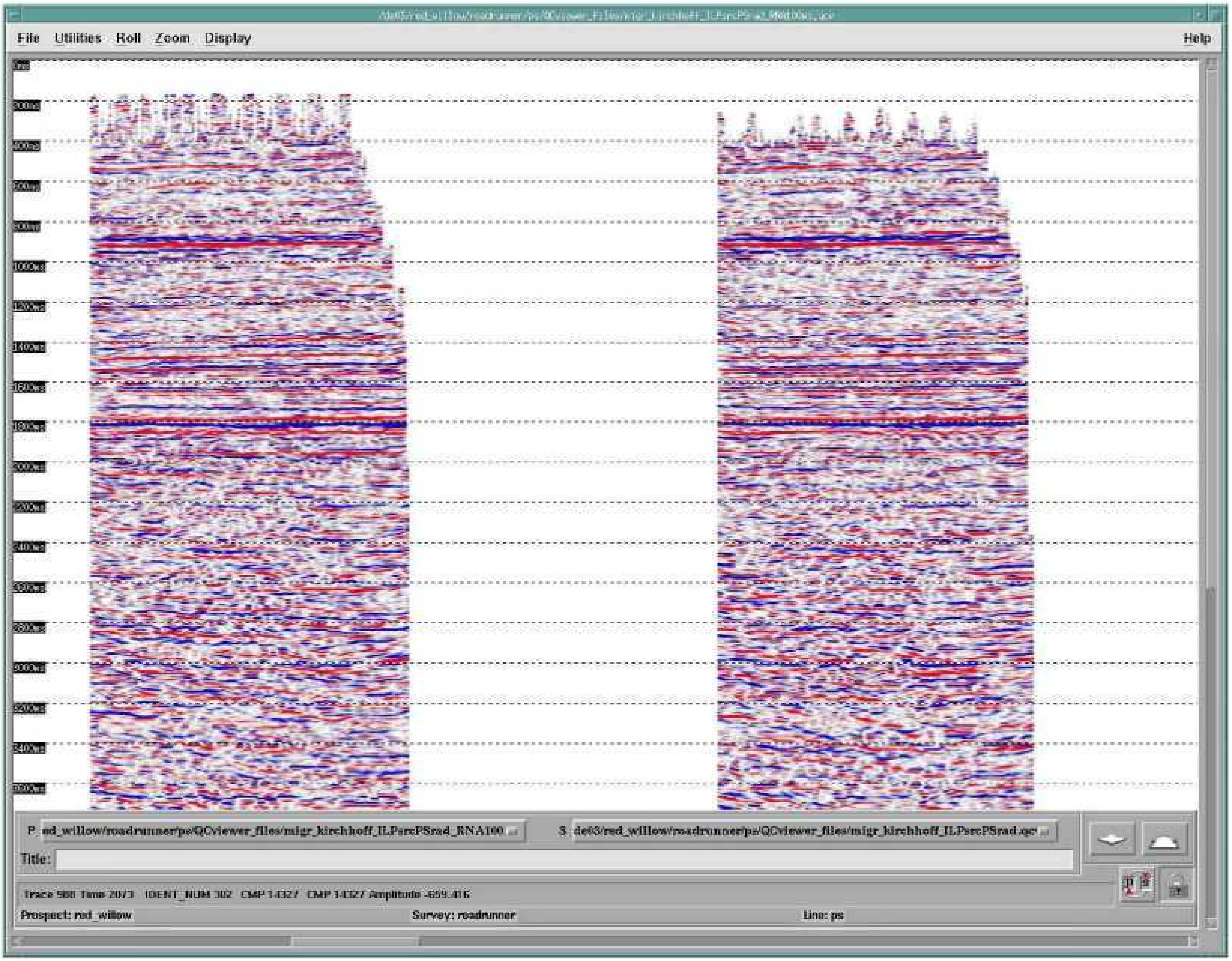

P: ed_willow/roadrunner/ps/QCviewer_files/migr_kirchhoff_ILPsrcPSrad_RNA100

S: de03/red_willow/roadrunner/ps/QCviewer_files/migr_kirchhoff_ILPsrcPSrad.qc

Title:

Trace 988 Time 2073 IDENT_NUM 302 CMP 14327 CMP 14327 Amplitude -659.416

Prospect: red_willow Survey: roadrunner Line: ps

Figure 4-30. Final Migration/FXY Dcn: P source – Radial component.

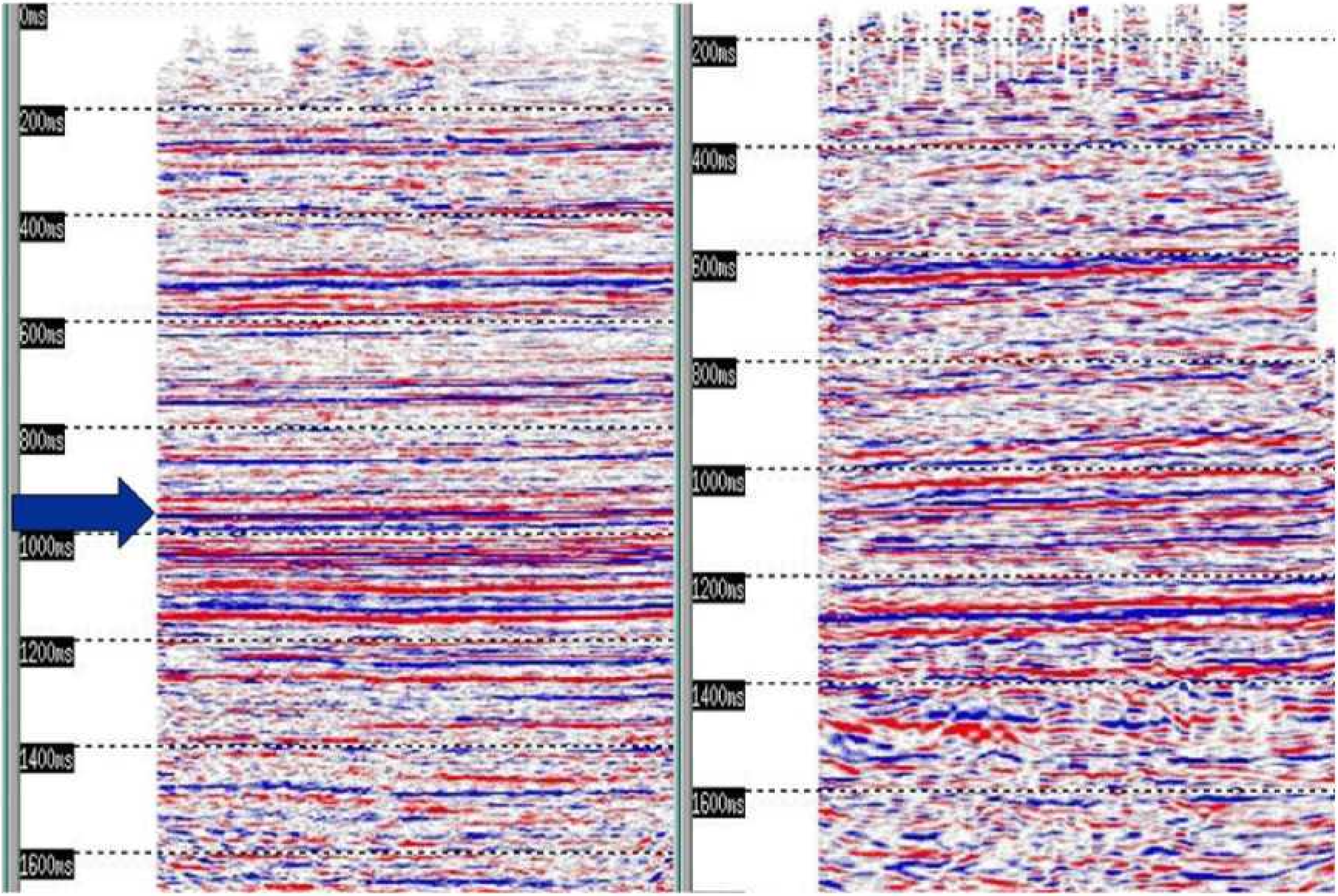

Figure 4-31. Final Migration Comparison: PP to PS.

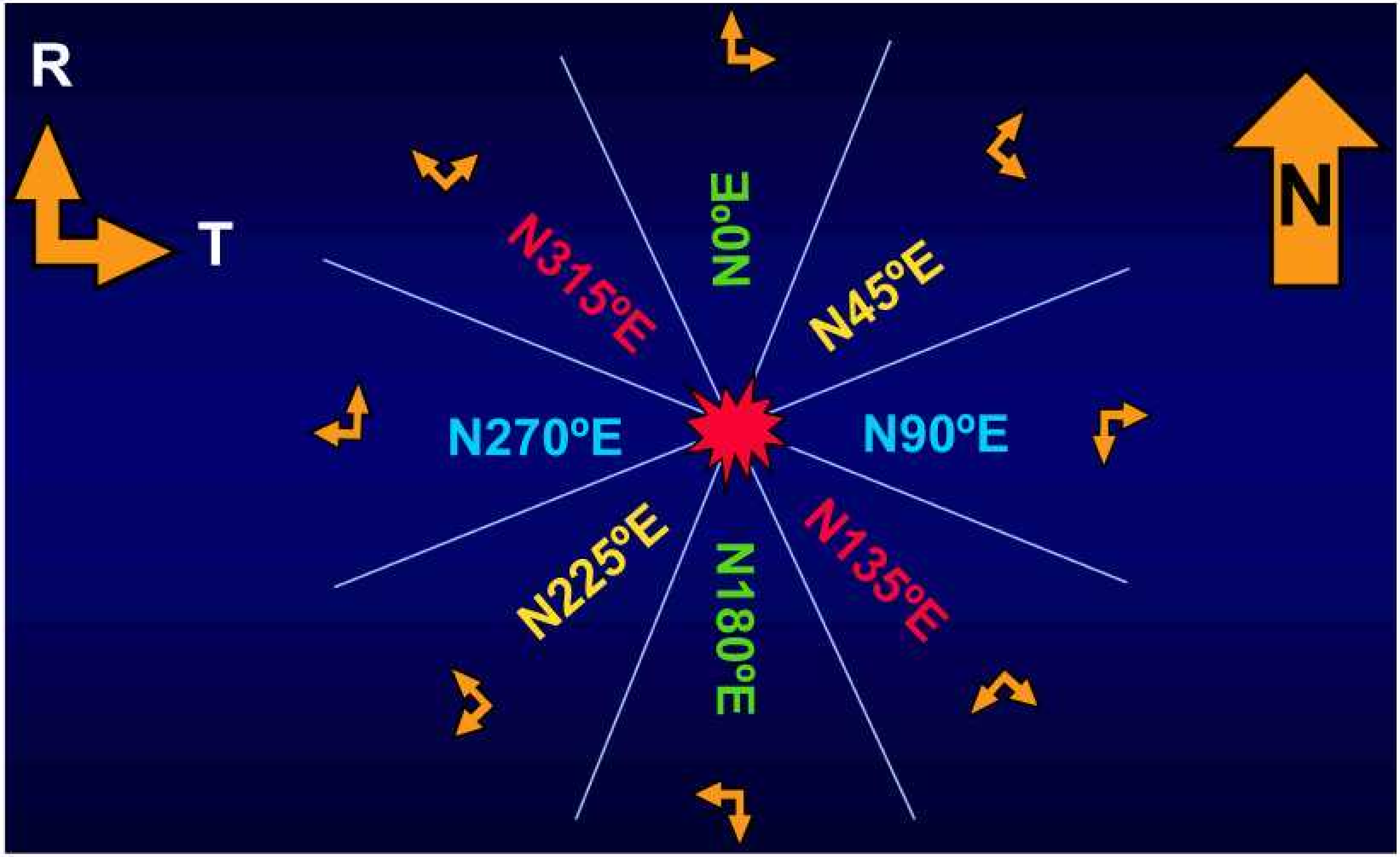

Figure 4-32. Source to Receiver Azimuth Limitation.

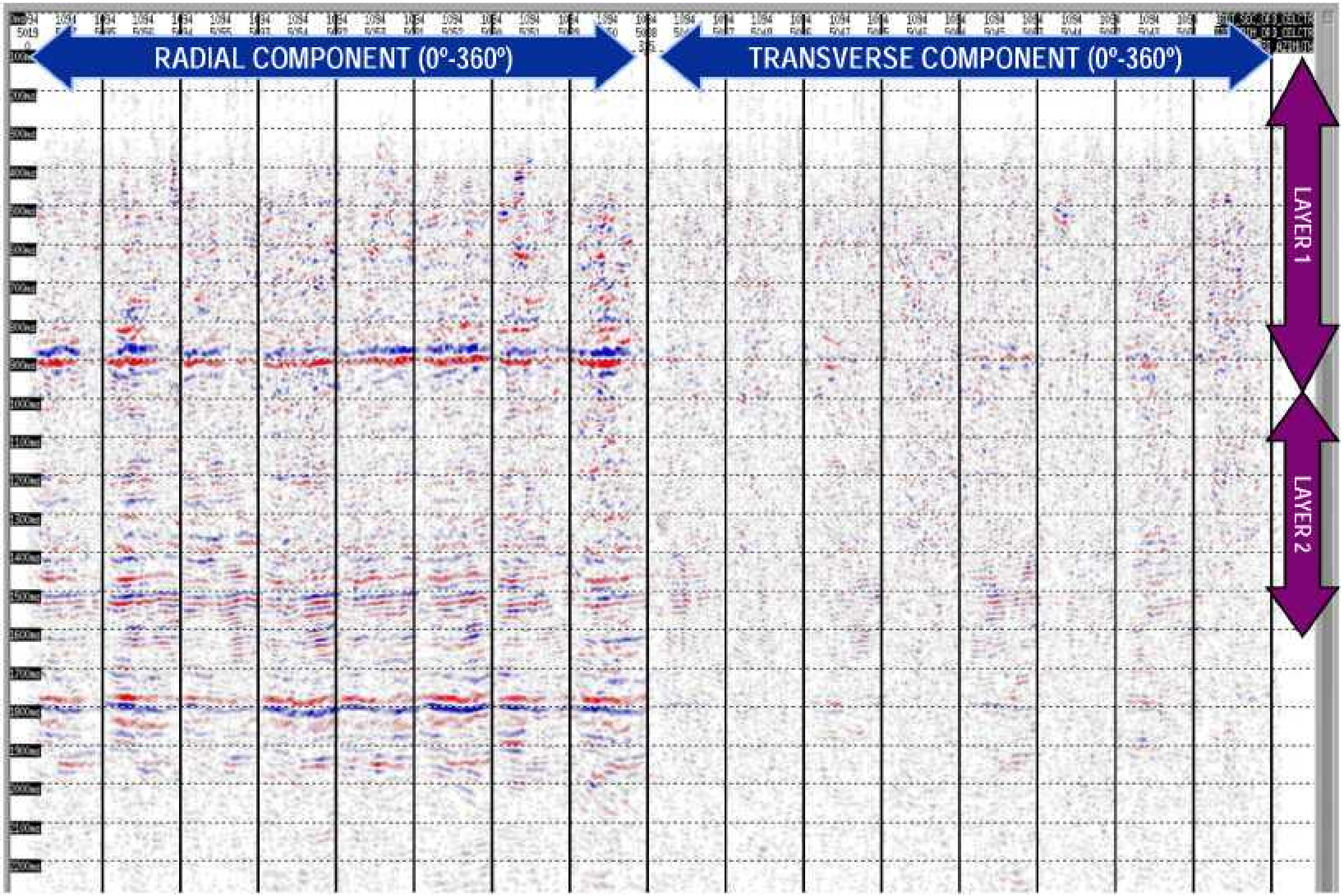

Figure 4-33. PS Input to 2Cx2C Layer Stripping.

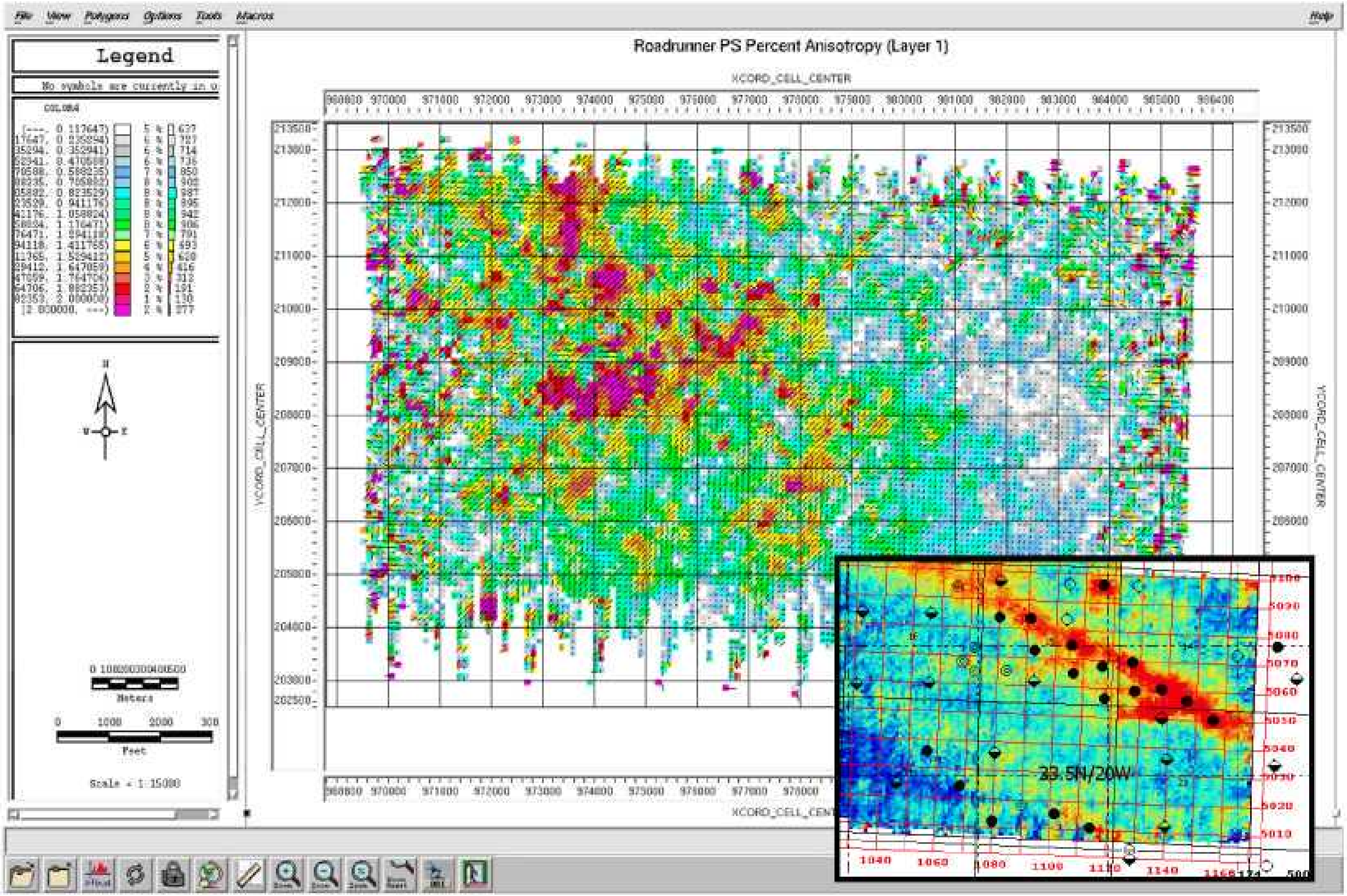

Figure 4-34. S-wave Birefringence: Layer 1.

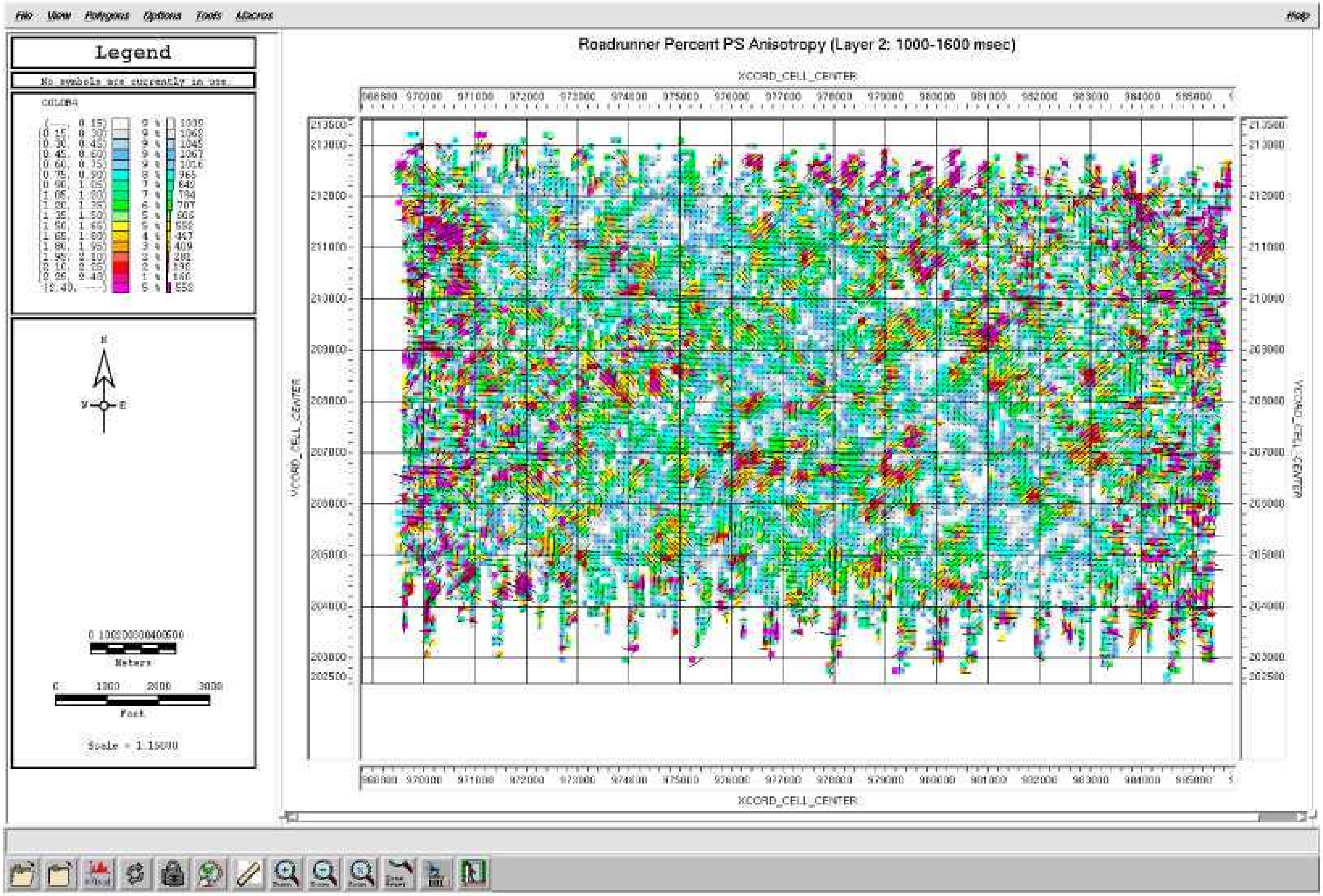

Figure 4-35. S-wave Birefringence: Layer 2.

4.2.4 S-WAVE PROCESSING

Figure 4-36 through Figure 4-39 show the shot records for the SS data as initially processed. These are believed to be in a radial and transverse orientation; however, subsequent analysis and discussion suggests that this is not the optimum orientation for processing. Figure 4-40 shows the results of the S-wave statics calculation using the SS (transverse) data. The results are encouraging and when applied show improvement on the stack sections.

In summary, the processing results show that:

1) Algal mound features were present on P-wave data
2) PS-wave data quality was good and the event correlation to the PP data was reasonable.
3) S-wave anisotropy measurements from the PS data were small but showed a possible correlation to the reservoir structure.
4) SS refraction statics correlated well with PP statics.

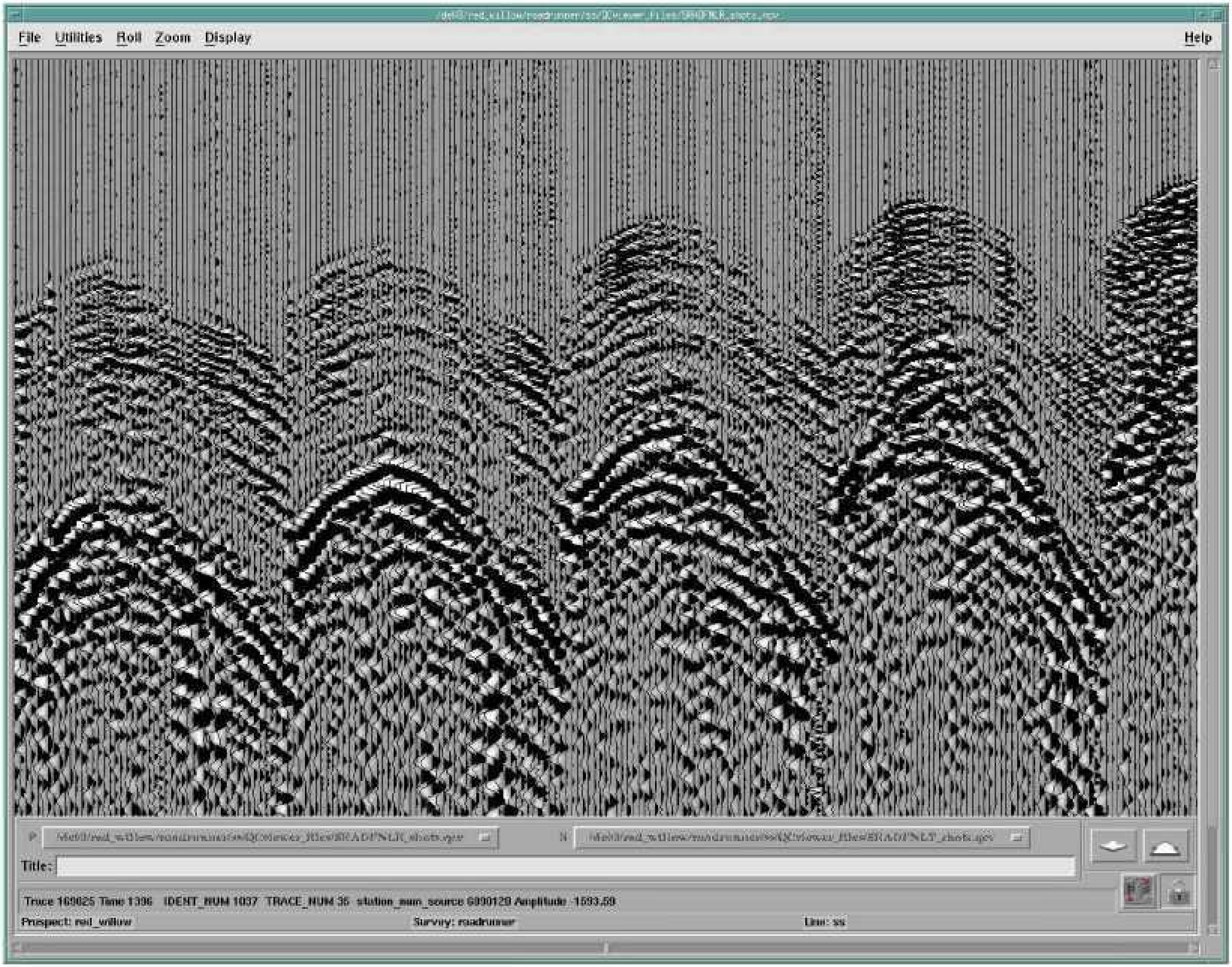

Title:

Trace 169625 Time 1396 IDENT_NUM 1037 TRACE_NUM 35 station_num_source 6890129 Amplitude 1593.59

Prospect: red_willow Survey: roadrunner Line: ss

Figure 4-36. Shot Record: Radial source – Radial detector.

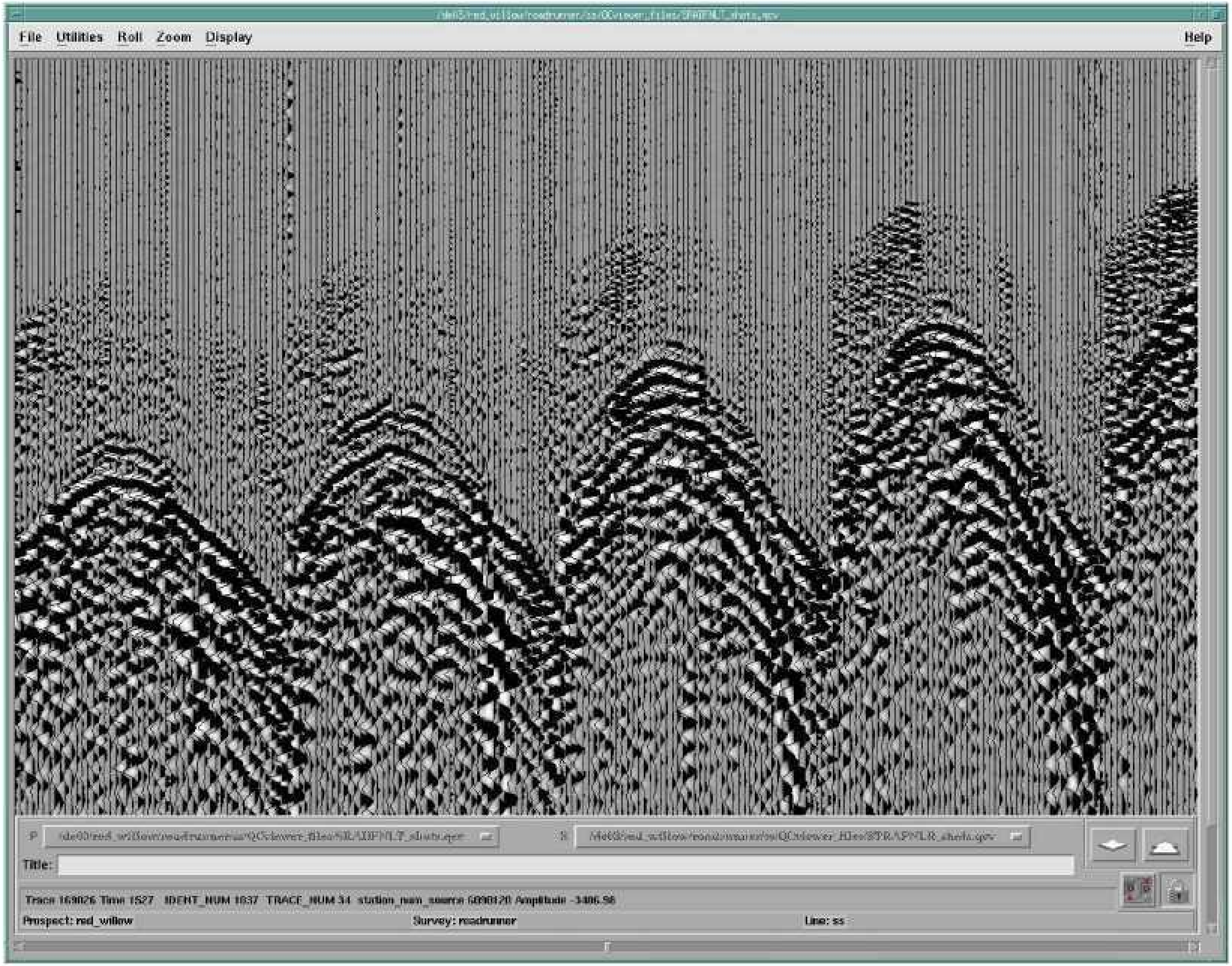

Trace 169026 Time 1527 IDENT_NUM 1037 TRACE_NUM 34 station_num_source 6090120 Amplitude -3406.98

Prospect: red_willow

Survey: roadrunner

Line: ss

Figure 4-37. Shot Record: Radial source – Trans detector.

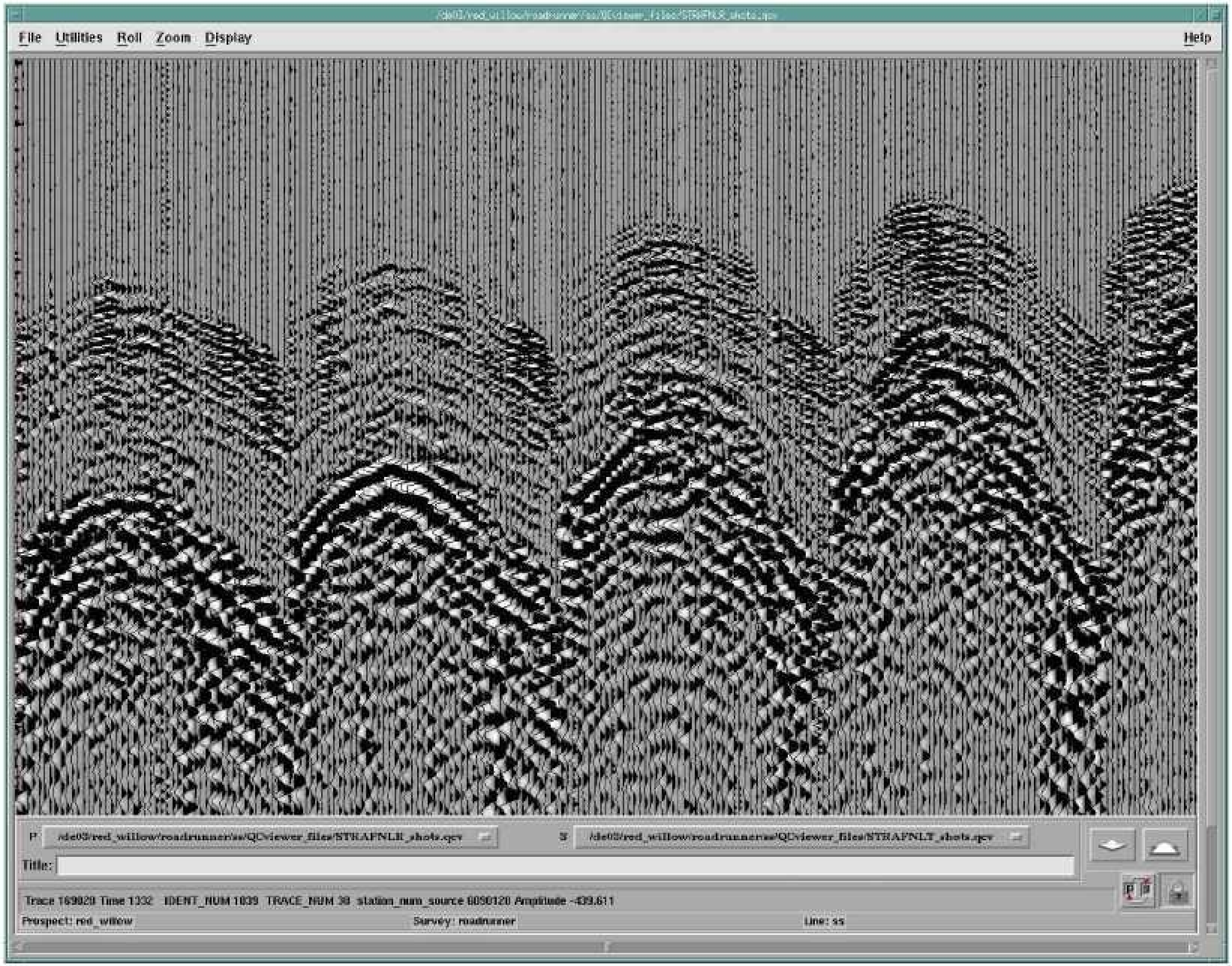

P /de03/red_willow/roadrunner/ss/QCviewer_files/STRAFNLR_shots.qcv

S /de03/red_willow/roadrunner/ss/QCviewer_files/STRAFNLT_shots.qcv

Title:

Trace 169029 Time 1332 IDENT_NUM 1039 TRACE_NUM 38 station_num_source 6050120 Amplitude -439.611

Prospect: red_willow Survey: roadrunner Line: ss

Figure 4-38. Shot Record: Trans source – Radial detector.

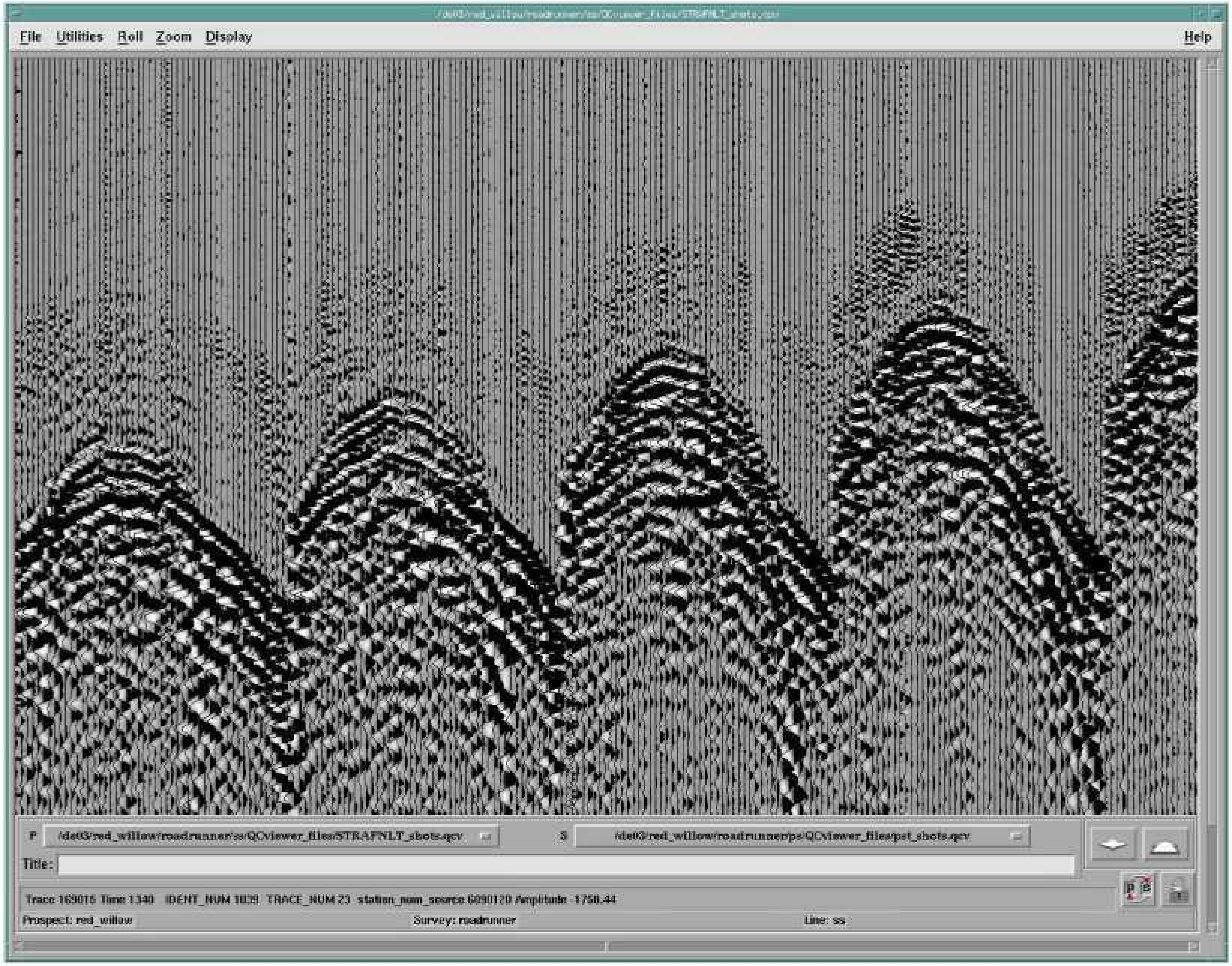

P: /det03/red_willow/roadrunner/ss/QCviewer_files/STRAFNLT_shots.qcv

S: /det03/red_willow/roadrunner/ps/QCviewer_files/pst_shots.qcv

Title:

Trace 169015 Time 1340 IDENT_NUM 1029 TRACE_NUM 23 station_num_source 6090120 Amplitude -1750.44

Prospect: red_willow

Survey: roadrunner

Line: ss

Figure 4-39. Shot Record: Trans source – Trans detector.

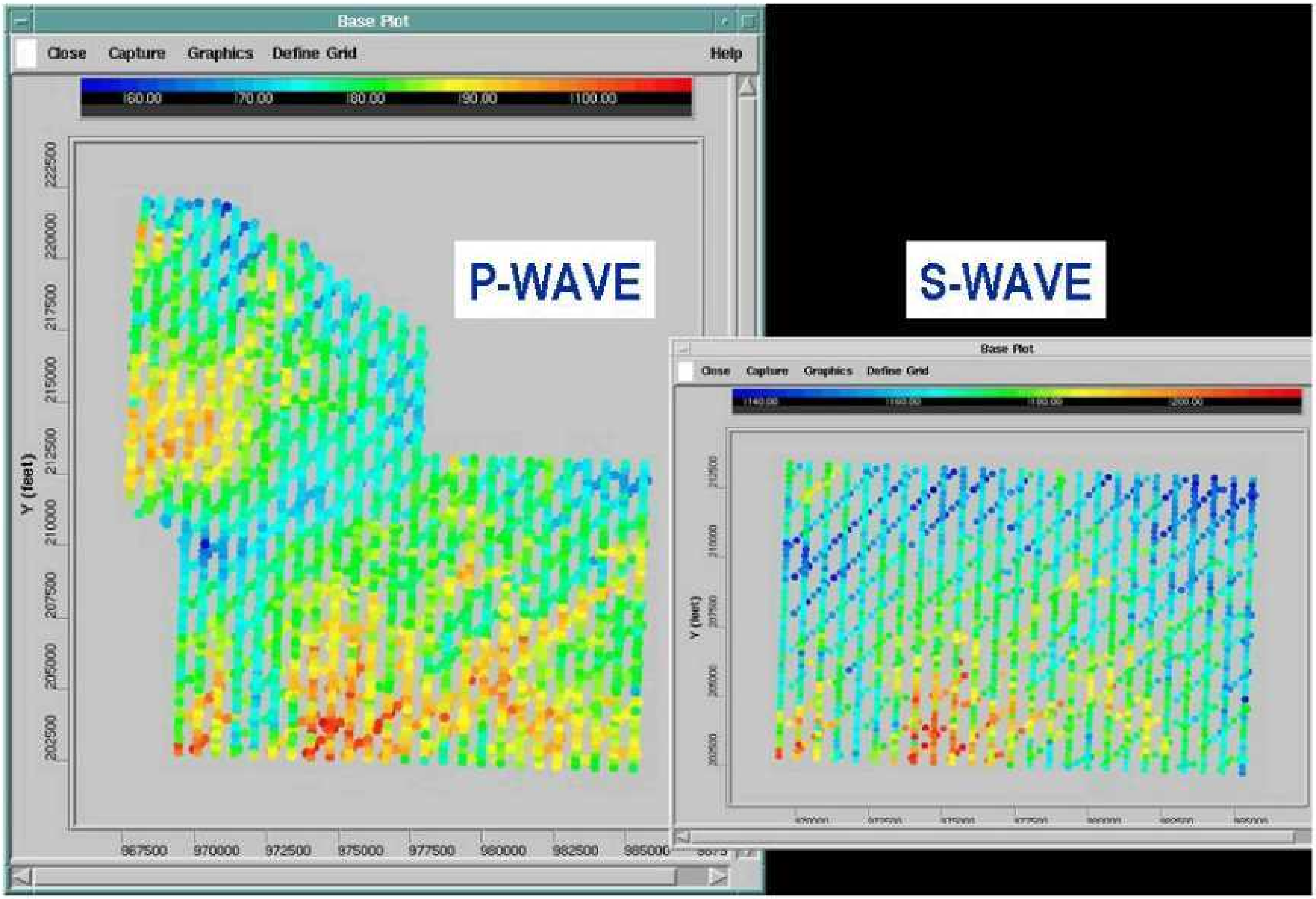

Figure 4-40. Source and receiver statics corrections.

A comparison of the various wave modes is shown in Figure 4-41 through Figure 4-46 for crossline and inline sections. The four data volumes have been referenced to the same vertical (PP) time frame using a regional Vp/Vs function. The slide for crossline 5050 (Figure 4-41) shows wave mode images for a vertical east/west section (crossline 5050). Each section has been corrected to the equivalent two-way PP travel time based on our best estimate of the average, vertical Vp/Vs ratio.

The **PP** section on the far left is the conventional wave mode used for most surface seismic applications and is from the volume used to locate and interpret the algal mound structure.

The PSv section (left center) is the section produced using a P-wave vibrator source and recorded on the two horizontal geophones. This is a measure of the mode-converted PSv-wave, which is comprised of a downgoing P-wave leg, and an upcoming Sv-wave leg. This mode is becoming increasingly popular due to the fact that one can obtain S-wave information for relatively little increased acquisition cost (1C vs 3C geophones).

The ShSh section (right center) is the section produced using the S-wave vibrator sources and the two horizontal geophones. Specifically, this section represents the data from sources and detectors oriented perpendicular to the wave propagation direction. The data are also azimuth limited to include only the strongest energy for this mode.

The SvSv section (far right) is the section also produced using the S-wave vibrator sources and the two horizontal geophones but this time using the sources and receivers parallel to the wave propagation direction. The data are also azimuth limited to include only the strongest energy for this mode.

The wave modes are organized from left to right in decreasing resolution and signal to noise (S/N) ratio.

The PP section (Figure 4-41; 1st section) shows good frequency content. It is somewhat noisier than the other profiles, but it hasn't been smoothed to the extent of the PS-data.

The PS data (Figure 4-41; 2nd section) shows an apparent higher resolution than the P-wave data over the reservoir interval. This is probably due to the shorter wavelengths of PS-wave data. It has apparently imaged something within the algal mound interval (Figure 4-42). In this enlarged portion of the section, the arrow points to a subtle blue trough. The PSv data shows good resolution compared to the PP data and possibly better in the zone surrounding the algal mound. The relation of this seismic feature to algal mound geometry or internal properties is discussed in Section 4.

The horizontal and vertical shear waves (Sections 3 and 4 in Figure 4-41) are noisy and do not have as much frequency content as the PP and PS sections. The reason for this is not yet understood, and is somewhat surprising given the good quality of the VSP velocity data for the X,Y source-detector cross terms (indicated by the red box in Figure

4-43). The resulting lack of time shift produces a relatively low amount (only a few percent) of birefringence (Figure 4-34 and Figure 4-35).

A closer examination of the SvSv and ShSh sections shows little offset between the two in time (Figure 4-44). The vertical shear component is noisier, partly due to the fact that much of the downgoing Sv energy converts to P-wave energy contaminating the results. This is not the case for the downgoing Sh which is a pure mode.

All data volumes now have comparable processing flows including DMO, post-stack time migration, model-based wavelet phase processing (MBWP), fxy deconvolution and radial predictive filter signal enhancement.

The results for inline 1107 (Figure 4-45 and Figure 4-46) show a similar result.

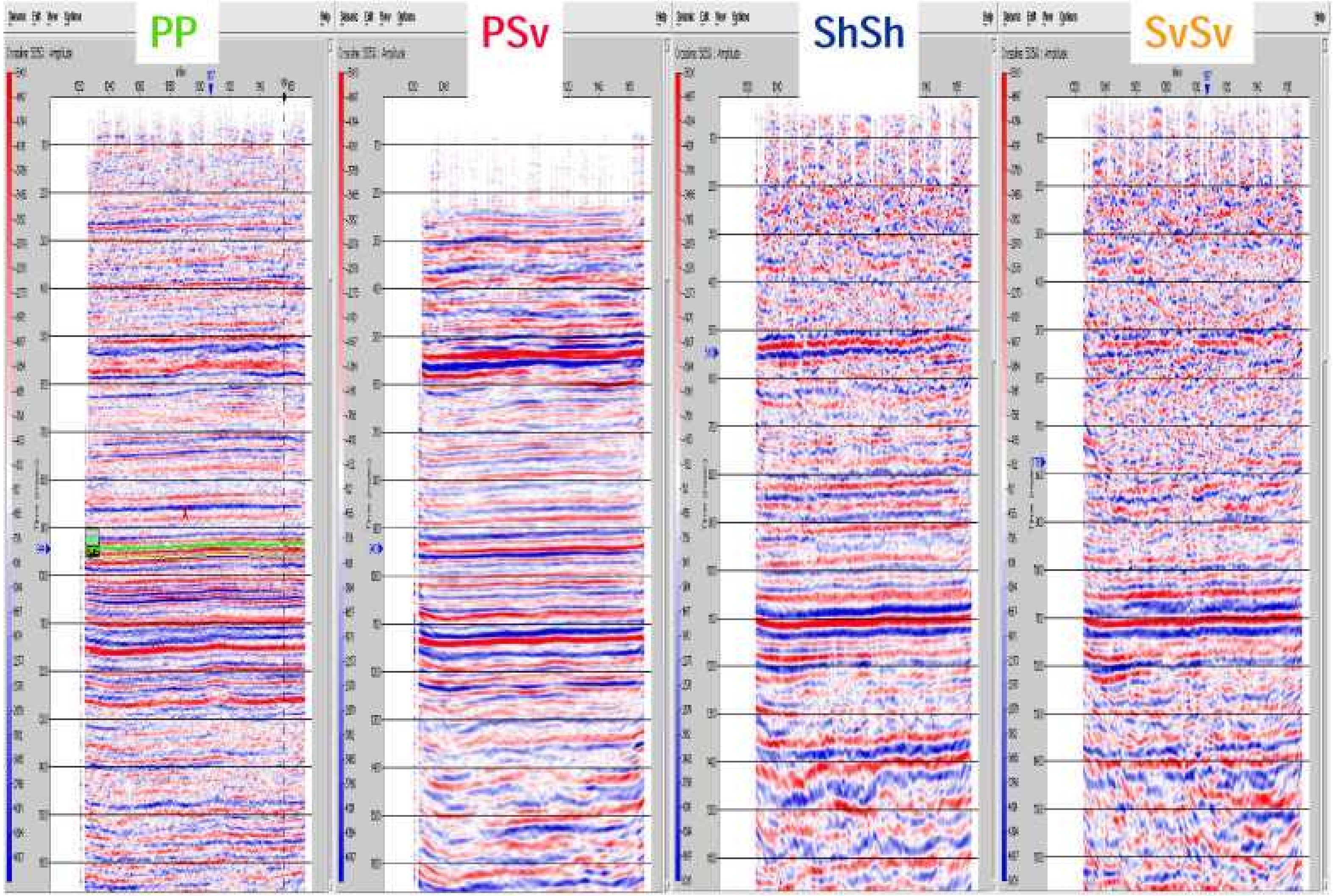

Figure 4-41. Example of PP, PS and SS-wave sections for Crossline 5050 (in PP time)

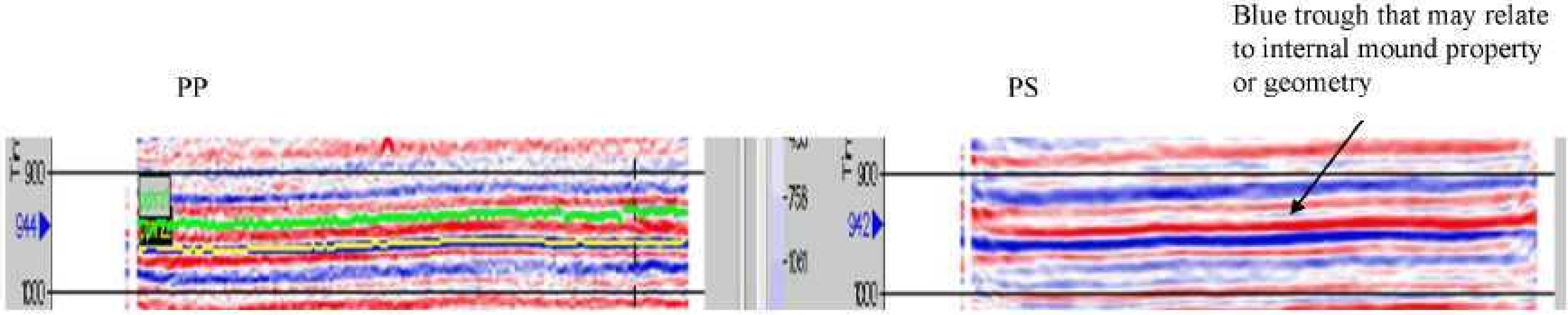

Blue trough that may relate to internal mound property or geometry

Figure 4-42. Enlarged portion of the PP (left) and PS-wave (right) sections shown in Figure 4-41. The green line superimposed on PP-wave diagram is a marker for the possible top of the Algal mounds, while the yellow line is a marker for the possible bottom of the mounds. On the right (PS-Wave) section, the arrow points to a faint blue trough that may relate to internal properties of the mounds.

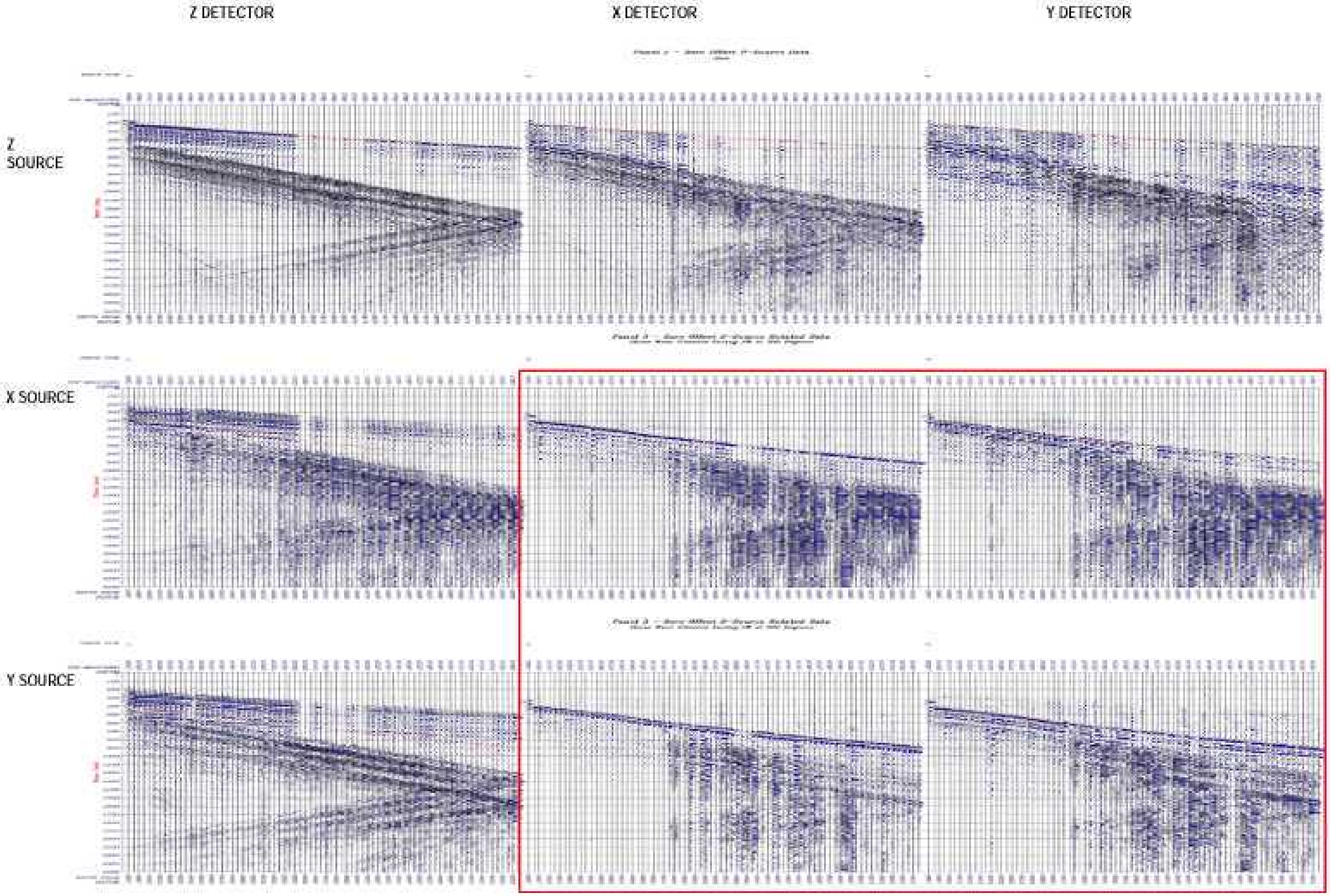

Figure 4-43. VSP Data – Zero-offset Source - Rotated 9C.

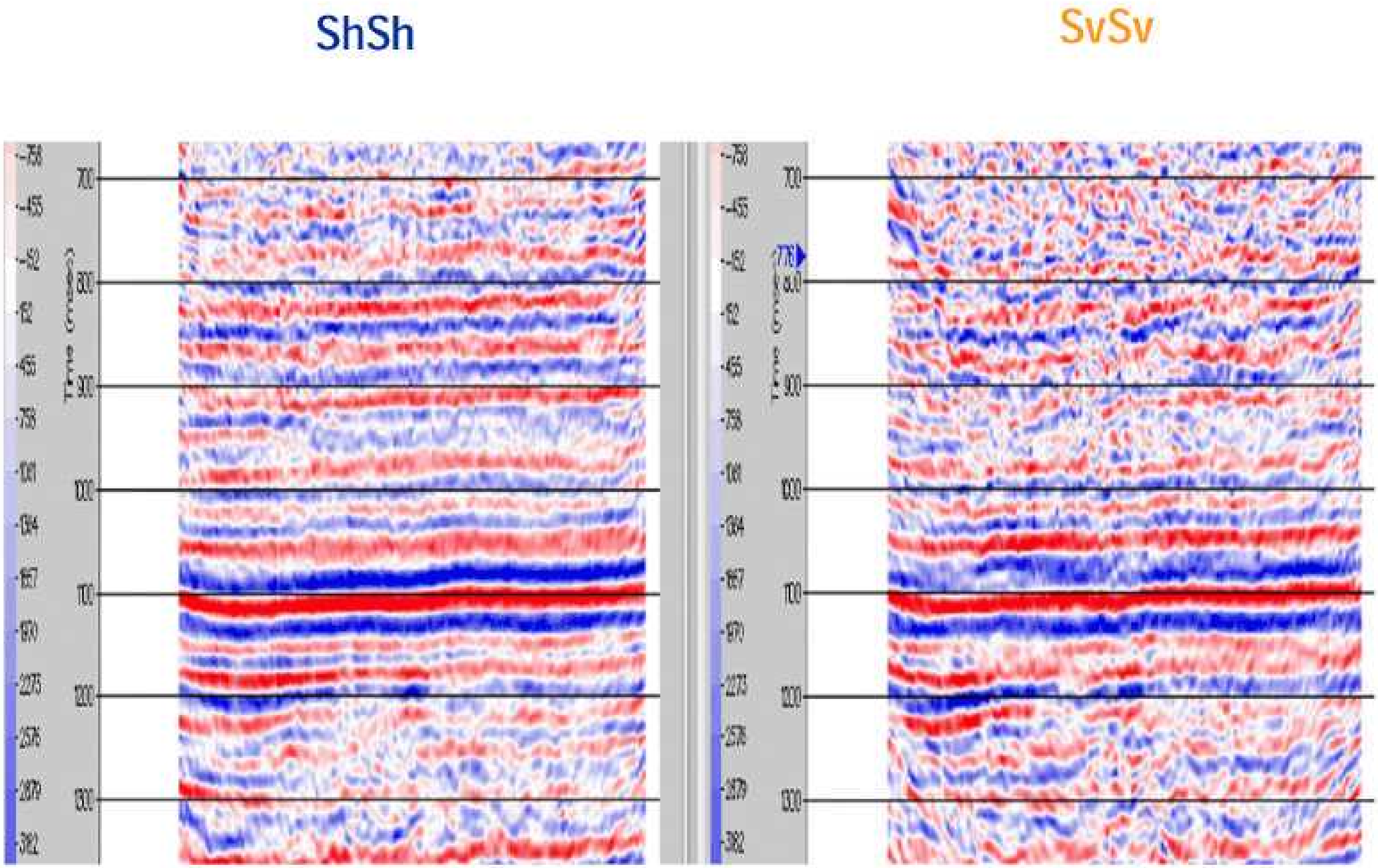

Figure 4-44. Enlarged portion of columns 3 and 4 of Figure 4-41.

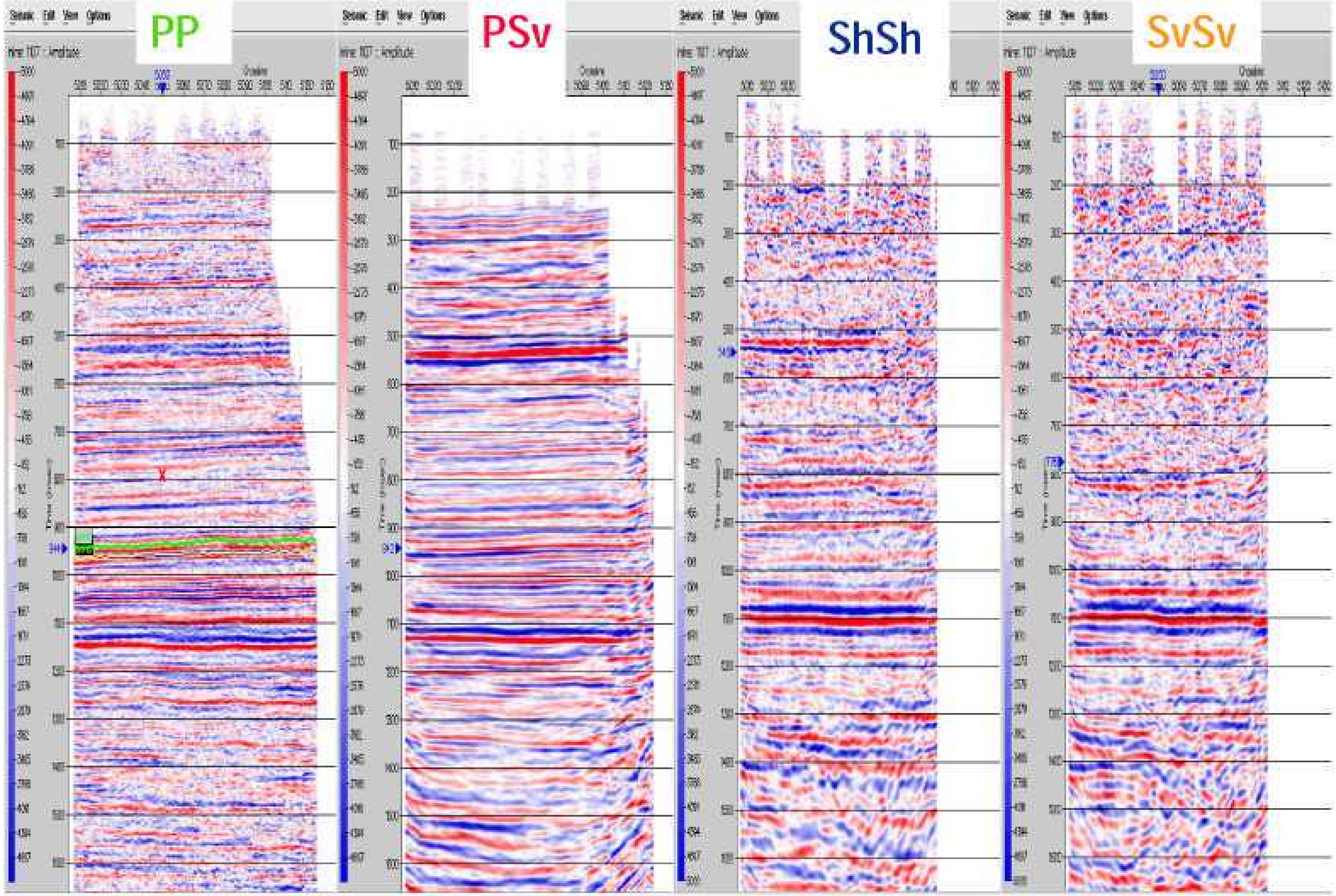

Figure 4-45. Example of PP, PS and SS-wave sections for inline 1107 (in PP time).

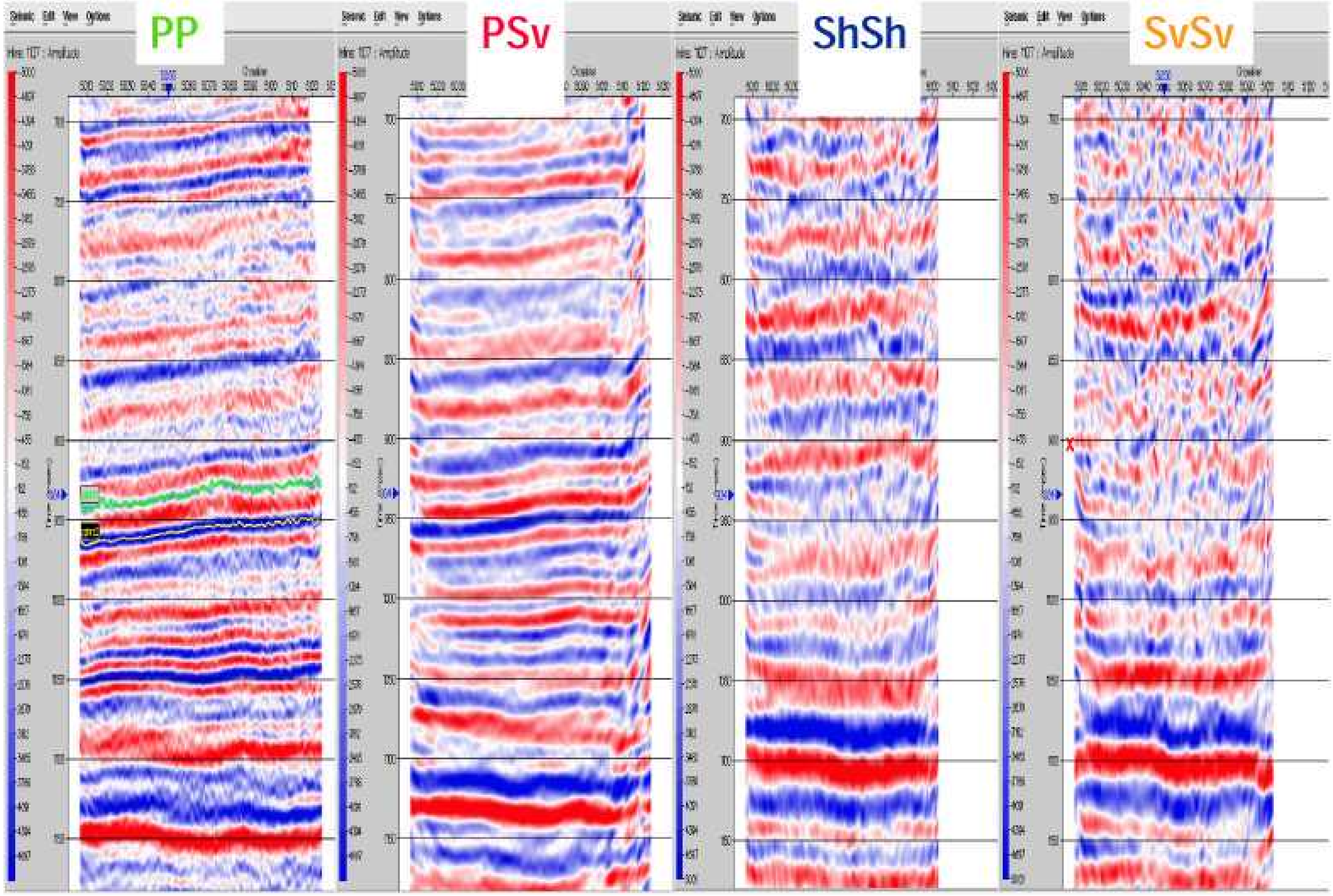

Figure 4-46. Close-up view of inline section 1107

4.3 Seismic Processing Results - AXIS

4.3.1 PROCESSING RESULTS

The following sections illustrate the P- and S-wave processing carried out by Axis (Figure 4-47 through Figure 4-55). AXIS Geophysics processed the 3D9C data using several different processing approaches. These included their WAVO™, AWAVO™ and AZIM™ processing algorithms.

WAVO™ is a wavelet-based AVO method (Figure 4-47 through Figure 4-49). By calculating the AVO gradient over a short time window that is proportional to the dominant frequency, incorrect values at zero crossings due to NMO stretch and tuning effects are mitigated. These potentially lead to more diagnostic crossplots and better resolution of layers.

AWAVO™ computes the AVO gradient on azimuthally sorted gathers (Figure 4-50 through Figure 4-51). The processing produces several parameters that potentially can delineate interfaces with high resolution. Parameters include:

- difference between the maximum and minimum gradients;
- direction of maximum gradient; and
- calculated error.

AZIM™ measures and corrects azimuthally varying time shifts related to azimuthally varying anisotropy (Figure 4-52 through Figure 4-55). This correction often leads to improved stack volumes. Moreover, their measurement and subsequent inversion yields velocity volumes related to the magnitude and azimuth of anisotropy as it varies both temporally and spatially.

There are a large number of attributes derived from pre- and post-stack seismic and velocities. The initial inspection shows anomalies west and north of the 06406 well at the reservoir level. The anomaly is especially consistent between the isotropic WAVO™ and AZIM™ Vfast azimuth volumes.

4.3.1.1 WAVO™

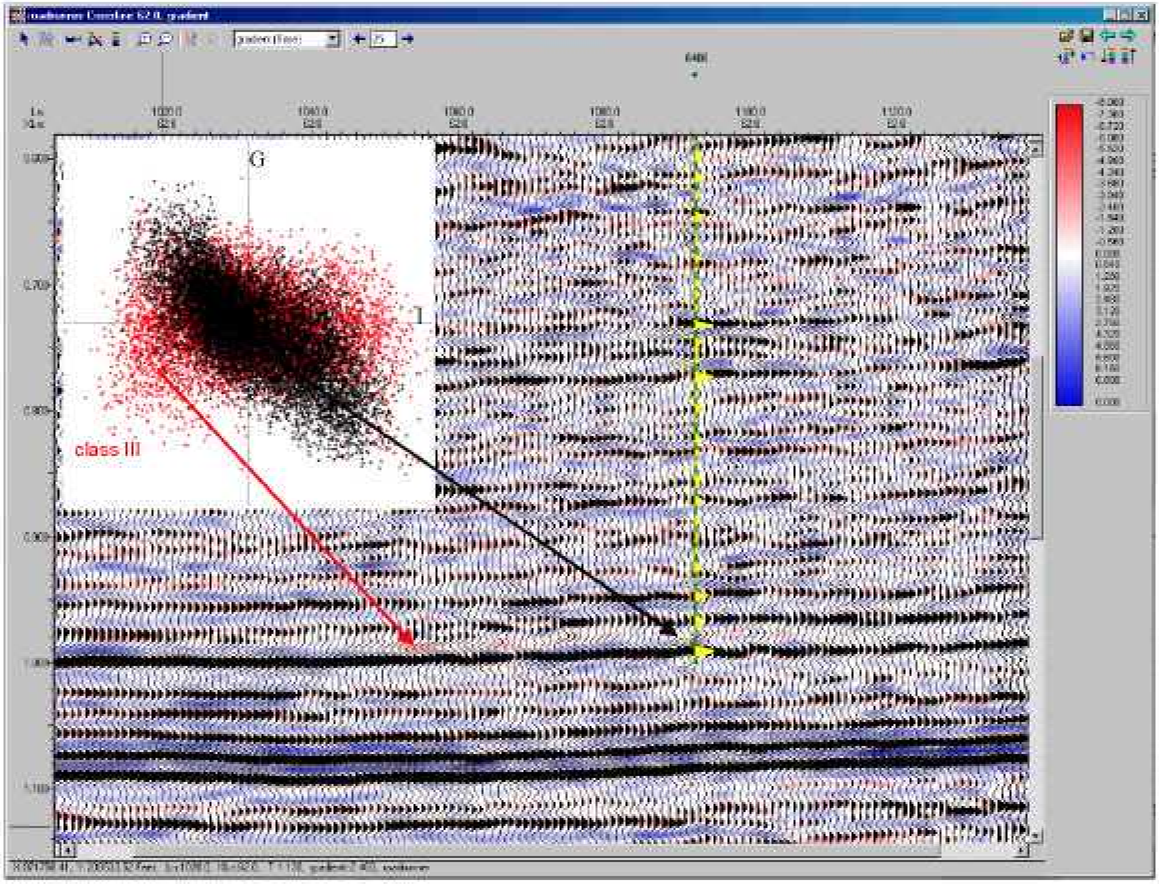

Figure 4-47. Gradient-intercept plot (isotropic) of two regions. Each is 20x20 cdps and 20 ms thick. The black is at the 06406 well location, red is at inline 1054, crossline 62.

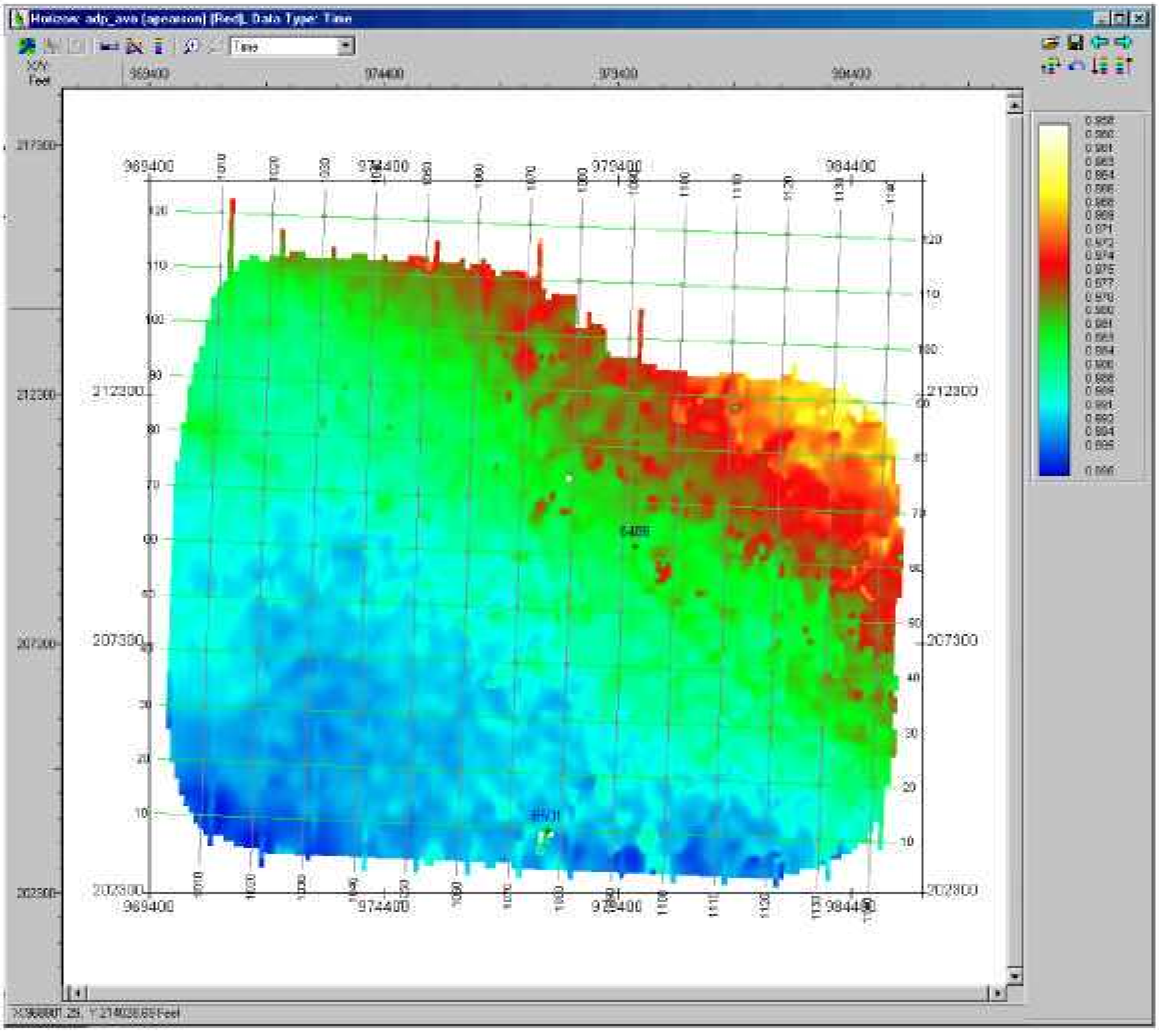

Figure 4-48. Time structure of a horizon picked at the trough at the top of the shale/carbonate interface near the bottom of the wells.

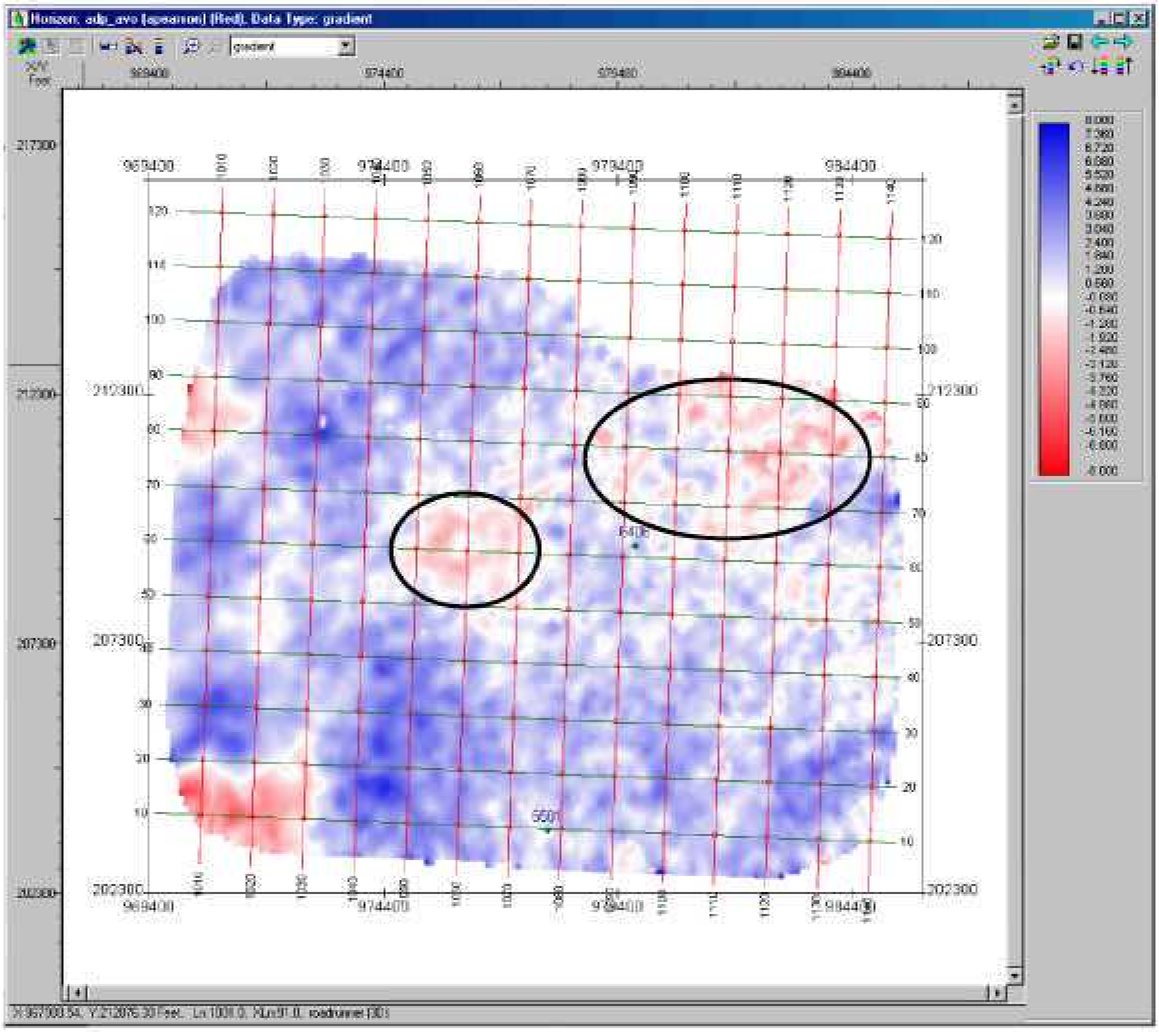

Figure 4-49. Amplitude extraction of gradient volume on the intercept-picked horizon (Figure 4-26). "Class III" anomalies (those with negative intercept and negative gradient) are circled.

4.3.1.2 AWAVO™

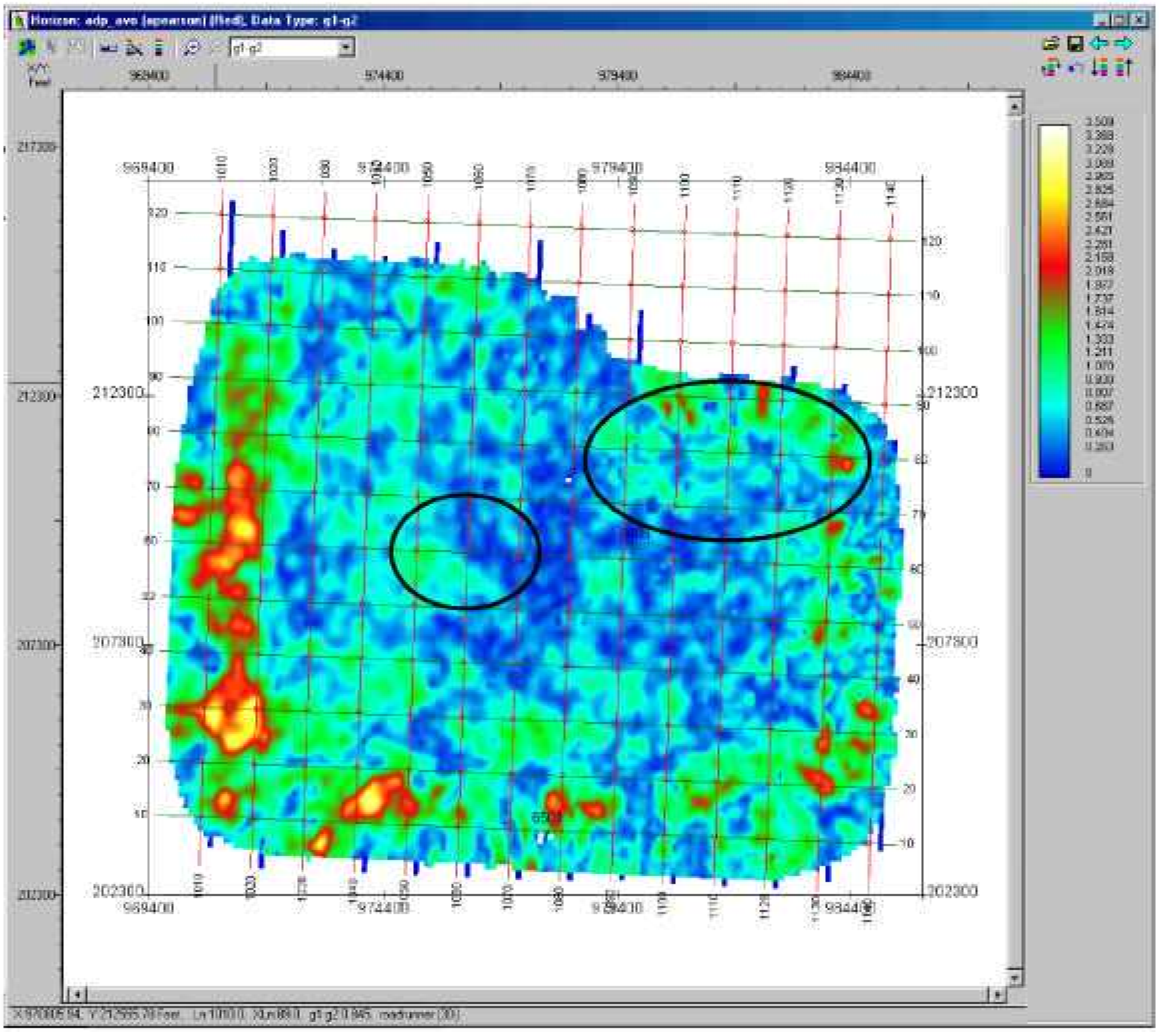

Figure 4-50. Example of amplitude extraction of the g1-g2 volume (highest azimuthal AVO gradient – lowest azimuthal AVO gradient) on the intercept-picked horizon. Circles are from the isotropic gradient extraction (Figure 4-49).

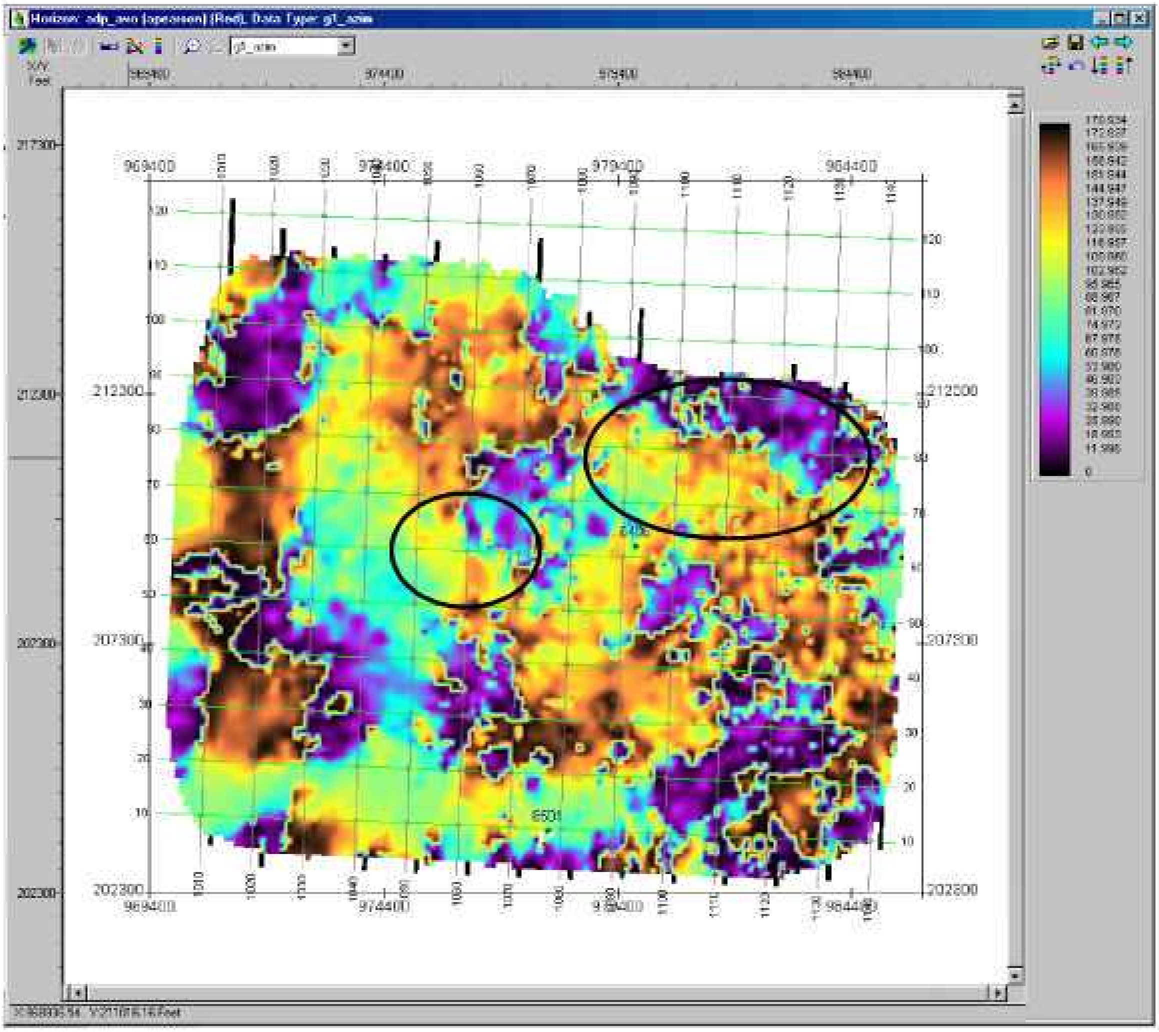

Figure 4-51. Example of amplitude extraction of the g1 azimuth volume (azimuth with the highest azimuthal AVO gradient) on the intercept-picked horizon. Circle are from the isotropic gradient extraction (Figure 4-49).

4.3.1.3 AZIM™

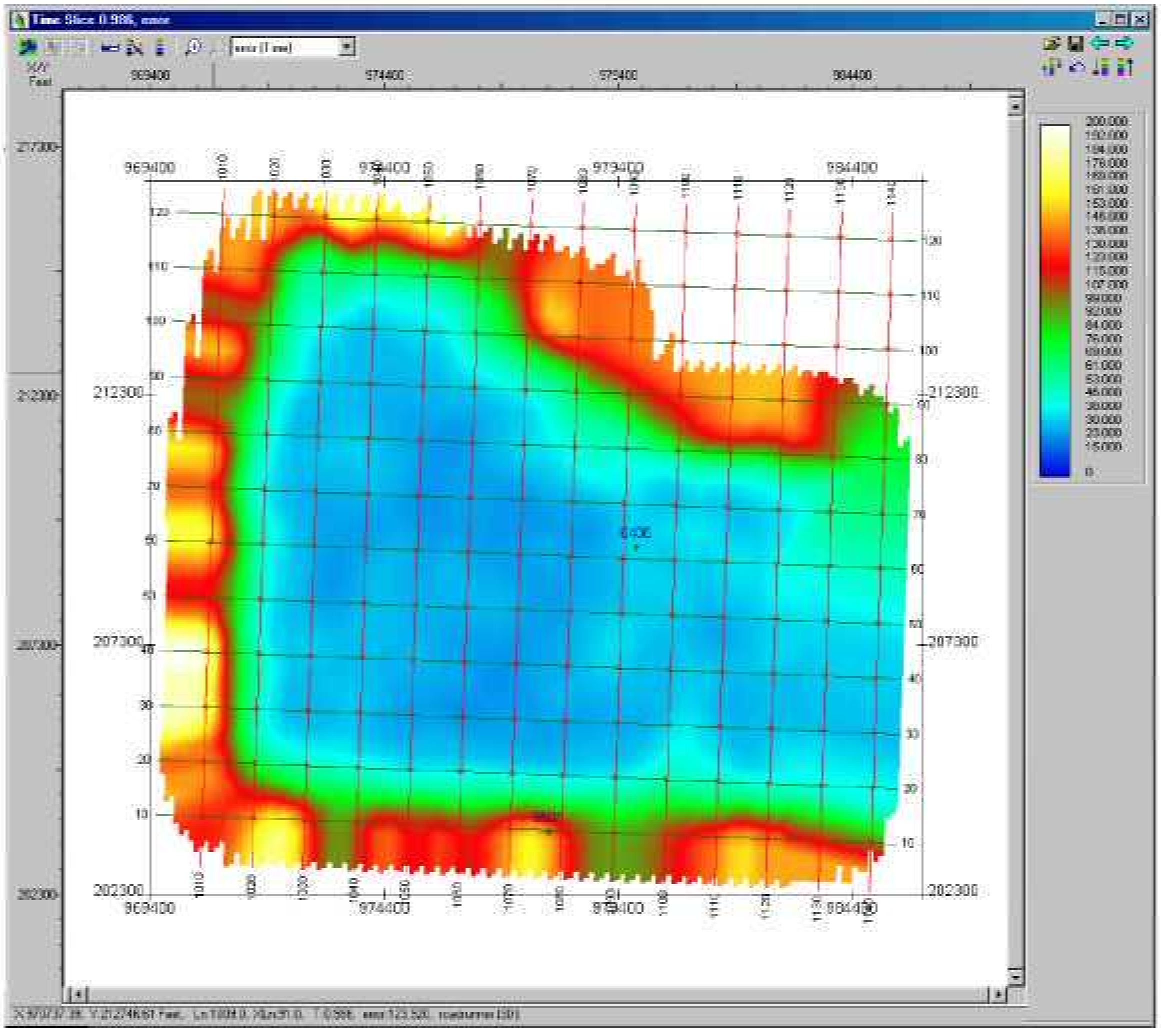

Figure 4-52. Example of an RMS velocity error volume. Time slice is through 986 ms.

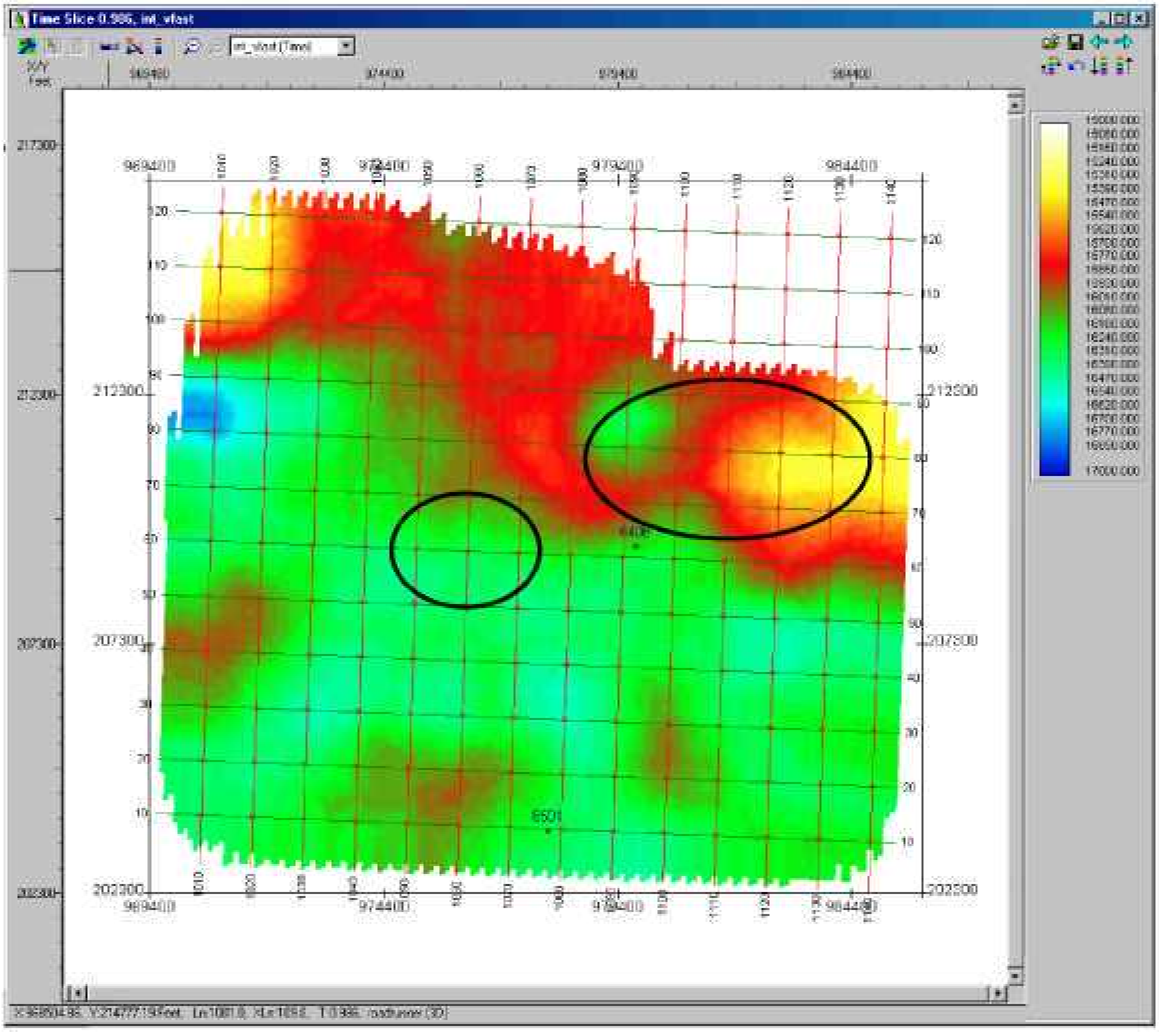

Figure 4-53. Time slice through the interval V_{fast} volume. Slice is at 986 ms. Circles are from the isotropic gradient extraction (Figure 4-49).

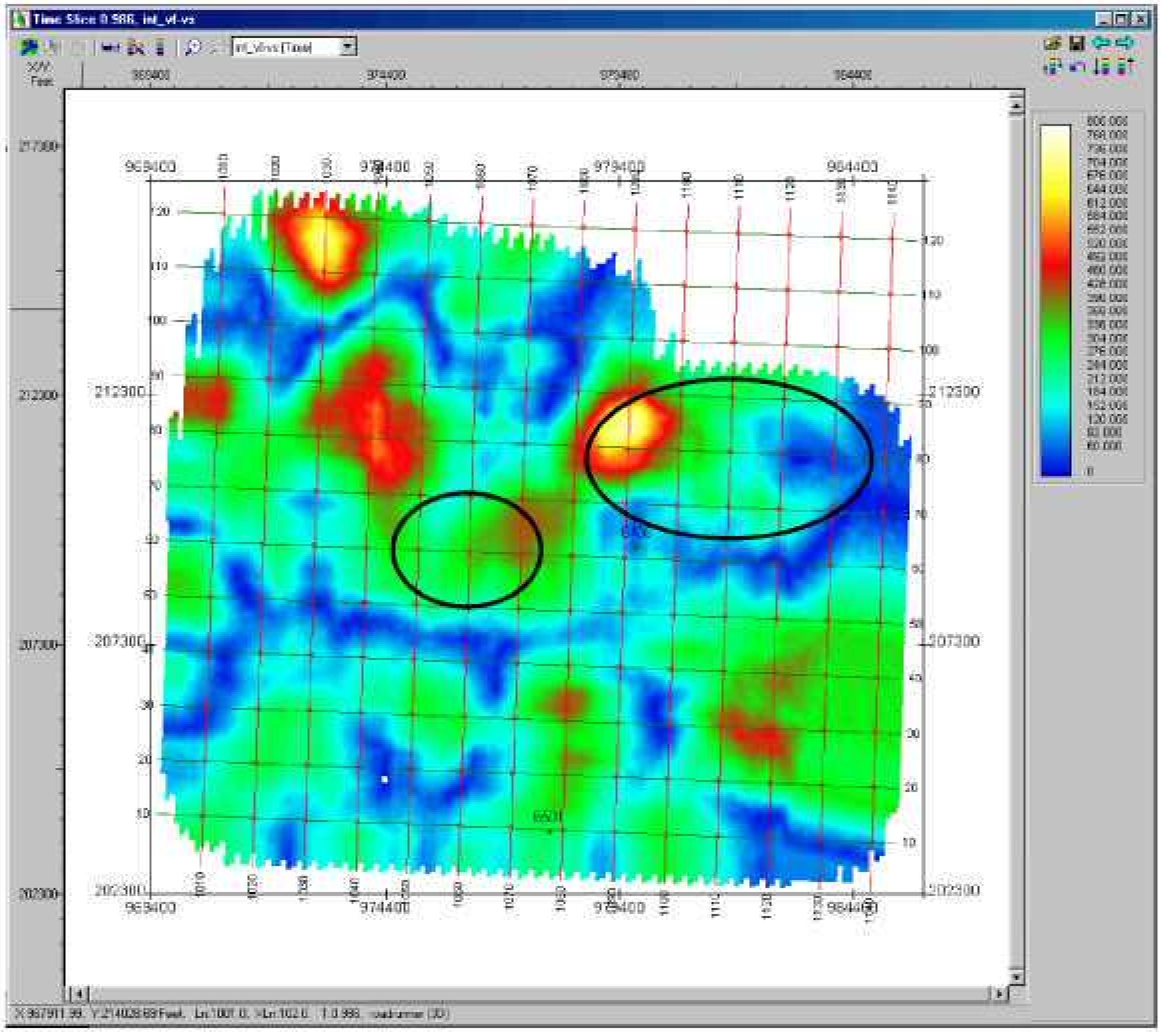

Figure 4-54. Time slice through the interval V_{fast} - V_{slow} volume. Slice is at 986 ms. Circles are from the isotropic gradient extraction (Figure 4-49).

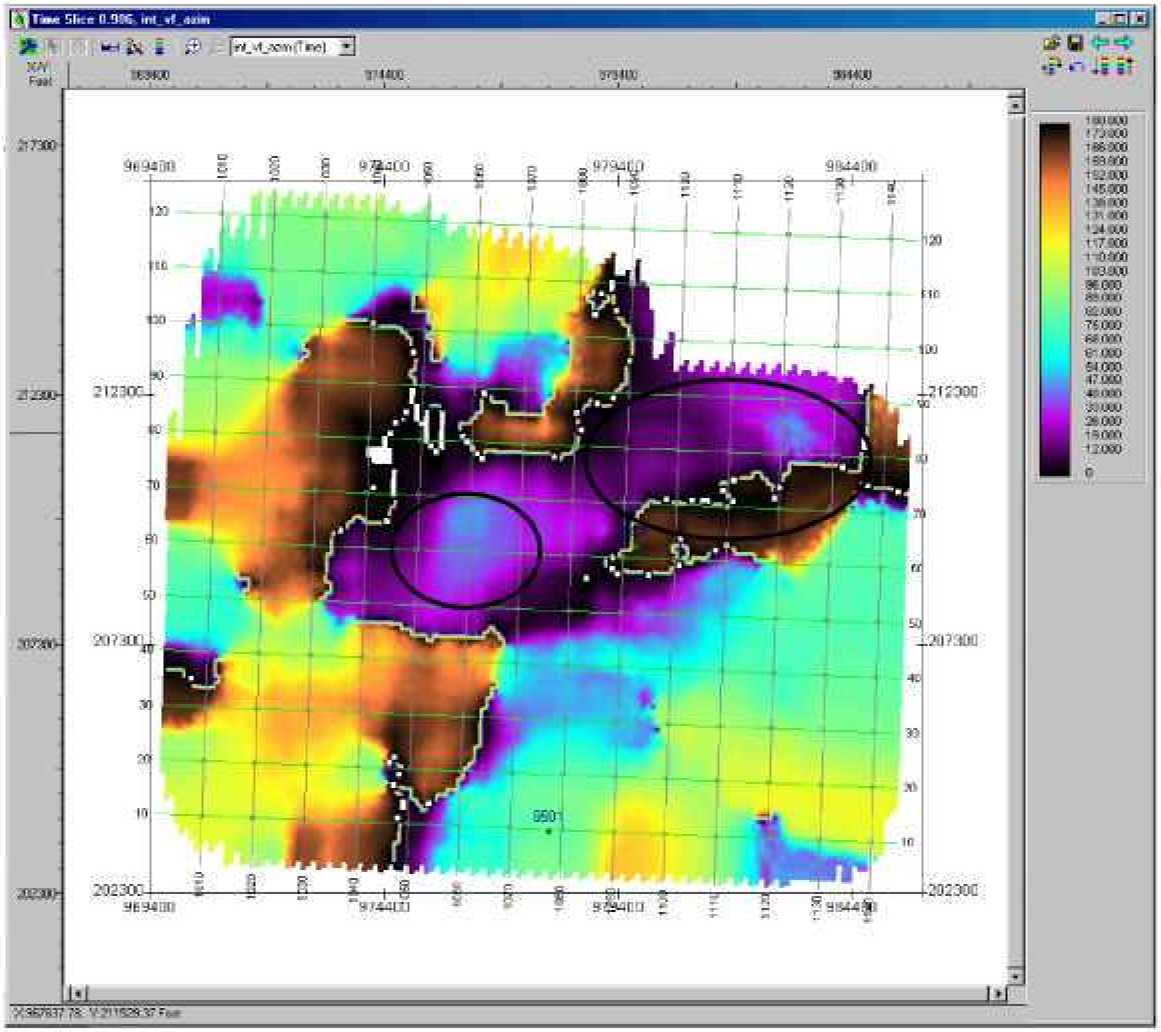

Figure 4-55. Time slice through the interval V_{fast} azimuth volume. Slice is at 986 ms. Circles are from the isotropic gradient extraction (Figure 4-49).

4.3.2 REFRACTION STATICS SOLUTION

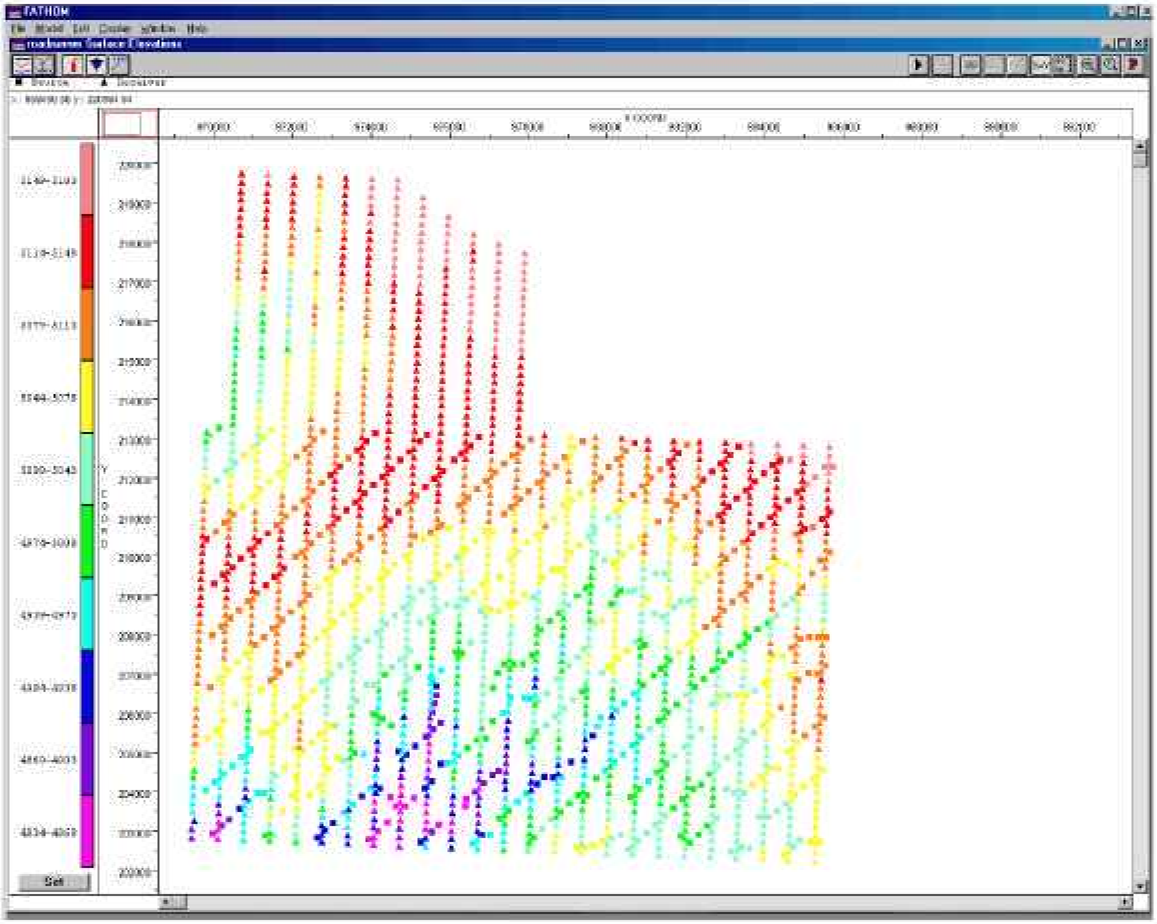

Figure 4-56. Surface elevations

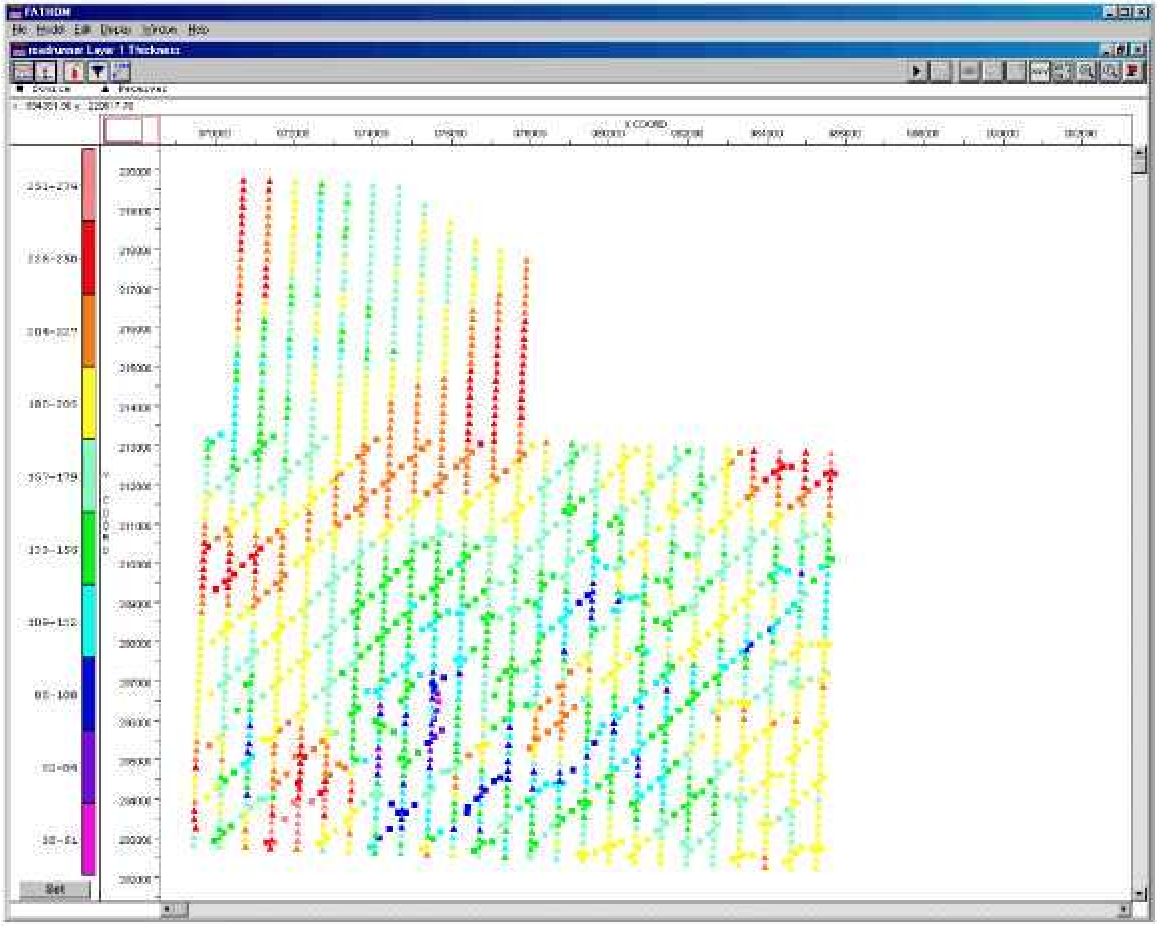

Figure 4-57. Weathering thickness.

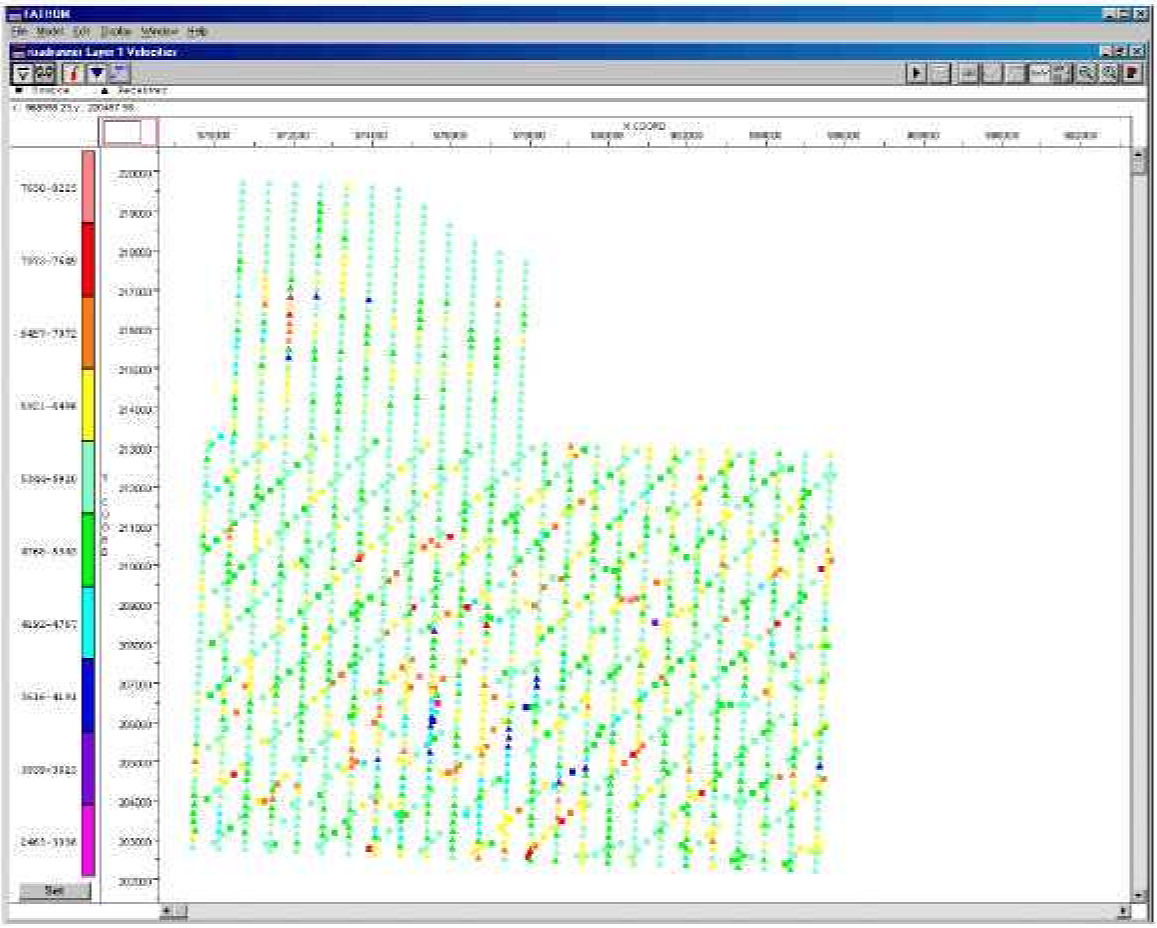

Figure 4-58. Weathering velocities.

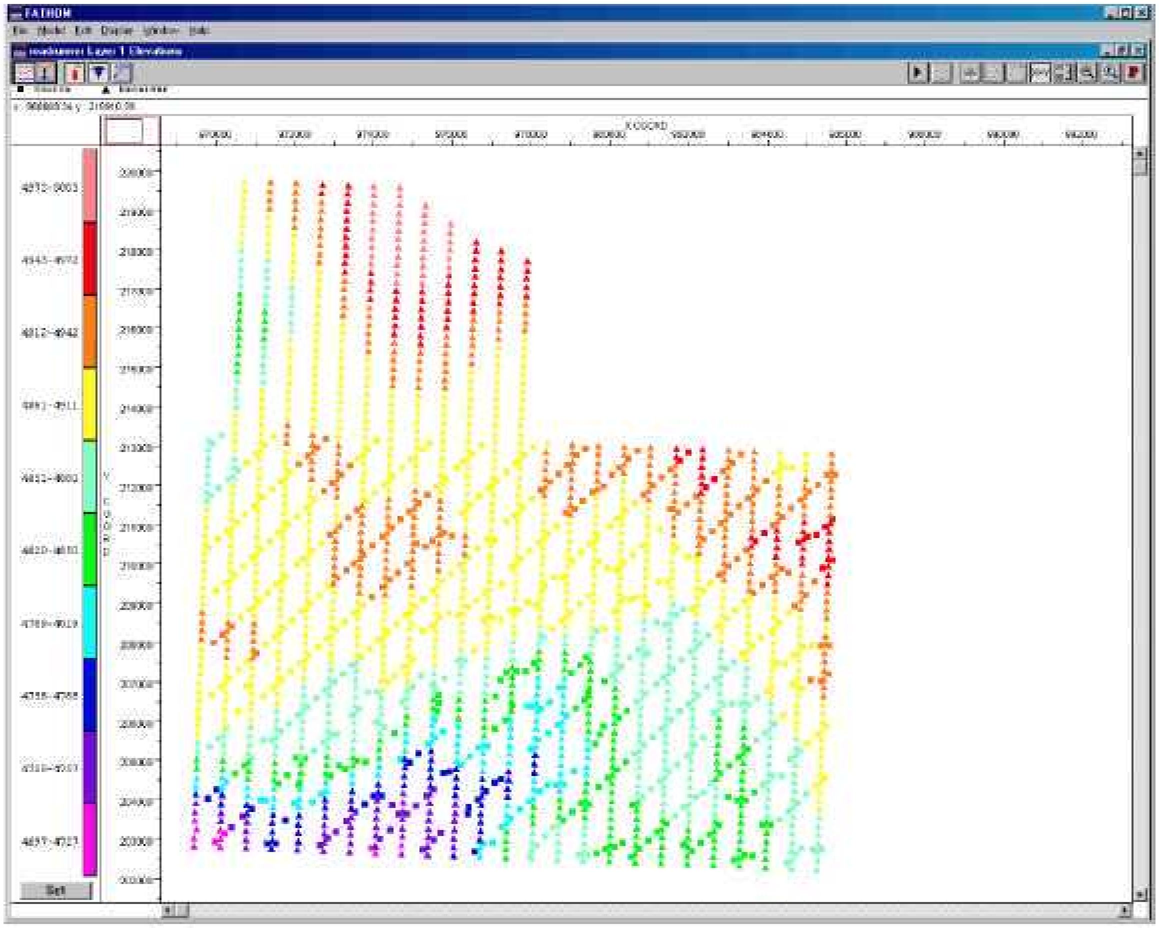

Figure 4-59. Elevations of top of refractor.

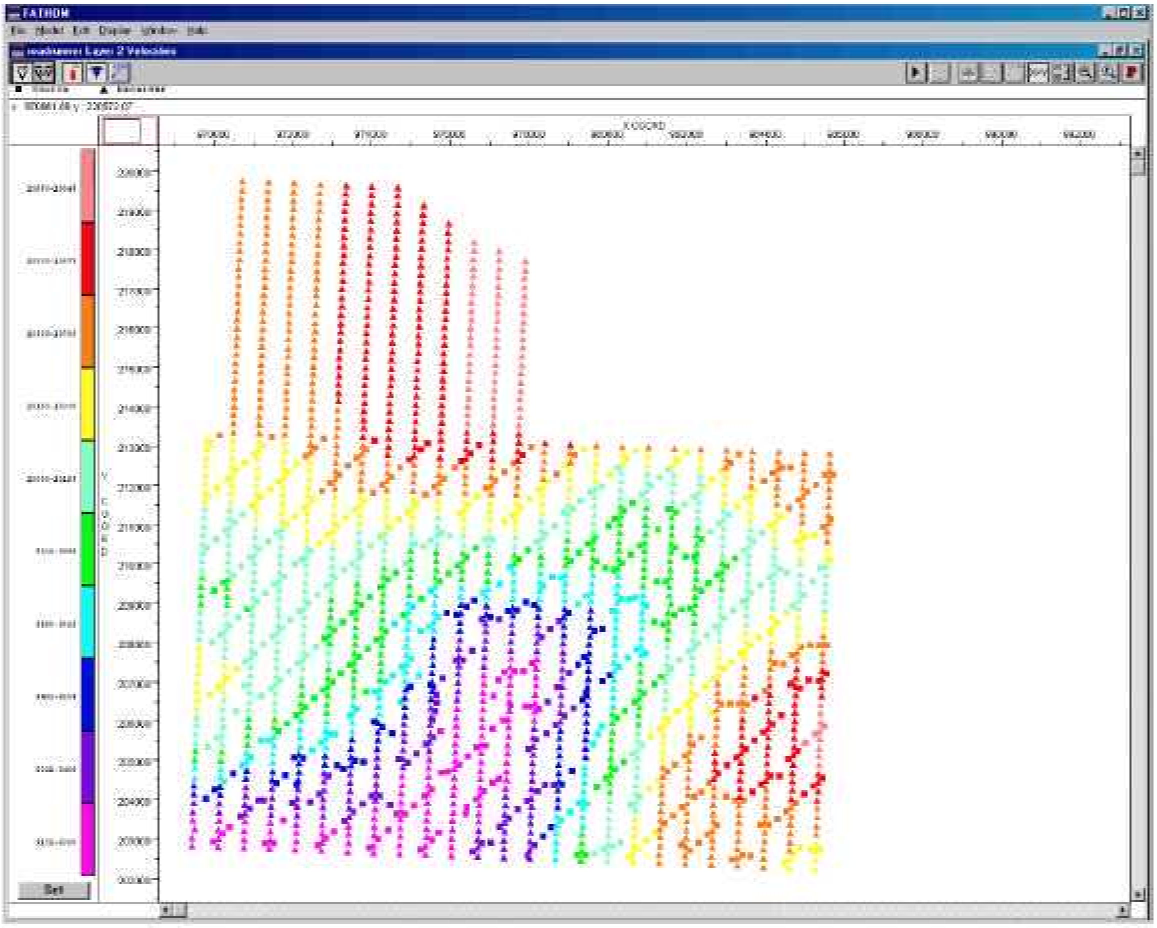

Figure 4-60. Refractor velocities.

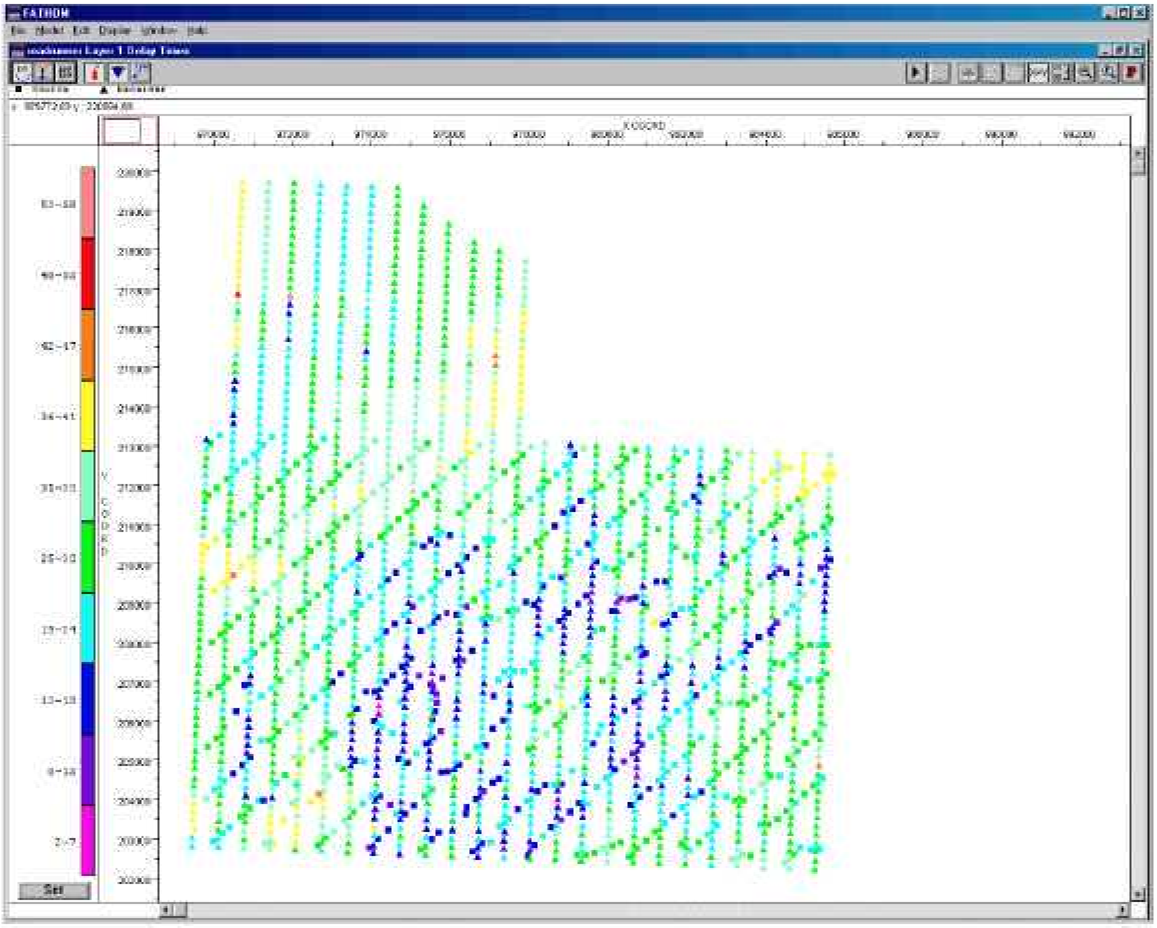

Figure 4-61. Delay times.

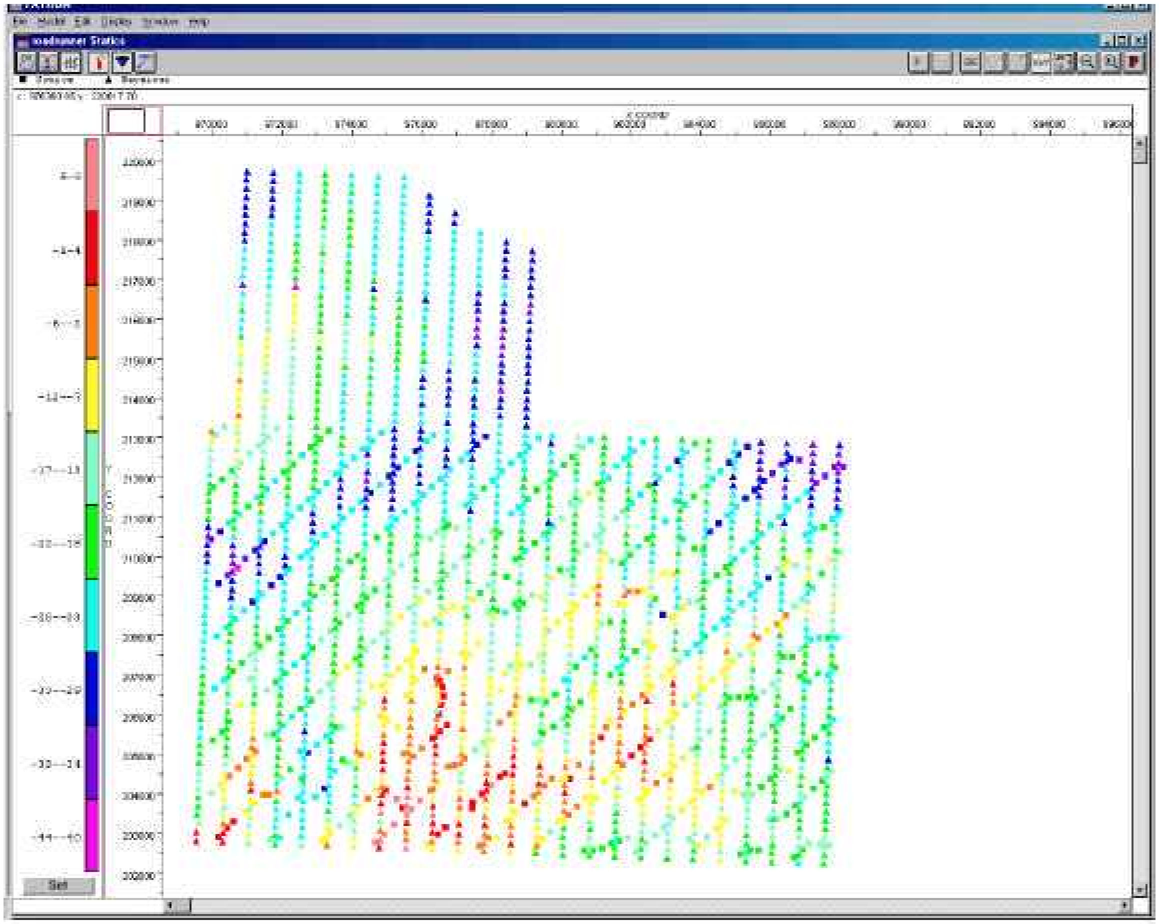

Figure 4-62. Refraction statics (including elevation statics).

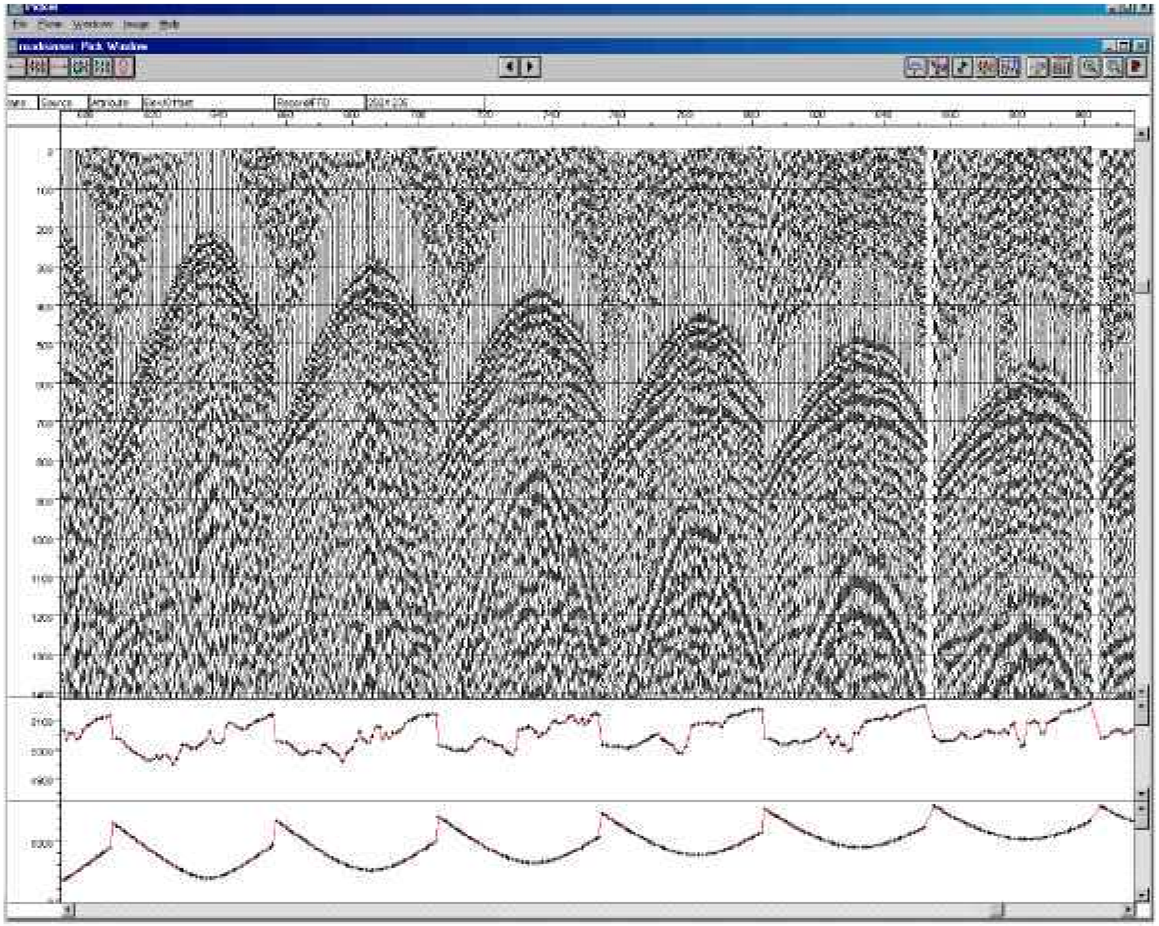

Figure 4-63. Elevation statics applied.

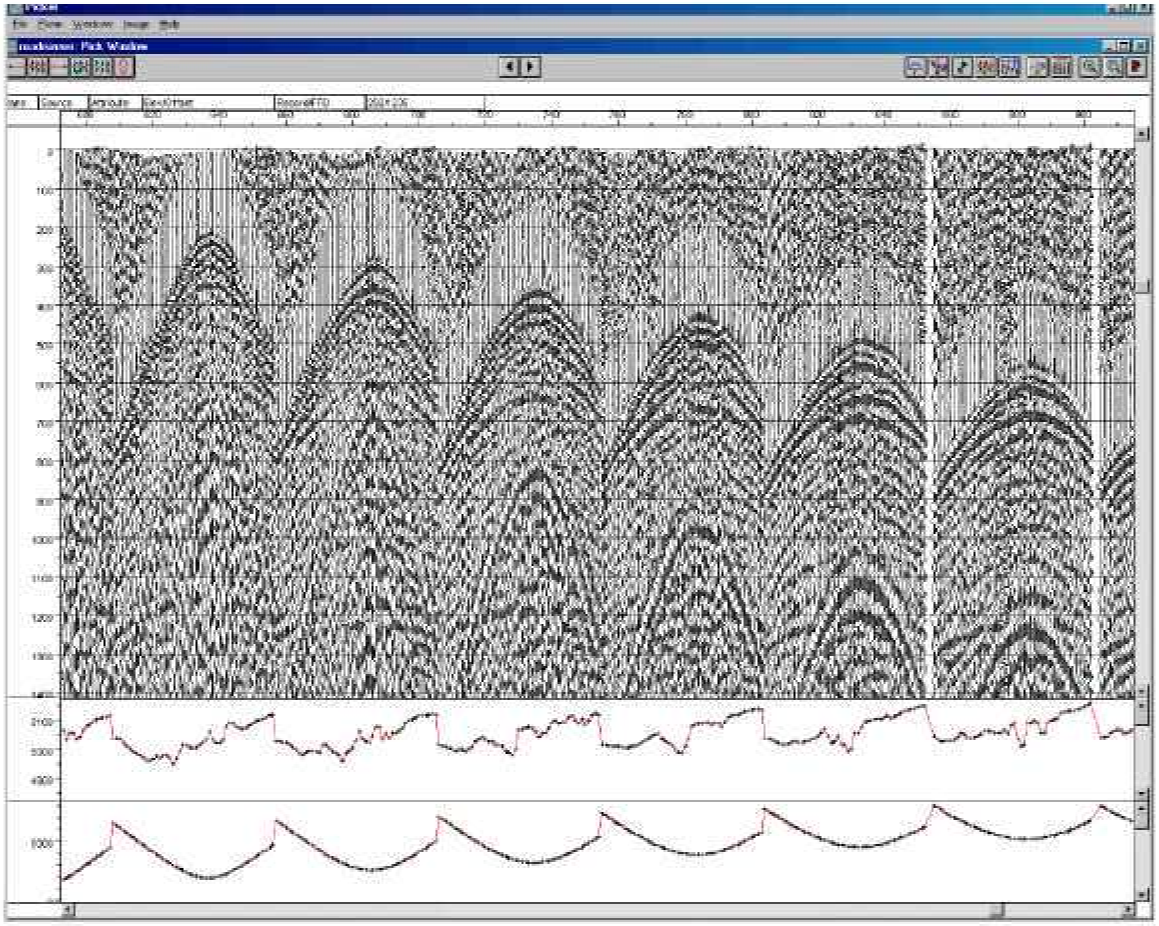

Figure 4-64. Refraction statics applied.

4.4 Comparison of AXIS and WesternGeco Processing Results

P-wave volumes were produced as a first step in both the WesternGeco and Axis processing. The algorithms used differed somewhat, and so the picks for the horizons and the resulting isochrons also differed. Moreover, WesternGeco produced two P-wave volumes. The differences that the processing makes are shown in Figure 4-65 through Figure 4-70.

There were two processing strategies used in the WesternGeco data. The first, called WesternGeco 1, has random noise attenuation applied, giving the "smoother" look to the results (Figure 4-69). The second, termed WesternGeco 2, did not have the random noise attenuation applied, but rather a spectral whitening was applied (Figure 4-70). In Figure 4-68 through Figure 4-70, the red color represents 25 ms, while the dark blue represents 20 ms. Note that the WesternGeco Version 1 processing leads to a less spatially varying result for this example. The WesternGeco Version 2 is probably the most "chaotic", with variations on a much smaller spatial scale. The Axis processing produces an intermediary result.

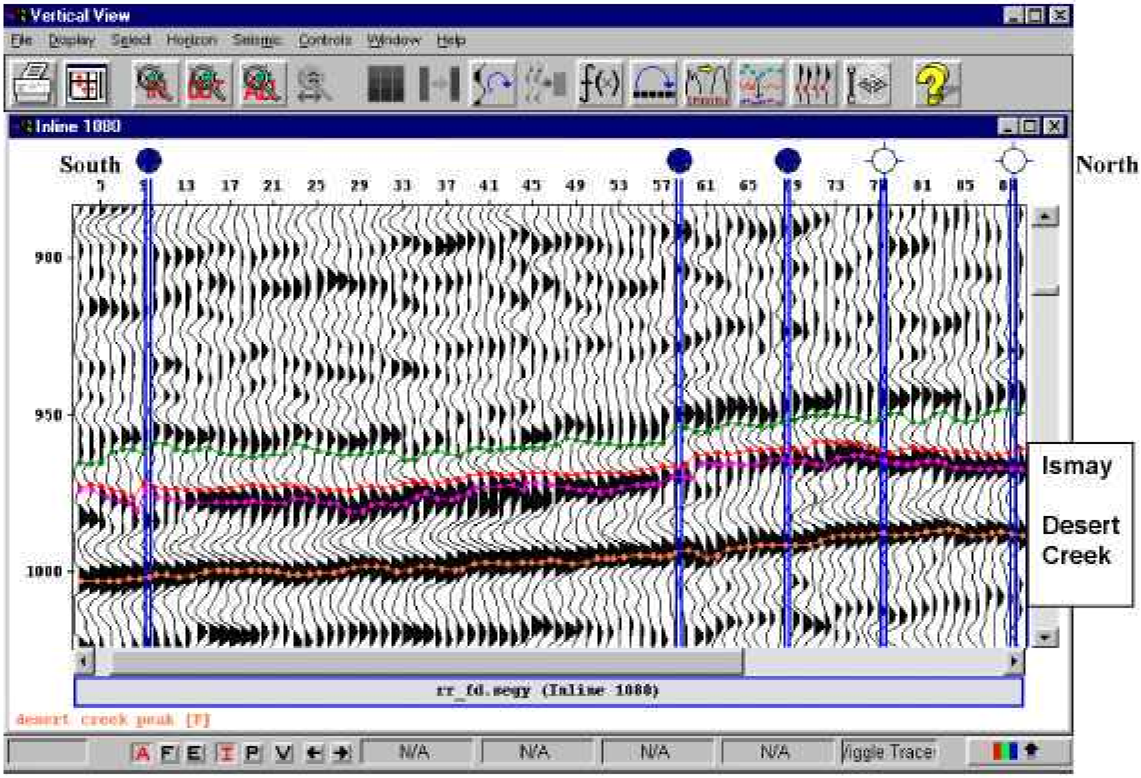

Figure 4-65. GMGAxis P-wave data, Inline 1080.

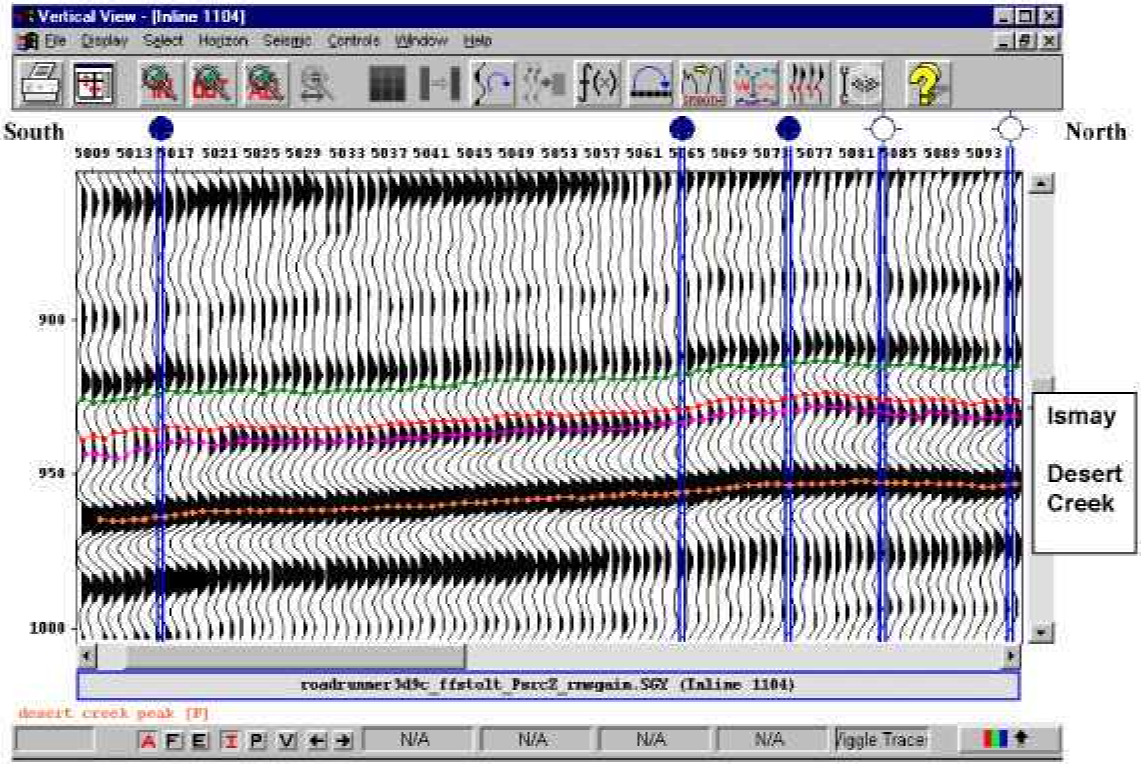

Figure 4-66. WesternGeco Version 1 P-wave data, Inline 1104.

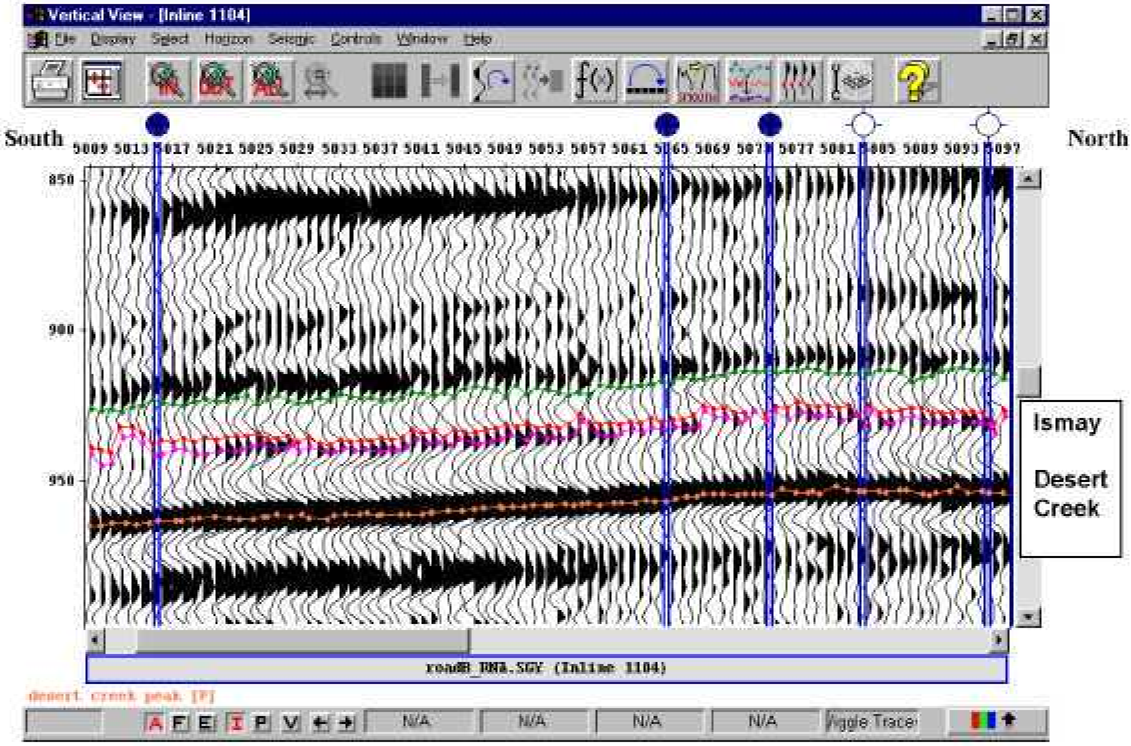

Figure 4-67. WesternGeco Version 2 P-wave data , Inline 1104.

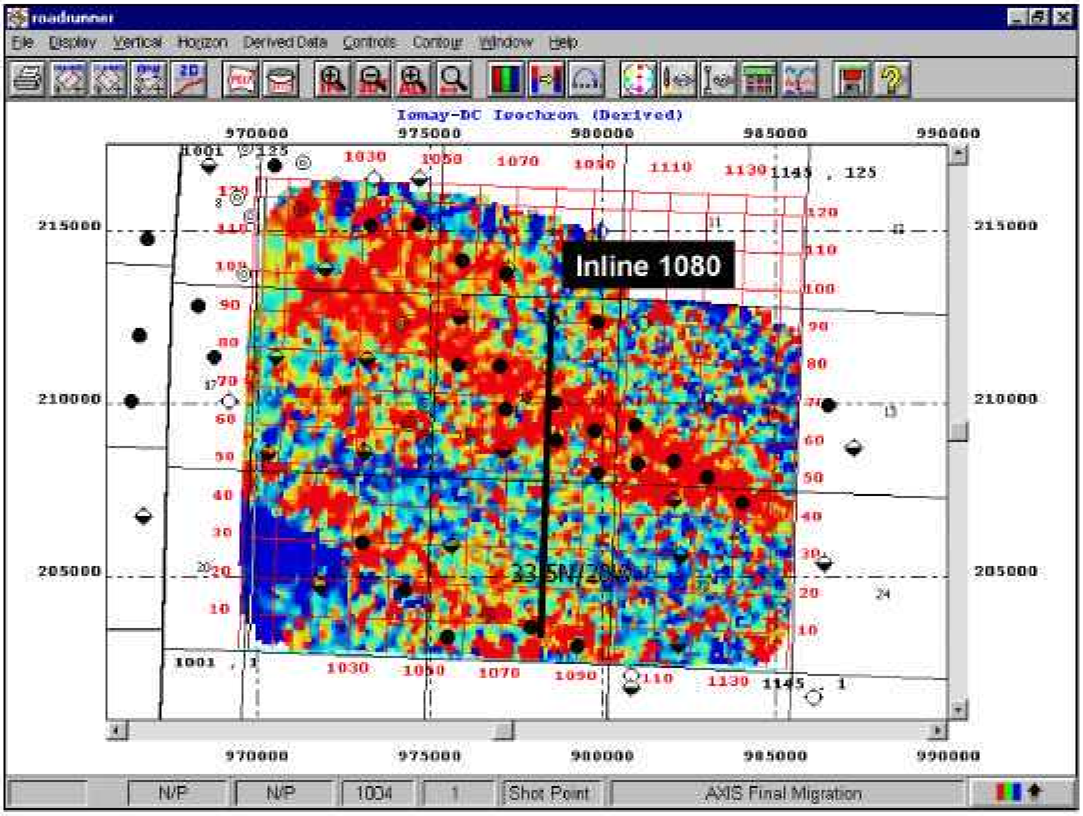

Figure 4-68. Ismay – Desert Creek Isochron (GMGAxis processing).

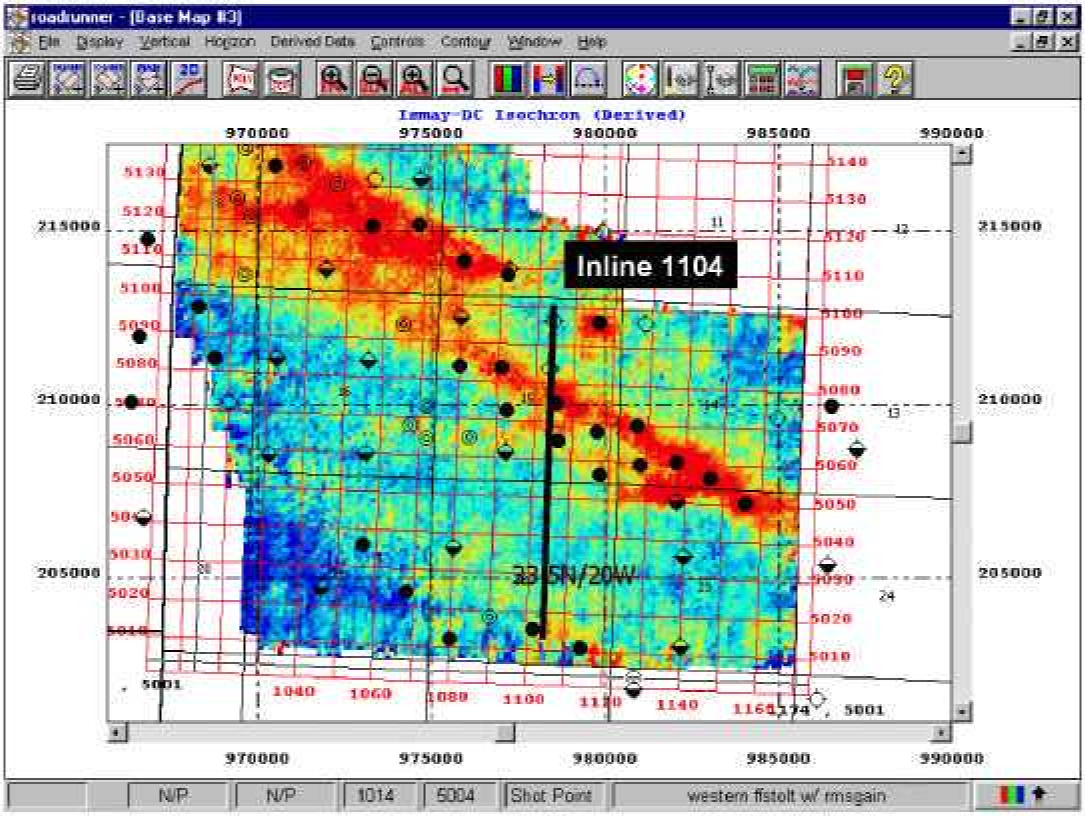

Figure 4-69. Ismay – Desert Creek Isochron (WesternGeco Version 1 processing).

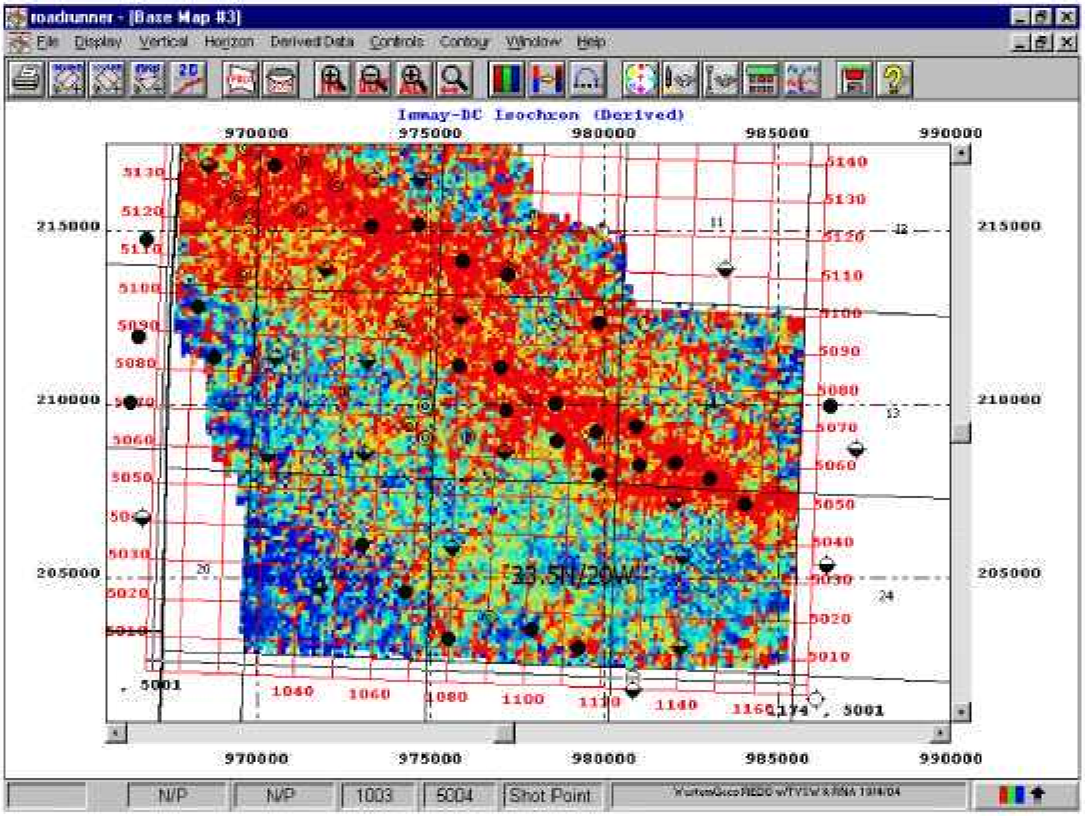

Figure 4-70. Ismay – Desert Creek Isochron (WesternGeco Version 2 processing).

4.5 Time-Structure, Isochron, Anomaly and Waveform Class Maps

The following figures show the results for the isochron, time-structure and attribute maps derived directly from the multicomponent seismic data.

Figure 4-71 shows the correlations that have been established for some of the major reservoir unit boundaries, including the top of the Upper Ismay, the Hovenweep Shale and the Desert Creek Formation. These three horizons represent major peaks or troughs in the P-wave seismic data. Figure 4-72 shows an enlarged version of the sonic and gamma ray log picks for these reservoir boundaries, and their corresponding seismic picks.

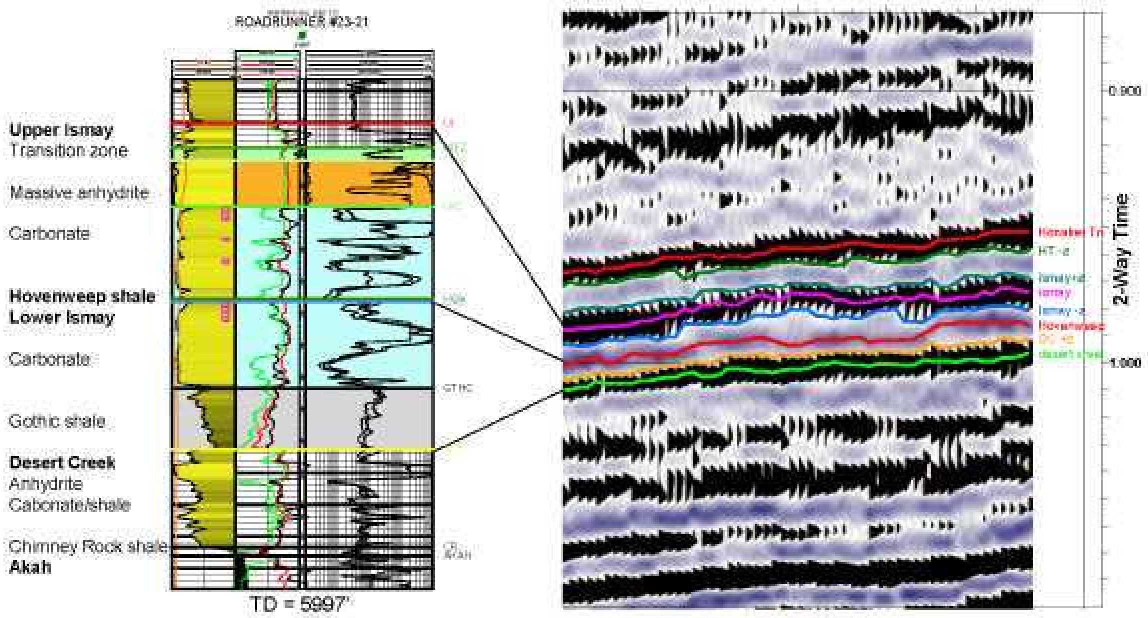

Figure 4-71. Correlation of lithostratigraphic boundaries with processed P-wave data.

The method used to construct the key horizons from seismic was to calibrate the picks to the well logs, as in the example above, and then to extend the picks away from well control in the seismic volumes to map out the horizon throughout the region of interest.

The next step was to create isochron maps that were related to isopachs of various units. The isochron maps were created by subtracting the time horizon maps. Isopachs between the units shown in Figure 4-71 were calculated at wells where the requisite logging suite is available. In all, it was possible to calculate at least some of the horizon tops and isopachs for the forty-six wells listed in Table 4-2.

API Number	Well Label	API Number	Well Label	API Number	Well Label
0508306332	SENTINEL PEAK #8-32	0508305104	CALCO-SUPERIOR-UTE #2	0508306331	SENTINEL PEAK #17-42
0508305137	UTE TRIBAL-GOVT #7	0508306420	UTE TRIBAL #6-15	0508306441	SENTINEL PEAK #17-2
0508306002	UTE-B #1	0508306421	UTE TRIBAL #11-15	0508305371	UTE MTN #1-17
0508305377	UTE A-GOVT #1	0508306424	UTE TRIBAL #5-15	0508306092	UTE MOUNTAIN TRIBAL #2
0508305111	CAL OIL-SUPERIOR #10	0508306406	UTE MTN UTE TRIBAL #15-43	0508305094	UTE MTN TRIBAL #1
0508306007	UTE-B #2	0508306410	ROADRUNNER #15-33	0508306091	UTE MTN TRIBAL #3
0508305138	UTE TRIBAL-GOVT #8	0508306445	ROAD RUNNER #15-34	0508306501	UTE #15-22
0508306005	UTE TRIBAL #9	0508306471	ROADRUNNER #15-44	0508306490	UTE #16-22
0508306008	UTE-AB #1	0508307002	UTE TRIBAL GOVT #9/11-1	0508306357	TOWAOC #1-22
0508306517	MARBLE UTE-AB #1	0508306015	UTE AB #2	0508306093	CALCO-SUPERIOR UTE #3
0508306399	UTE MOUNTAIN #14-13	0508306428	ROAD RUNNNER #15-32	0508306481	ROADRUNNER #23-21
0508306405	UTE MTN UTE TRIBAL #14-24	0508306440	UTE MTN TRIBAL #14-15	0508306419	ROADRUNNER UTE MTN #23-31
0508306467	ROADRUNNER #14-14	0508305102	UTE TRIBAL #1	0508305095	UTE-2 #1
0508306469	ROADRUNNER #14-34	0508306020	UTE D #1	0508307001	MCLISH-UTE TRIBAL #1-23
0508306026	UTE #76-1	0508305098	CALCO-SUPERIOR-UTE #4		
0508305427	UTE #1-14	0508306508	UTE #13-16		

Table 4-2. List of wells used for calibration and cross-correlation between lithostratigraphic picks in wells and seismic picks in the P-wave data.

P-wave volumes were produced as a first step in both the WesternGeco and GMGAxis processing. The algorithms used differ somewhat, and so the picks for the horizons and the resulting isochrons also differed. Moreover, WesternGeco produced two P-wave volumes. The differences that the processing makes are shown in Figure 4-65 through Figure 4-70.

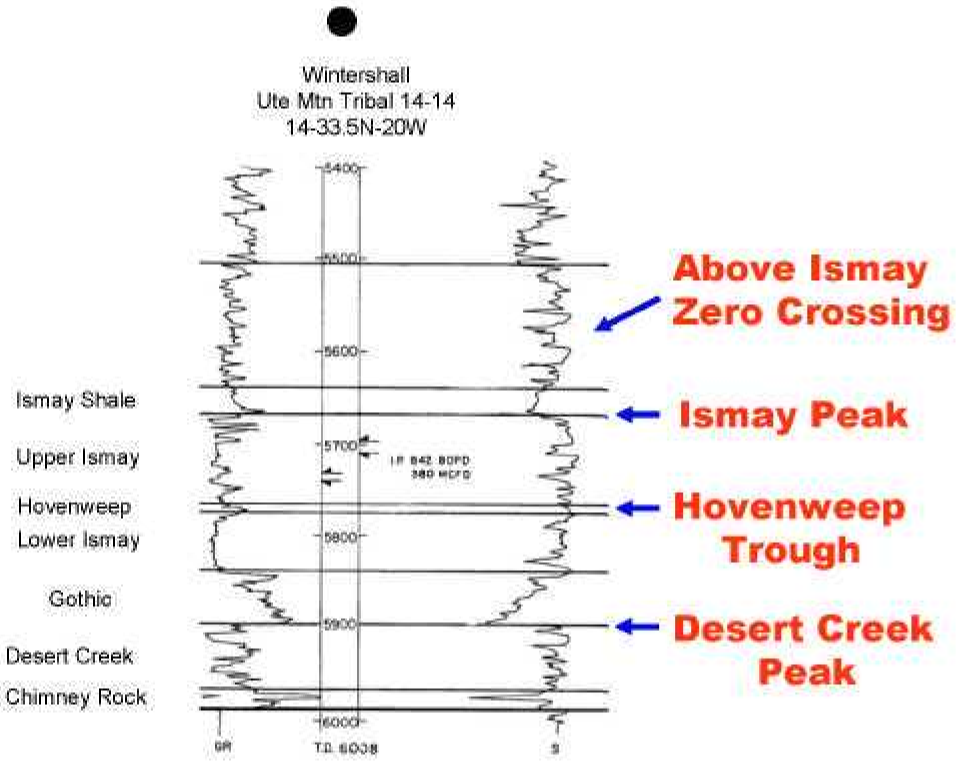

Figure 4-72. Detail of log expressions for the lithostratigraphic boundaries and their corresponding seismic picks.

P-wave seismic horizons interpreted include the Cutler (CUTL), Upper Ismay (UI), Upper Ismay seismic peak (UIC), Hovenweep Shale (LI), Gothic Shale (GTHC), Desert Creek (UDC), and the AKAH Salt (AKAH) (Figure 4-73 to Figure 4-79, respectively). Time structure maps show a gentle monoclinal dip from the northeast to the southwest across the survey area. Time structure maps of the Upper Ismay (Figure 4-74), Upper Ismay seismic peak (Figure 4-75), and the Hovenweep Shale (Figure 4-76) show a significant nose and a slight structural closure over the Roadrunner Field and only a nose across the Towaoc Field.

Many of the same time horizons could be picked on the PS- and S-wave data. PS-wave seismic horizons interpreted include the Upper Ismay (UI), Upper Ismay seismic peak (UIC), and the AKAH Salt (AKAH) (Figure 4-80 through Figure 4-82, respectively). S-wave seismic horizons interpreted include approximate Upper Ismay (aUI), the Upper Ismay Carbonate (UIC), and the AKAH Salt (AKAH) (Figure 4-83 through Figure 4-86, respectively)

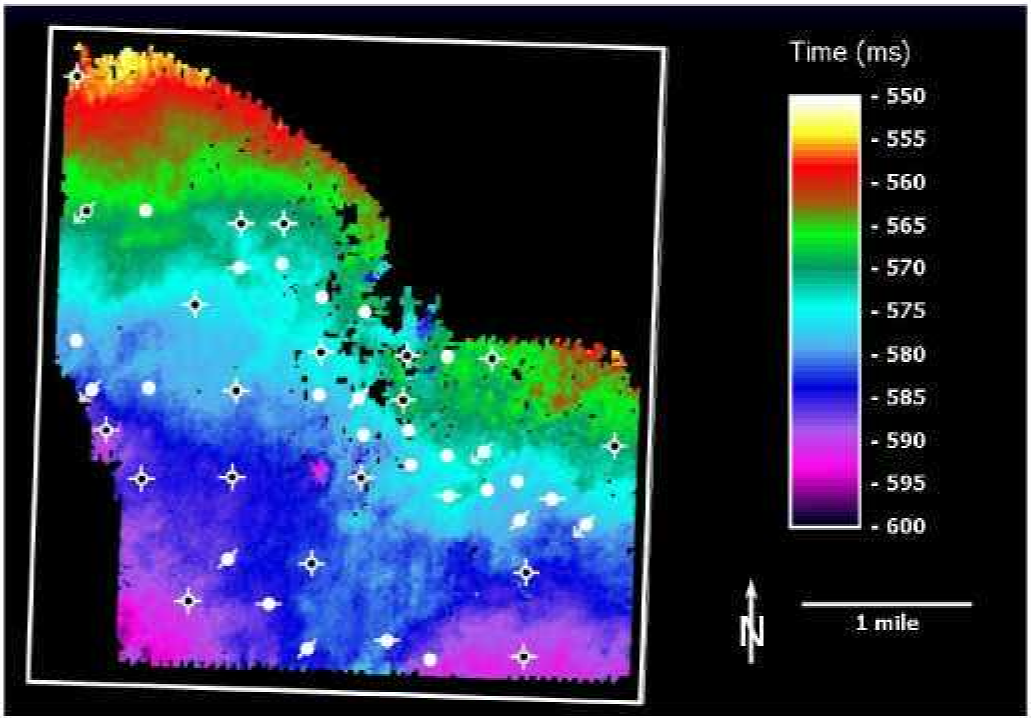

Figure 4-73. Cutler (CUTL) time structure map (P-wave).

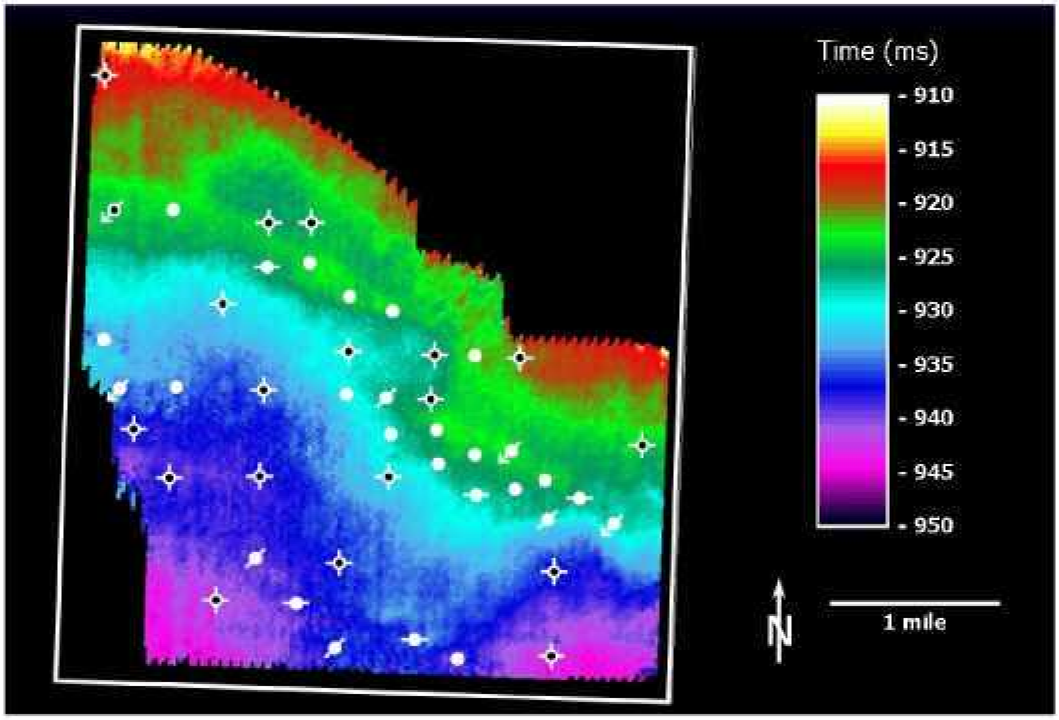

Figure 4-74. Upper Ismay (UI) time structure map (P-wave).

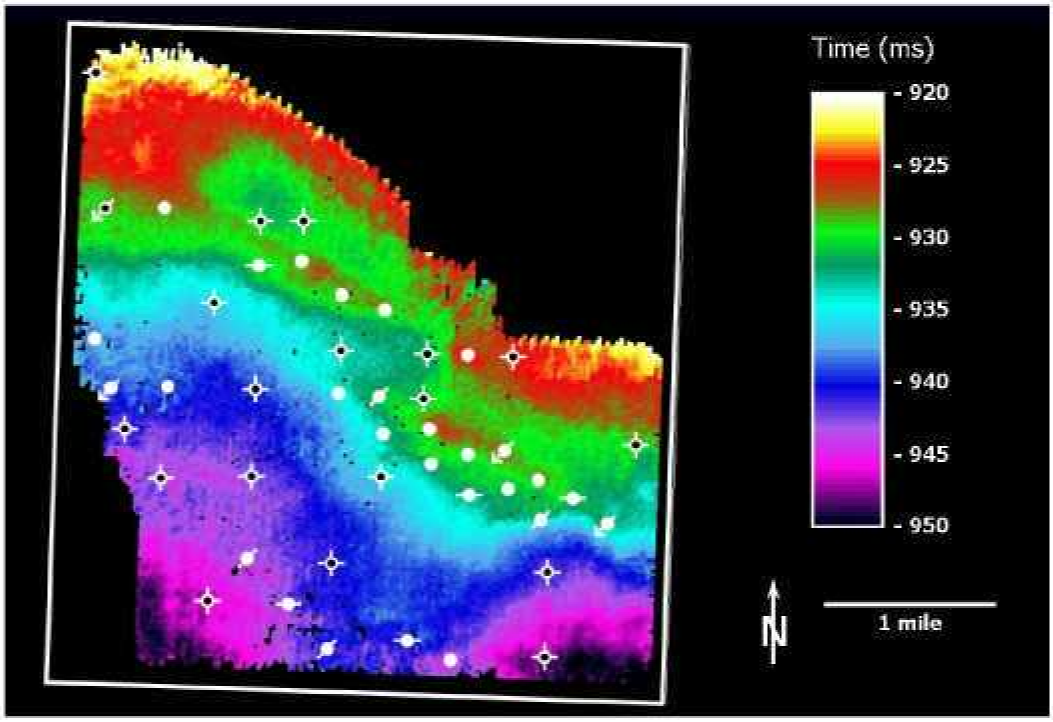

Figure 4-75. Upper Ismay seismic peak (UIC) time structure map (P-wave). Note the strong structural nosing from the northeast to the southwest across Roadrunner and Towaoc fields, and the structural closure associated with Roadrunner field.

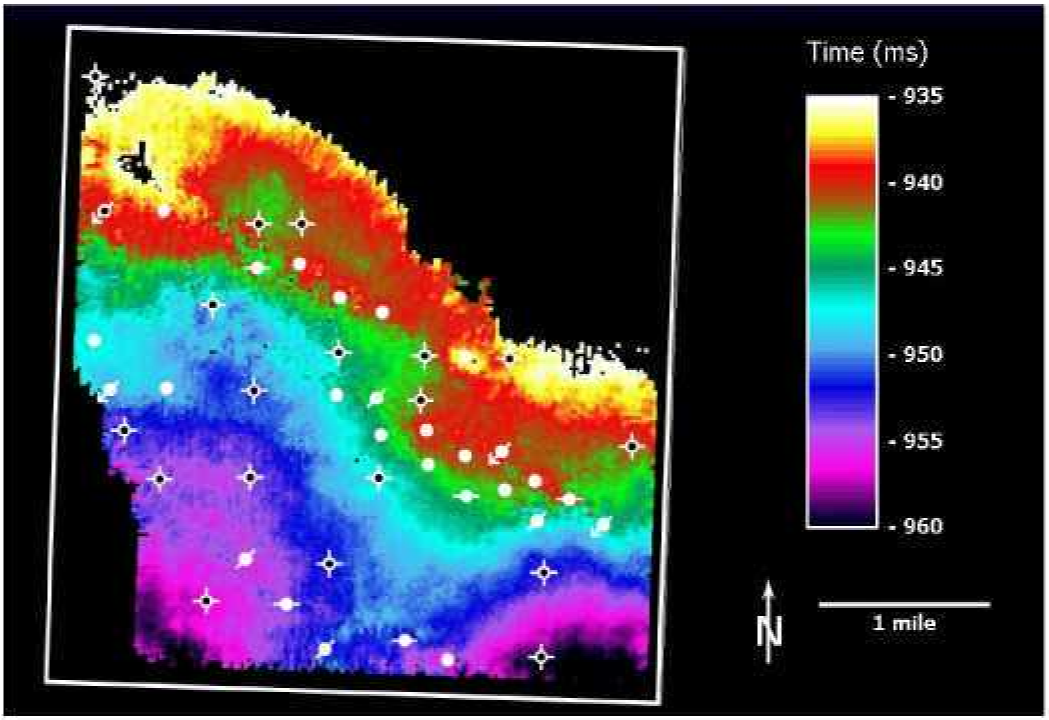

Figure 4-76. Hovenweep (LI) time structure map (P-wave). Note the strong structural nosing from the northeast to the southwest across Roadrunner and Towaoc fields.

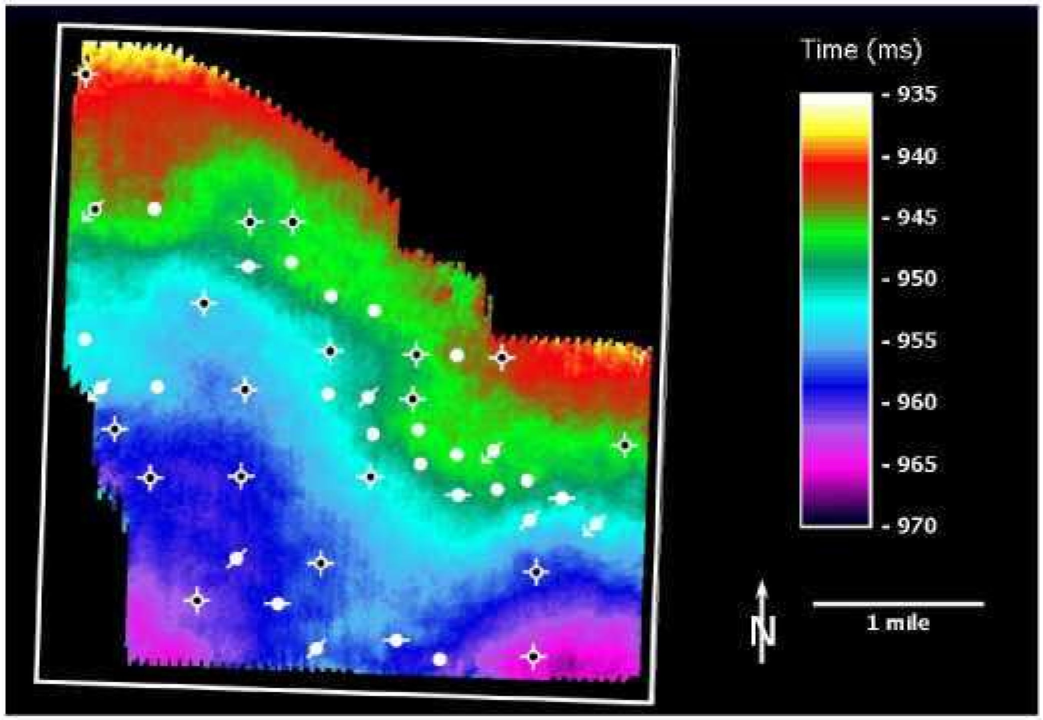

Figure 4-77 Gothic shale (GTHC) time structure map (P-wave).

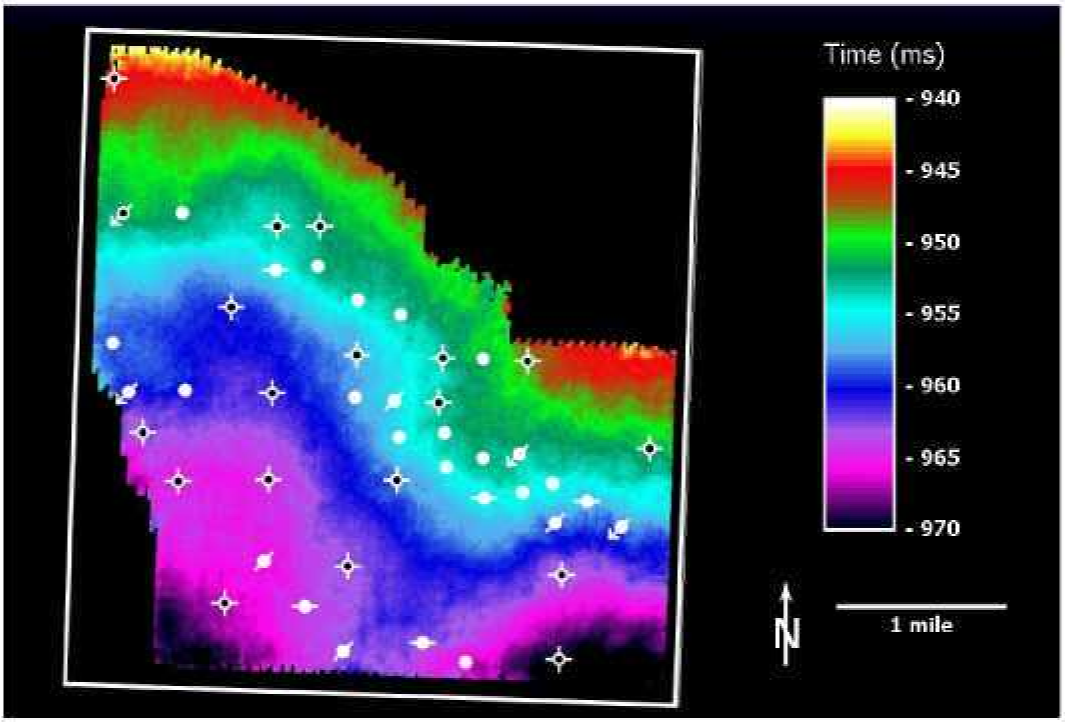

Figure 4-78 Desert Creek (UDC) time structure map (P-wave).

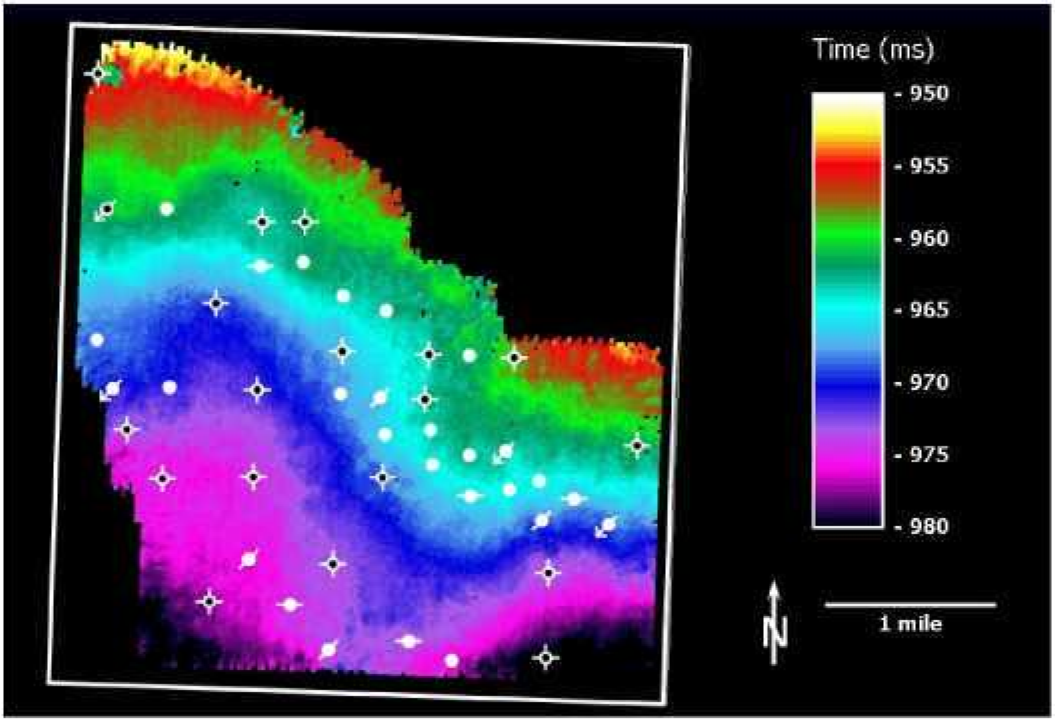

Figure 4-79 AKAH salt (AKAH) time structure map (P-wave).

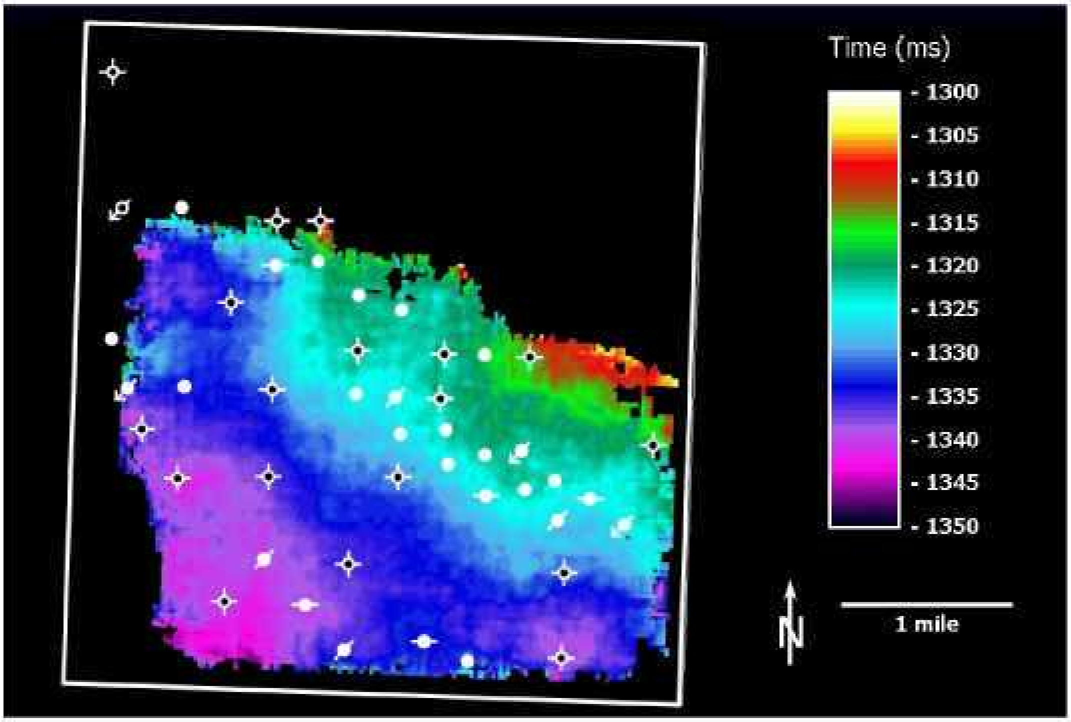

Figure 4-80. Upper Ismay (UI) Time Structure Map (PS-wave).

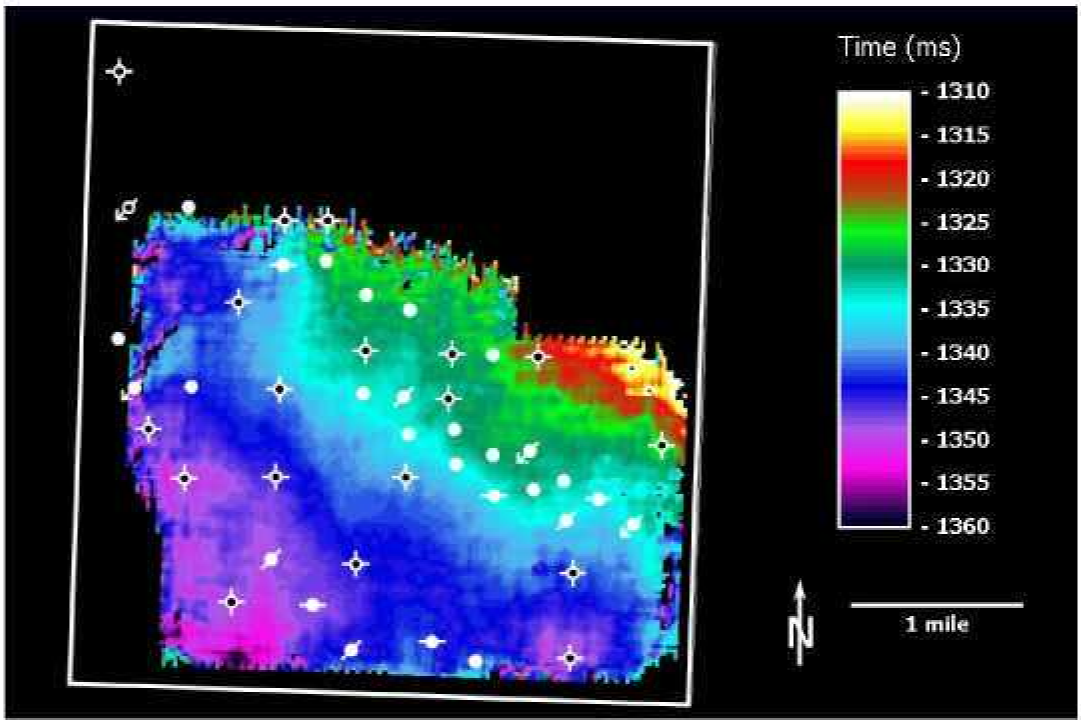

Figure 4-81 Upper Ismay seismic peak (UIC) Time Structure Map (PS-wave).

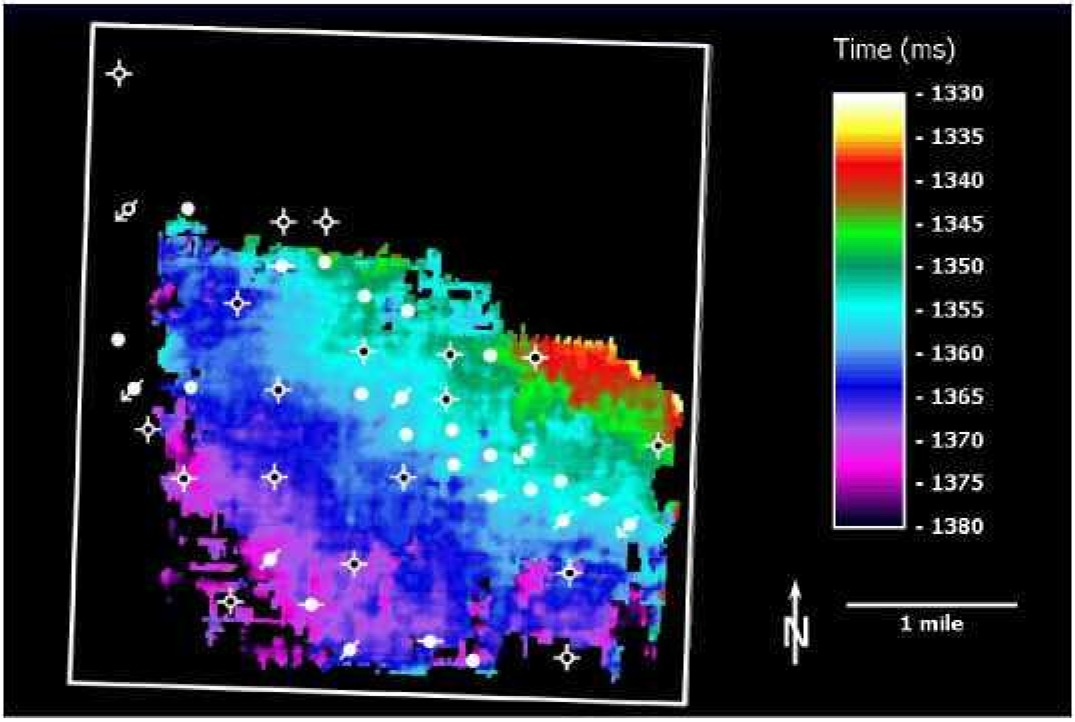

Figure 4-82 Gothic shale (GTHC) Time Structure Map (PS-wave).

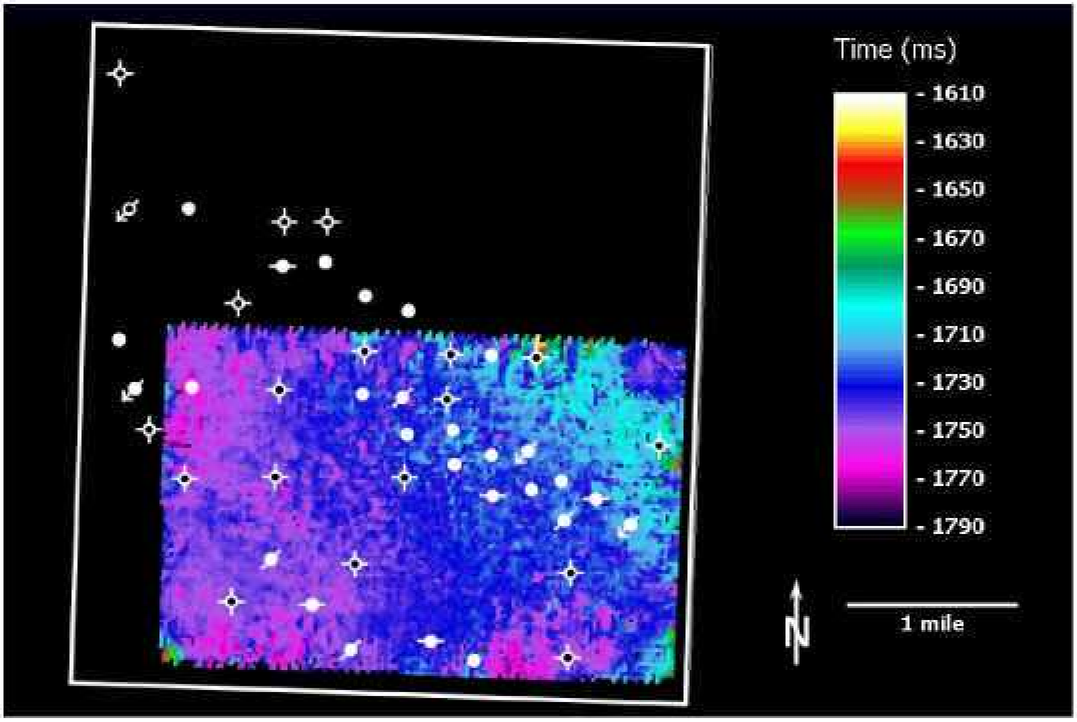

Figure 4-83 Approximate Upper Ismay (aUI) time structure map (S-wave).

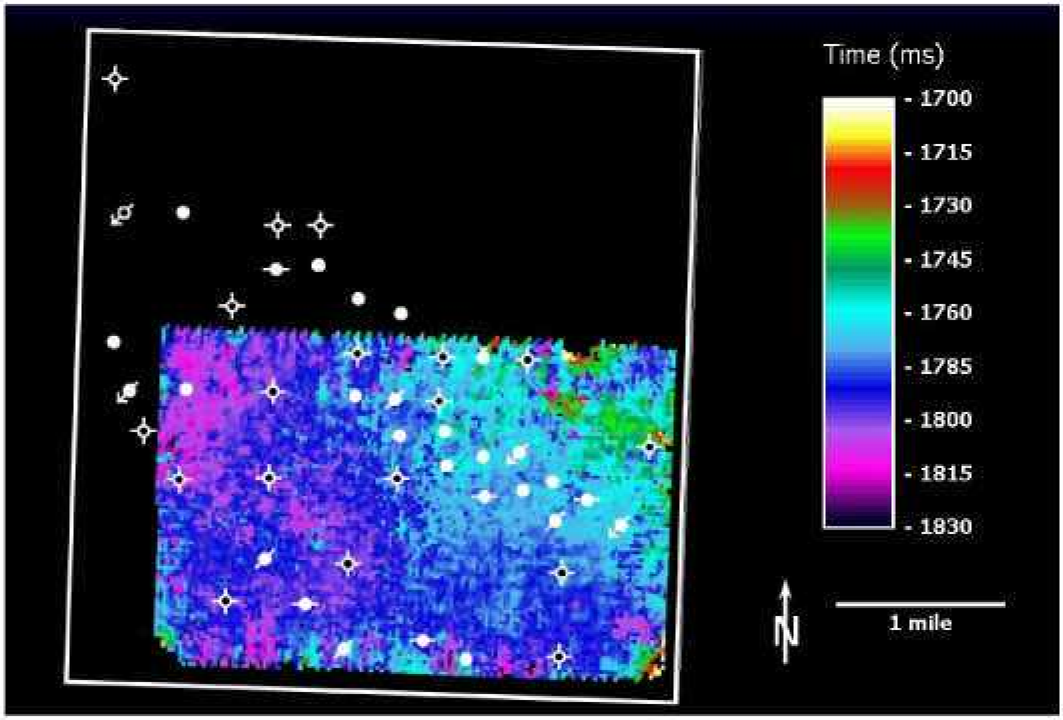

Figure 4-84 Upper Ismay seismic peak (UIC) time structure map (S-wave).

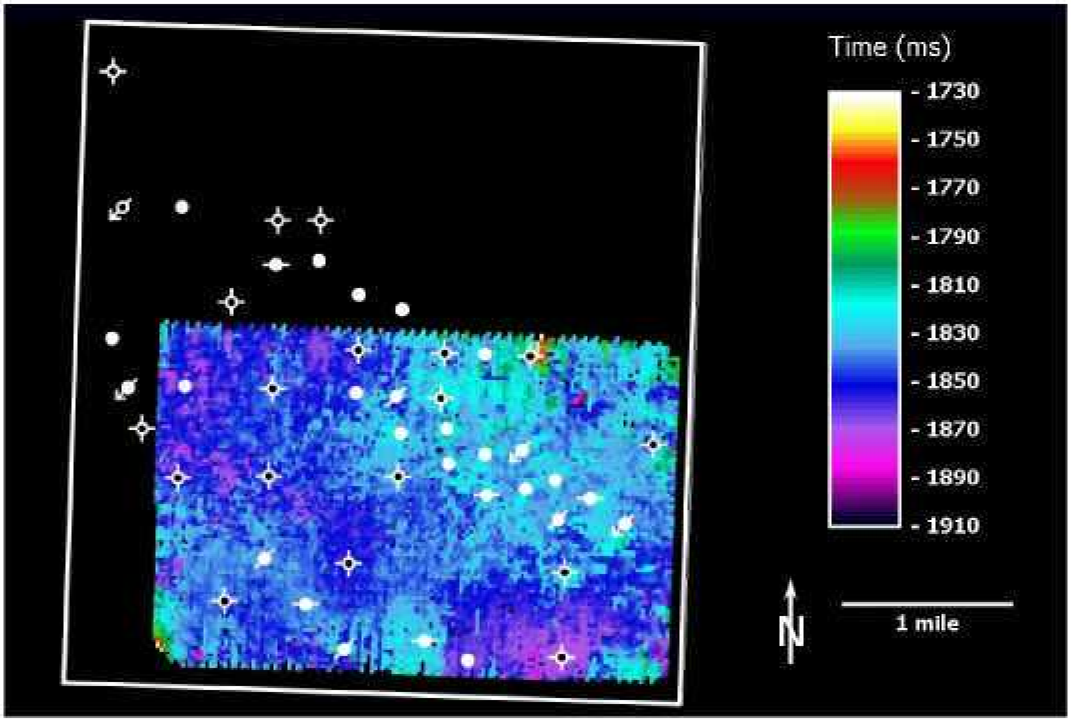

Figure 4-85 AKAH salt (AKAH) time structure map (S-wave).

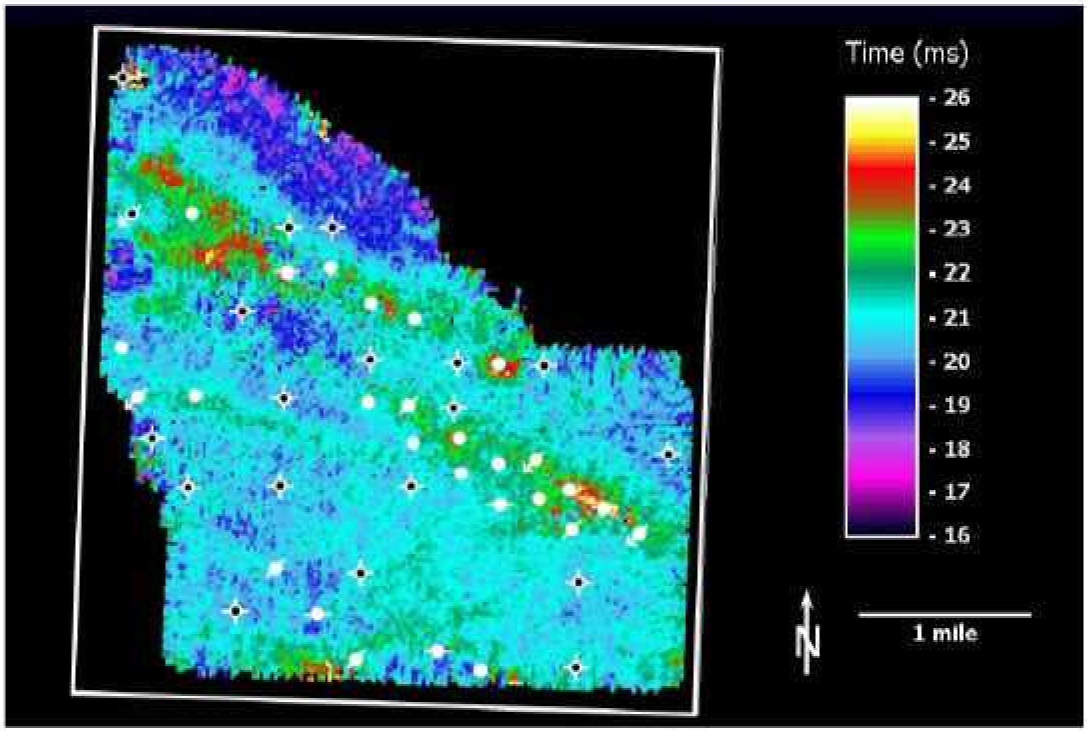

Figure 4-86. Akah Salt to Hovenweep (Top Lower Ismay) isochron (P-wave).

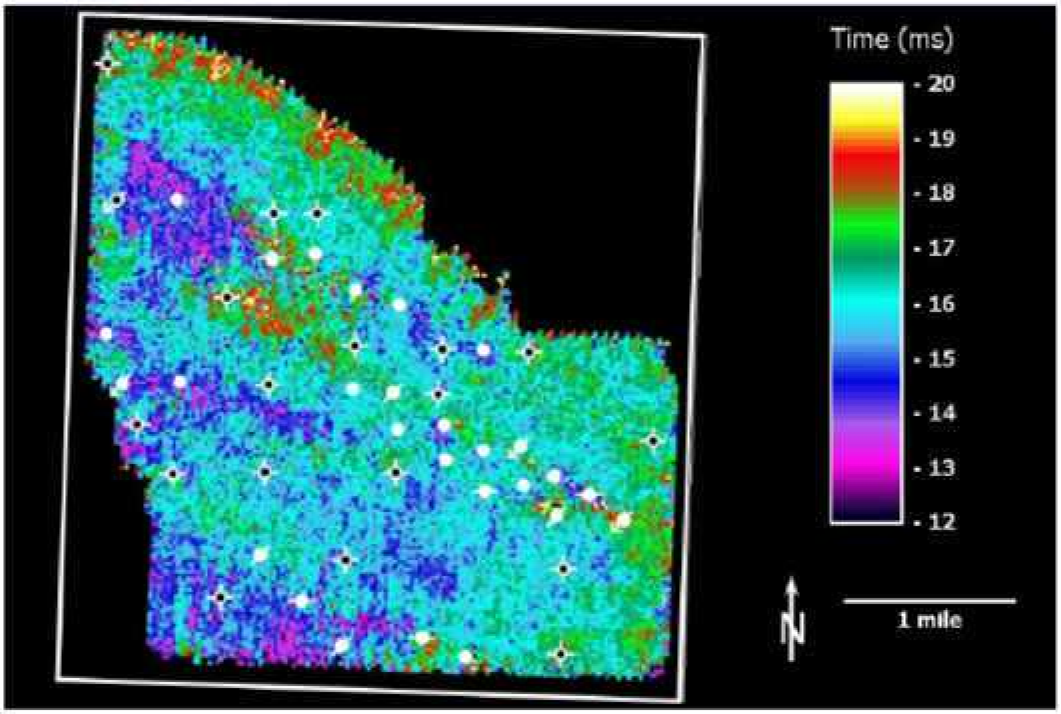

Figure 4-87. Top of Upper Ismay to Hovenweep isochron (P-wave).

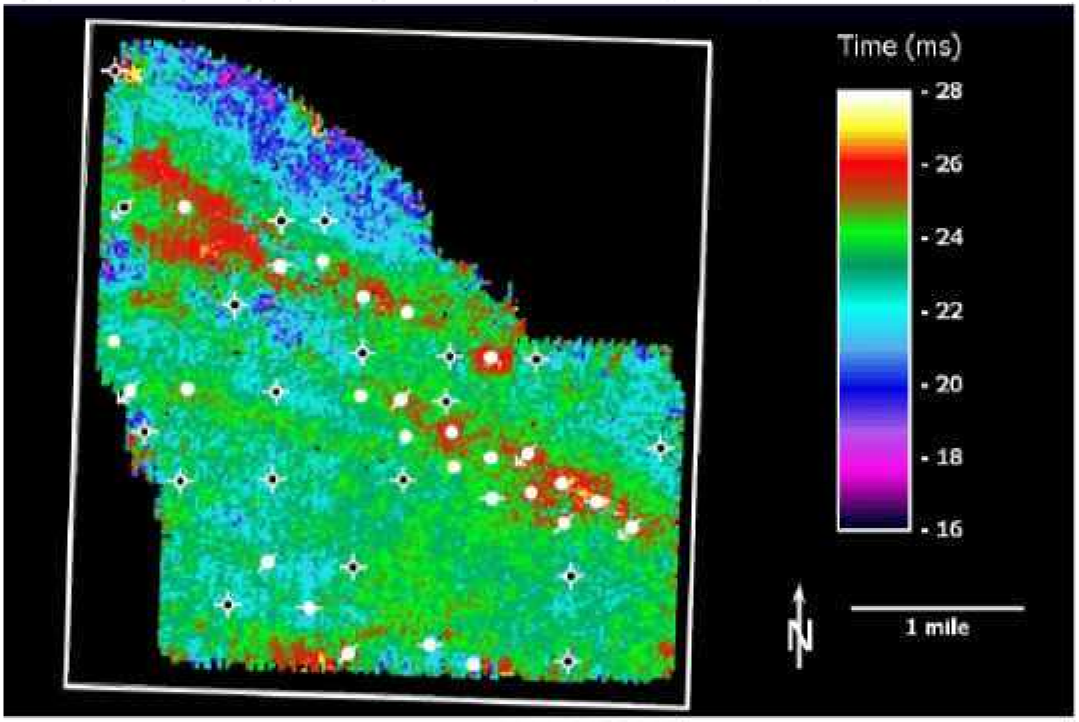

Figure 4-88. Top of Upper Ismay to Gothic Shale isochron (P-wave).

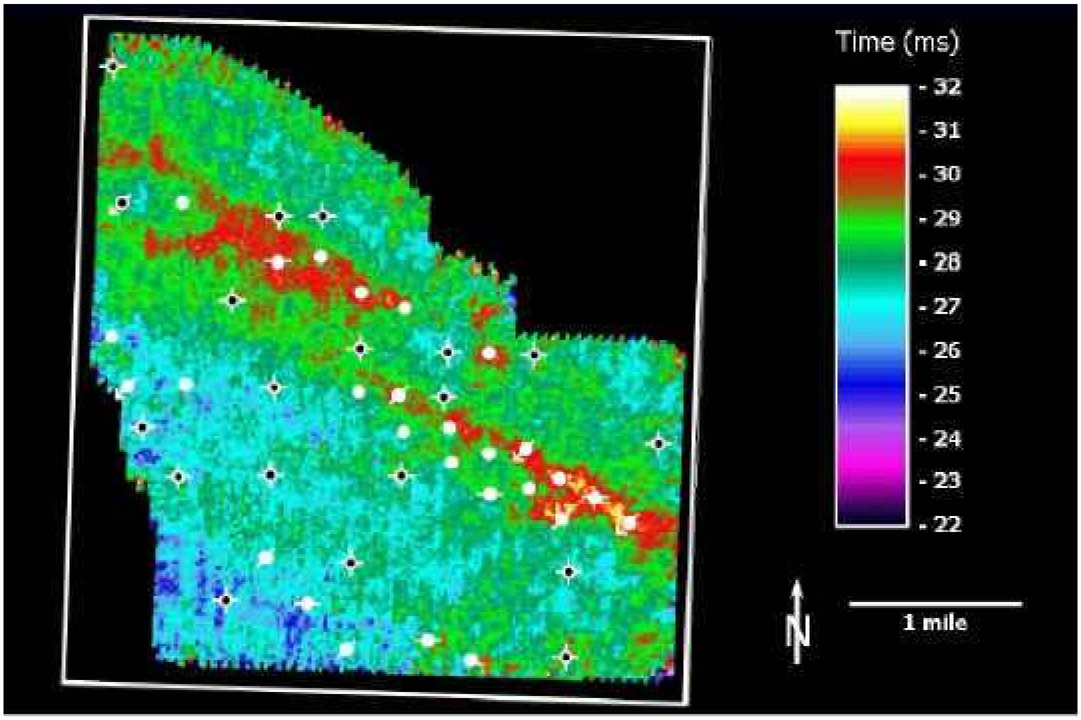

Figure 4-89. Top of Upper Ismay to Top of Desert Creek isochron (P-wave).

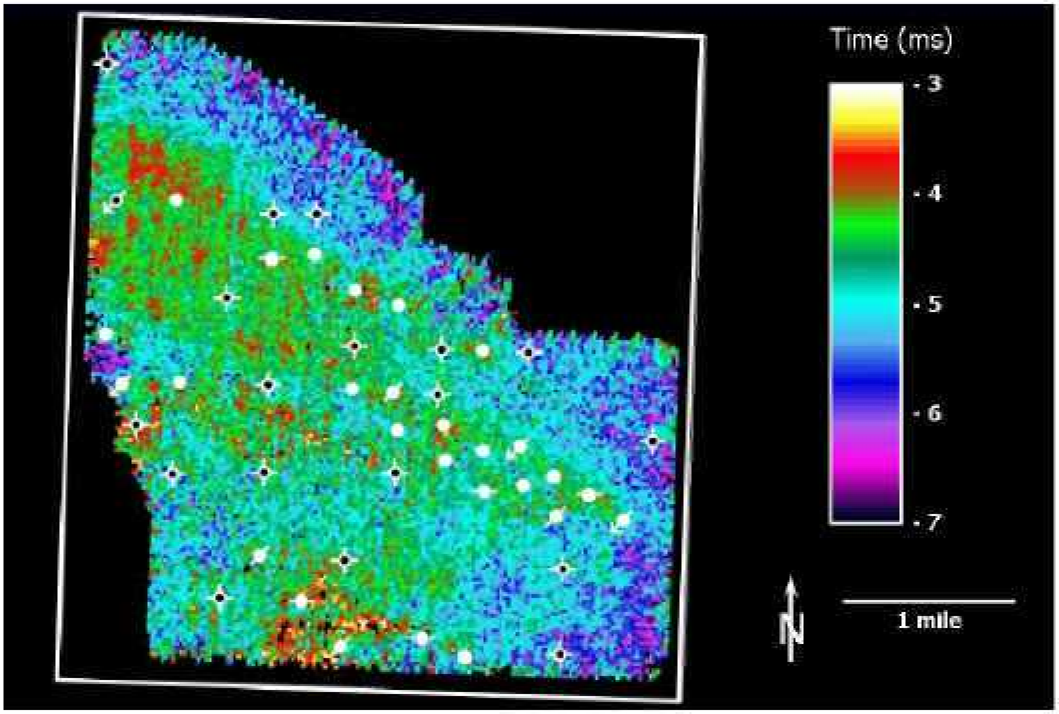

Figure 4-90. Top of Upper Ismay to Top of Upper Ismay Carbonate (P-wave).

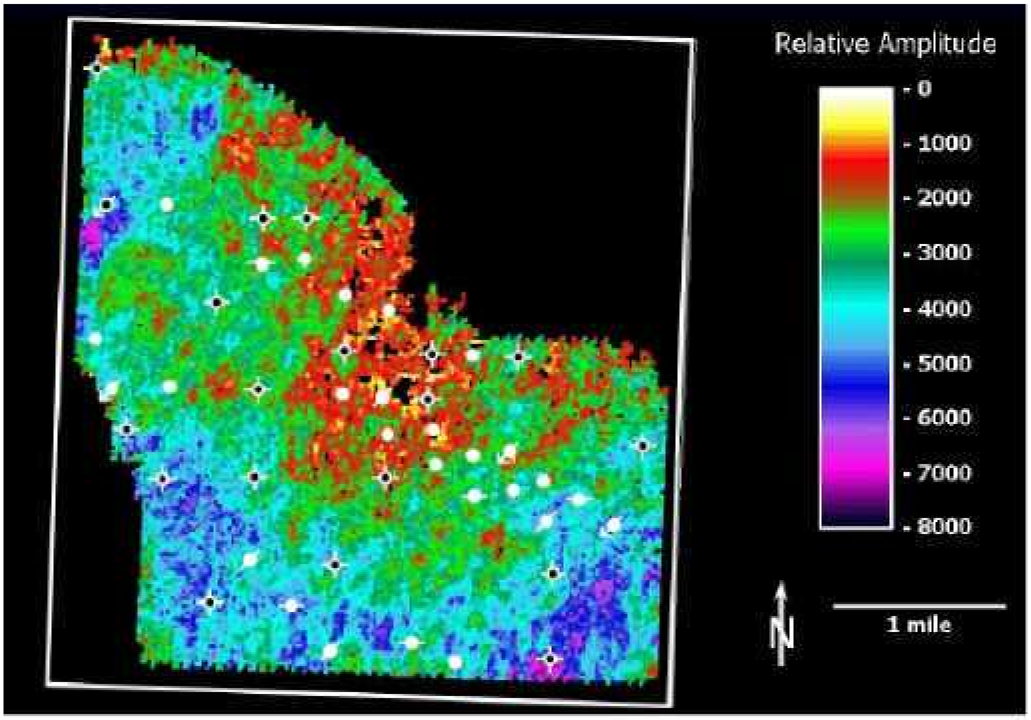

Figure 4-91. Cutler seismic amplitude (P-wave).

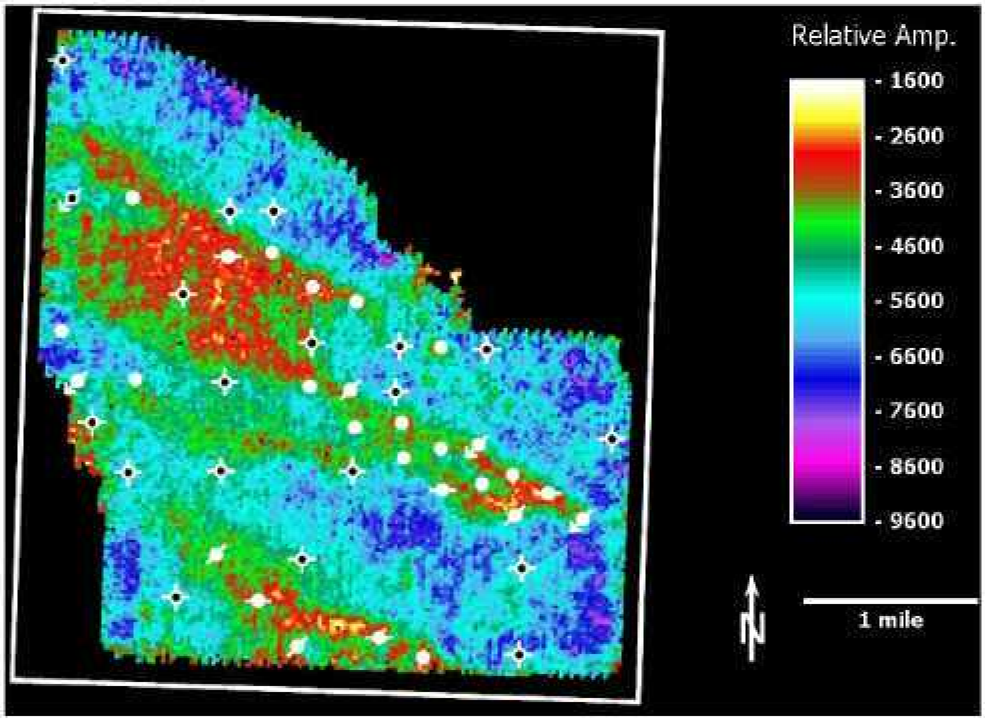

Figure 4-92. Upper Ismay amplitude (P-wave).

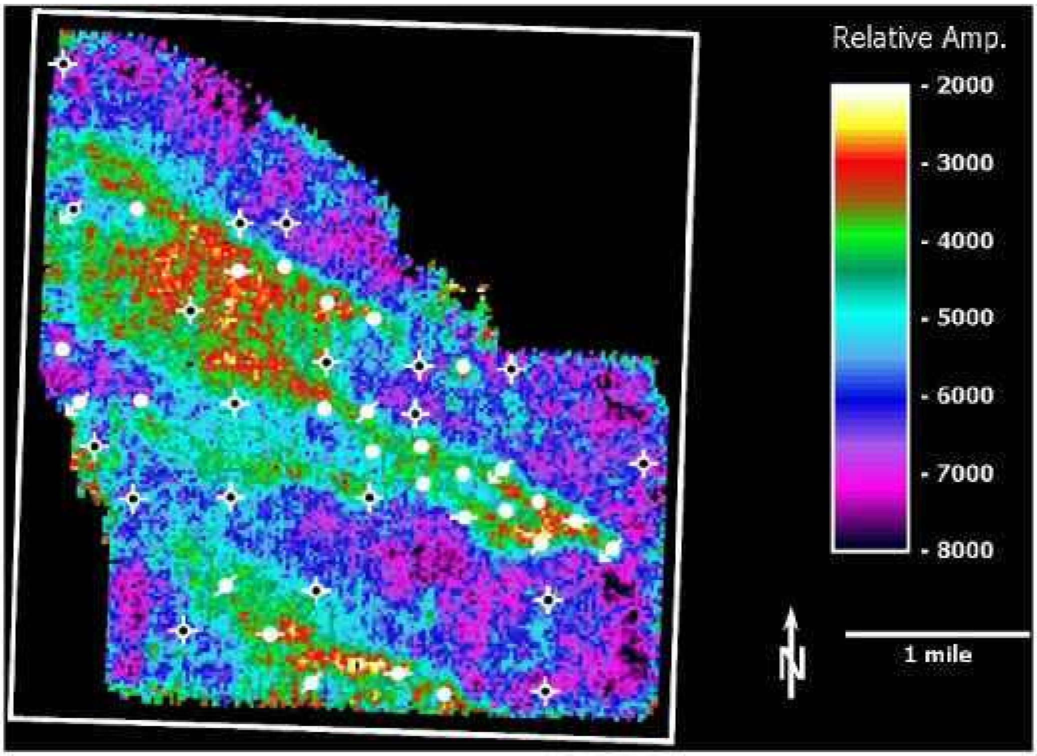

Figure 4-93. Upper Ismay maximum trough amplitude (P-wave).

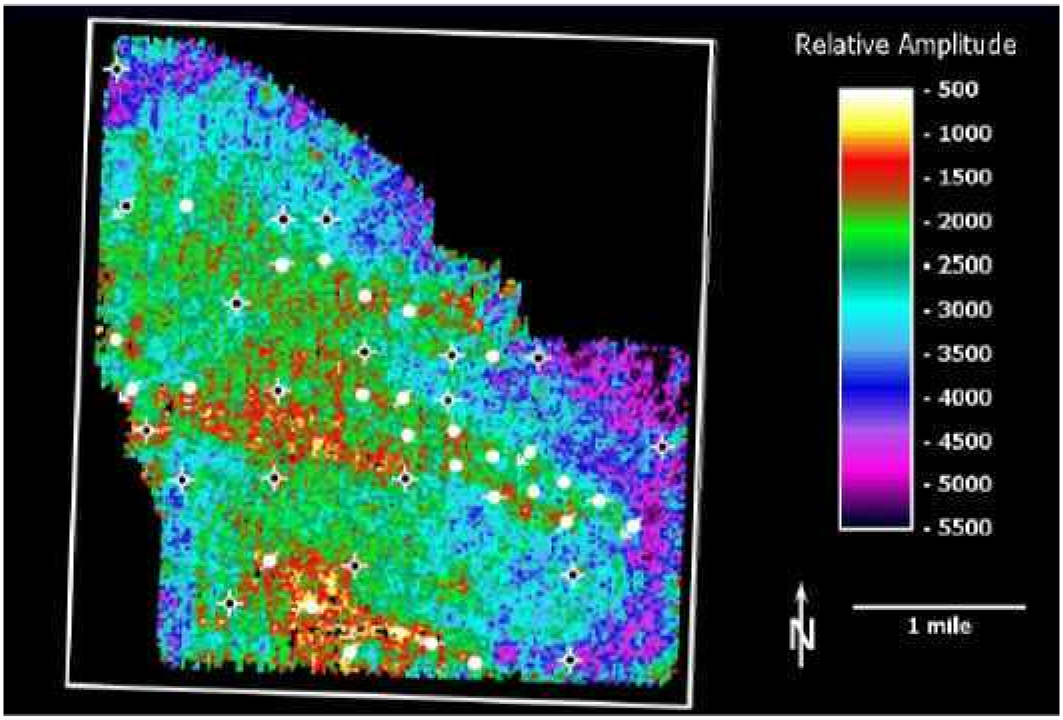

Figure 4-94. Upper Ismay Carbonate amplitude (P-wave).

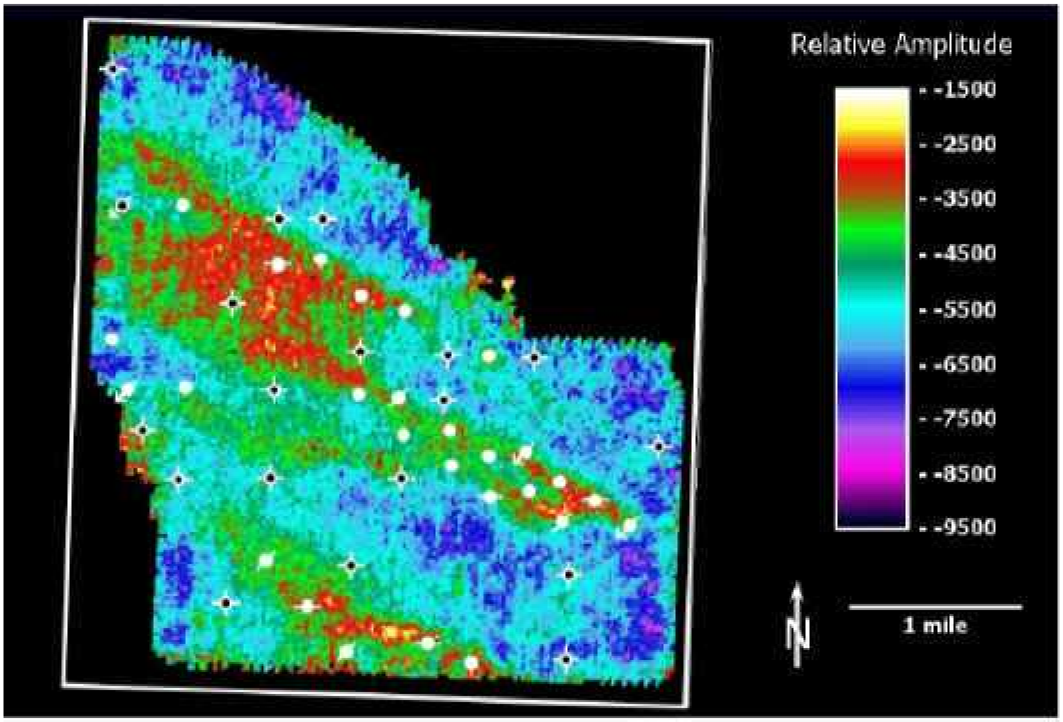

Figure 4-95. Lower Ismay amplitude (P-wave).

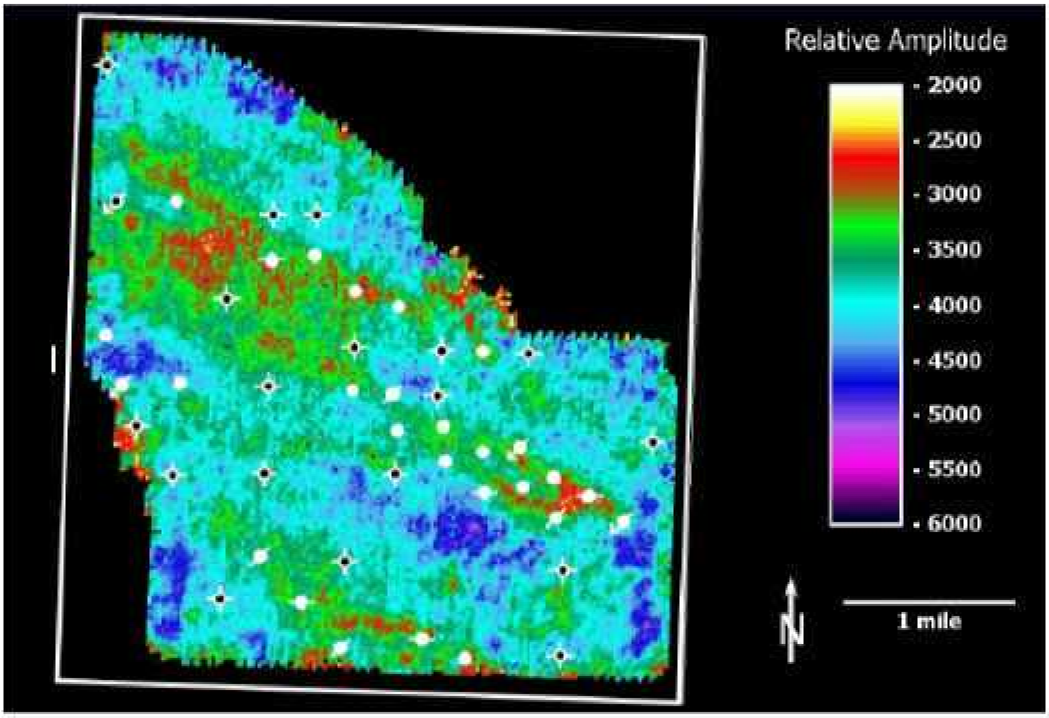

Figure 4-96. Lower Ismay RMS amplitude (P-wave).

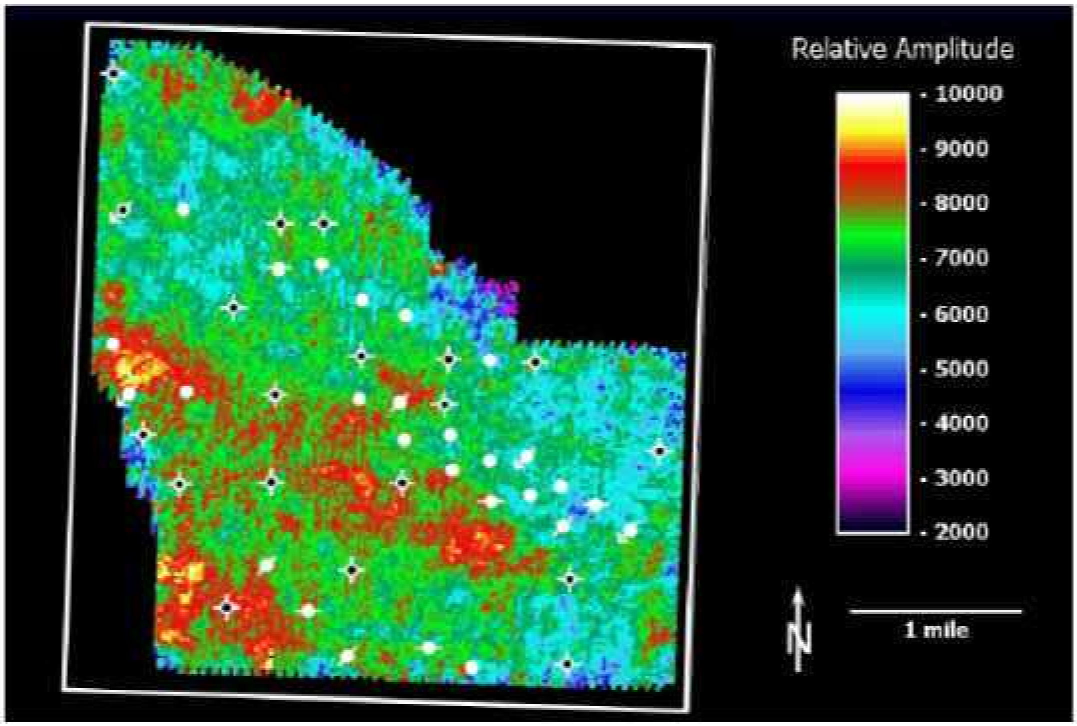

Figure 4-97. Desert Creek amplitude (P-wave).

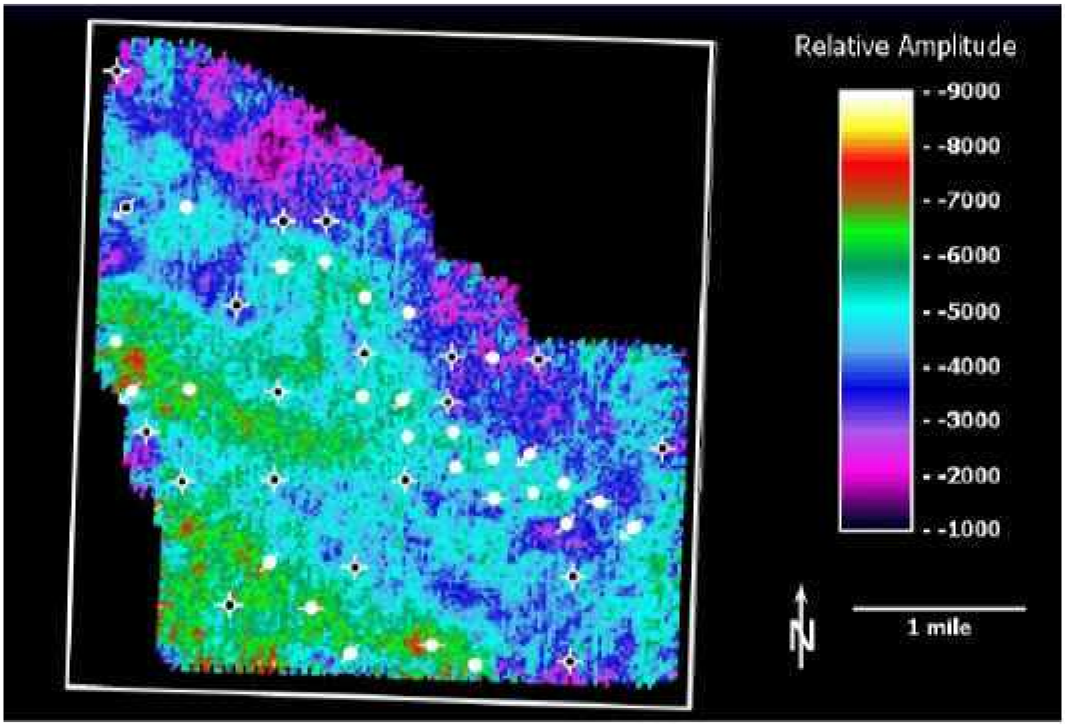

Figure 4-98. Akah Salt amplitude (P-wave).

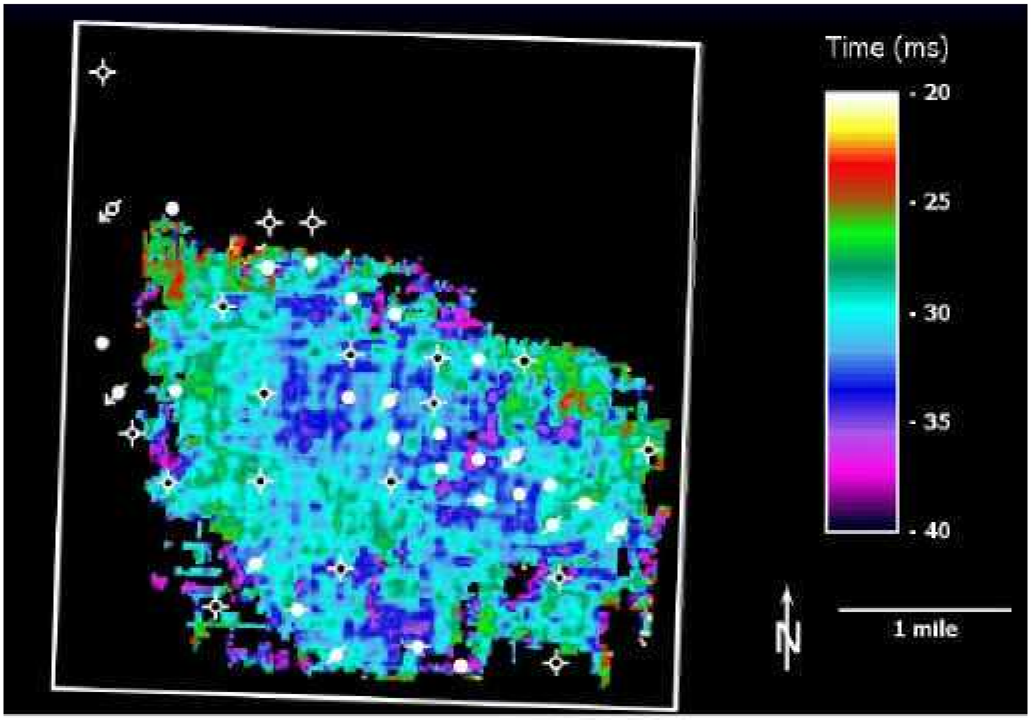

Figure 4-99. Upper Ismay to Gothic Shale isochron (PS-wave).

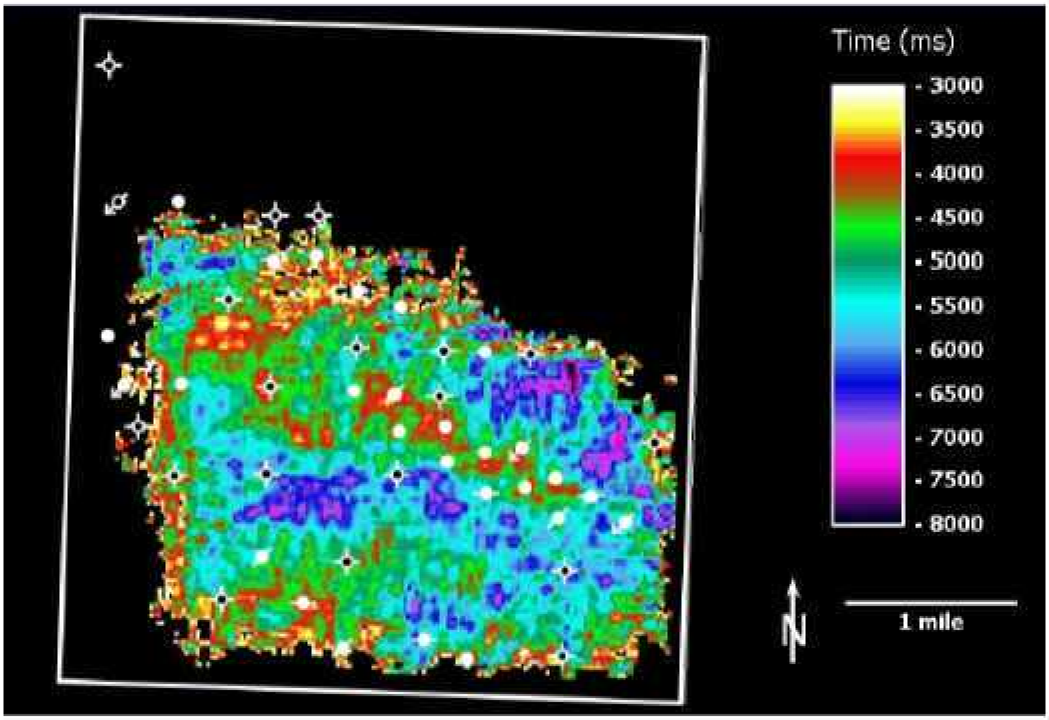

Figure 4-100. Approximate Upper Ismay amplitude (PS-wave).

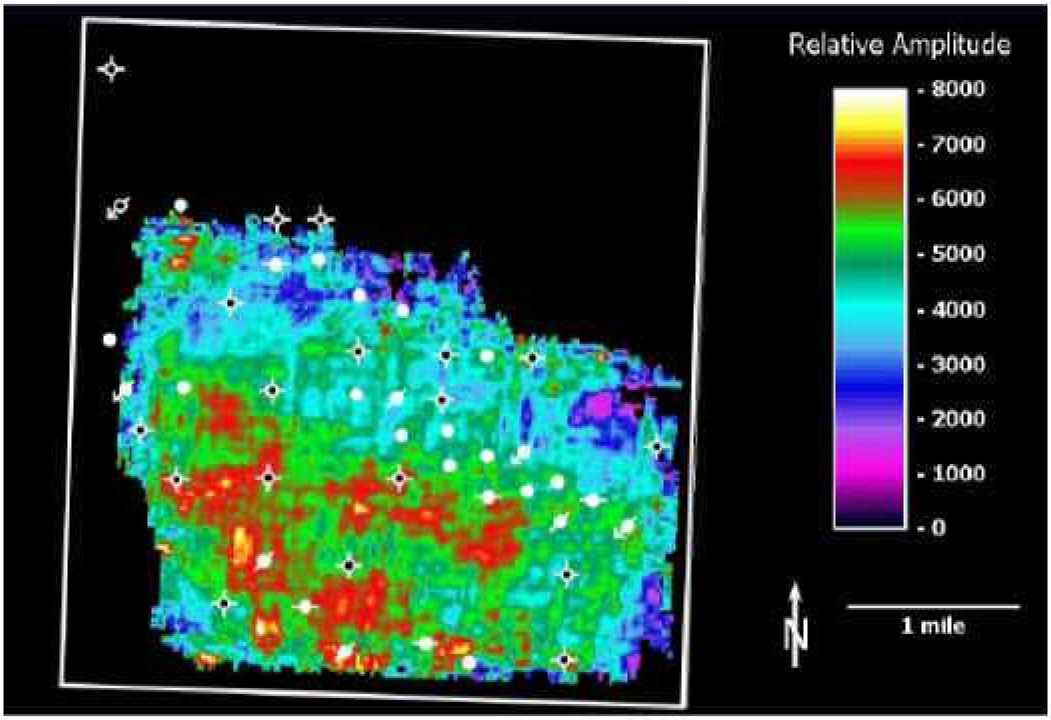

Figure 4-101. Upper Ismay amplitude (PS-wave).

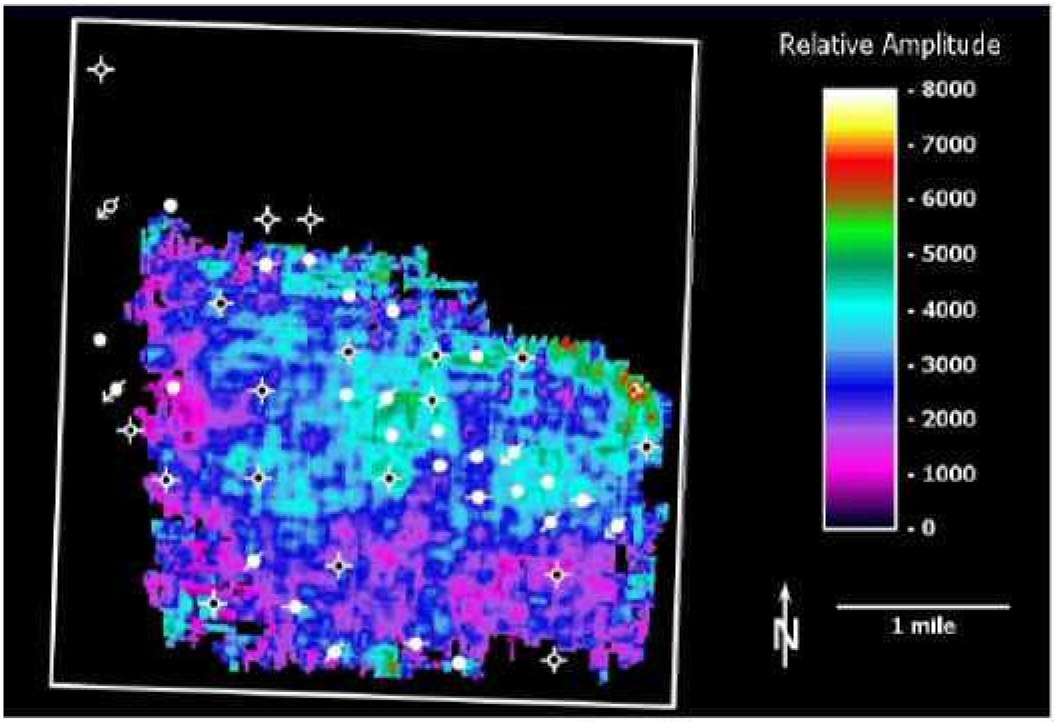

Figure 4-102. Gothic amplitude (PS-wave).

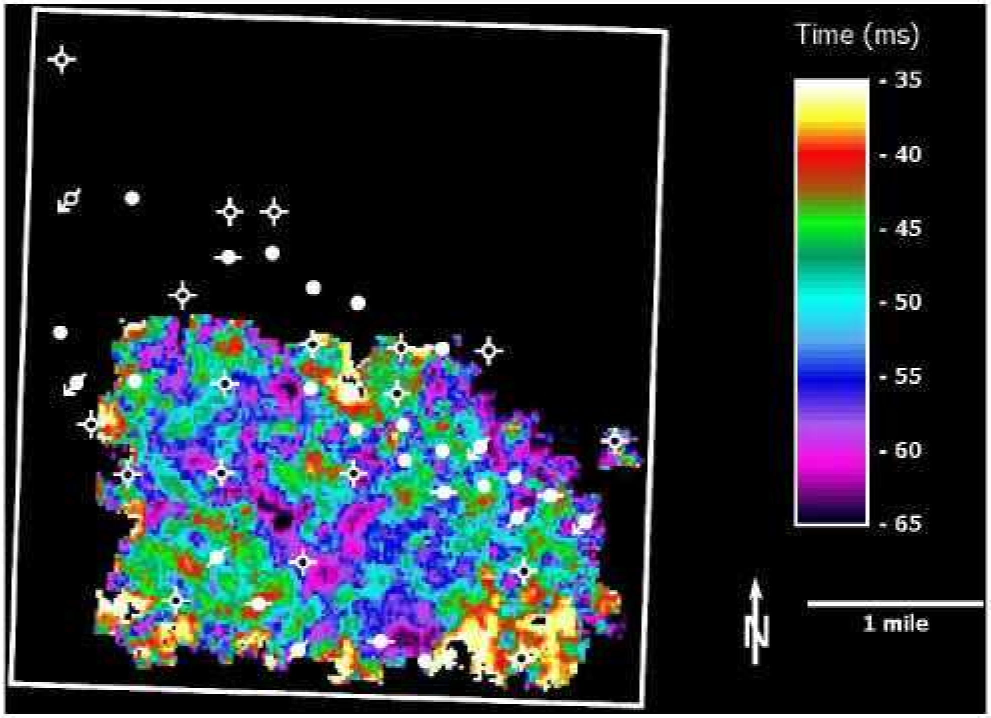

Figure 4-103. Approximate Upper Ismay to Upper Ismay Carbonate isochron (S-wave).

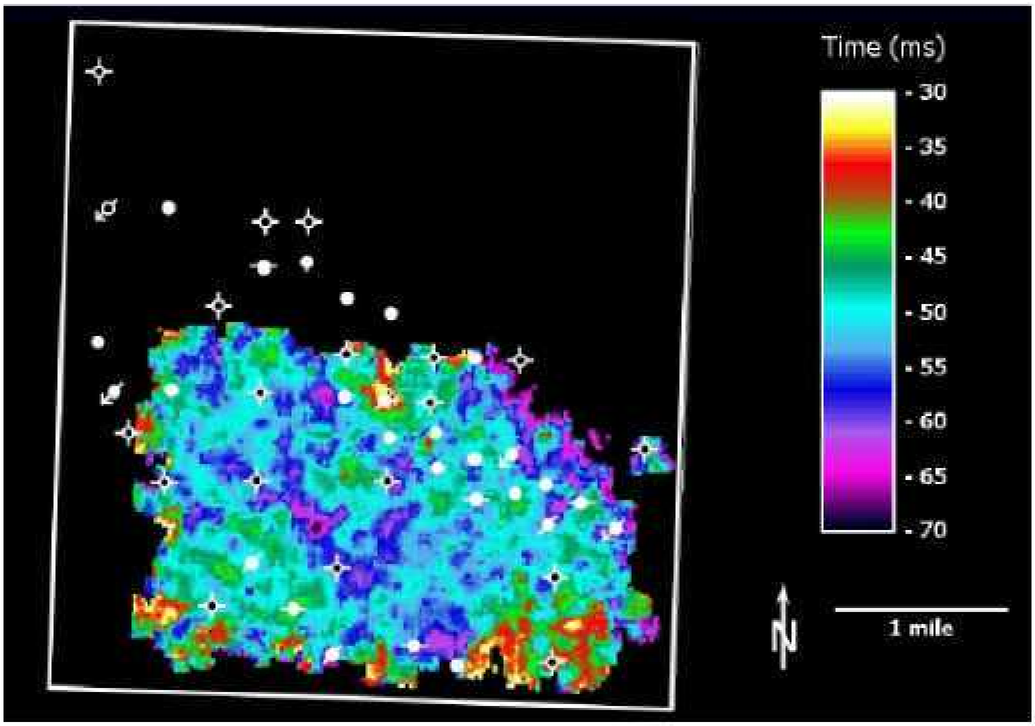

Figure 4-104. Approximate Upper Ismay to Desert Creek isochron (S-wave).

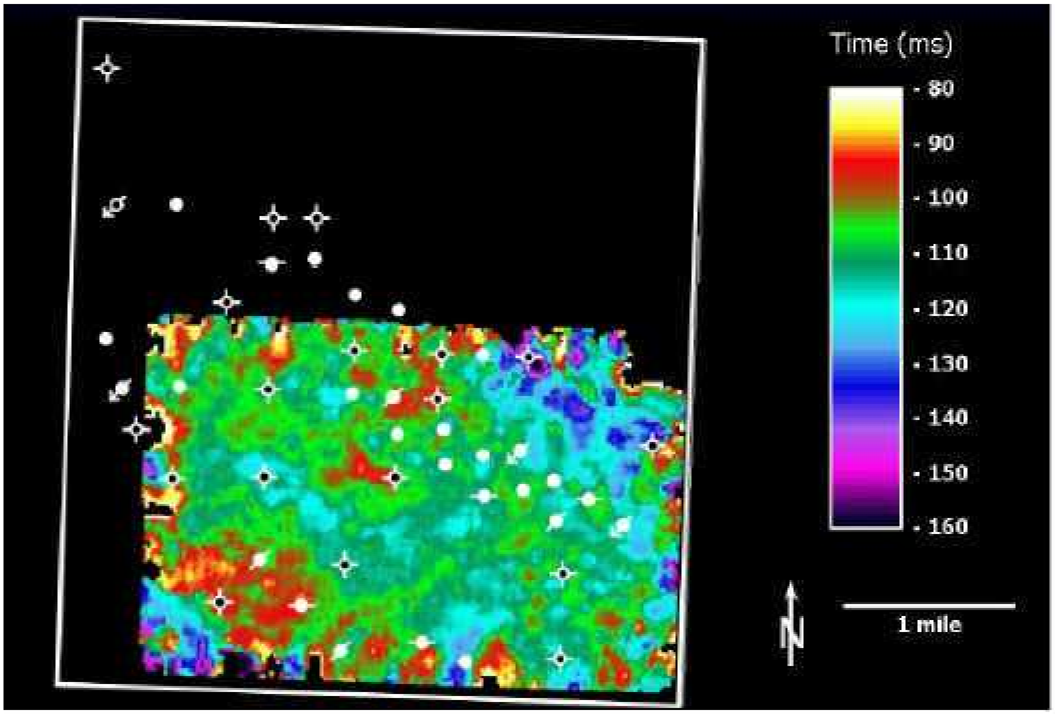

Figure 4-105. Approximate Upper Ismay to Akah salt isochron (S-wave).

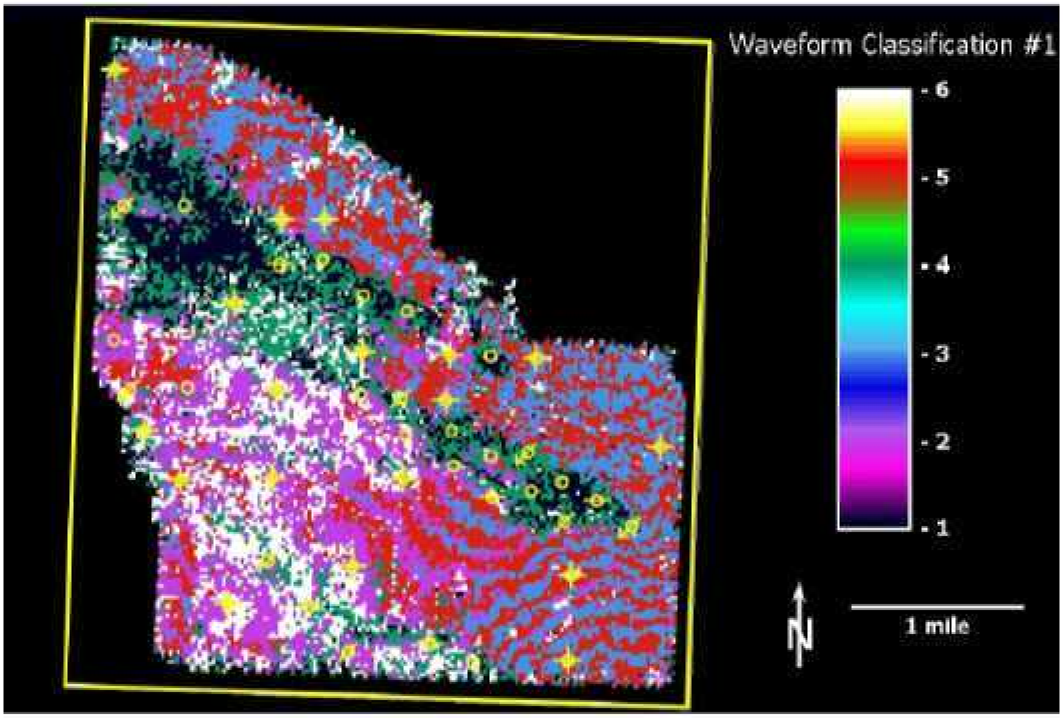

Figure 4-106. Waveform classification alternative #1 (P-wave).

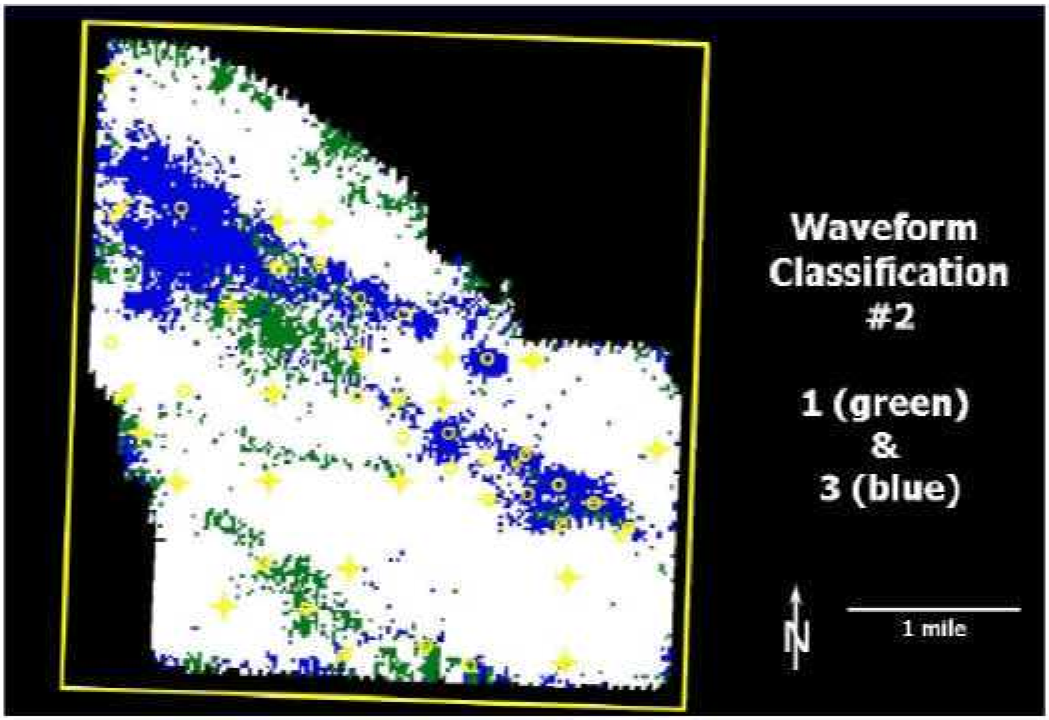

Figure 4-107. Waveform classification alternative #2 (P-wave).

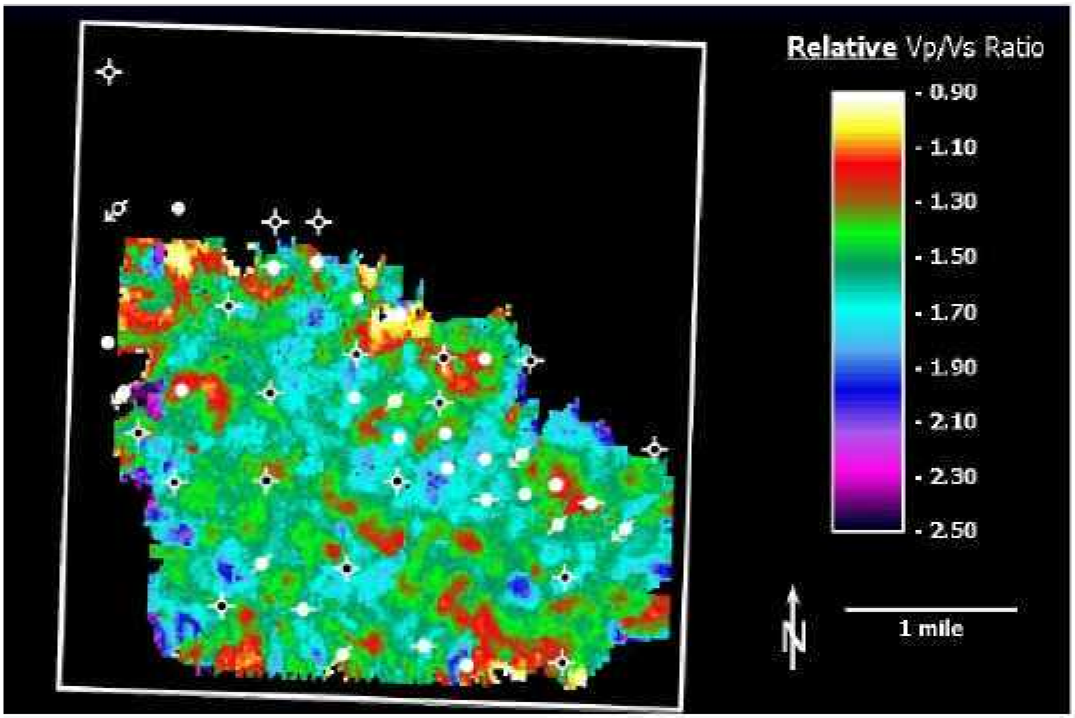

Figure 4-108. Relative Vp/Vs ratio (PS-wave).

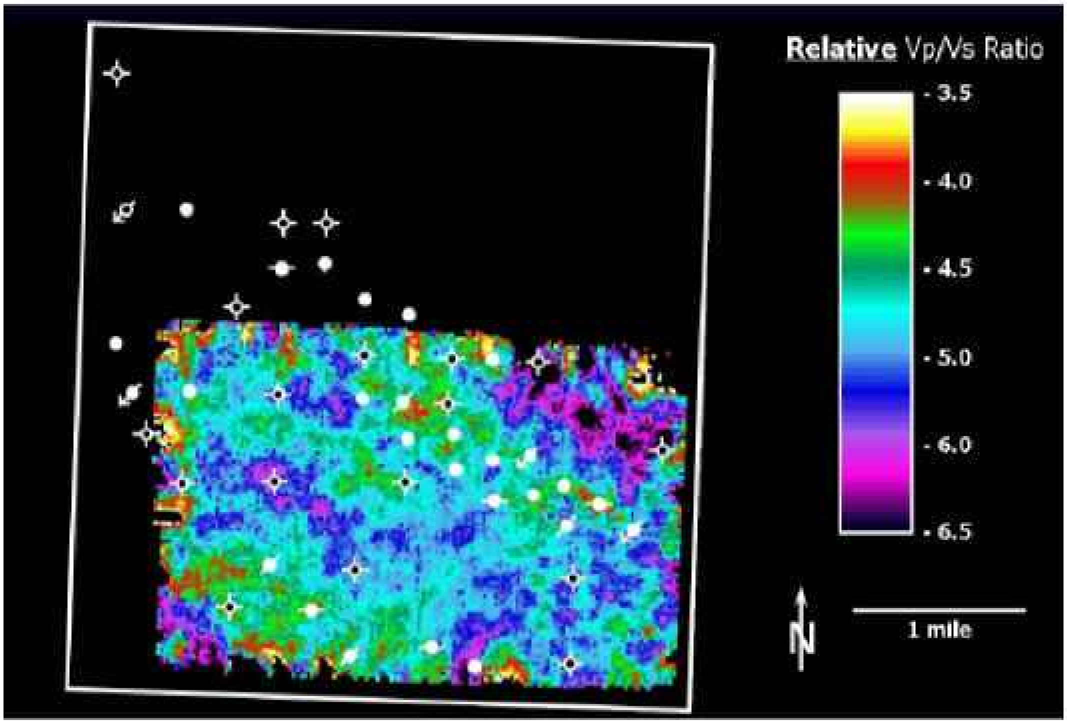

Figure 4-109. Relative Vp/Vs ratio (S-wave).

4.5.1 ISOPACH MAPS

Multivariate regression analysis using various seismic attributes from the WesternGeco Version 1 data was used to calculate isopach maps, as previously described. Red colors indicate isopach thicks, while blue colors illustrate isopach thins.

Figure 4-114 shows the resulting Ismay to Desert Creek Isopach Map. Note that Ismay productive mound areas are associated with Ismay-Desert Creek isopach thicks. Note that there are prospective isopach thick areas located primarily in the northwest portion of the survey.

The Top Ismay to Top Upper Ismay Carbonate isopach (Figure 4-115) includes the Ismay Massive Anhydrite which is known to be thin in mound areas and thick in off-mound regions. Red colors are associated with isopach thins, whereas blue colors represent isopach thicks. As expected, this isopach interval is anomalously thin in Ismay producing areas. The isopach thins are most dramatic in the Towaoc Field area which is located in the southern portion of the survey. It is possible that there may be at least one more new drilling location in the southern portion of the 3D based on this isopach.

The Top Lower Ismay to Top Desert Creek isopach is shown in Figure 4-116. Isopach thicks are noted in red, while thins are illustrated with blue colors. This interval is anomalously thick in producing areas, especially in the Marble Wash and Roadrunner fields which trend through the northwest and center of the 3D survey. This isopach map indicates undrilled Lower Ismay mound areas may exist in the northwest portion of the survey.

4.5.2 DEPTH STRUCTURE MAPS

Depth maps were also constructed from seismic data. In constructing depth maps, velocity maps must first be generated. Horizon seismic times and actual horizon depth values at wells are used to calculate velocity. The velocity and seismic time grids are then used to create a depth structure map.

The Top Ismay depth map (Figure 4-110) was generated by using Ismay Zero Crossing time and Top Ismay velocity grids. For all depth maps, structurally high areas are noted in red and structurally low areas are indicated in blue. Subtle southwest plunging noses are noted, however, no large structural closures on the Top Ismay depth map are observed.

The Top Desert Creek depth map is shown in Figure 4-111. The Desert Creek Peak time structure map was used along with the associated velocity grid to generate the Desert Creek depth map.

In order to construct a depth map on the top of the Upper Ismay Carbonate reservoir, it was necessary to combine the Top Ismay depth map with the Top Ismay to Top Upper Ismay Carbonate isopach map. In other words, the isopach map was subtracted from the Top Ismay depth map to give the resulting Upper Ismay Carbonate depth map (Figure 4-112).

A Lower Ismay depth map (Figure 4-113) was generated by combining the Desert Creek depth map with the Top Lower Ismay to Top Desert Creek isopach map. The isopach grid was added to the Desert Creek depth grid to create the resulting Lower Ismay depth map.

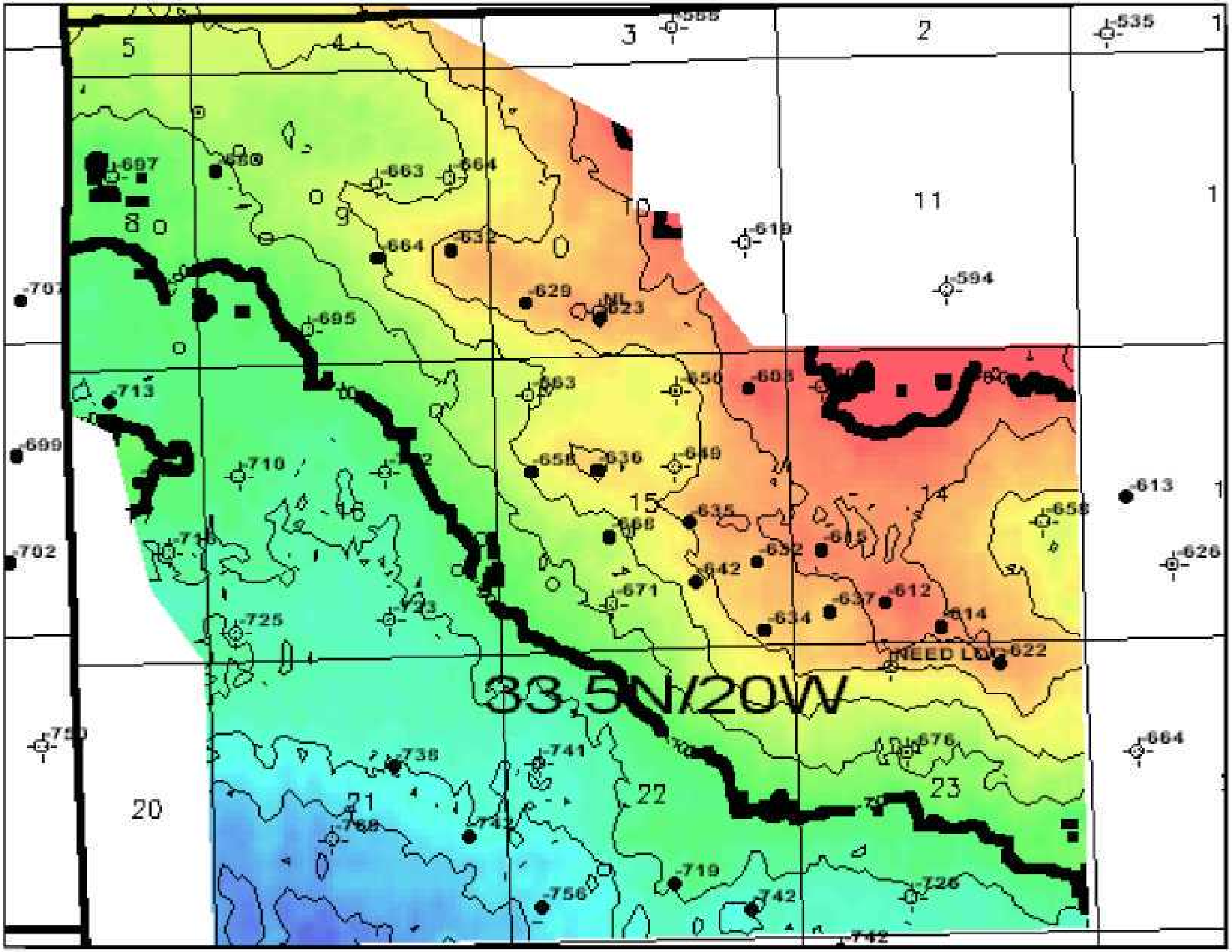

Figure 4-110. Top Ismay Depth Map CI = 20 ft

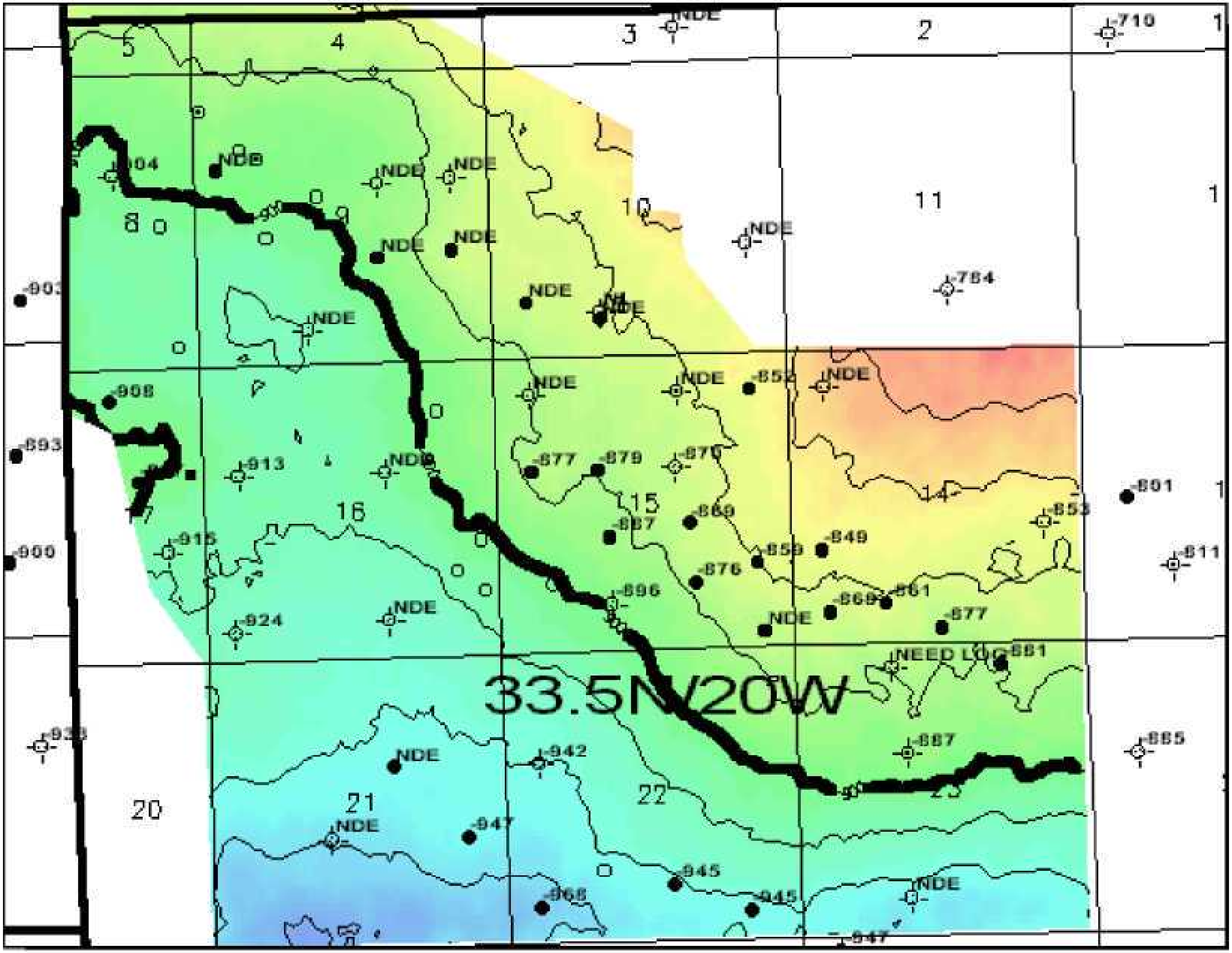

Figure 4-111. Top Desert Creek Depth Map, CI = 20 ft.

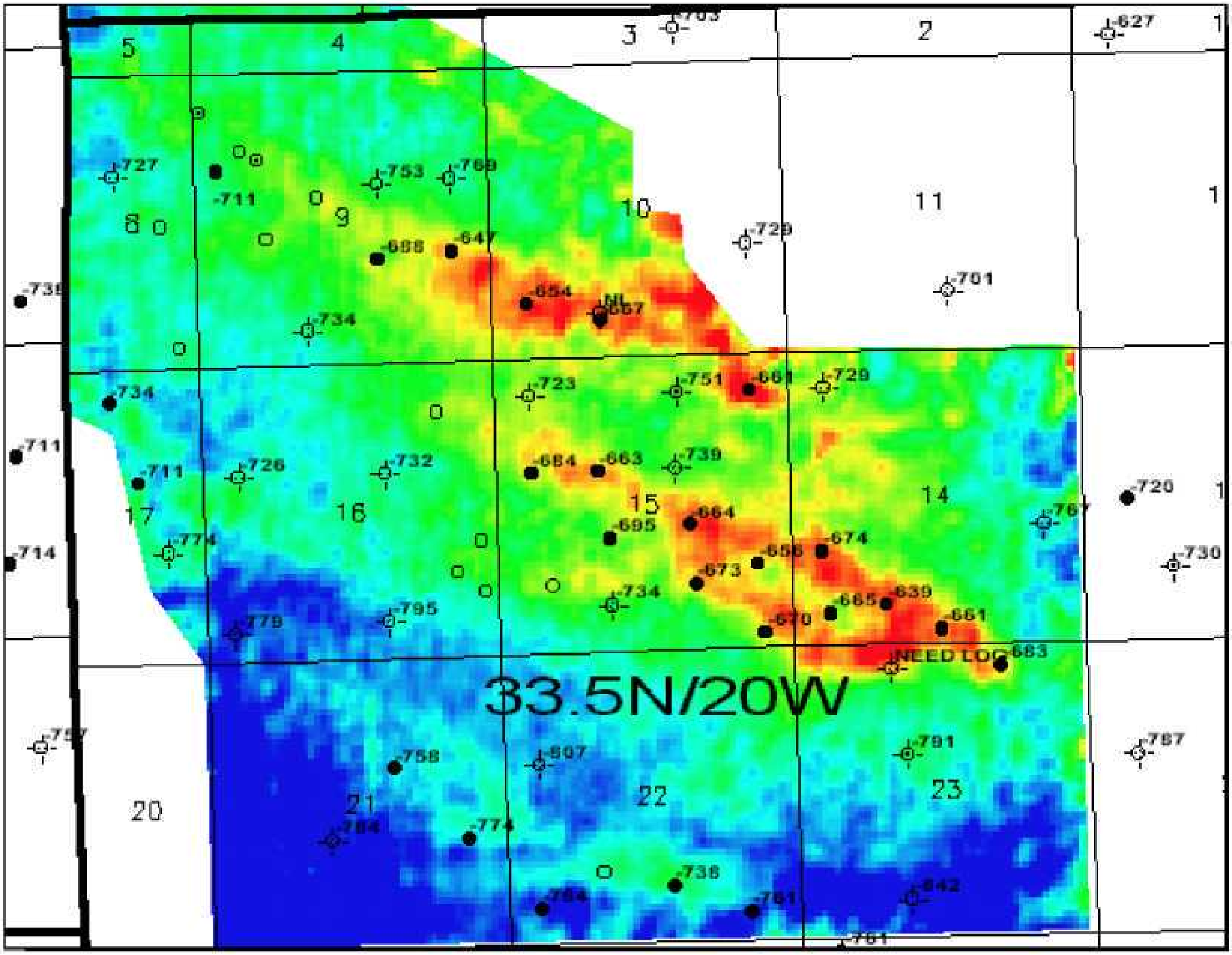

Figure 4-112. Upper Ismay Carbonate Depth Map.

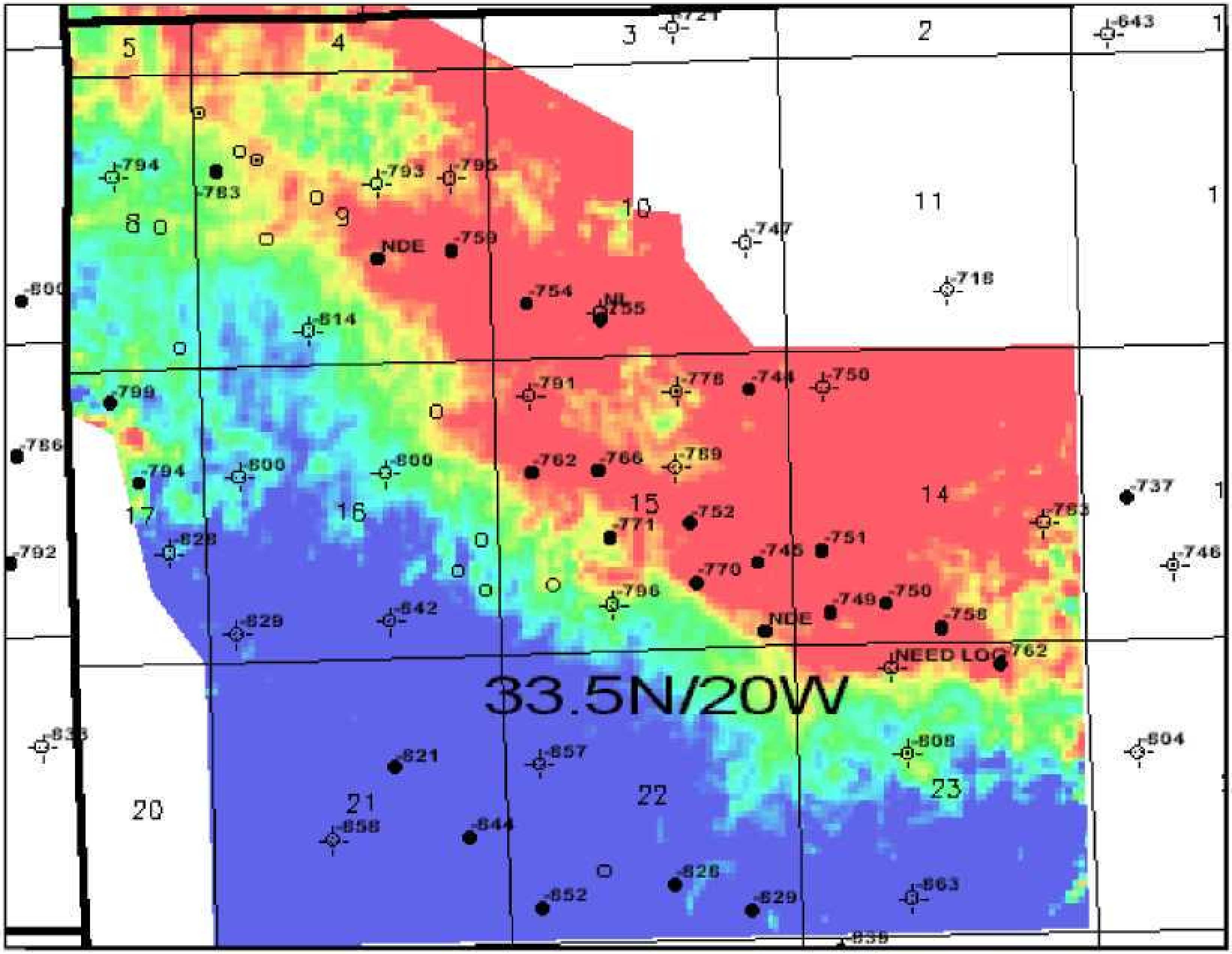

Figure 4-113. Lower Ismay Depth Map.

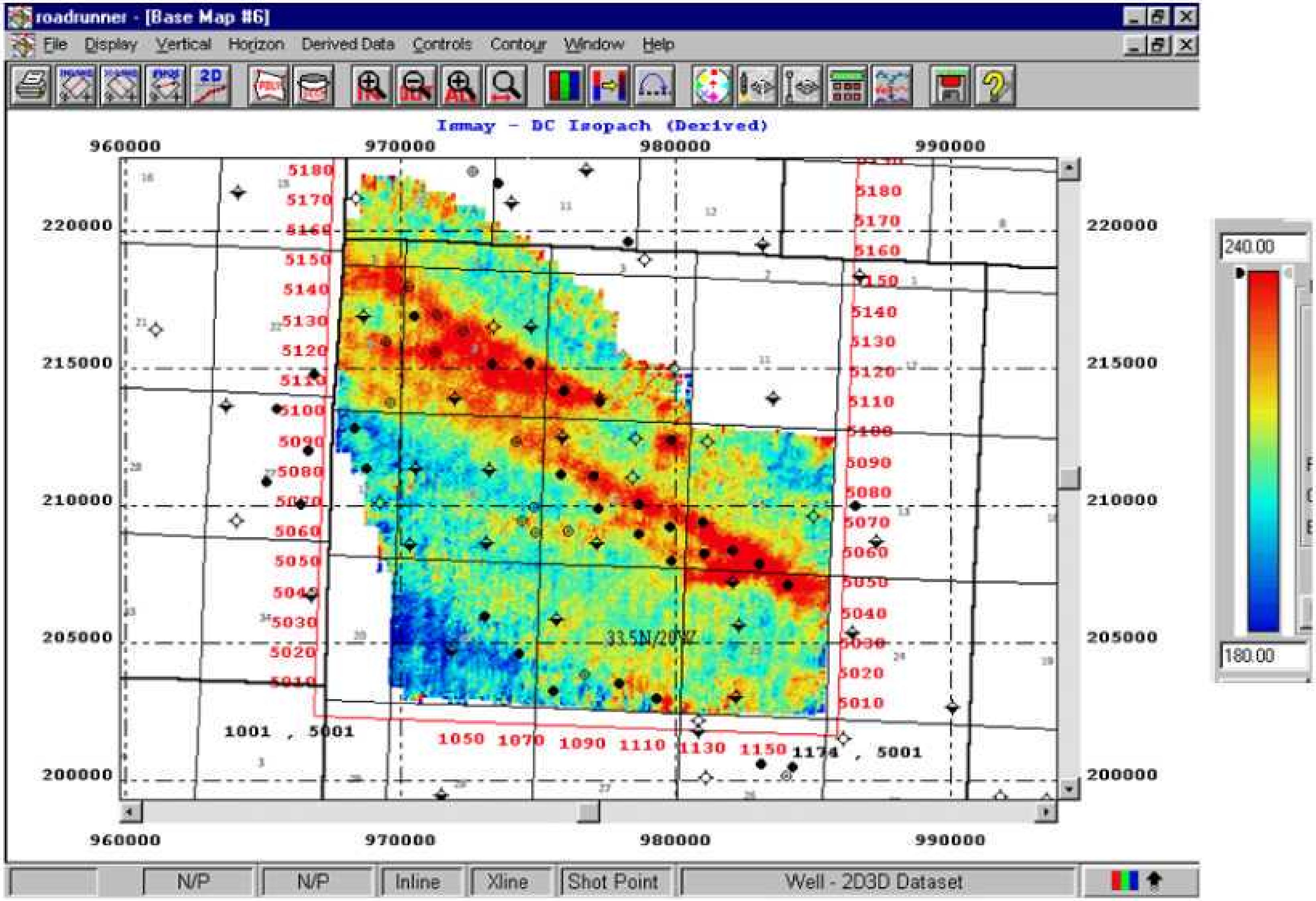

Figure 4-114. Top Ismay to Top Desert Creek Isopach Map.

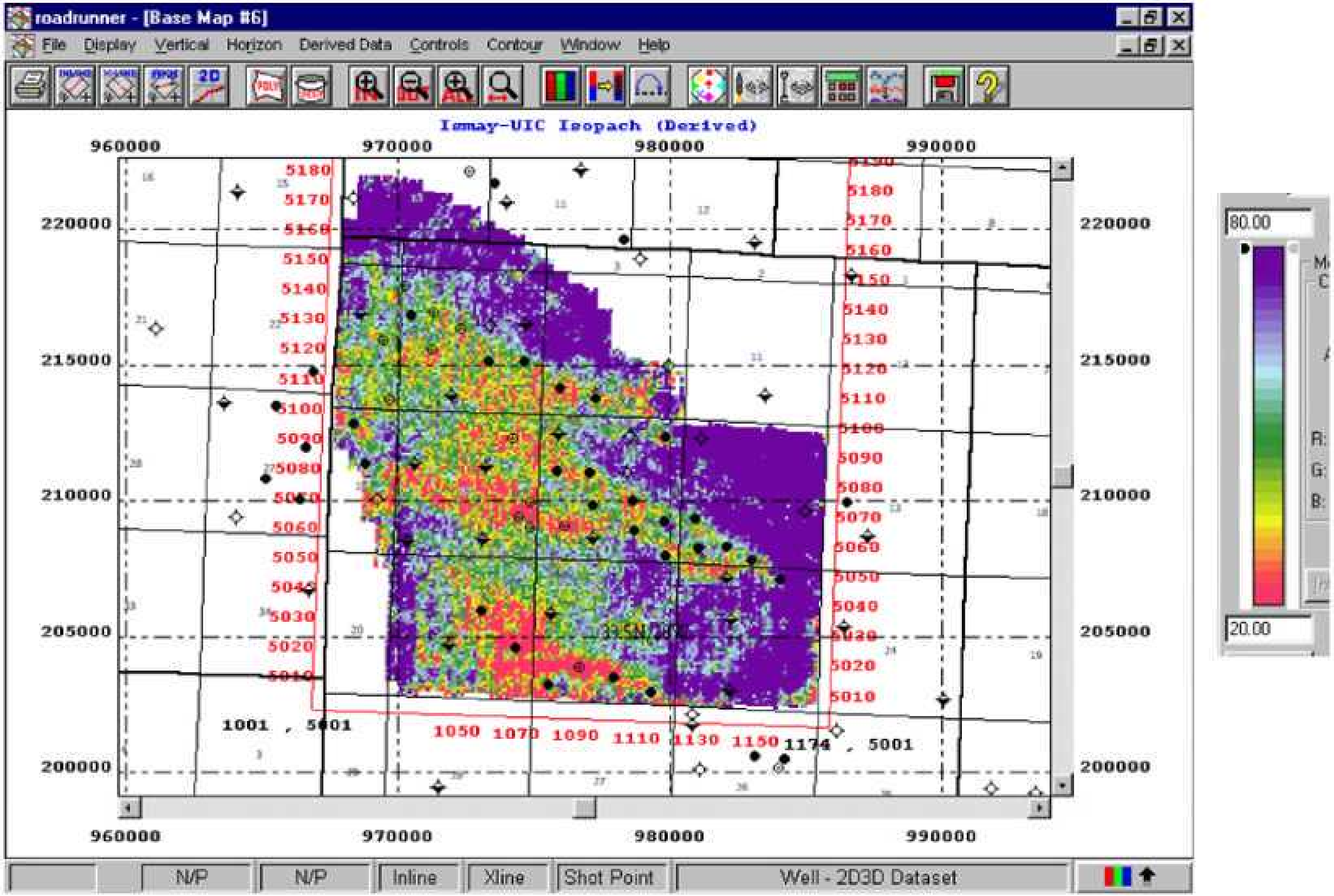

Figure 4-115. Top Ismay to Top Upper Ismay Carbonate Isopach Map.

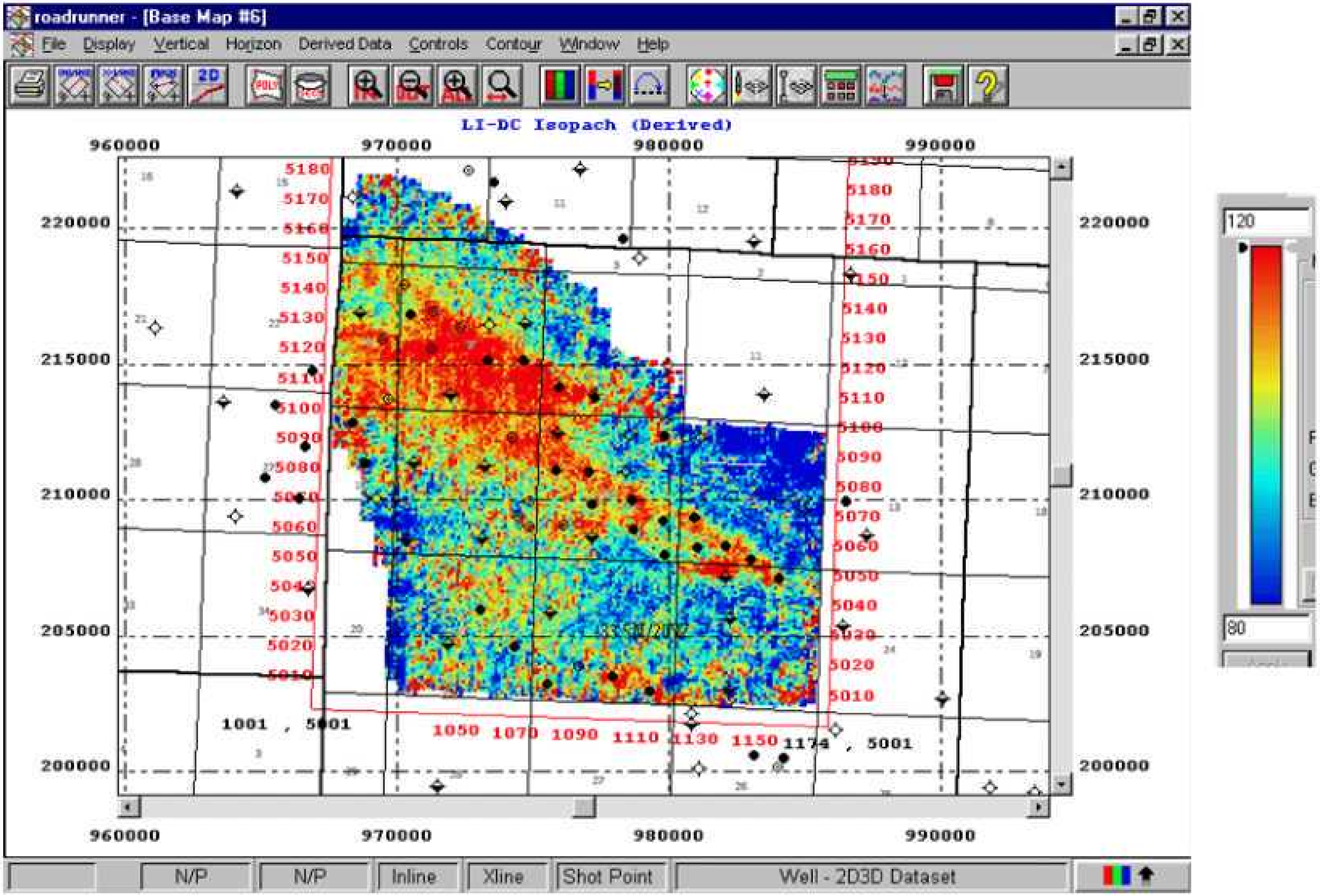

Figure 4-116. Top Lower Ismay to Top Desert Creek Isopach Map.

4.6 Drilling Results

4.6.1 BASIS FOR LOCATION SELECTION

There are several criteria that were considered for selecting well locations:

- The thickness of the potentially productive Upper and Lower Ismay;
- The potential for being in a more productive area of the mound complexes; and
- The potential for being in an unexploited area of the mounds.

The thickness of the Upper and Lower Ismay reservoirs can be examined by evaluating various isochrons/isopachs. The isochron between the Upper Ismay (UI) and Desert Creek (UDC) provides a measure of the total mound thickness. The thickness between the Upper Ismay (UI) and the Upper Ismay Carbonate (UIC) seismic marker reflects the combined thickness of the massive anhydrite and the upper transition zone. The thickness between the Upper Ismay Carbonate (UIC) and the Gothic Shale (GTHC) relates to the gross thickness of the Lower Ismay reservoir. Joint consideration of these thicknesses delineates regions where there may be higher-than-average reservoir volumes available.

Productive characteristics of the mounds in the project area were not uniform (Figure 4-117 through Figure 4-119). In order to extent knowledge of what areas may have higher potential for oil & gas rates and recovery, seismic attributes as a function of productivity were examined. This made it possible to step away from the immediate vicinity of the wells and use seismic to identify regions that are both undrilled and may have higher rates and recoveries. This was done by comparing measured initial production (IP), cumulative production and estimated ultimate recovery (EUR) to derived seismic attributes. Areas with high water cuts are also less attractive.

The potential for locating a well in under-exploited regions of the prospective area relates to existing production, dry holes and injectors. If promising mound thicks are identified in areas with potentially good rates and recoveries, then a final consideration is whether this location is likely to already have been depleted by existing production or flushed by injector wells.

Figures 4-1 through 4-3 show the production values for several wells overlain on the isopach between the Upper Ismay and the Desert Creek, reflecting the gross thickness of the Ismay algal mound targets. Figure 4-117 shows the IP rates for oil and gas; Figure 4-118 shows the cumulative production for oil and gas; and Figure 4-119 shows the EUR for oil and gas.

All three of these figures show a close association between productive wells and the gross thickness of the Upper Ismay – Desert Creek interval, with the exception of oil production from Ute Mountain Tribal #2, which is located in the southwest corner of the project area. In general, the best producers of oil and gas lie in two areas, circled in white in Figure 4-117.

These three figures show that, while total mound thickness does often delineate between productive wells and dry holes, the extent of productivity within the mound is not obviously related to the gross mound thickness. This lack of a strong relation is shown more clearly in the crossplots of the Upper Ismay to Desert Creek thickness vs. IP and EUR (Figure 4-121). Together these maps show that it is generally necessary to be in thick mound sequences to get good wells, but that the thickness itself is not strongly correlated with productivity measures.

What is important to note in reviewing these maps is what attributes or isochrons relate to productivity within the algal mound complexes. It is clear that the various isochrons for the gross mound thickness, as well as the thicknesses of some of the target reservoirs within the mounds, correlate well with productive versus dry holes.

Perhaps one of the best correspondences is between productivity (IP & EUR) and the Upper Ismay amplitude and trough amplitude as imaged in the P-wave volume (Figure 4-92 and Figure 4-93). Thick amplitudes for these two attributes correspond to the wells with highest EUR in the main mound complex in the northern portion of the project area, and also the productive wells in the south mound complex (Ute Mountain Tribal #2 and #1). Another apparent correlation is between Waveform Class alternative #2 (Figure 4-107) and relative productivity. Class 3 (blue) generally corresponds to more productive wells and Class 1 (green). Water cuts tend to be higher in the south of the project area as well.

Consideration of these maps and the criteria for well selection suggested that the northern complex might be more attractive than the southern complex. Within the northern complex, the location needed to be within a region with reasonably high gross mound thickness. Additional positive factors included being within waveform class #3, and having highs in Upper Ismay amplitude anomalies. Based on these evaluations and distance from existing wells, the location for Marble Wash #9-2 was selected (Figure 4-120). This location was within the thickest area of the northern mound complex; was within waveform class #3; and was distant from previous wells and in an area of the mound complex with more undrilled mound volume than most locations. Some of the negative factors include being outside the main thick areas of internal units to the mounds, such as the the Lower Ismay amplitude (Figure 4-95) and the Upper Ismay amplitude (Figure 4-92). So while the overall mound may be thick, the reservoir facies may be thin.

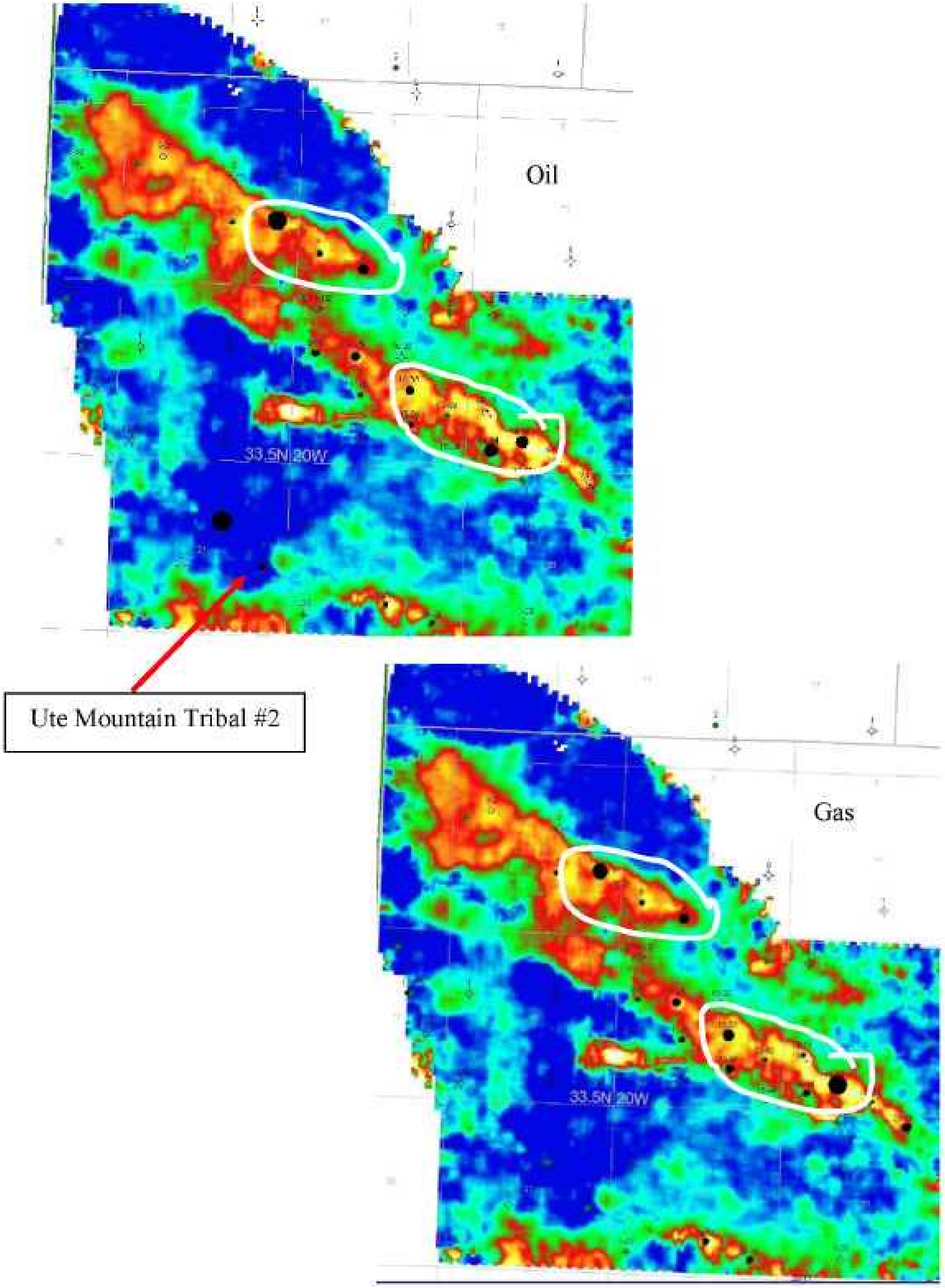

Figure 4-117. Initial production values for oil (top) and gas (bottom). Diameter of circles are proportional to IP rates. Contours are for Upper Ismay to Desert Creek thickness.

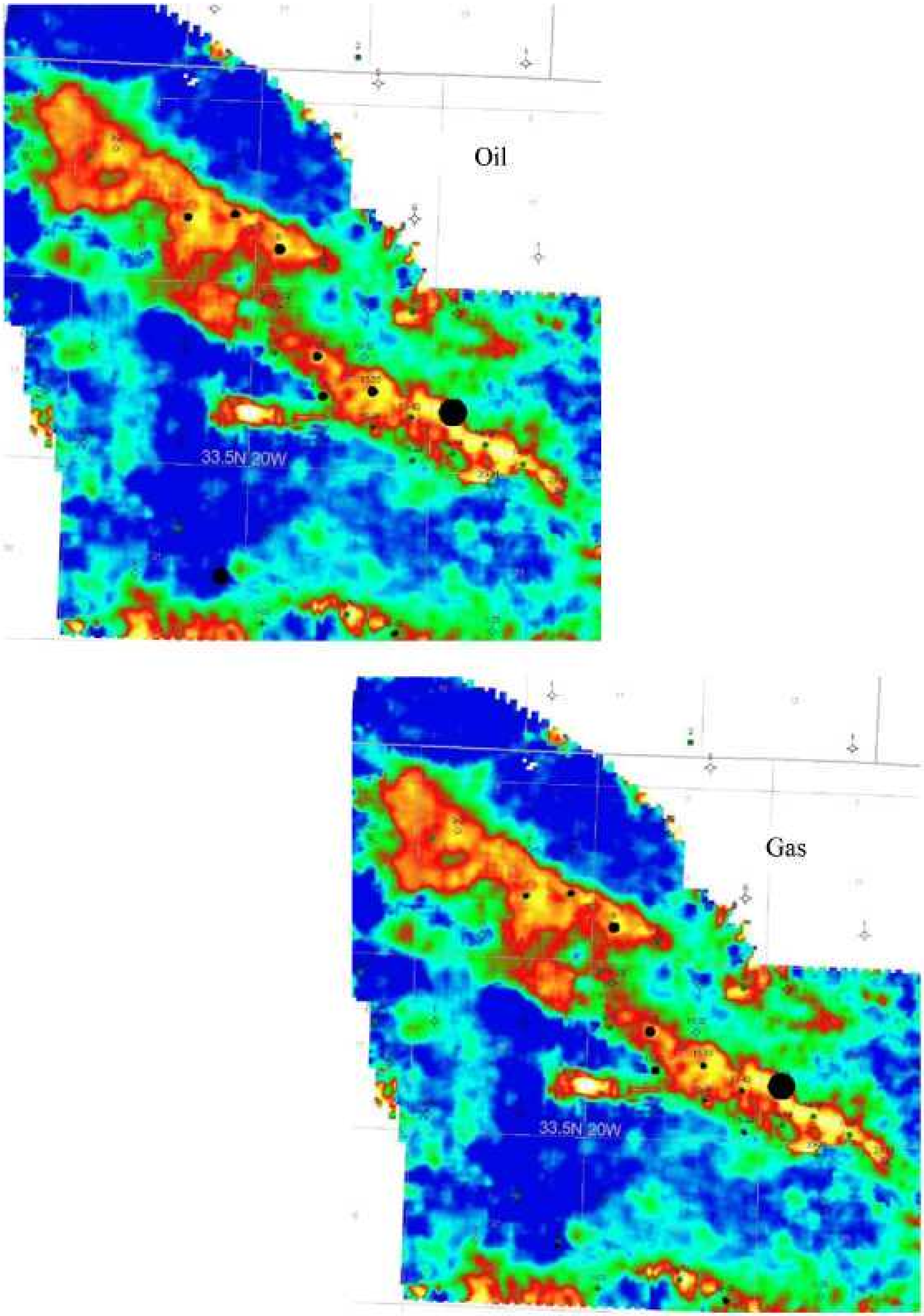

Figure 4-118. Cumulative production values for oil (top) and gas (bottom). Diameter of circles are proportional to production. Contours are for Upper Ismay to Desert Creek thickness.

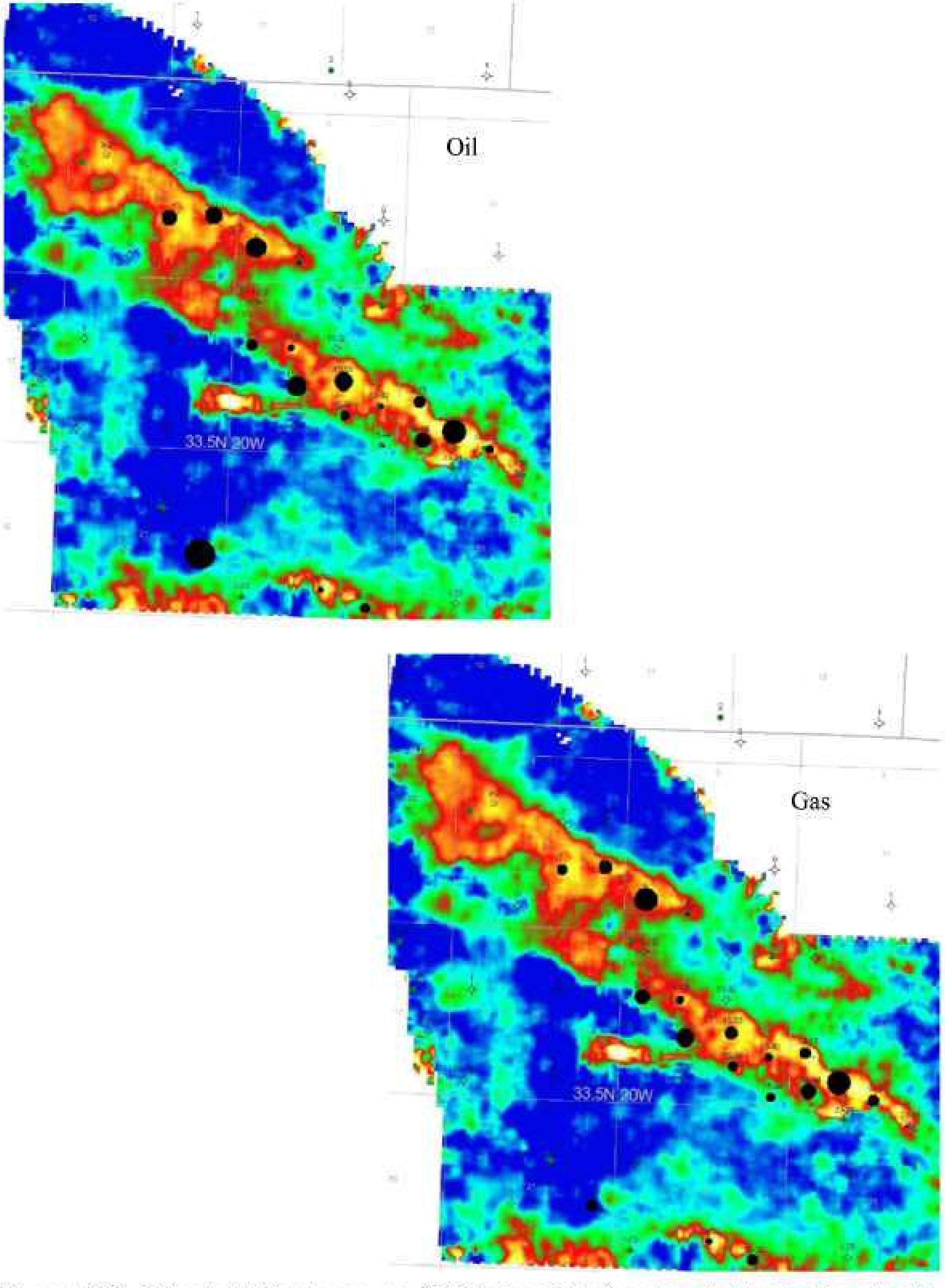

Figure 4-119. Estimated Ultimate recovery (EUR)s for oil (top) and gas (bottom). Diameter of circles are proportional to EUR. Contours are for Upper Ismay to Desert Creek thickness.

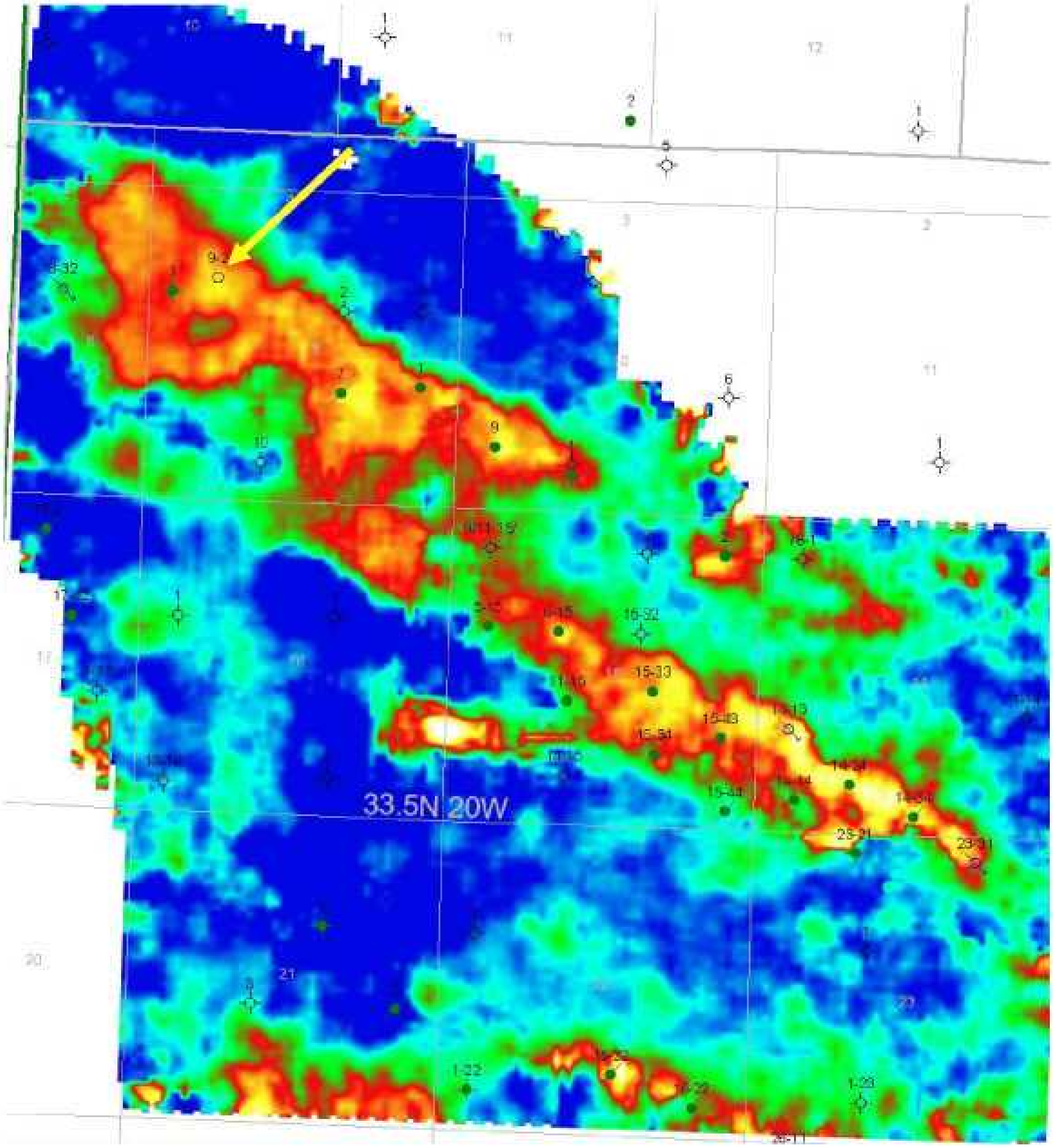

Figure 4-120. Upper Ismay to Desert Creek isochron thickness map and selected drilling location 9-2 (yellow arrow)

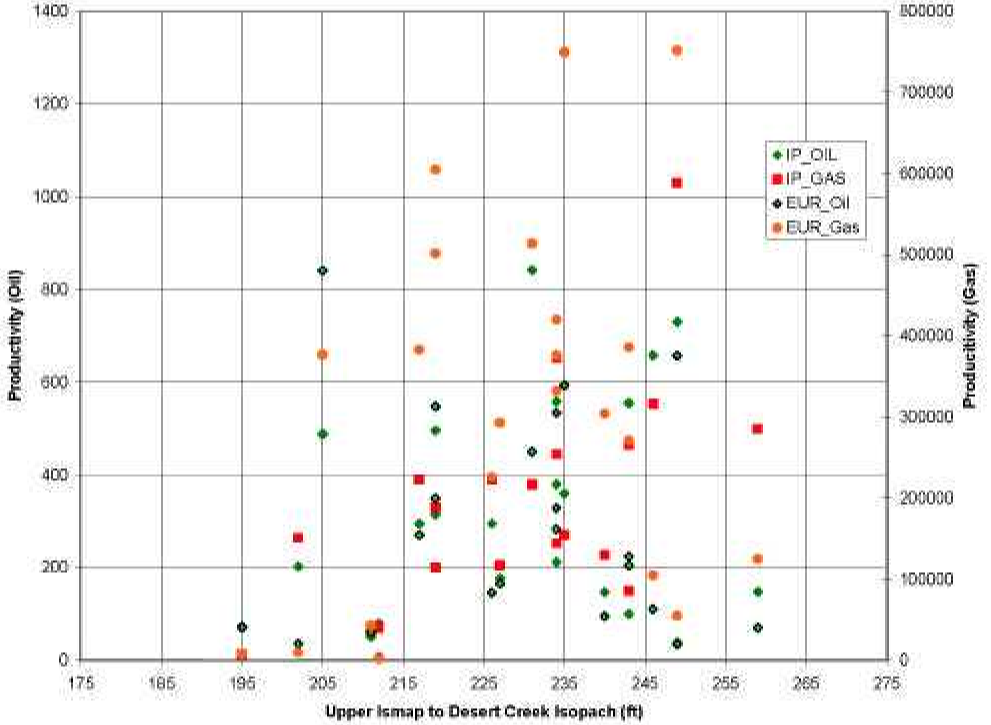

Figure 4-121. Graph showing relation between gross mound thickness, IP and EUR for oil and gas.

4.6.2 DRILLING RESULTS

The Marble Wash #9-2 was completed on January 7, 2006. Specifics concerning the well are shown in the scout ticket (Figure 4-122).

The Lower Ismay, which tends to have better reservoir quality has a higher risk of water than in the Upper Ismay. The Upper Ismay is typically less dolomitic and has lower porosity and permeability than the Lower Ismay, but generally has lower risk of water.

Water with traces of oil and gas were found in the Lower Ismay and portions of the Upper Ismay. The uppermost Upper Ismay zone tested approximately 100BOPD and 100 BWPD. The well probably was detrimentally impacted by a nearby injection well, as the pipe was stuck for approximately two weeks. There was oil in the Lower Ismay at this location, but the injection well appears to have swept the oil and pressured up the reservoir. The higher water cut in the Upper Ismay was not expected. It is possible that the overpressured Lower Ismay could have flushed much of the oil out of the Upper Ismay during the time the pipes were stuck.

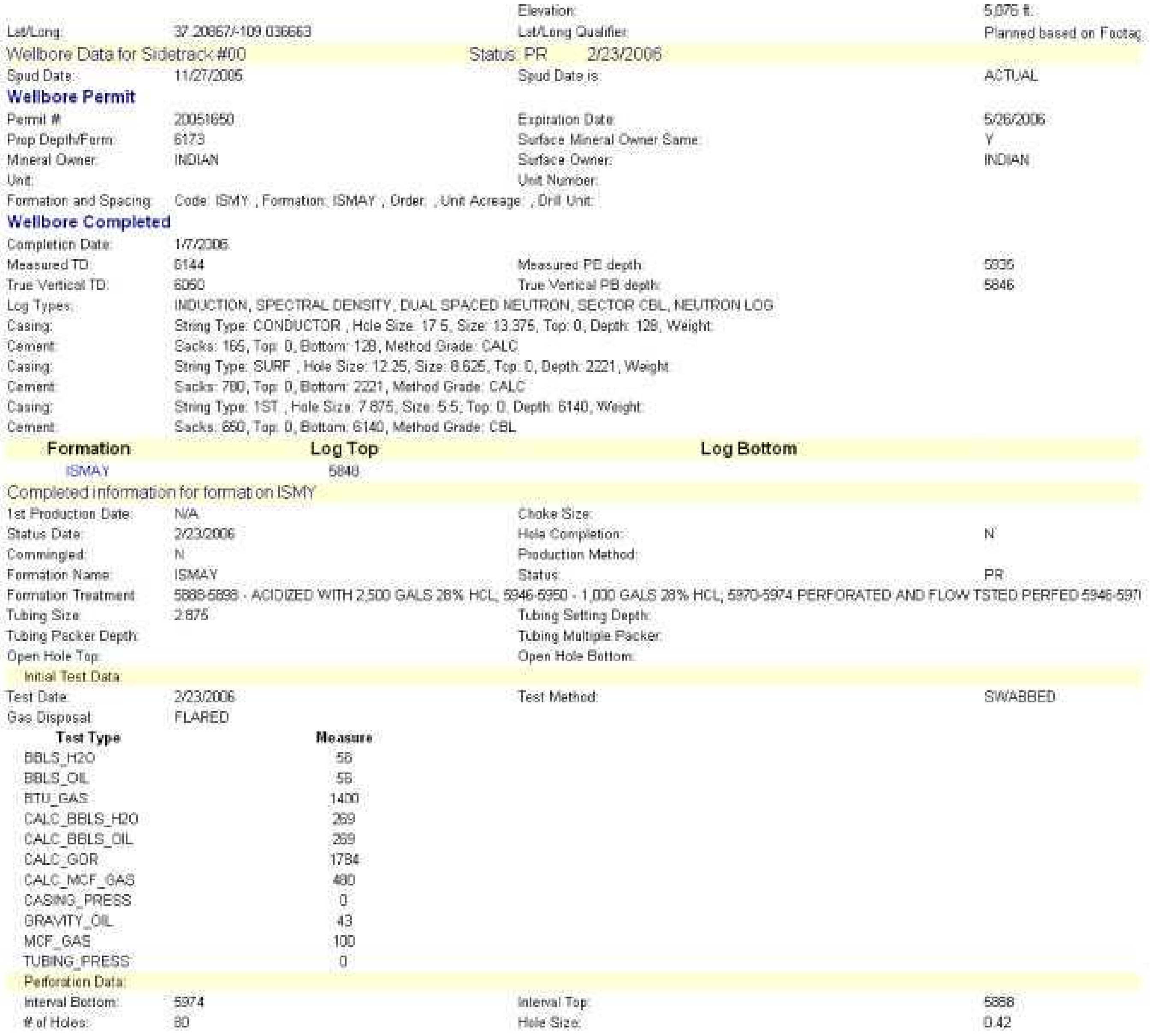

		Elevation:	5,076 ft.
Lat/Long:	37.20867/-109.036663	Lat/Long Qualifier:	Planned based on Footag

Wellbore Data for Sidetrack #00 Status: PR 2/23/2006

Spud Date:	11/27/2005	Spud Date is:	ACTUAL

Wellbore Permit

Permit #:	20051650	Expiration Date:	5/26/2006
Prop Depth/Form:	6173	Surface Mineral Owner Same:	Y
Mineral Owner:	INDIAN	Surface Owner:	INDIAN
Unit:		Unit Number:	

Formation and Spacing: Code: ISMY , Formation: ISMAY , Order: , Unit Acreage: , Drill Unit:

Wellbore Completed

Completion Date:	1/7/2006		
Measured TD:	6144	Measured PB depth:	5935
True Vertical TD:	6050	True Vertical PB depth:	5846

Log Types: INDUCTION, SPECTRAL DENSITY, DUAL SPACED NEUTRON, SECTOR CBL, NEUTRON LOG
Casing: String Type: CONDUCTOR , Hole Size: 17.5, Size: 13.375, Top: 0, Depth: 128, Weight:
Cement: Sacks: 165, Top: 0, Bottom: 128, Method Grade: CALC
Casing: String Type: SURF , Hole Size: 12.25, Size: 8.625, Top: 0, Depth: 2221, Weight:
Cement: Sacks: 780, Top: 0, Bottom: 2221, Method Grade: CALC
Casing: String Type: 1ST , Hole Size: 7.875, Size: 5.5, Top: 0, Depth: 6140, Weight:
Cement: Sacks: 650, Top: 0, Bottom: 6140, Method Grade: CBL

Formation	**Log Top**	**Log Bottom**
ISMAY	5848	

Completed information for formation ISMY

1st Production Date:	N/A	Choke Size:	
Status Date:	2/23/2006	Hole Completion:	N
Commingled:	N	Production Method:	
Formation Name:	ISMAY	Status:	PR

Formation Treatment: 5888-5898 - ACIDIZED WITH 2,500 GALS 28% HCL; 5946-5950 - 1,000 GALS 28% HCL; 5970-5974 PERFORATED AND FLOW TSTED PERFED 5946-597

Tubing Size:	2.875	Tubing Setting Depth:	
Tubing Packer Depth:		Tubing Multiple Packer:	
Open Hole Top:		Open Hole Bottom:	

Initial Test Data:

Test Date:	2/23/2006	Test Method:	SWABBED
Gas Disposal:	FLARED		

Test Type	**Measure**
BBLS_H2O	56
BBLS_OIL	56
BTU_GAS	1400
CALC_BBLS_H2O	269
CALC_BBLS_OIL	269
CALC_GOR	1784
CALC_MCF_GAS	480
CASING_PRESS	0
GRAVITY_OIL	43
MCF_GAS	100
TUBING_PRESS	0

Perforation Data:

Interval Bottom:	5974	Interval Top:	5888
# of Holes:	80	Hole Size:	0.42

Figure 4-122. Scout ticket for Marble Wash #9-2.

The numbers shown in Table 4-3 indicate that the P-wave seismic accurately predicted gross carbonate thickness. The depths listed below have been corrected for wellbore deviation. Figure 4-123 shows the gamma ray log obtained through the casing for the well.

Predicted Ismay – Gothic Shale isopach based on seismic isochron anomaly:	173’
Actual Ismay – Gothic isopach:	177’
Isopach range within 1 mile of well:	142’-201’
Predicted gross Ismay carbonate isopach based on seismic isochron anomaly:	157’
Actual gross Ismay carbonate thickness:	148’
Isopach range within 1 mile of well:	65’-171’

Table 4-3. Predicted vs. actual depths and thicknesses for Marble Wash #9-2.

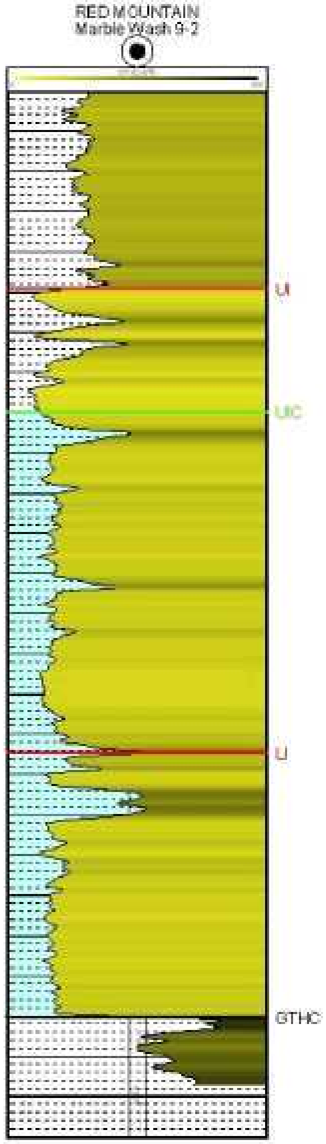

Figure 4-123. Cased hole gamma ray log for Marble Wash #9-2.

4.6.3 PRODUCTION RESULTS THROUGH JUNE 2007

The Marble Wash #9-2 well (Figure 4-124) was completed in April, 2006, and has been on production since that data. Production figures through August, 2007, are listed in Table 4-4. .

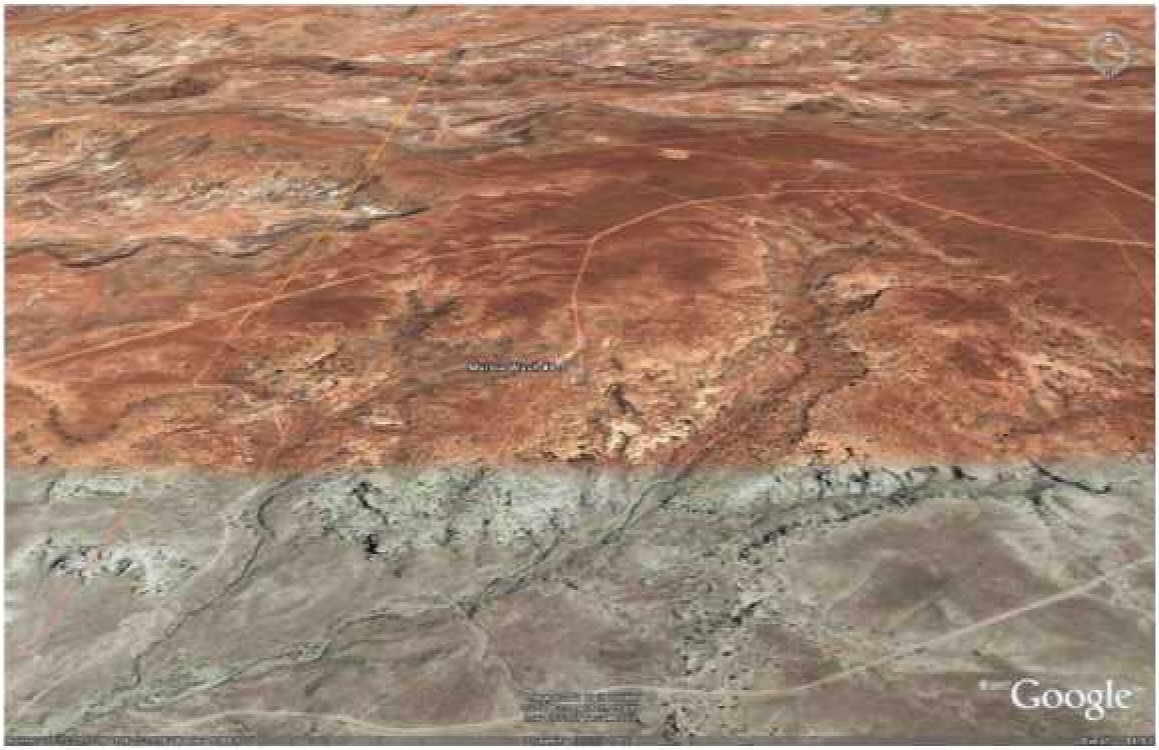

Figure 4-124. GoogleEarth™ image of the Marble Wash #9-2 and surrounding area. Marble Wash lies to the east (right) of the well location. Marble Wash #9-2 is in the center of the image.

As shown in Table 4-4 and Figure 4-125 through Figure 4-127, the cumulative oil production has passed 12,000 barrels and 32,000 mcf of gas. Water cuts have fluctuated between 30% - 40% in 2007, and there has been a slight increase in the GOR.

The Marble Wash #9-2 well lies near the 40th percentile of oil IP rates for historical wells in the producing area (Figure 4-128). When compared to the oil EUR for those same wells, those with the most similar IP rates have an estimated oil EUR of from 150,000 to 200,000 barrels (Figure 4-129).

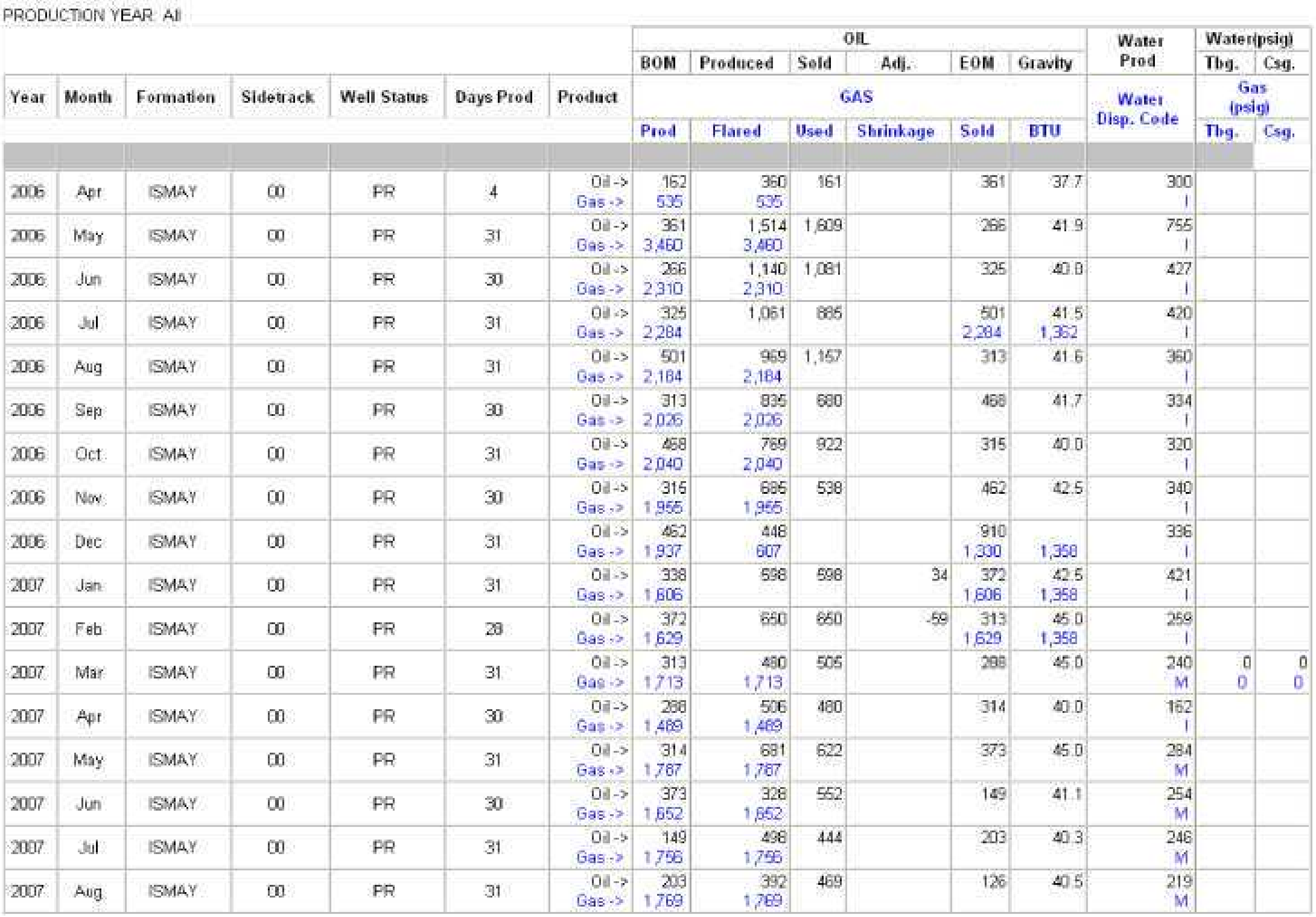

PRODUCTION YEAR: All

							OIL						Water Prod	Water(psig)	
							BOM	Produced	Sold	Adj.	EOM	Gravity		Tbg.	Csg.
Year	Month	Formation	Sidetrack	Well Status	Days Prod	Product	GAS						Water Disp. Code	Gas (psig)	
							Prod	Flared	Used	Shrinkage	Sold	BTU		Tbg.	Csg.
2006	Apr	ISMAY	00	PR	4	Oil -> Gas ->	162 535	360 535	161		361	37.7	300 I		
2006	May	ISMAY	00	PR	31	Oil -> Gas ->	361 3,460	1,514 3,460	1,609		266	41.9	755 I		
2006	Jun	ISMAY	00	PR	30	Oil -> Gas ->	266 2,310	1,140 2,310	1,081		325	40.0	427 I		
2006	Jul	ISMAY	00	PR	31	Oil -> Gas ->	325 2,284	1,061	885		501 2,284	41.5 1,362	420 I		
2006	Aug	ISMAY	00	PR	31	Oil -> Gas ->	501 2,184	969 2,184	1,157		313	41.6	360 I		
2006	Sep	ISMAY	00	PR	30	Oil -> Gas ->	313 2,026	835 2,026	680		468	41.7	334 I		
2006	Oct	ISMAY	00	PR	31	Oil -> Gas ->	468 2,040	769 2,040	922		315	40.0	320 I		
2006	Nov	ISMAY	00	PR	30	Oil -> Gas ->	315 1,955	685 1,955	538		462	42.5	340 I		
2006	Dec	ISMAY	00	PR	31	Oil -> Gas ->	462 1,937	448 607			910 1,330	 1,358	336 I		
2007	Jan	ISMAY	00	PR	31	Oil -> Gas ->	338 1,606	598	598	34	372 1,606	42.5 1,358	421 I		
2007	Feb	ISMAY	00	PR	28	Oil -> Gas ->	372 1,629	650	650	-59	313 1,629	45.0 1,358	259 I		
2007	Mar	ISMAY	00	PR	31	Oil -> Gas ->	313 1,713	480 1,713	505		288	45.0	240 M	0 0	0 0
2007	Apr	ISMAY	00	PR	30	Oil -> Gas ->	288 1,489	506 1,489	480		314	40.0	162 I		
2007	May	ISMAY	00	PR	31	Oil -> Gas ->	314 1,787	681 1,787	622		373	45.0	284 M		
2007	Jun	ISMAY	00	PR	30	Oil -> Gas ->	373 1,652	328 1,652	552		149	41.1	254 M		
2007	Jul	ISMAY	00	PR	31	Oil -> Gas ->	149 1,756	498 1,756	444		203	40.3	246 M		
2007	Aug	ISMAY	00	PR	31	Oil -> Gas ->	203 1,769	392 1,769	469		126	40.5	219 M		

Table 4-4. Marble Wash #9-2 production data through August 2007. Source: Colorado Oil & Gas Commission.

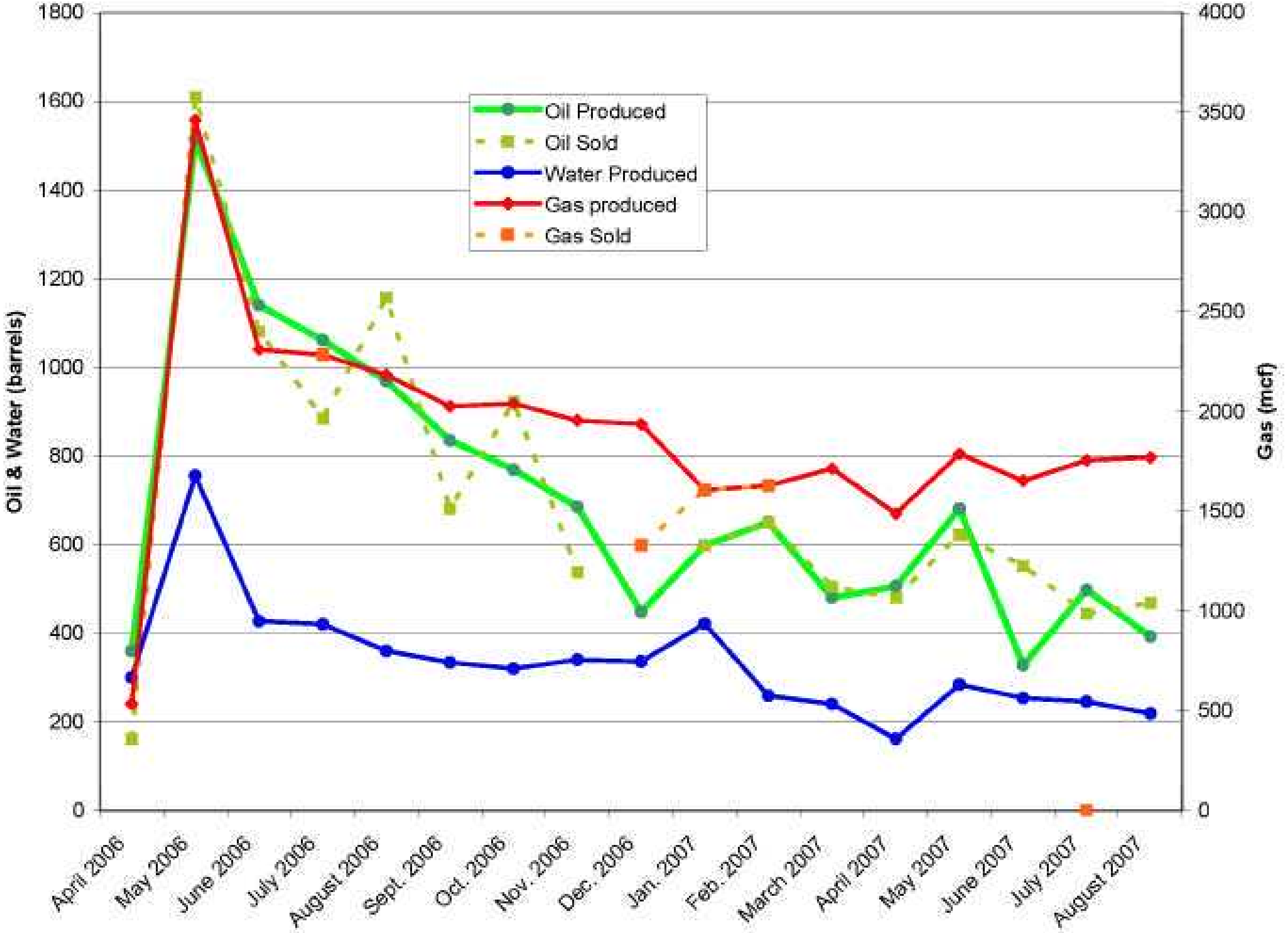

Figure 4-125. Production history of Marble Wash #9-2 through August 2007.

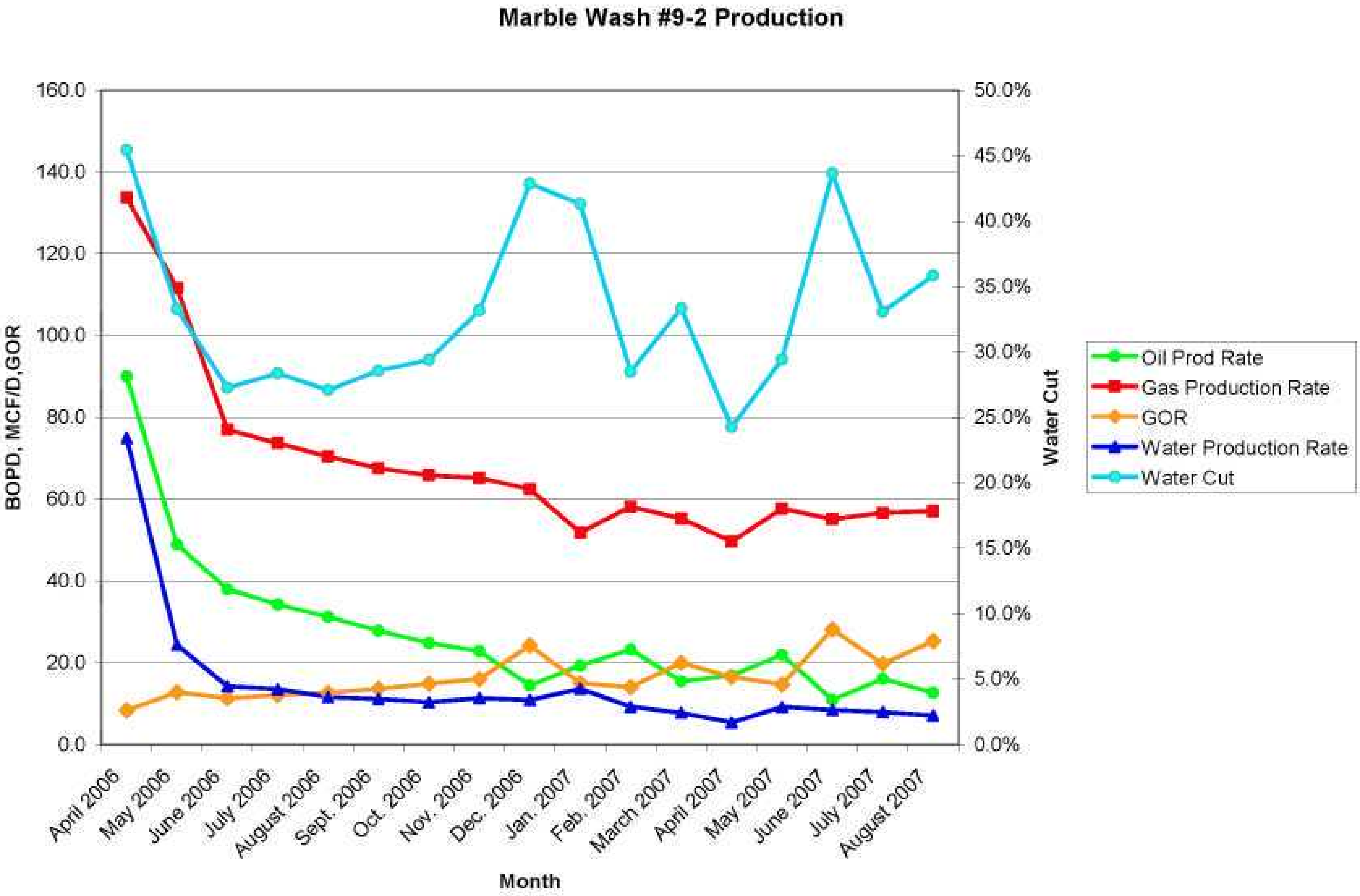

Figure 4-126. Production rates and water cut for Marble Wash #9-2 through August 2007.

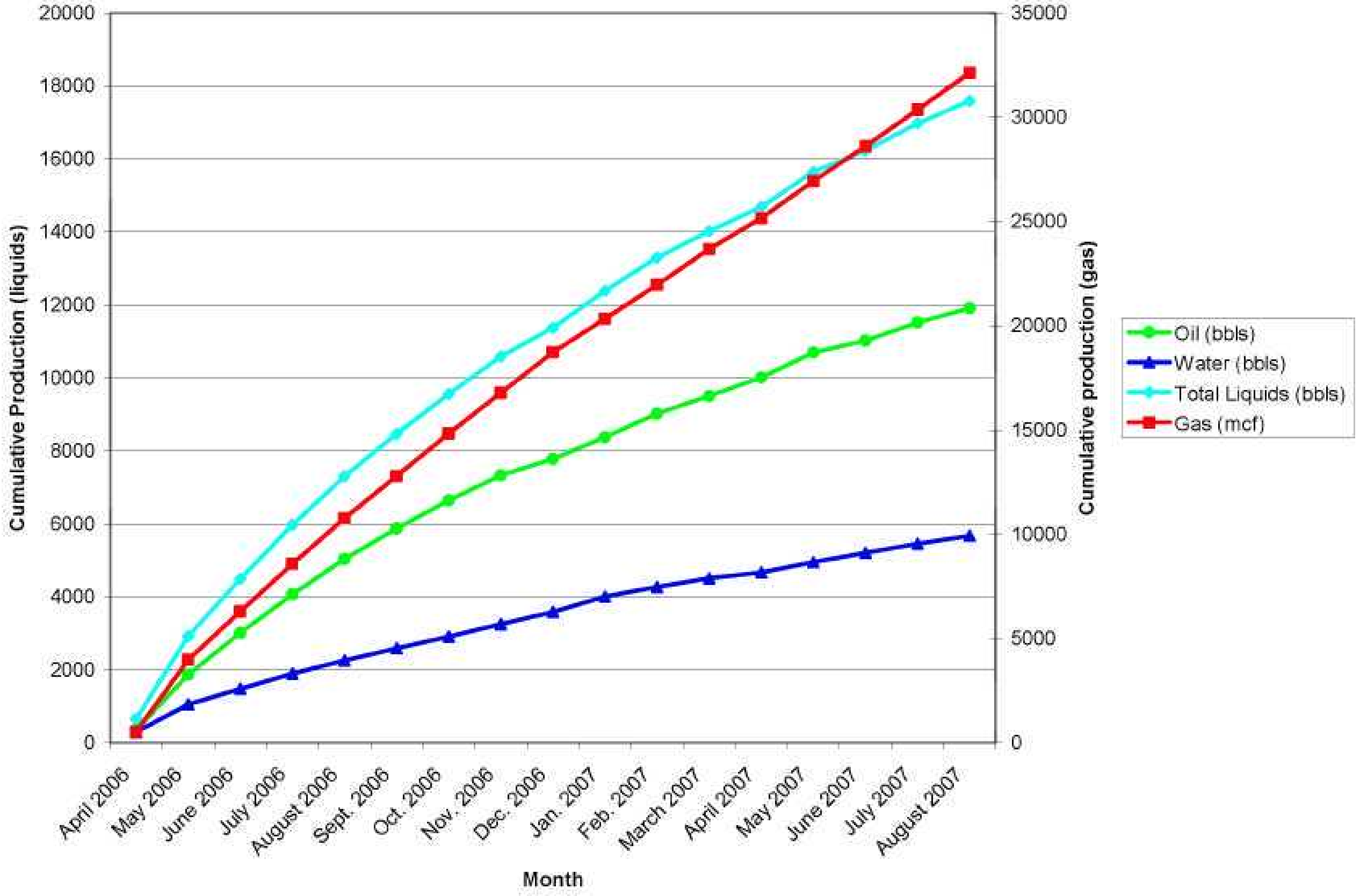

Figure 4-127. Cumulative production for Marble Wash #9-2 through June 2007.

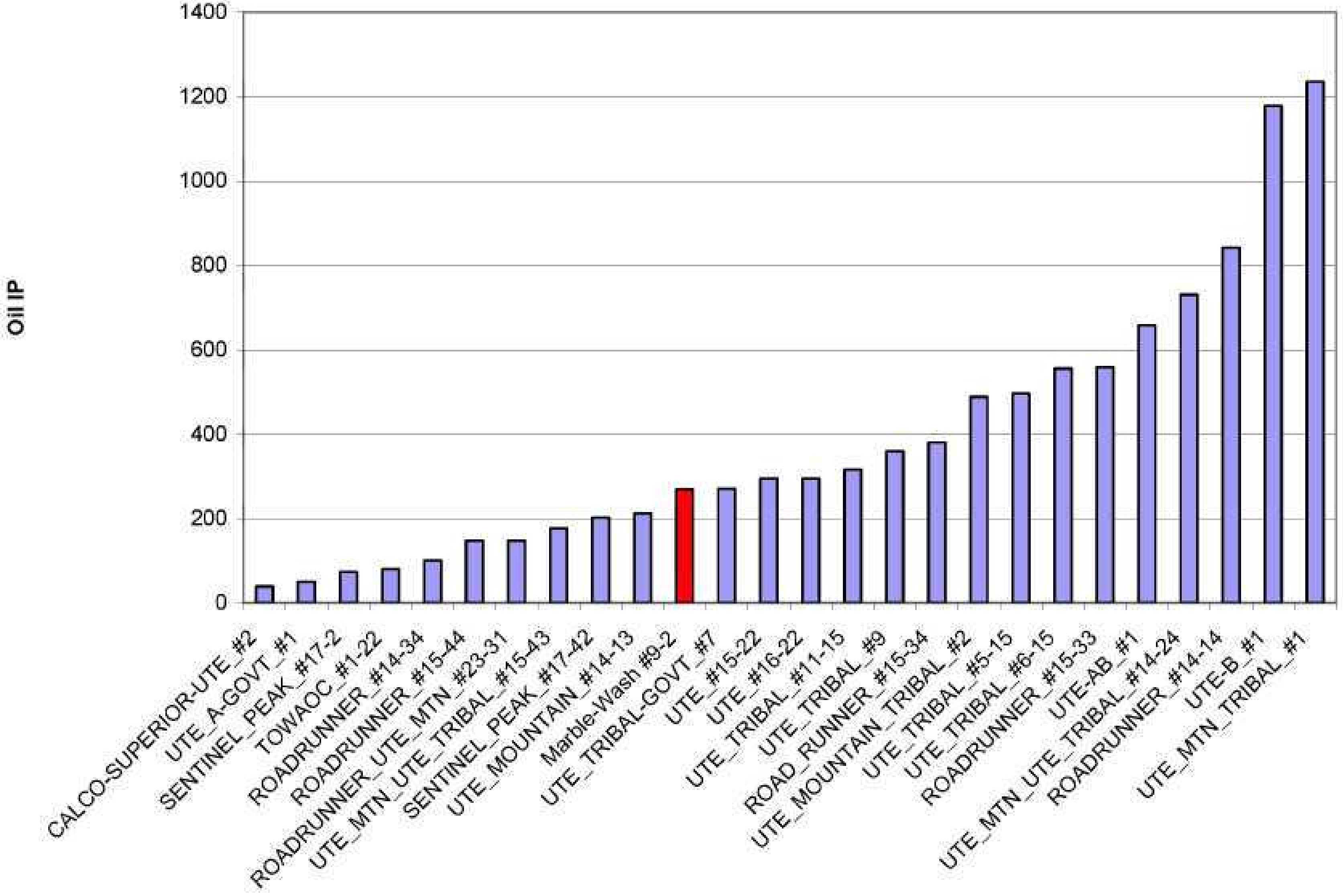

Figure 4-128. Comparison of oil IP rates for historical producing wells in the project area. Red bar corresponds to marble Wash #9-2.

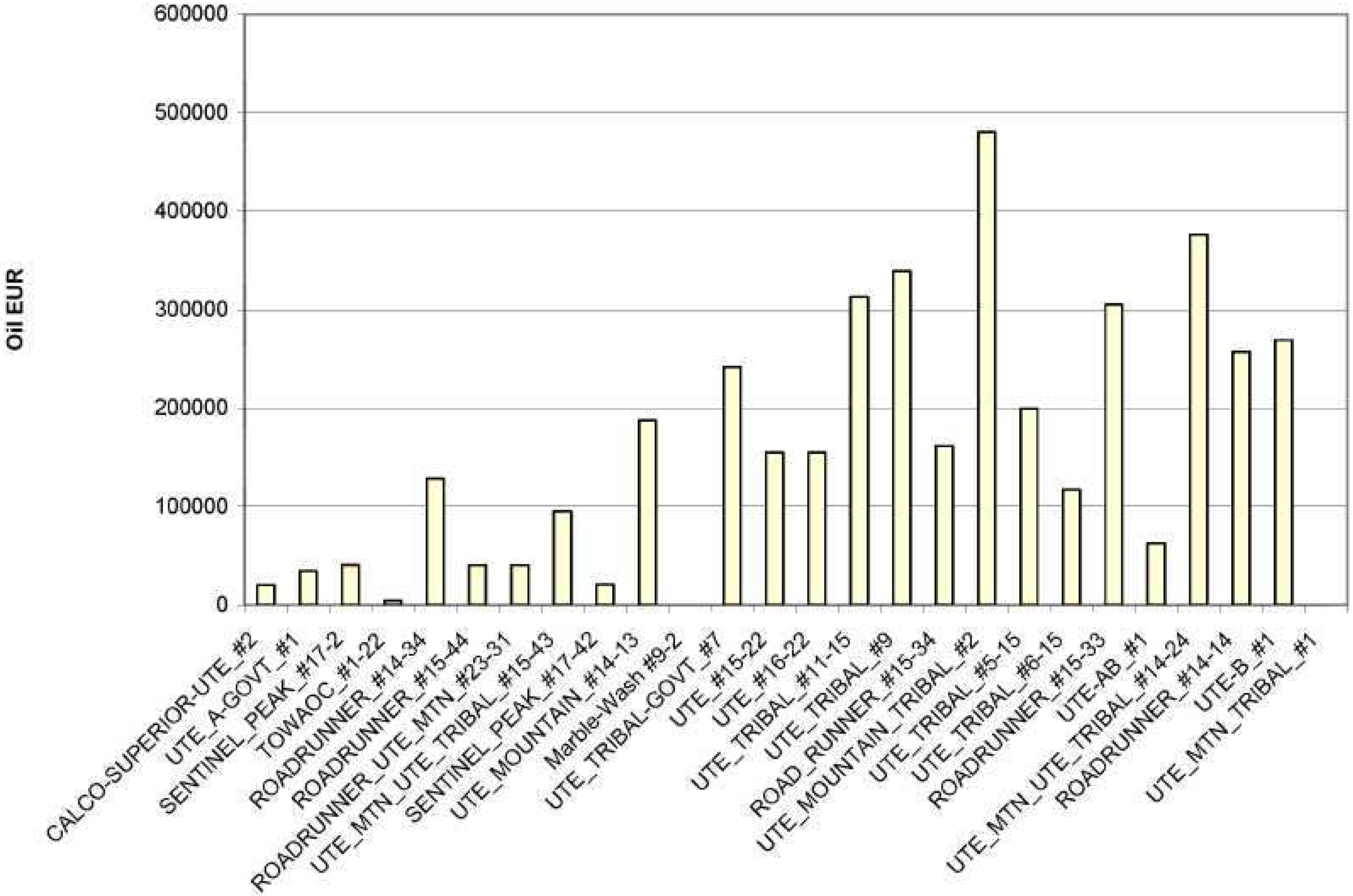

Figure 4-129. Comparison of Oil EUR for historical producing well in the project area (same order as in Figure 4-4). Wells with the nearest IP rates to the Marble Wash #9-2 had calculated EUR's for oil on the order of 150,000 to 200,000 barrels.

4.7 Development of Static Reservoir Model

4.7.1 MULTIVARIATE ANALYSES FOR RESERVOIR PROPERTY DETERMINATION IN THE ISMAY

The Spearman correlation coefficients are shown for the reservoir variables and the seismic variables in Tables 4-1 through 4-5. For each cell, three values are shown: the Spearman correlation coefficient; the associated probability or two-tailed significance; and the number of data points used to calculate the correlation coefficient and its significance. Correlation coefficients become more significant as the probability approaches 0.0. Correlation coefficients with significance values near 1.0 indicate no correlation. A probability of 0.05 or less is generally taken by statisticians to indicate a high probability of correlation (Gilbert, 1987). Values in bold have probabilities less than 0.05 and are evidence of correlation.

The regression analyses are voluminous, and the full data supporting the results may be found on the project web site at http://utemountain.golder.com.

An example of the output for the regression analyses is shown in Figure 4-130. These data pertain to the Upper Ismay U1 interval only. The figure is divided into three portions: an upper portion that shows the statistical significance of the final regression model; a middle portion that shows the significance and collinearity of the independent variables used to predict the dependent variable, in this example, gross thickness; and a bottom portion that displays the true value of the dependent variable that is to be predicted on the horizontal axis vs. the value predicted by the regression.

For a regression to be acceptable, the probability of the F-statistic must be below 0.05. In the example shown, the value is 0.002, which indicates a highly significant regression.

The middle portion of the figure indicates the importance and significance of the independent variables. The probability, given in column 6, shows the significance. Coefficients for the seismic parameters are considered to be statistically significant if the probability value is less than 0.05. All of the coefficients for seismic variables in this example are below 0.05, and are thus statistically significant.

The importance of each coefficient and its relation to the dependent variable are shown in column 4. These normalized coefficients have a sign and a magnitude. The larger the magnitude, the more important the seismic variable is for predicting the reservoir variable. The sign indicates whether the impact is positive or negative. For example, the isopach between the Top of the Ismay and the Desert Creek is 0.495. This means that (1) the thickness of this interval positively correlates with the gross thickness of the U1 interval, and that (2) the correlation is not 100% by any means, but is one of the contributing factors, since there are other variables that are also important.

		Gross_Interval	Net_Pay_Int_TVD	Avg_Phi_Pay	Avg_Net_Sw_Pay	Avg_VclayPay	PayGross_Ratio	HPVH_Pay	PHIH_Pay	Net_Res_Int_TVD	Avg_Phi_Res	Avg_Vclay_Res	ResGross_Res	PHIH_Res
PARAK_Amp	Correlation Coefficient	0.590	0.016	0.006	-0.006	0.027	0.006	0.006	0.006	0.100	0.084	0.112	0.091	0.091
	Sig. (2-tailed)	0.000	0.933	0.977	0.977	0.890	0.977	0.977	0.977	0.607	0.665	0.562	0.639	0.639
	N	29	29	29	29	29	29	29	29	29	29	29	29	29
PCUTL_Amp	Correlation Coefficient	-0.239	-0.114	-0.104	0.104	-0.123	-0.104	-0.104	-0.104	-0.276	-0.263	-0.286	-0.271	-0.271
	Sig. (2-tailed)	0.212	0.556	0.590	0.590	0.524	0.590	0.590	0.590	0.142	0.168	0.132	0.155	0.155
	N	29	29	29	29	29	29	29	29	29	29	29	29	29
PLI_Amp	Correlation Coefficient	0.193	-0.130	-0.127	0.127	-0.133	-0.127	-0.127	-0.127	-0.032	-0.032	-0.046	-0.029	-0.029
	Sig. (2-tailed)	0.315	0.501	0.512	0.512	0.490	0.512	0.512	0.512	0.868	0.868	0.812	0.880	0.880
	N	29	29	29	29	29	29	29	29	29	29	29	29	29
PLI_RMS_Amp	Correlation Coefficient	-0.236	0.179	0.178	-0.178	0.179	0.178	0.178	0.178	0.071	0.076	0.082	0.071	0.071
	Sig. (2-tailed)	0.218	0.353	0.355	0.355	0.352	0.355	0.355	0.355	0.713	0.697	0.672	0.715	0.715
	N	29	29	29	29	29	29	29	29	29	29	29	29	29
PLI_WaveformClass	Correlation Coefficient	-0.183	-0.115	-0.113	0.113	-0.116	-0.113	-0.113	-0.113	-0.289	-0.282	-0.282	-0.287	-0.287
	Sig. (2-tailed)	0.341	0.553	0.559	0.559	0.547	0.559	0.559	0.559	0.128	0.138	0.138	0.131	0.131
	N	29	29	29	29	29	29	29	29	29	29	29	29	29
PUDC_amp	Correlation Coefficient	0.004	-0.293	-0.296	0.296	-0.289	-0.296	-0.296	-0.296	-0.394	-0.397	-0.386	-0.397	-0.397
	Sig. (2-tailed)	0.983	0.123	0.119	0.119	0.128	0.119	0.119	0.119	0.034	0.033	0.039	0.033	0.033
	N	29	29	29	29	29	29	29	29	29	29	29	29	29
CAKAH_Amp	Correlation Coefficient	0.369	0.164	0.154	-0.154	0.174	0.154	0.154	0.154	0.160	0.148	0.180	0.152	0.152
	Sig. (2-tailed)	0.049	0.396	0.427	0.427	0.367	0.427	0.427	0.427	0.406	0.440	0.350	0.431	0.431
	N	29	29	29	29	29	29	29	29	29	29	29	29	29
CGTHC_Amp	Correlation Coefficient	-0.194	0.171	0.173	-0.173	0.169	0.173	0.173	0.173	0.036	0.044	0.044	0.038	0.038
	Sig. (2-tailed)	0.313	0.374	0.369	0.369	0.380	0.369	0.369	0.369	0.853	0.820	0.820	0.846	0.846
	N	29	29	29	29	29	29	29	29	29	29	29	29	29
CLI_Amp	Correlation Coefficient	-0.228	0.033	0.044	-0.044	0.021	0.044	0.044	0.044	0.127	0.139	0.103	0.137	0.137
	Sig. (2-tailed)	0.233	0.867	0.822	0.822	0.913	0.822	0.822	0.822	0.510	0.473	0.594	0.479	0.479
	N	29	29	29	29	29	29	29	29	29	29	29	29	29
CUI_Amp	Correlation Coefficient	0.084	-0.049	-0.058	0.058	-0.039	-0.058	-0.058	-0.058	-0.010	-0.024	0.002	-0.018	-0.018
	Sig. (2-tailed)	0.666	0.801	0.764	0.764	0.840	0.764	0.764	0.764	0.958	0.902	0.990	0.925	0.925
	N	29	29	29	29	29	29	29	29	29	29	29	29	29
CVpVs_GTHCIoUI	Correlation Coefficient	0.469	0.171	0.168	-0.168	0.174	0.168	0.168	0.168	0.239	0.234	0.242	0.236	0.236
	Sig. (2-tailed)	0.010	0.374	0.383	0.383	0.366	0.383	0.383	0.383	0.212	0.221	0.205	0.217	0.217
	N	29	29	29	29	29	29	29	29	29	29	29	29	29
SUBoUIC_RMS_Amplitude	Correlation Coefficient	0.067	-0.222	-0.218	0.218	-0.226	-0.218	-0.218	-0.218	-0.142	-0.141	-0.157	-0.138	-0.138
	Sig. (2-tailed)	0.730	0.247	0.257	0.257	0.238	0.257	0.257	0.257	0.464	0.467	0.415	0.475	0.475
	N	29	29	29	29	29	29	29	29	29	29	29	29	29
SUIC_RMS_Amplitude	Correlation Coefficient	0.131	-0.239	-0.235	0.235	-0.242	-0.235	-0.235	-0.235	-0.104	-0.105	-0.122	-0.101	-0.101
	Sig. (2-tailed)	0.499	0.213	0.220	0.220	0.206	0.220	0.220	0.220	0.592	0.587	0.527	0.604	0.604
	N	29	29	29	29	29	29	29	29	29	29	29	29	29
sVpVs_AKAHtoUI	Correlation Coefficient	-0.049	-0.156	-0.150	0.150	-0.163	-0.150	-0.150	-0.150	-0.198	-0.190	-0.209	-0.193	-0.193
	Sig. (2-tailed)	0.801	0.418	0.439	0.439	0.399	0.439	0.439	0.439	0.302	0.322	0.277	0.316	0.316
	N	29	29	29	29	29	29	29	29	29	29	29	29	29
Top_Ismay_West	Correlation Coefficient	0.620	0.000	-0.011	0.011	0.011	-0.011	-0.011	-0.011	0.058	0.042	0.073	0.048	0.048
	Sig. (2-tailed)	0.000	1.000	0.954	0.954	0.954	0.954	0.954	0.954	0.765	0.828	0.708	0.803	0.803
	N	29	29	29	29	29	29	29	29	29	29	29	29	29
UIC_West	Correlation Coefficient	0.687	0.049	0.038	-0.038	0.059	0.038	0.038	0.038	0.213	0.194	0.220	0.204	0.204
	Sig. (2-tailed)	0.000	0.802	0.844	0.844	0.759	0.844	0.844	0.844	0.268	0.312	0.251	0.290	0.290
	N	29	29	29	29	29	29	29	29	29	29	29	29	29
LI_West	Correlation Coefficient	0.637	0.033	0.020	-0.020	0.045	0.020	0.020	0.020	0.156	0.137	0.169	0.146	0.146
	Sig. (2-tailed)	0.000	0.867	0.917	0.917	0.817	0.917	0.917	0.917	0.419	0.478	0.381	0.450	0.450
	N	29	29	29	29	29	29	29	29	29	29	29	29	29
DC_West	Correlation Coefficient	0.551	0.016	0.004	-0.004	0.028	0.004	0.004	0.004	0.158	0.136	0.168	0.148	0.148
	Sig. (2-tailed)	0.002	0.933	0.982	0.982	0.885	0.982	0.982	0.982	0.414	0.474	0.383	0.445	0.445
	N	29	29	29	29	29	29	29	29	29	29	29	29	29
UIC_Echo	Correlation Coefficient	0.496	-0.033	-0.039	0.039	-0.026	-0.039	-0.039	-0.039	0.089	0.077	0.092	0.084	0.084
	Sig. (2-tailed)	0.006	0.867	0.840	0.840	0.894	0.840	0.840	0.840	0.644	0.692	0.634	0.665	0.665
	N	29	29	29	29	29	29	29	29	29	29	29	29	29
LI_Echo	Correlation Coefficient	0.550	0.016	0.009	-0.009	0.025	0.009	0.009	0.009	0.186	0.171	0.190	0.179	0.179
	Sig. (2-tailed)	0.002	0.933	0.963	0.963	0.899	0.963	0.963	0.963	0.333	0.376	0.325	0.352	0.352
	N	29	29	29	29	29	29	29	29	29	29	29	29	29
TopIsmay_UIC	Correlation Coefficient	-0.114	-0.260	-0.263	0.263	-0.257	-0.263	-0.263	-0.263	-0.397	-0.398	-0.386	-0.399	-0.399
	Sig. (2-tailed)	0.554	0.173	0.167	0.167	0.179	0.167	0.167	0.167	0.033	0.032	0.039	0.032	0.032
	N	29	29	29	29	29	29	29	29	29	29	29	29	29
TopIsmay_DC	Correlation Coefficient	0.620	-0.081	-0.089	0.089	-0.074	-0.089	-0.089	-0.089	0.036	0.022	0.039	0.030	0.030
	Sig. (2-tailed)	0.000	0.675	0.648	0.648	0.703	0.648	0.648	0.648	0.853	0.908	0.840	0.878	0.878
	N	29	29	29	29	29	29	29	29	29	29	29	29	29
LI_DC	Correlation Coefficient	0.434	0.146	0.139	-0.139	0.154	0.139	0.139	0.139	0.117	0.110	0.134	0.111	0.111
	Sig. (2-tailed)	0.019	0.449	0.472	0.472	0.426	0.472	0.472	0.472	0.544	0.569	0.489	0.565	0.565
	N	29	29	29	29	29	29	29	29	29	29	29	29	29

Table 4-5. Spearman correlation coefficients among the reservoir and seismic variables for Upper Ismay interval.

		Gross_Interval	Net_Pay_Int_TVD	Avg_Phi_Pay	Avg_Net_Sw_Pay	Avg_VClayPay	PayGross_Ratio	HPVH_Pay	PHIH_Pay	Net_Res_Int_TVD	Avg_Phi_Res	Avg_VClay_Res	ResGross_Res	PHIH_Res
PAHAK_Amp	Correlation Coefficient	-0.365	-0.047	-0.013	0.130	-0.051	0.031	-0.071	-0.050	-0.190	0.045	-0.176	0.041	-0.137
	Sig. (2-tailed)	0.051	0.809	0.947	0.503	0.676	0.873	0.716	0.796	0.322	0.817	0.361	0.836	0.479
	N	29	29	29	29	29	29	29	29	29	29	29	29	29
PCUTL_Amp	Correlation Coefficient	-0.390	-0.393	-0.152	0.431	-0.560	-0.357	-0.398	-0.395	-0.172	-0.049	-0.074	-0.005	-0.185
	Sig. (2-tailed)	0.037	0.035	0.431	0.020	0.002	0.057	0.032	0.034	0.371	0.799	0.699	0.969	0.337
	N	29	29	29	29	29	29	29	29	29	29	29	29	29
PLI_Amp	Correlation Coefficient	0.053	0.227	0.148	-0.165	0.400	0.259	0.185	0.211	0.116	-0.128	0.154	0.018	0.075
	Sig. (2-tailed)	0.784	0.236	0.444	0.394	0.031	0.176	0.335	0.272	0.549	0.508	0.426	0.926	0.699
	N	29	29	29	29	29	29	28	29	29	29	29	29	29
PLI_RMS_Amp	Correlation Coefficient	0.111	-0.199	-0.131	0.046	-0.382	-0.271	-0.169	-0.201	-0.127	0.083	-0.244	-0.162	-0.102
	Sig. (2-tailed)	0.566	0.301	0.499	0.813	0.041	0.155	0.393	0.296	0.511	0.670	0.197	0.402	0.598
	N	29	29	29	29	29	29	29	29	29	29	29	29	29
PLI_WaveformClass	Correlation Coefficient	-0.029	-0.093	-0.159	0.074	-0.085	-0.143	-0.098	-0.112	-0.137	-0.218	0.140	-0.108	-0.153
	Sig. (2-tailed)	0.881	0.632	0.409	0.702	0.660	0.459	0.611	0.563	0.480	0.256	0.469	0.578	0.429
	N	29	29	29	29	29	29	28	29	29	29	29	29	29
PLIDC_amp	Correlation Coefficient	-0.309	-0.174	-0.117	0.236	-0.139	-0.139	-0.192	-0.179	-0.419	-0.060	-0.025	-0.284	-0.367
	Sig. (2-tailed)	0.102	0.366	0.547	0.218	0.471	0.476	0.319	0.361	0.024	0.758	0.896	0.135	0.050
	N	29	29	29	29	29	29	29	29	29	29	29	29	29
CAKAH_Amp	Correlation Coefficient	0.027	0.120	0.051	-0.115	0.251	0.114	0.051	0.066	-0.136	-0.253	-0.122	-0.258	-0.148
	Sig. (2-tailed)	0.891	0.534	0.791	0.551	0.189	0.556	0.792	0.734	0.483	0.185	0.529	0.177	0.444
	N	29	29	29	29	29	29	29	29	29	29	29	29	29
CGTHC_Amp	Correlation Coefficient	-0.257	-0.456	-0.234	0.370	-0.341	-0.450	-0.416	-0.439	-0.103	0.048	-0.001	0.041	-0.110
	Sig. (2-tailed)	0.179	0.013	0.222	0.048	0.070	0.014	0.025	0.018	0.594	0.803	0.996	0.834	0.570
	N	29	29	29	29	29	29	29	29	29	29	29	29	29
CLI_Amp	Correlation Coefficient	0.554	0.593	0.362	-0.676	0.405	0.524	0.606	0.574	0.214	-0.080	-0.026	0.122	0.180
	Sig. (2-tailed)	0.002	0.001	0.054	0.000	0.029	0.004	0.000	0.001	0.265	0.680	0.895	0.530	0.350
	N	29	29	29	29	29	29	29	29	29	29	29	29	29
CUI_Amp	Correlation Coefficient	-0.027	-0.189	-0.407	0.229	0.013	-0.181	-0.237	-0.219	-0.079	-0.103	0.150	-0.175	-0.094
	Sig. (2-tailed)	0.889	0.327	0.028	0.232	0.949	0.347	0.215	0.254	0.684	0.594	0.437	0.364	0.627
	N	29	29	29	29	29	29	28	29	29	29	29	29	29
CVpVs_GTHCtoLI	Correlation Coefficient	0.097	0.331	0.523	-0.375	0.387	0.379	0.313	0.334	0.006	0.237	-0.159	-0.107	0.032
	Sig. (2-tailed)	0.617	0.080	0.003	0.045	0.038	0.043	0.098	0.077	0.975	0.216	0.410	0.579	0.870
	N	29	29	29	29	29	29	29	29	29	29	29	29	29
SUltoUIC_RMS_Amplitude	Correlation Coefficient	0.106	0.489	0.591	-0.446	0.343	0.529	0.505	0.521	0.286	0.289	0.018	0.301	0.295
	Sig. (2-tailed)	0.584	0.007	0.001	0.015	0.068	0.003	0.006	0.004	0.130	0.128	0.924	0.113	0.120
	N	29	29	29	29	29	29	28	29	29	29	29	29	29
SUIC_RMS_Amplitude	Correlation Coefficient	0.154	0.629	0.571	-0.441	0.409	0.690	0.633	0.654	0.366	0.270	0.150	0.487	0.387
	Sig. (2-tailed)	0.425	0.000	0.001	0.017	0.028	0.000	0.000	0.000	0.051	0.156	0.439	0.007	0.038
	N	29	29	29	29	29	29	29	29	29	29	29	29	29
sVpVs_AKAHtoUI	Correlation Coefficient	-0.117	0.296	0.503	-0.241	0.204	0.342	0.344	0.351	0.049	0.255	0.095	0.208	0.073
	Sig. (2-tailed)	0.546	0.120	0.005	0.208	0.289	0.070	0.068	0.062	0.802	0.181	0.625	0.279	0.706
	N	29	29	29	29	29	29	29	29	29	29	29	29	29
Top_Ismay_West	Correlation Coefficient	0.138	0.365	0.359	-0.284	0.447	0.421	0.312	0.341	0.001	0.224	-0.088	-0.105	0.049
	Sig. (2-tailed)	0.476	0.052	0.056	0.135	0.015	0.023	0.099	0.070	0.996	0.243	0.650	0.589	0.800
	N	29	29	29	29	29	29	29	29	29	29	29	29	29
UIC_West	Correlation Coefficient	0.233	0.428	0.368	-0.357	0.494	0.473	0.378	0.403	0.106	0.210	-0.103	-0.031	0.137
	Sig. (2-tailed)	0.225	0.020	0.049	0.057	0.006	0.010	0.044	0.030	0.583	0.273	0.596	0.875	0.477
	N	29	29	29	29	29	29	29	29	29	29	29	29	29
LI_West	Correlation Coefficient	0.211	0.375	0.318	-0.341	0.475	0.418	0.327	0.351	0.046	0.221	-0.124	-0.112	0.079
	Sig. (2-tailed)	0.271	0.048	0.092	0.070	0.009	0.024	0.083	0.062	0.811	0.260	0.523	0.562	0.683
	N	29	29	29	29	29	29	29	29	29	29	29	29	29
DC_West	Correlation Coefficient	0.329	0.493	0.334	-0.404	0.509	0.532	0.450	0.472	0.154	0.250	-0.010	-0.018	0.202
	Sig. (2-tailed)	0.081	0.007	0.076	0.030	0.005	0.003	0.014	0.010	0.426	0.191	0.958	0.924	0.293
	N	29	29	29	29	29	29	29	29	29	29	29	29	29
UIC_Echo	Correlation Coefficient	0.242	0.430	0.370	-0.362	0.515	0.442	0.390	0.404	0.017	0.178	-0.118	-0.140	0.057
	Sig. (2-tailed)	0.205	0.020	0.048	0.054	0.004	0.016	0.042	0.030	0.929	0.355	0.542	0.470	0.768
	N	29	29	29	29	29	29	28	29	29	29	29	29	29
LI_Echo	Correlation Coefficient	0.295	0.467	0.349	-0.373	0.470	0.495	0.419	0.444	0.100	0.236	-0.116	-0.084	0.142
	Sig. (2-tailed)	0.116	0.011	0.064	0.046	0.010	0.006	0.024	0.016	0.606	0.218	0.551	0.667	0.461
	N	29	29	29	29	29	29	29	29	29	29	29	29	29
TopIsmay_UIC	Correlation Coefficient	-0.274	-0.216	-0.119	0.213	-0.140	-0.185	-0.202	-0.197	-0.402	0.012	0.060	-0.285	-0.341
	Sig. (2-tailed)	0.151	0.261	0.540	0.268	0.470	0.338	0.293	0.307	0.031	0.952	0.758	0.134	0.070
	N	29	29	29	29	29	29	28	29	29	29	29	29	29
TopIsmay_DC	Correlation Coefficient	-0.018	0.263	0.221	-0.148	0.340	0.308	0.188	0.219	-0.138	-0.032	-0.216	-0.133	-0.120
	Sig. (2-tailed)	0.926	0.168	0.248	0.445	0.071	0.104	0.338	0.254	0.474	0.870	0.260	0.493	0.535
	N	29	29	29	29	29	29	29	29	29	29	29	29	29
LI_DC	Correlation Coefficient	-0.021	0.183	0.170	-0.122	0.337	0.185	0.127	0.144	0.083	-0.019	-0.170	-0.016	0.048
	Sig. (2-tailed)	0.914	0.343	0.378	0.527	0.074	0.338	0.512	0.455	0.667	0.922	0.379	0.933	0.804
	N	29	29	29	29	29	29	29	29	29	29	29	29	29

Table 4-6. Spearman correlation coefficients among the reservoir and seismic variables for Upper Ismay L1 interval.

		Gross_Interval	Net_Pay_Int_TVD	Avg_Phi_Pay	Avg_Net_Sw_Pay	Avg_VClay/Pay	Pay/Gross_Ratio	HPVH_Pay	PHIH_Pay	Net_Res_Int_TVD	Avg_Phi_Res	Avg_VClay_Res	Res/Gross_Ratio	PHIH_Res
PAHAK_Amp	Correlation Coefficient	0.291	0.095	0.128	-0.184	-0.019	0.072	0.082	0.085	-0.024	-0.140	-0.245	-0.113	-0.036
	Sig (2-tailed)	0.156	0.664	0.524	0.359	0.927	0.723	0.682	0.658	0.905	0.478	0.213	0.574	0.860
	N	27	27	27	27	27	27	27	27	27	27	27	27	27
PCUTL_Amp	Correlation Coefficient	-0.210	-0.394	-0.401	0.469	-0.136	-0.397	-0.397	-0.378	-0.120	-0.136	0.046	-0.103	-0.110
	Sig (2-tailed)	0.293	0.046	0.038	0.014	0.498	0.040	0.040	0.053	0.549	0.501	0.821	0.609	0.584
	N	27	27	27	27	27	27	27	27	27	27	27	27	27
PUI_Amp	Correlation Coefficient	0.501	0.318	0.308	-0.203	0.125	0.310	0.309	0.309	0.610	0.658	0.244	0.582	0.622
	Sig (2-tailed)	0.008	0.106	0.117	0.310	0.535	0.116	0.118	0.117	0.001	0.000	0.221	0.001	0.001
	N	27	27	27	27	27	27	27	27	27	27	27	27	27
PUI_RMS_Amp	Correlation Coefficient	-0.366	-0.185	-0.212	0.077	-0.133	-0.170	-0.166	-0.172	-0.489	-0.497	-0.184	-0.463	-0.500
	Sig (2-tailed)	0.060	0.356	0.288	0.702	0.510	0.398	0.408	0.391	0.010	0.008	0.358	0.014	0.008
	N	27	27	27	27	27	27	27	27	27	27	27	27	27
PUI_WaveformClass	Correlation Coefficient	-0.105	-0.352	-0.430	0.426	-0.338	-0.368	-0.361	-0.358	-0.044	-0.022	0.036	-0.040	-0.070
	Sig (2-tailed)	0.603	0.072	0.026	0.027	0.084	0.058	0.064	0.067	0.827	0.913	0.857	0.843	0.729
	N	27	27	27	27	27	27	27	27	27	27	27	27	27
PUDC_amp	Correlation Coefficient	0.036	-0.050	-0.134	0.051	0.148	-0.061	-0.064	-0.063	-0.284	-0.462	-0.196	-0.414	-0.306
	Sig (2-tailed)	0.860	0.805	0.507	0.799	0.462	0.762	0.752	0.755	0.152	0.015	0.328	0.032	0.122
	N	27	27	27	27	27	27	27	27	27	27	27	27	27
CAKAH_Amp	Correlation Coefficient	0.560	0.282	0.246	-0.296	-0.012	0.275	0.275	0.276	0.315	0.312	0.015	0.204	0.317
	Sig (2-tailed)	0.002	0.154	0.216	0.134	0.954	0.165	0.165	0.164	0.109	0.113	0.941	0.309	0.107
	N	27	27	27	27	27	27	27	27	27	27	27	27	27
CGTHC_Amp	Correlation Coefficient	-0.371	-0.284	-0.244	0.255	-0.154	-0.278	-0.276	-0.273	-0.260	-0.295	-0.035	-0.210	-0.258
	Sig (2-tailed)	0.057	0.152	0.220	0.200	0.442	0.160	0.160	0.168	0.190	0.135	0.864	0.293	0.193
	N	27	27	27	27	27	27	27	27	27	27	27	27	27
CLI_Amp	Correlation Coefficient	0.053	0.329	0.337	-0.286	0.337	0.338	0.332	0.324	0.240	0.210	-0.087	0.347	0.247
	Sig (2-tailed)	0.793	0.094	0.085	0.148	0.086	0.084	0.091	0.099	0.228	0.294	0.665	0.077	0.215
	N	27	27	27	27	27	27	27	27	27	27	27	27	27
CUI_Amp	Correlation Coefficient	0.098	0.098	0.104	-0.085	-0.067	0.085	0.095	0.083	0.045	0.014	-0.028	-0.017	0.017
	Sig (2-tailed)	0.623	0.627	0.605	0.673	0.738	0.675	0.637	0.680	0.823	0.946	0.889	0.934	0.932
	N	27	27	27	27	27	27	27	27	27	27	27	27	27
CVpVs_GTHCtoUI	Correlation Coefficient	0.594	0.546	0.546	-0.515	0.311	0.557	0.541	0.555	0.395	0.310	0.087	0.325	0.417
	Sig (2-tailed)	0.001	0.003	0.003	0.006	0.114	0.003	0.004	0.003	0.041	0.115	0.665	0.095	0.031
	N	27	27	27	27	27	27	27	27	27	27	27	27	27
SUItoUIC_RMS_Amplitude	Correlation Coefficient	0.161	0.167	0.159	-0.145	0.271	0.178	0.166	0.184	0.288	0.317	0.234	0.314	0.317
	Sig (2-tailed)	0.422	0.406	0.427	0.471	0.171	0.375	0.408	0.357	0.146	0.107	0.240	0.111	0.107
	N	27	27	27	27	27	27	27	27	27	27	27	27	27
SUIC_RMS_Amplitude	Correlation Coefficient	0.257	0.154	0.197	-0.200	0.205	0.148	0.161	0.168	0.184	0.171	0.147	0.172	0.202
	Sig (2-tailed)	0.196	0.442	0.324	0.318	0.305	0.462	0.423	0.403	0.357	0.393	0.464	0.392	0.313
	N	27	27	27	27	27	27	27	27	27	27	27	27	27
sVpVs_AKAHtoUI	Correlation Coefficient	0.023	0.163	0.109	-0.117	0.298	0.156	0.153	0.159	0.083	-0.024	0.218	0.102	0.087
	Sig (2-tailed)	0.910	0.417	0.588	0.561	0.131	0.438	0.447	0.428	0.682	0.907	0.278	0.614	0.664
	N	27	27	27	27	27	27	27	27	27	27	27	27	27
Top_Ismay_West	Correlation Coefficient	0.719	0.524	0.516	-0.591	0.272	0.512	0.515	0.515	0.295	0.126	-0.015	0.143	0.287
	Sig (2-tailed)	0.000	0.005	0.006	0.001	0.170	0.006	0.006	0.006	0.134	0.531	0.939	0.476	0.146
	N	27	27	27	27	27	27	27	27	27	27	27	27	27
UIC_West	Correlation Coefficient	0.728	0.602	0.638	-0.646	0.168	0.592	0.606	0.606	0.419	0.319	-0.042	0.312	0.417
	Sig (2-tailed)	0.000	0.001	0.000	0.000	0.400	0.001	0.001	0.001	0.029	0.105	0.835	0.113	0.030
	N	27	27	27	27	27	27	27	27	27	27	27	27	27
LI_West	Correlation Coefficient	0.678	0.665	0.691	-0.720	0.240	0.652	0.666	0.669	0.391	0.259	-0.039	0.285	0.384
	Sig (2-tailed)	0.000	0.000	0.000	0.000	0.228	0.000	0.000	0.000	0.044	0.192	0.849	0.150	0.048
	N	27	27	27	27	27	27	27	27	27	27	27	27	27
DC_West	Correlation Coefficient	0.556	0.492	0.528	-0.599	0.295	0.487	0.492	0.469	0.185	0.074	-0.026	0.099	0.176
	Sig (2-tailed)	0.003	0.009	0.005	0.001	0.135	0.010	0.009	0.011	0.354	0.715	0.896	0.627	0.379
	N	27	27	27	27	27	27	27	27	27	27	27	27	27
UIC_Echo	Correlation Coefficient	0.697	0.561	0.522	-0.577	0.263	0.558	0.563	0.555	0.395	0.256	-0.044	0.238	0.380
	Sig (2-tailed)	0.000	0.002	0.006	0.002	0.186	0.002	0.002	0.003	0.041	0.197	0.828	0.233	0.060
	N	27	27	27	27	27	27	27	27	27	27	27	27	27
LI_Echo	Correlation Coefficient	0.558	0.530	0.584	-0.604	0.336	0.528	0.530	0.528	0.234	0.137	-0.032	0.140	0.232
	Sig (2-tailed)	0.002	0.005	0.002	0.001	0.086	0.005	0.004	0.005	0.232	0.497	0.876	0.485	0.244
	N	27	27	27	27	27	27	27	27	27	27	27	27	27
TopIsmay_UIC	Correlation Coefficient	-0.120	-0.076	-0.165	0.066	0.240	-0.078	-0.092	-0.095	-0.354	-0.543	-0.124	-0.449	-0.378
	Sig (2-tailed)	0.551	0.707	0.411	0.744	0.228	0.699	0.645	0.637	0.070	0.003	0.622	0.018	0.052
	N	27	27	27	27	27	27	27	27	27	27	27	27	27
TopIsmay_DC	Correlation Coefficient	0.789	0.569	0.566	-0.558	0.126	0.549	0.570	0.575	0.414	0.283	-0.204	0.247	0.413
	Sig (2-tailed)	0.000	0.002	0.002	0.002	0.532	0.003	0.002	0.002	0.032	0.152	0.306	0.213	0.032
	N	27	27	27	27	27	27	27	27	27	27	27	27	27
LI_DC	Correlation Coefficient	0.646	0.392	0.386	-0.307	-0.154	0.363	0.396	0.406	0.618	0.578	-0.045	0.523	0.622
	Sig (2-tailed)	0.000	0.043	0.047	0.119	0.444	0.063	0.041	0.035	0.001	0.002	0.822	0.005	0.001
	N	27	27	27	27	27	27	27	27	27	27	27	27	27

Table 4-7. Spearman correlation coefficients among the reservoir and seismic variables for Upper Ismay L2 interval.

		Gross_Interval	Net_Pay_Int_TVD	Avg_Phi_Pay	Avg_Net_Sw_Pay	Avg_VClayPay	PayGross_Ratio	HPVH_Pay	PHIH_Pay	Net_Res_Int_TVD	Avg_Phi_Res	Avg_VClay_Res	ResGross_Res	PHIH_Res
PAHAK_Amp	Correlation Coefficient	0.398	-0.108	-0.115	0.007	-0.402	-0.136	-0.090	-0.072	-0.158	-0.143	-0.417	-0.213	-0.177
	Sig. (2-tailed)	0.040	0.591	0.568	0.971	0.038	0.499	0.655	0.719	0.429	0.475	0.030	0.284	0.377
	N	27	27	27	27	27	27	27	27	27	27	27	27	27
PCUTL_Amp	Correlation Coefficient	-0.412	-0.629	-0.423	0.715	-0.280	-0.598	-0.639	-0.628	-0.516	-0.386	-0.294	-0.407	-0.462
	Sig. (2-tailed)	0.033	0.000	0.028	0.000	0.157	0.001	0.000	0.000	0.006	0.047	0.136	0.035	0.015
	N	27	27	27	27	27	27	27	27	27	27	27	27	27
PLI_Amp	Correlation Coefficient	0.214	0.085	0.003	-0.148	-0.022	0.051	0.044	0.046	0.003	-0.062	0.069	-0.043	-0.019
	Sig. (2-tailed)	0.283	0.673	0.990	0.462	0.913	0.801	0.827	0.821	0.987	0.758	0.732	0.830	0.926
	N	27	27	27	27	27	27	27	27	27	27	27	27	27
PLI_RMS_Amp	Correlation Coefficient	-0.239	-0.035	0.083	0.088	0.075	-0.010	0.005	0.000	0.059	0.150	0.006	0.105	0.094
	Sig. (2-tailed)	0.229	0.863	0.682	0.663	0.711	0.962	0.979	1.000	0.771	0.455	0.976	0.604	0.638
	N	27	27	27	27	27	27	27	27	27	27	27	27	27
PLI_WaveformClass	Correlation Coefficient	-0.119	-0.055	0.011	0.387	-0.095	-0.088	-0.083	-0.074	-0.039	0.014	0.020	-0.062	-0.026
	Sig. (2-tailed)	0.553	0.785	0.955	0.046	0.637	0.664	0.681	0.714	0.845	0.947	0.920	0.760	0.899
	N	27	27	27	27	27	27	27	27	27	27	27	27	27
PUDC_amp	Correlation Coefficient	-0.012	-0.472	-0.368	0.414	-0.329	-0.451	-0.474	-0.464	-0.433	-0.358	-0.443	-0.369	-0.409
	Sig. (2-tailed)	0.954	0.013	0.059	0.032	0.094	0.018	0.013	0.015	0.024	0.067	0.021	0.058	0.034
	N	27	27	27	27	27	27	27	27	27	27	27	27	27
CAKAH_Amp	Correlation Coefficient	0.315	-0.078	-0.281	-0.054	-0.195	-0.109	-0.105	-0.100	-0.264	-0.354	-0.141	-0.347	-0.309
	Sig. (2-tailed)	0.109	0.699	0.156	0.788	0.330	0.588	0.602	0.620	0.183	0.070	0.484	0.076	0.117
	N	27	27	27	27	27	27	27	27	27	27	27	27	27
CGTHC_Amp	Correlation Coefficient	-0.256	-0.028	0.063	0.177	0.164	0.018	-0.024	-0.029	0.101	0.138	0.083	0.200	0.119
	Sig. (2-tailed)	0.197	0.890	0.755	0.378	0.414	0.931	0.906	0.885	0.615	0.493	0.683	0.318	0.555
	N	27	27	27	27	27	27	27	27	27	27	27	27	27
CLI_Amp	Correlation Coefficient	-0.079	-0.093	-0.208	-0.158	0.349	-0.119	-0.102	-0.106	-0.210	-0.242	0.424	-0.327	-0.246
	Sig. (2-tailed)	0.696	0.646	0.298	0.433	0.075	0.554	0.612	0.600	0.294	0.224	0.027	0.096	0.215
	N	27	27	27	27	27	27	27	27	27	27	27	27	27
CUI_Amp	Correlation Coefficient	0.179	0.337	0.217	-0.211	0.054	0.364	0.321	0.322	0.345	0.267	0.025	0.347	0.307
	Sig. (2-tailed)	0.372	0.086	0.277	0.291	0.789	0.062	0.103	0.101	0.078	0.178	0.900	0.076	0.120
	N	27	27	27	27	27	27	27	27	27	27	27	27	27
CVpVs_GTHCtoUI	Correlation Coefficient	0.256	-0.055	-0.225	-0.256	-0.004	-0.073	-0.076	-0.078	-0.214	-0.274	0.003	-0.282	-0.251
	Sig. (2-tailed)	0.198	0.787	0.259	0.198	0.982	0.719	0.705	0.699	0.284	0.167	0.988	0.154	0.207
	N	27	27	27	27	27	27	27	27	27	27	27	27	27
SUItoUIC_RMS_Amplitude	Correlation Coefficient	0.187	-0.049	0.014	-0.219	-0.013	-0.094	-0.029	-0.028	-0.048	-0.022	0.102	-0.125	-0.034
	Sig. (2-tailed)	0.349	0.809	0.946	0.272	0.950	0.641	0.888	0.890	0.811	0.915	0.613	0.533	0.867
	N	27	27	27	27	27	27	27	27	27	27	27	27	27
SUIC_RMS_Amplitude	Correlation Coefficient	0.164	-0.116	-0.085	-0.228	-0.031	-0.164	-0.075	-0.074	-0.202	-0.125	0.040	-0.305	-0.199
	Sig. (2-tailed)	0.415	0.563	0.672	0.252	0.879	0.413	0.709	0.715	0.313	0.534	0.844	0.122	0.321
	N	27	27	27	27	27	27	27	27	27	27	27	27	27
sVpVs_AKAHtoUI	Correlation Coefficient	-0.161	-0.225	-0.094	0.001	-0.119	-0.266	-0.205	-0.202	-0.279	-0.147	-0.059	-0.324	-0.240
	Sig. (2-tailed)	0.423	0.258	0.641	0.995	0.553	0.180	0.306	0.312	0.159	0.465	0.770	0.099	0.228
	N	27	27	27	27	27	27	27	27	27	27	27	27	27
Top_Ismay_West	Correlation Coefficient	0.438	-0.040	-0.176	-0.332	-0.138	-0.063	-0.039	-0.032	-0.194	-0.193	-0.159	-0.261	-0.232
	Sig. (2-tailed)	0.022	0.843	0.381	0.091	0.493	0.755	0.848	0.874	0.333	0.334	0.428	0.189	0.244
	N	27	27	27	27	27	27	27	27	27	27	27	27	27
UIC_West	Correlation Coefficient	0.421	0.221	0.007	-0.506	-0.014	0.191	0.215	0.219	0.029	-0.021	-0.001	-0.073	-0.030
	Sig. (2-tailed)	0.029	0.268	0.971	0.007	0.946	0.341	0.280	0.271	0.886	0.919	0.996	0.718	0.882
	N	27	27	27	27	27	27	27	27	27	27	27	27	27
LI_West	Correlation Coefficient	0.391	0.234	0.048	-0.566	-0.005	0.207	0.233	0.238	0.049	0.032	-0.002	-0.048	-0.001
	Sig. (2-tailed)	0.044	0.239	0.814	0.002	0.981	0.299	0.242	0.230	0.809	0.873	0.993	0.814	0.996
	N	27	27	27	27	27	27	27	27	27	27	27	27	27
DC_West	Correlation Coefficient	0.389	0.116	-0.041	-0.517	-0.014	0.095	0.135	0.138	-0.028	-0.048	-0.024	-0.115	-0.072
	Sig. (2-tailed)	0.045	0.565	0.840	0.006	0.943	0.637	0.502	0.494	0.888	0.812	0.904	0.570	0.722
	N	27	27	27	27	27	27	27	27	27	27	27	27	27
UIC_Echo	Correlation Coefficient	0.512	0.153	-0.031	-0.350	-0.009	0.125	0.136	0.144	0.010	-0.061	-0.033	-0.066	-0.044
	Sig. (2-tailed)	0.006	0.445	0.877	0.073	0.963	0.535	0.498	0.473	0.961	0.762	0.871	0.744	0.828
	N	27	27	27	27	27	27	27	27	27	27	27	27	27
LI_Echo	Correlation Coefficient	0.496	0.117	-0.054	-0.475	-0.024	0.094	0.126	0.131	-0.018	-0.069	-0.048	-0.103	-0.064
	Sig. (2-tailed)	0.009	0.562	0.788	0.012	0.905	0.642	0.531	0.515	0.931	0.733	0.812	0.610	0.751
	N	27	27	27	27	27	27	27	27	27	27	27	27	27
TopIsmay_UIC	Correlation Coefficient	-0.085	-0.432	-0.316	0.367	-0.223	-0.401	-0.430	-0.423	-0.368	-0.294	-0.350	-0.290	-0.339
	Sig. (2-tailed)	0.673	0.025	0.108	0.059	0.263	0.038	0.025	0.028	0.059	0.137	0.073	0.142	0.084
	N	27	27	27	27	27	27	27	27	27	27	27	27	27
TopIsmay_DC	Correlation Coefficient	0.394	-0.079	-0.242	-0.161	-0.241	-0.110	-0.101	-0.090	-0.250	-0.294	-0.259	-0.324	-0.300
	Sig. (2-tailed)	0.042	0.697	0.224	0.422	0.227	0.583	0.616	0.656	0.209	0.136	0.193	0.099	0.128
	N	27	27	27	27	27	27	27	27	27	27	27	27	27
LI_DC	Correlation Coefficient	0.309	0.302	0.109	-0.200	0.053	0.272	0.260	0.271	0.118	0.061	0.100	0.040	0.068
	Sig. (2-tailed)	0.116	0.125	0.588	0.318	0.793	0.170	0.190	0.171	0.556	0.761	0.619	0.842	0.734
	N	27	27	27	27	27	27	27	27	27	27	27	27	27

Table 4-8. Spearman correlation coefficients among the reservoir and seismic variables for Lowers Ismay L1 interval.

		Gross_Interval	Net_Pay_ft_TVD	Avg_Phi_Pay	Avg_Net_Sw_Pay	Avg_VClayPay	PayGross_Ratio	HPVH_Pay	PHIH_Pay	Net_Res_ft_TVD	Avg_Phi_Res	Avg_VClay_Res	ResGross_Res	PHIH_Res
PAHAK_Amp	Correlation Coefficient	0.278	-0.114	-0.155	0.076	0.064	-0.169	-0.107	-0.112	-0.032	-0.042	0.266	-0.256	-0.078
	Sig. (2-tailed)	0.161	0.571	0.440	0.706	0.753	0.398	0.597	0.579	0.874	0.836	0.181	0.198	0.701
	N	27	27	27	27	27	27	27	27	27	27	27	27	27
PCUTL_Amp	Correlation Coefficient	0.272	0.222	0.217	-0.135	0.235	0.173	0.201	0.202	0.151	0.277	0.167	-0.073	0.194
	Sig. (2-tailed)	0.169	0.267	0.278	0.503	0.238	0.389	0.315	0.312	0.452	0.162	0.406	0.718	0.333
	N	27	27	27	27	27	27	27	27	27	27	27	27	27
PLI_Amp	Correlation Coefficient	0.039	0.142	0.140	-0.066	0.059	0.125	0.148	0.142	0.117	-0.168	0.017	-0.079	-0.013
	Sig. (2-tailed)	0.846	0.480	0.486	0.742	0.771	0.535	0.462	0.480	0.561	0.402	0.931	0.694	0.949
	N	27	27	27	27	27	27	27	27	27	27	27	27	27
PLI_RMS_Amp	Correlation Coefficient	-0.103	-0.177	-0.144	0.057	-0.117	-0.151	-0.170	-0.170	-0.079	0.141	-0.089	0.169	0.044
	Sig. (2-tailed)	0.608	0.378	0.475	0.779	0.563	0.452	0.395	0.397	0.695	0.482	0.659	0.400	0.829
	N	27	27	27	27	27	27	27	27	27	27	27	27	27
PLI_WaveformClass	Correlation Coefficient	0.215	0.003	-0.021	0.061	0.123	0.009	-0.021	-0.007	-0.150	-0.240	0.243	-0.155	-0.143
	Sig. (2-tailed)	0.281	0.989	0.918	0.762	0.541	0.965	0.916	0.972	0.456	0.229	0.222	0.440	0.476
	N	27	27	27	27	27	27	27	27	27	27	27	27	27
PUDC_amp	Correlation Coefficient	0.234	-0.001	0.077	-0.011	-0.134	-0.018	-0.002	-0.014	0.232	0.316	0.095	0.123	0.228
	Sig. (2-tailed)	0.240	0.996	0.703	0.956	0.504	0.929	0.992	0.944	0.244	0.108	0.636	0.540	0.252
	N	27	27	27	27	27	27	27	27	27	27	27	27	27
CAKAH_Amp	Correlation Coefficient	0.292	0.100	0.040	-0.181	0.312	0.097	0.096	0.087	-0.266	-0.361	0.377	-0.448	-0.399
	Sig. (2-tailed)	0.140	0.618	0.843	0.366	0.113	0.631	0.634	0.666	0.181	0.090	0.052	0.019	0.039
	N	27	27	27	27	27	27	27	27	27	27	27	27	27
CGTHC_Amp	Correlation Coefficient	0.053	0.062	0.069	-0.096	0.036	0.067	0.079	0.089	0.194	0.261	0.006	0.228	0.259
	Sig. (2-tailed)	0.794	0.758	0.734	0.633	0.857	0.740	0.694	0.657	0.333	0.188	0.976	0.253	0.192
	N	27	27	27	27	27	27	27	27	27	27	27	27	27
CLI_Amp	Correlation Coefficient	-0.107	-0.060	-0.067	0.176	-0.178	-0.044	-0.068	-0.073	-0.287	-0.371	-0.030	-0.239	-0.323
	Sig. (2-tailed)	0.596	0.766	0.739	0.380	0.374	0.828	0.737	0.718	0.147	0.057	0.883	0.229	0.101
	N	27	27	27	27	27	27	27	27	27	27	27	27	27
CUI_Amp	Correlation Coefficient	0.041	0.066	0.156	-0.182	-0.064	0.072	0.084	0.090	0.372	0.199	-0.081	0.369	0.318
	Sig. (2-tailed)	0.841	0.743	0.436	0.364	0.753	0.721	0.679	0.693	0.056	0.321	0.689	0.058	0.106
	N	27	27	27	27	27	27	27	27	27	27	27	27	27
CVpVs_GTHCtoUI	Correlation Coefficient	0.176	0.149	0.059	-0.102	0.203	0.118	0.152	0.141	-0.019	-0.205	0.252	-0.272	-0.173
	Sig. (2-tailed)	0.380	0.457	0.772	0.614	0.311	0.559	0.449	0.484	0.924	0.306	0.204	0.170	0.387
	N	27	27	27	27	27	27	27	27	27	27	27	27	27
SUItoUIC_RMS_Amplitude	Correlation Coefficient	-0.251	-0.008	-0.112	0.161	0.024	-0.046	-0.024	-0.027	-0.028	-0.118	-0.088	-0.118	-0.067
	Sig. (2-tailed)	0.207	0.968	0.579	0.422	0.904	0.821	0.907	0.892	0.890	0.556	0.661	0.558	0.742
	N	27	27	27	27	27	27	27	27	27	27	27	27	27
SUIC_RMS_Amplitude	Correlation Coefficient	-0.106	-0.099	-0.211	0.258	-0.008	-0.142	-0.124	-0.125	-0.090	-0.097	0.041	-0.149	-0.085
	Sig. (2-tailed)	0.600	0.625	0.292	0.193	0.967	0.480	0.538	0.535	0.656	0.631	0.840	0.458	0.672
	N	27	27	27	27	27	27	27	27	27	27	27	27	27
sVpVs_AKAHtoUI	Correlation Coefficient	0.052	0.031	-0.063	0.127	0.008	0.000	0.005	0.000	0.107	0.128	0.094	0.027	0.153
	Sig. (2-tailed)	0.797	0.877	0.756	0.527	0.970	1.000	0.979	1.000	0.595	0.526	0.641	0.893	0.447
	N	27	27	27	27	27	27	27	27	27	27	27	27	27
Top_Ismay_West	Correlation Coefficient	0.152	-0.091	-0.102	0.051	-0.091	-0.111	-0.078	-0.092	0.019	-0.062	0.168	-0.156	-0.099
	Sig. (2-tailed)	0.448	0.651	0.611	0.801	0.653	0.583	0.700	0.648	0.927	0.760	0.401	0.438	0.624
	N	27	27	27	27	27	27	27	27	27	27	27	27	27
UIC_West	Correlation Coefficient	0.097	-0.126	-0.170	0.105	-0.060	-0.147	-0.117	-0.125	-0.077	-0.231	0.133	-0.212	-0.199
	Sig. (2-tailed)	0.632	0.532	0.396	0.601	0.764	0.465	0.560	0.533	0.703	0.245	0.507	0.289	0.320
	N	27	27	27	27	27	27	27	27	27	27	27	27	27
LI_West	Correlation Coefficient	0.068	-0.149	-0.185	0.109	-0.125	-0.170	-0.139	-0.152	0.008	-0.124	0.103	-0.118	-0.105
	Sig. (2-tailed)	0.736	0.459	0.354	0.587	0.535	0.396	0.488	0.451	0.970	0.537	0.609	0.559	0.602
	N	27	27	27	27	27	27	27	27	27	27	27	27	27
DC_West	Correlation Coefficient	-0.015	-0.187	-0.182	0.135	-0.219	-0.190	-0.174	-0.187	-0.077	-0.114	0.031	-0.125	-0.165
	Sig. (2-tailed)	0.941	0.351	0.363	0.503	0.274	0.343	0.386	0.350	0.704	0.572	0.877	0.534	0.411
	N	27	27	27	27	27	27	27	27	27	27	27	27	27
UIC_Echo	Correlation Coefficient	-0.060	-0.162	-0.131	0.143	-0.212	-0.151	-0.148	-0.156	-0.045	-0.138	-0.072	-0.061	-0.140
	Sig. (2-tailed)	0.766	0.420	0.514	0.475	0.287	0.453	0.461	0.438	0.824	0.492	0.721	0.762	0.487
	N	27	27	27	27	27	27	27	27	27	27	27	27	27
LI_Echo	Correlation Coefficient	-0.107	-0.179	-0.155	0.150	-0.223	-0.183	-0.168	-0.179	-0.092	-0.073	-0.075	-0.119	-0.167
	Sig. (2-tailed)	0.596	0.372	0.440	0.457	0.263	0.361	0.403	0.372	0.638	0.716	0.710	0.554	0.404
	N	27	27	27	27	27	27	27	27	27	27	27	27	27
TopIsmay_UIC	Correlation Coefficient	0.162	-0.011	0.062	-0.009	-0.175	-0.013	-0.009	-0.020	0.267	0.368	0.069	0.226	0.284
	Sig. (2-tailed)	0.419	0.955	0.760	0.966	0.384	0.950	0.966	0.921	0.179	0.059	0.732	0.257	0.151
	N	27	27	27	27	27	27	27	27	27	27	27	27	27
TopIsmay_DC	Correlation Coefficient	0.276	-0.082	-0.076	0.072	-0.079	-0.118	-0.072	-0.085	-0.028	-0.161	0.172	-0.263	-0.155
	Sig. (2-tailed)	0.165	0.684	0.705	0.722	0.697	0.556	0.720	0.673	0.891	0.422	0.391	0.186	0.440
	N	27	27	27	27	27	27	27	27	27	27	27	27	27
LI_DC	Correlation Coefficient	0.193	0.204	0.105	-0.159	0.301	0.184	0.198	0.201	-0.024	-0.209	0.166	-0.194	-0.095
	Sig. (2-tailed)	0.334	0.309	0.601	0.429	0.127	0.359	0.326	0.314	0.904	0.296	0.407	0.331	0.637
	N	27	27	27	27	27	27	27	27	27	27	27	27	27

Table 4-9. Spearman correlation coefficients among the reservoir and seismic variables for Lower Ismay L2 interval.

	Sum of Squares	df	Mean Square	F	Sig.
Regression	2522.395	8	315.299	4.655	.002(k)
Residual	1354.640	20	67.732		
Total	3877.034	28			

k Predictors: (Constant), LI_DC, PAHAK_Amp, CGTHC_Amp, PUDC_amp, CAKAH_Amp, CVpVs_GTHCtoUI, TopIsmay_DC, sVpVs_AKAHtoUI
l Dependent Variable: Gross_Interval

	Unstandardized Coefficients		Standardized Coefficients	t	Sig.	95% Confidence Interval for B		Correlations			Collinearity Statistics	
	B	Std. Error	Beta			Lower Bound	Upper Bound	Zero-order	Partial	Part	Tolerance	VIF
(Constant)	37.4165	35.7209		1.0475	0.3074	-37.0961	111.9291					
CAKAH_Amp	-0.0035	0.0019	-0.5317	-1.8656	0.0768	-0.0075	0.0004	0.1370	-0.3850	-0.2466	0.2151	4.6497
CGTHC_Amp	-0.0067	0.0030	-0.5598	-2.2502	0.0359	-0.0129	-0.0005	-0.3582	-0.4495	-0.2974	0.2823	3.5421
CVpVs_GTHCtoUI	0.0201	0.0098	0.6559	2.0467	0.0541	-0.0004	0.0405	0.4256	0.4162	0.2705	0.1701	5.8777
sVpVs_AKAHtoUI	-0.0211	0.0074	-0.8172	-2.8518	0.0099	-0.0365	-0.0057	0.0707	-0.5377	-0.3769	0.2128	4.7001
TopIsmay_DC	0.3078	0.1531	0.4950	2.0101	0.0581	-0.0116	0.6272	-0.0043	0.4100	0.2657	0.2880	3.4717
PAHAK_Amp	-0.0059	0.0024	-0.4199	-2.4351	0.0244	-0.0110	-0.0008	-0.5025	-0.4782	-0.3219	0.5875	1.7021
PUDC_amp	-0.0078	0.0040	-0.3859	-1.9455	0.0659	-0.0162	0.0006	-0.3964	-0.3989	-0.2571	0.4939	2.0247
LI_DC	-0.7305	0.3236	-0.5448	-2.2577	0.0353	-1.4054	-0.0556	0.0976	-0.4507	-0.2984	0.3000	3.3336

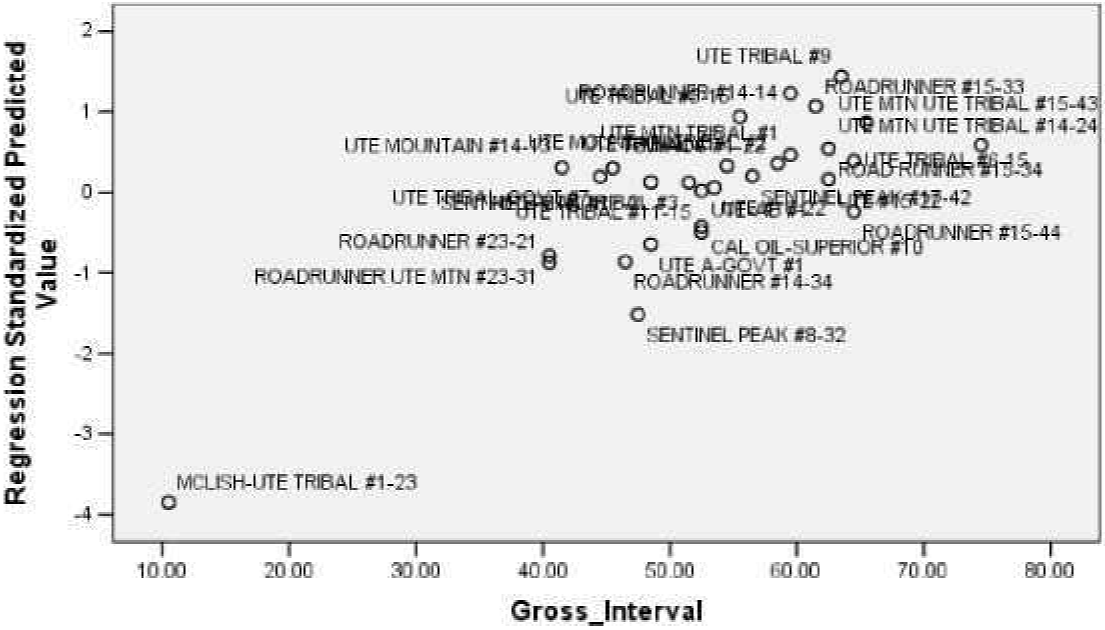

Figure 4-130. Multivariate regression results for prediction of gross interval thickness as a function of seismic attributes.

The variables that were found to be significant for each reservoir property are listed below in Table 4-10. This table shows that the C- and S-wave, in addition to the P-wave data, do in fact play an important role in predicting reservoir properties. As previously mentioned, details on the regressions for the U1 and other intervals can be found on the project web site, file ***Ute Mountain Static Model Version 1.pet***.

Reservoir Division (gross, net reservoir, net pay)	Reservoir Variable	Seismic Variables
Gross Interval		LI_DC, PAHAK_Amp, CGTHC_Amp, PUDC_amp, CAKAH_Amp, CVpVs_GTHCtoUI, TopIsmay_DC, sVpVs_AKAHtoUI
Net Pay		
	Thickness	Gross_Interval, PAHAK_Amp, sVpVs_AKAHtoUI
	Water Saturation	LI_West, PLI_Amp, PAHAK_Amp, CAKAH_Amp, LI_DC, PCUTL_Amp, PLI_RMS_Amp, CGTHC_Amp, TopIsmay_DC, SUIC_RMS_Amplitude, Top_Ismay_West
	Average Porosity	LI_West, LI_DC, CGTHC_Amp, CVpVs_GTHCtoUI, TopIsmay_DC, sVpVs_AKAHtoUI
	Average VClay	LI_DC, DC_West, PLI_RMS_Amp, TopIsmay_UIC, PCUTL_Amp, SUItoUIC_RMS_Amplitude, TopIsmay_DC
	Pay to Gross Ratio	SUIC_RMS_Amplitude, Gross_Interval, LI_DC, CUI_Amp
	Cumulative Pore Volume	Gross_Interval, SUIC_RMS_Amplitude, SUItoUIC_RMS_Amplitude
	Porosity thickness	Gross_Interval, sVpVs_AKAHtoUI
Net Reservoir		
	Thickness	TopIsmay_DC, Gross_Interval, sVpVs_AKAHtoUI, PUDC_amp, PLI_RMS_Amp, PLI_Amp, UIC_West
	Average Porosity	UIC_West, TopIsmay_UIC, CLI_Amp, LI_DC, CGTHC_Amp, CVpVs_GTHCtoUI, sVpVs_AKAHtoUI, DC_West
	Average VClay	PLI_RMS_Amp, CGTHC_Amp, PUDC_amp, PAHAK_Amp, CAKAH_Amp, PCUTL_Amp, SUItoUIC_RMS_Amplitude, CVpVs_GTHCtoUI, TopIsmay_DC, sVpVs_AKAHtoUI, SUIC_RMS_Amplitude, TopIsmay_UIC, UIC_West
	Reservoir to Gross Ratio	DC_West, PUDC_amp, TopIsmay_DC, sVpVs_AKAHtoUI, SUIC_RMS_Amplitude, TopIsmay_UIC
	Porosity Thickness	TopIsmay_DC, sVpVs_AKAHtoUI, PUDC_amp, CAKAH_Amp, CGTHC_Amp

Table 4-10. Seismic predictors for reservoir variables for Upper Ismay U1 interval.

4.7.2 STATIC MODEL DEVELOPMENT

A preliminary static reservoir model has been developed using Petrel™. The current working project file can be found on the website. The model is based on the seismic data. Figure 4-131 and Figure 4-133 show snapshots of the model.

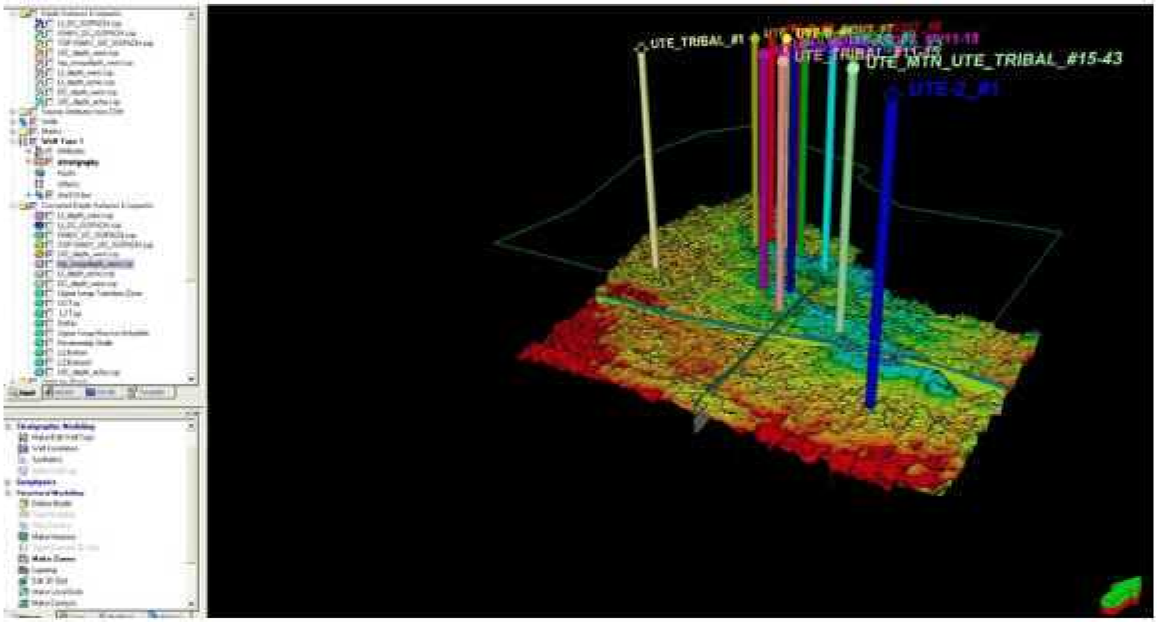

Figure 4-131. Upper Ismay Carbonate structural contour surface.

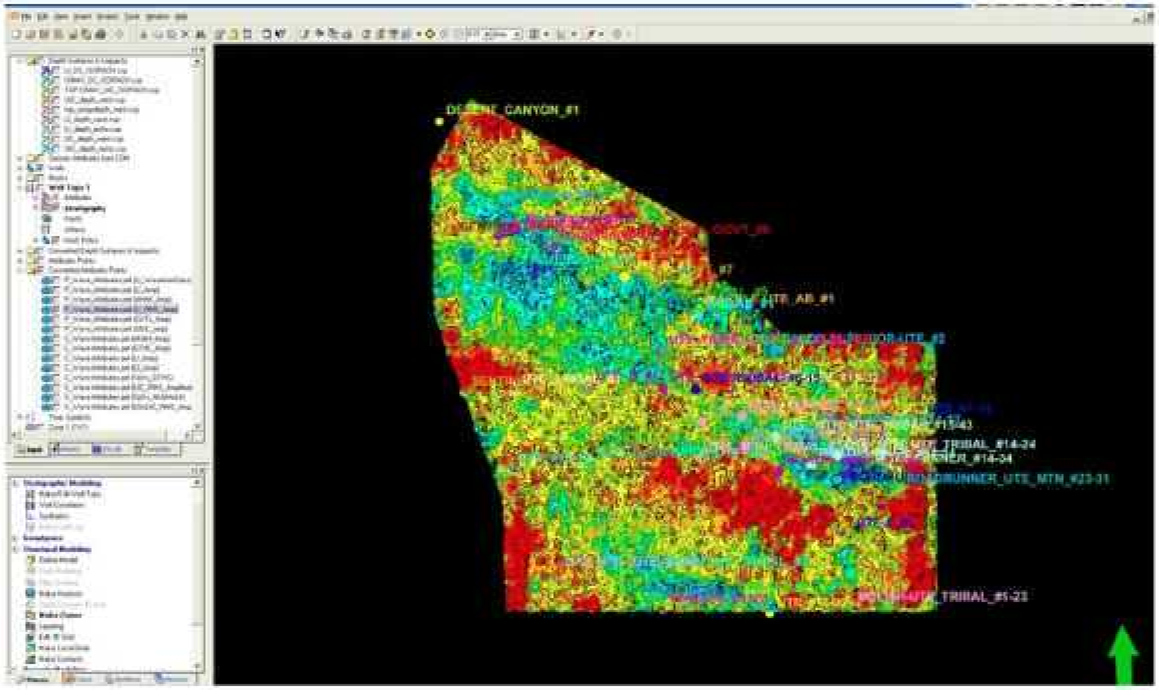

Figure 4-132. Lower Ismay root-mean-squared (RMS) amplitude.

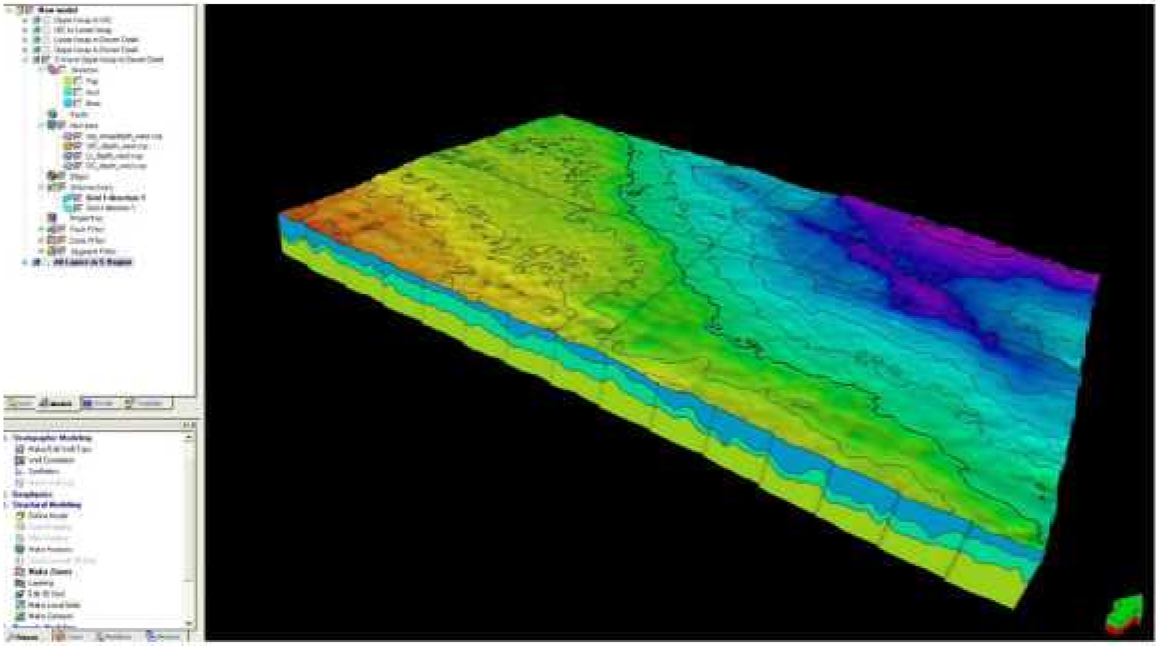

Figure 4-133. 3D model of the major seismic horizons (Top Ismay, Top Upper Ismay Carbonate, Top Lower Ismay and Top Desert Creek) in the project area.

4.7.3 UNCALIBRATED STATIC MODEL

The static model consists of ten layers, which are listed in Table 4-11.

Layer Number	Stratigraphy (Tops)
1	Top Ismay – Upper Ismay Transition
2	Upper Ismay Transition – Upper Ismay Massive Anhydrite
3	Upper Ismay Massive Anhydrite – Upper Ismay Carbonate
4	Upper Ismay Carbonate – U2 Marker Top
5	U2 Marker Top – Hovenweep
6	Hovenweep – Lower Ismay
7	Lower Ismay – L2 Marker
8	L2 Marker – Gothic
9	Gothic – L2 Marker Bottom
10	L2 Marker Bottom – Desert Creek

Table 4-11. List of static model layers and their stratigraphic definition.

Several examples of the isopachs for these layers are shown in
Figure 4-134 through Figure 4-139. The thickening related to mound development is apparent in these isopachs. These layers are based on the seismic and calibrated against tops picked in wells. Figure 4-140 shows the composite model with some of the major layers and producing wells visible. The layer thickness is variable, but the layer-parallel gridding (
Figure 4-141) is oriented east-west, north-south with a grid interval of 50 ft by 50 ft (15.24 m by 15.24 m).

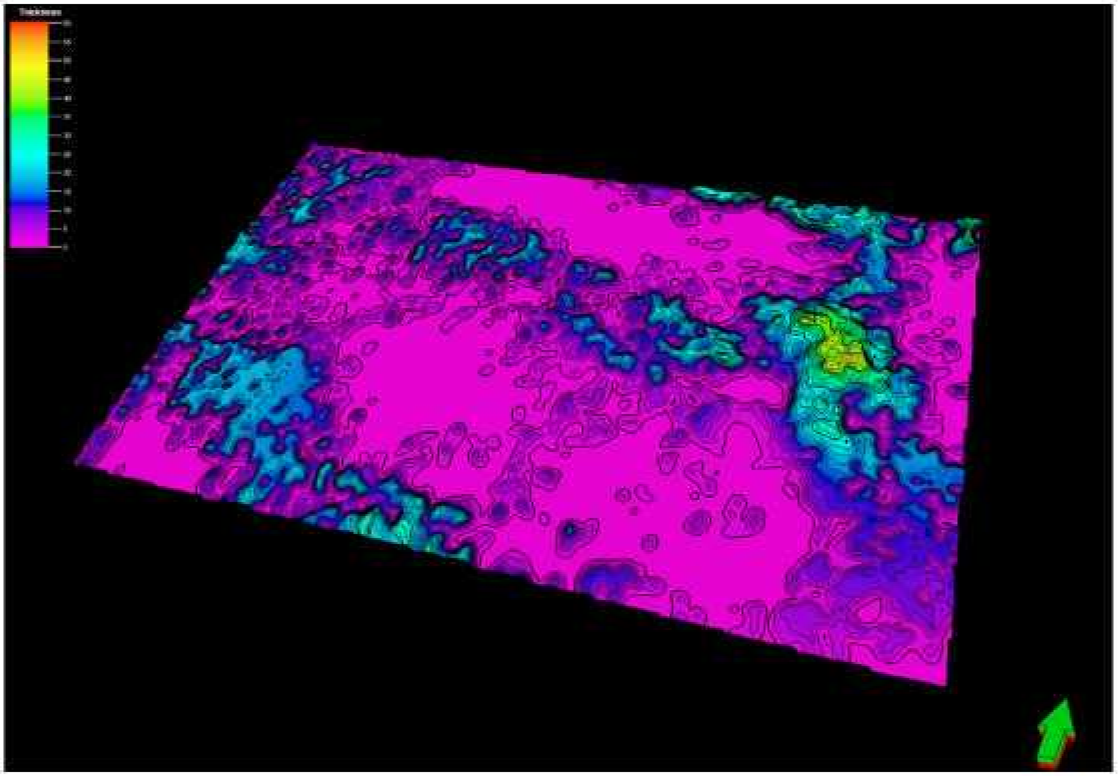

Figure 4-134. Upper Ismay to Upper Ismay Transition Zone isopach.

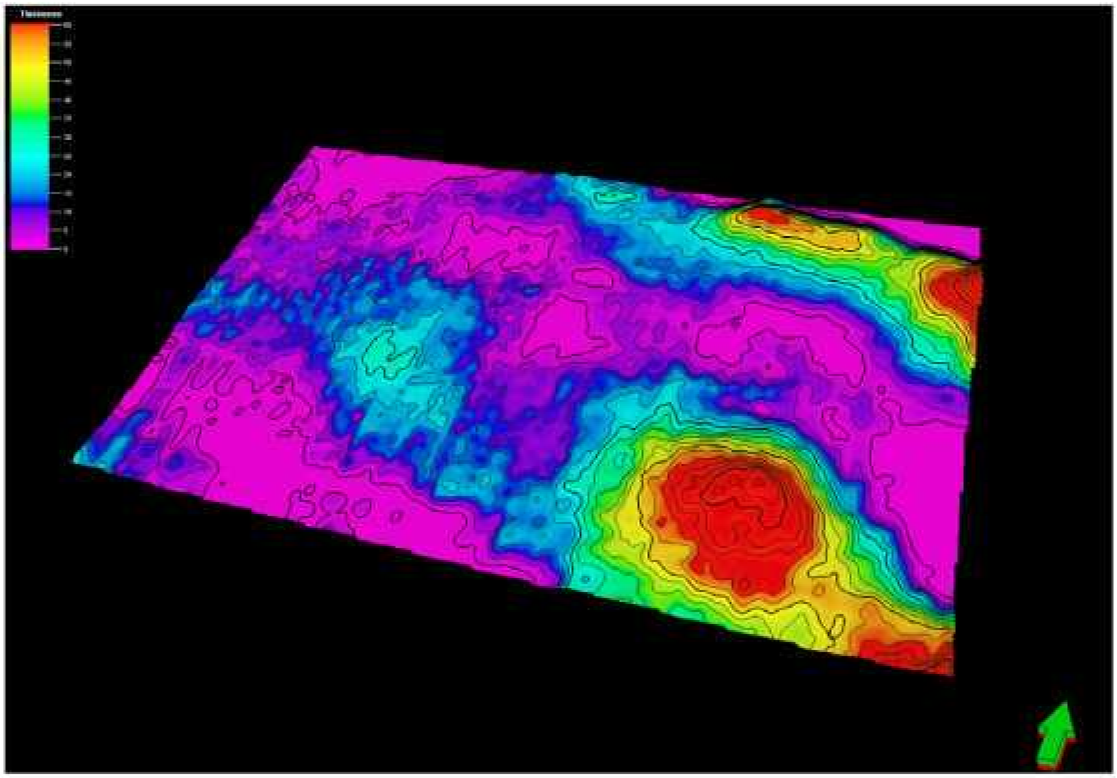

Figure 4-135. Upper Ismay Massive Anhydrite to Upper Ismay Carbonate isopach.

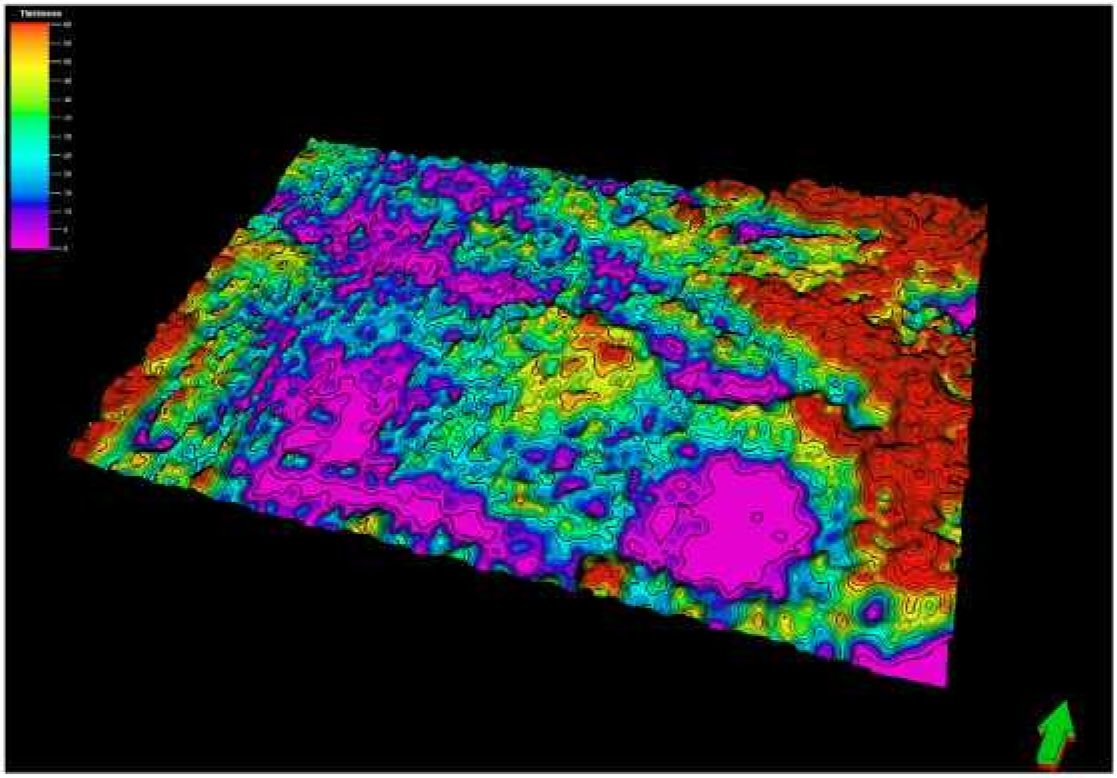

Figure 4-136. Upper Ismay 2 marker to Hovenweep Shale isopach.

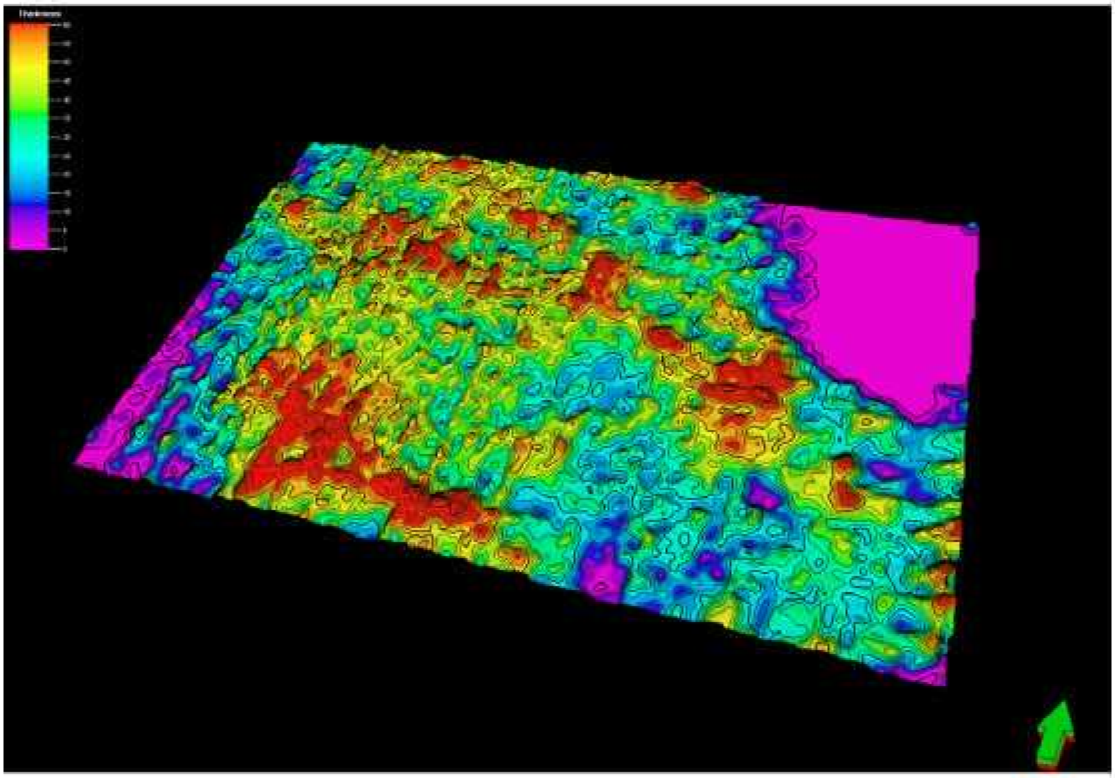

Figure 4-137. Upper Ismay 2 marker to Hovenweep isopach.

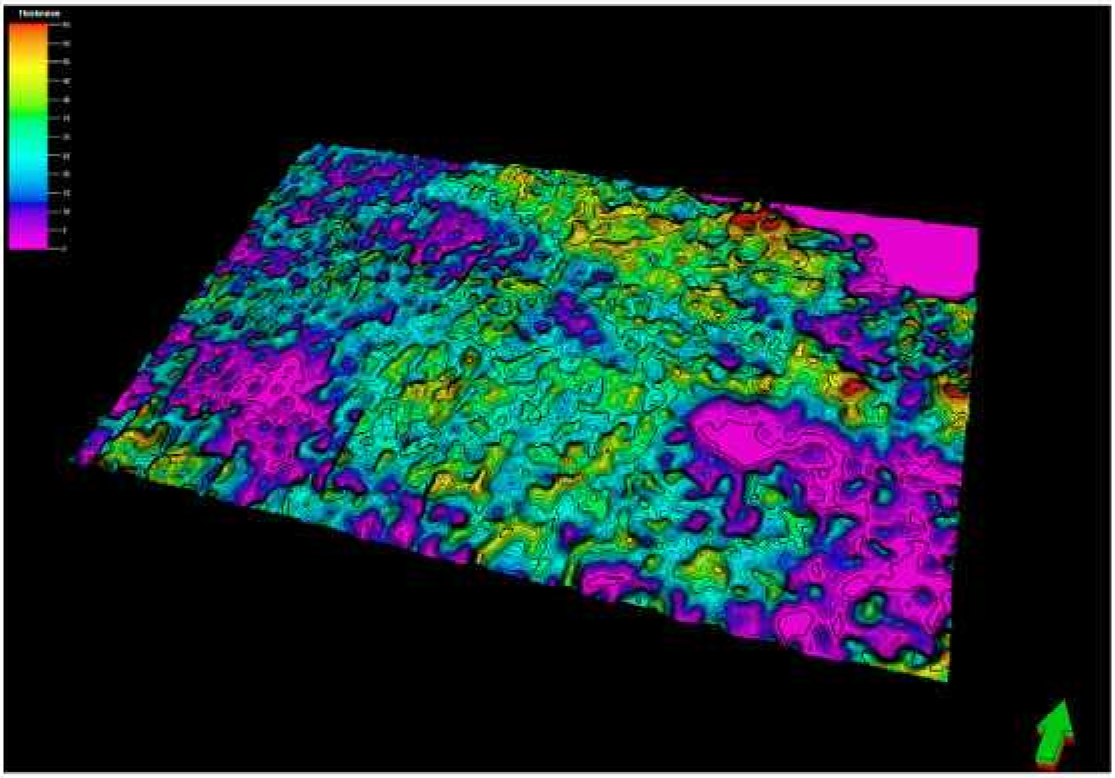

Figure 4-138. Hovenweep to Lower Ismay Top isopach.

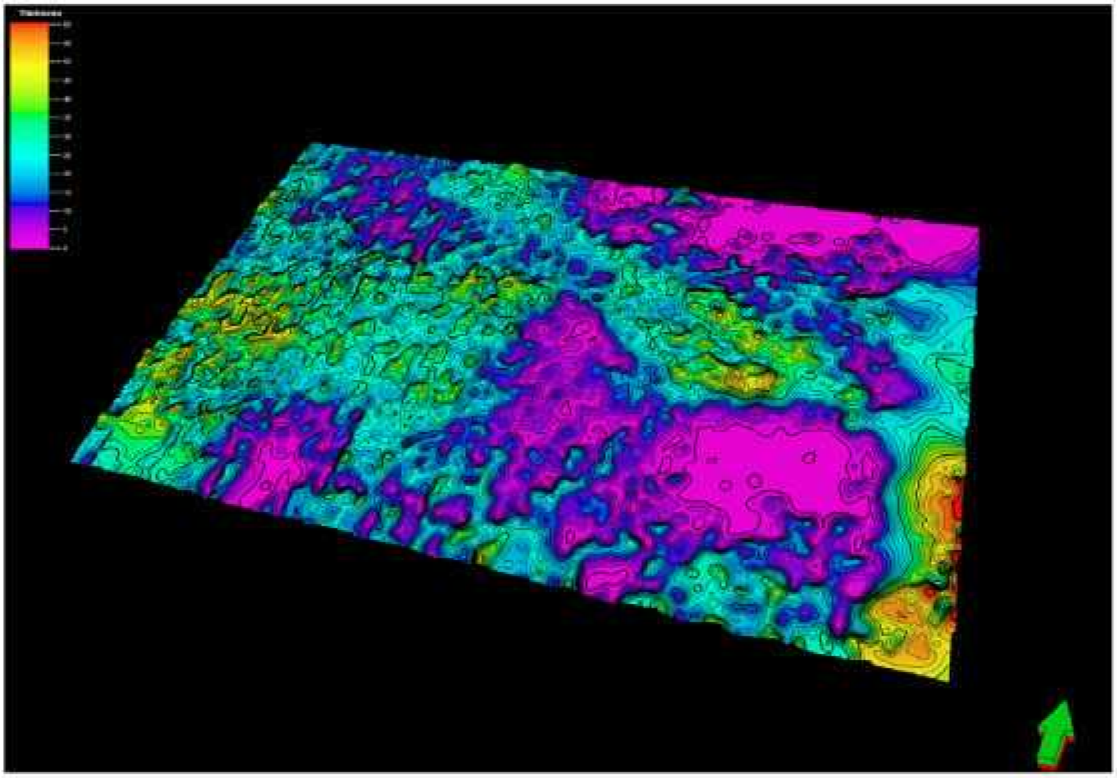

Figure 4-139. Lower Ismay 2 marker to Gothic isopach.

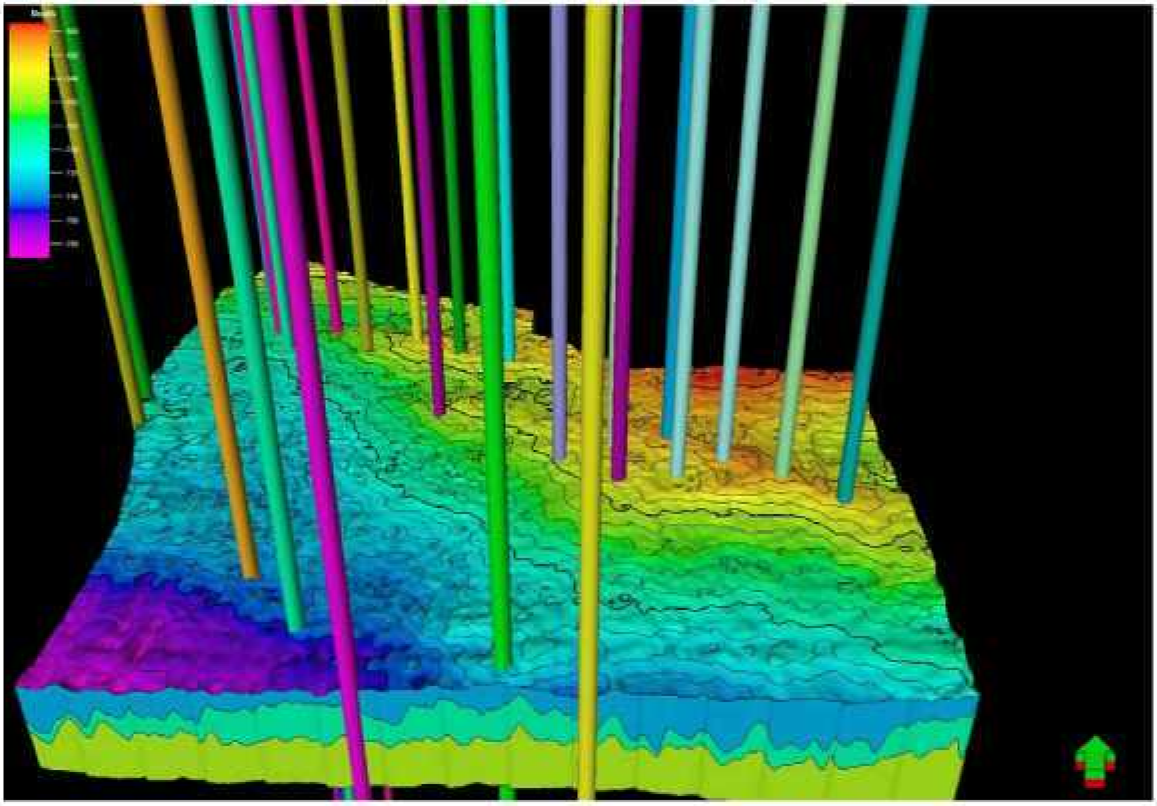

Figure 4-140. 3D model of the major seismically-defined layers in the project area and locations of productive wells.

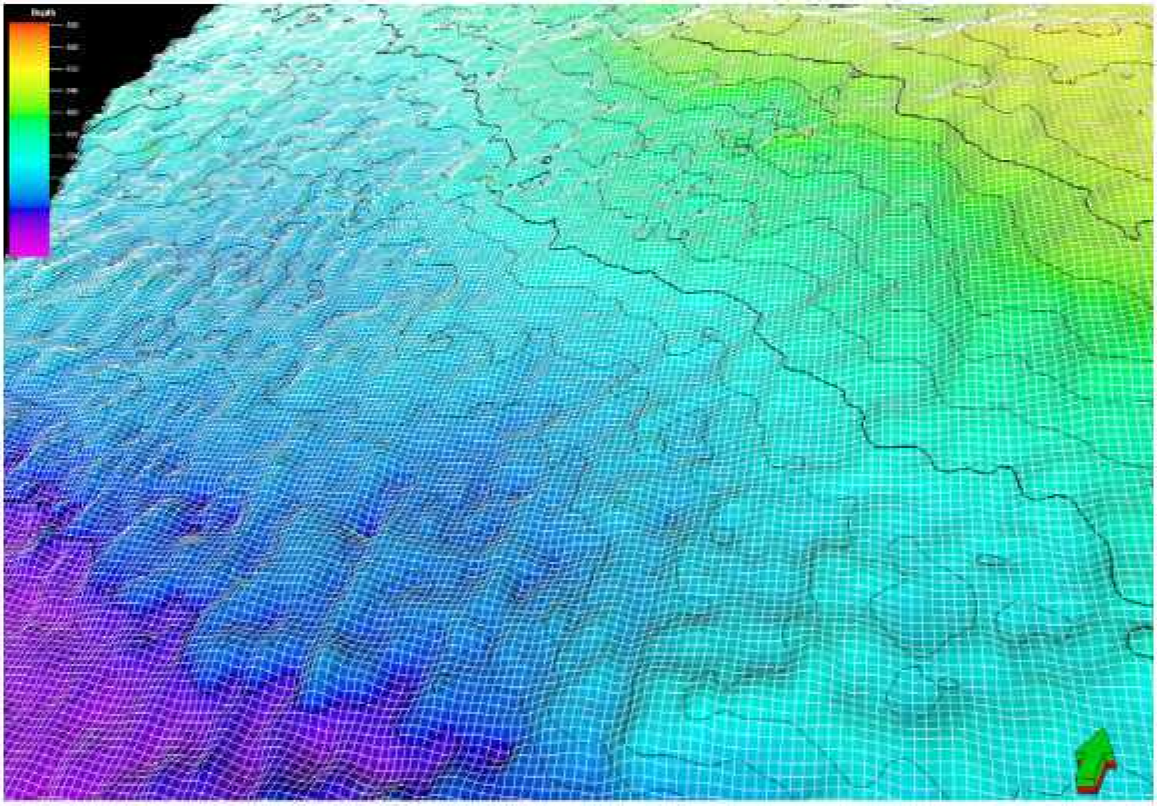

Figure 4-141. Visualization of 50 ft (15.24 m) gridding for static model.

4.7.4 DYNAMIC MODEL DEVELOPMENT

In the dynamic model, only the mounds were assigned initial fluid and gas saturations of oil and gas. The approximate outlines of the mounds used for the dynamic simulations are shown superimposed on the Desert Creek to Upper Ismay isochron (Figure 4-142)

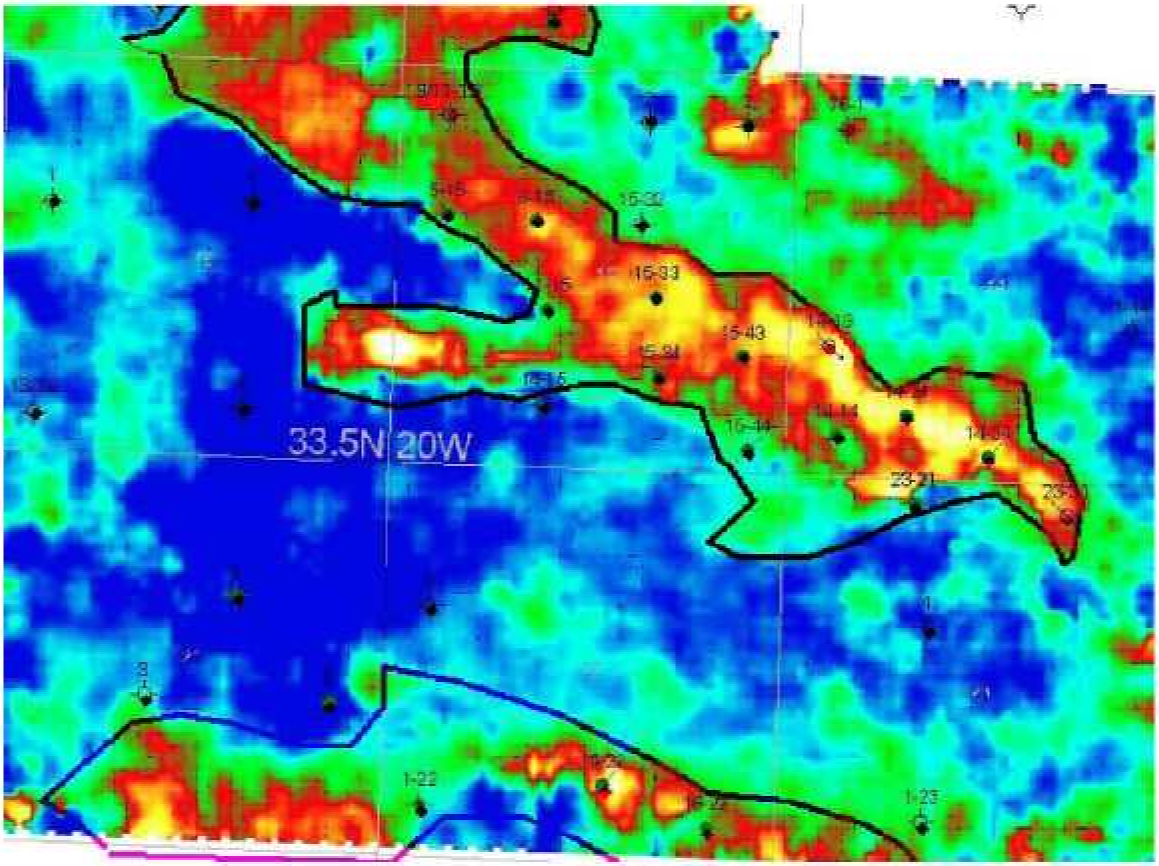

Figure 4-142. Approximate outline of mound compolexes for dyamic simulation.

With these imposed saturation limits and the multivariate regressions to specify thicknesses, porosity and water saturation, the OOIP in the mounds within the study area is about 24 million barrels. EUR for oil in the project region is approximately 4 million barrels, which implies that the recovery factor for oil is about 17%. Published recovery factors for other algal mound fields in the Paradox Basin (Chidsey, 2003) cite values between 15%-20% for vertical wells under primary recovery, so the estimated OOIP from the regressions yield recovery factors consistent with other fields in the Basin. The oil saturation in the reservoir was determined as one minus the water saturation. This may be incorrect since the reservoir pressure is very close to the bubble point pressure and there may be pockets of free gas in the reservoir. There is also likely to be oil in place outside the primary mound complexes, but it is volumetrically negligible.

Eclipse™ input file also require PVT data and relative permeability information. PVT data was generated using the oil analysis data provided. The solution gas oil ratios, formation volume factors, oil and gas viscosities, relative permeabilities and capillary pressure curves are shown in Figure 4-143 through Figure 4-151. These relations were not derived from wells in the immediate project area, as no such data was available, but instead were taken from reported analyses performed on the North Heron 35-C well in San Juan Co, Utah, located approximately 10 miles west of the project area, and penetrating the same reservoir section (Core Laboratories, 1991).

Initial conditions for the Eclipse simulation are shown in Table 4-12.

Temperature 132°F
Pressure 1934 psi
Initial bubble point pressure 1922 psi
Initial Rs 0.644 Mcf/stb
Initial Sg 0.0

Table 4-12. Eclipse™ model initial conditions

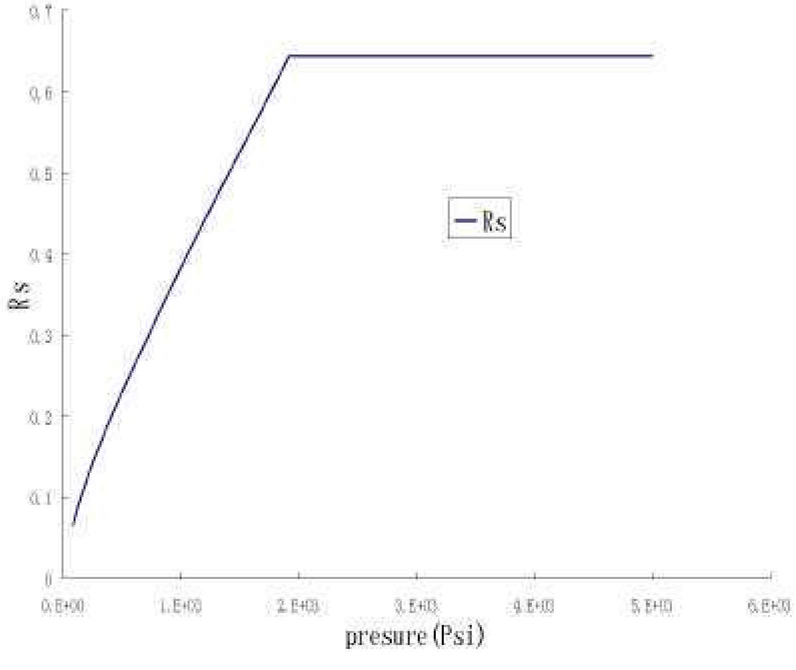

Figure 4-143. Solution gas oil ratio as a function of pressure

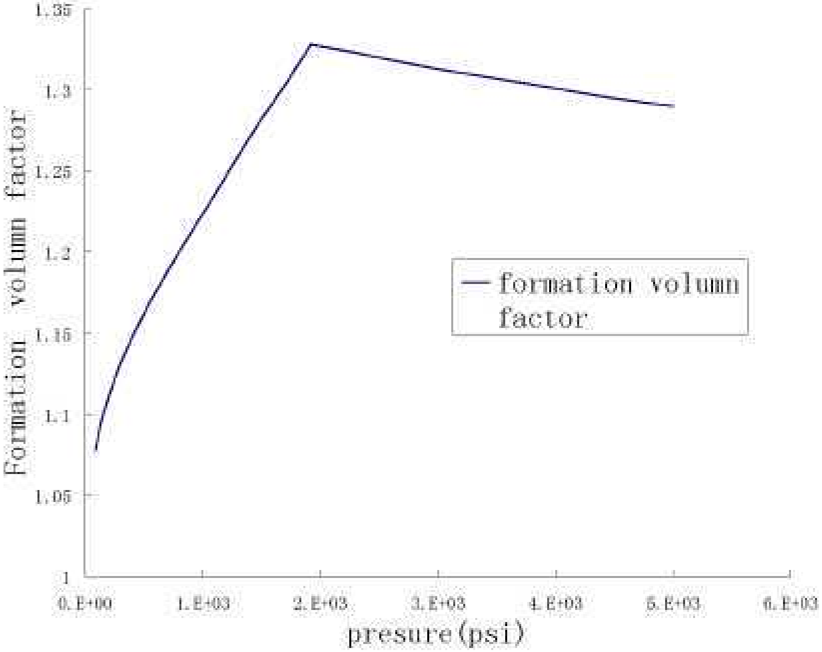

Figure 4-144. Oil formation volume factor as a function of pressure

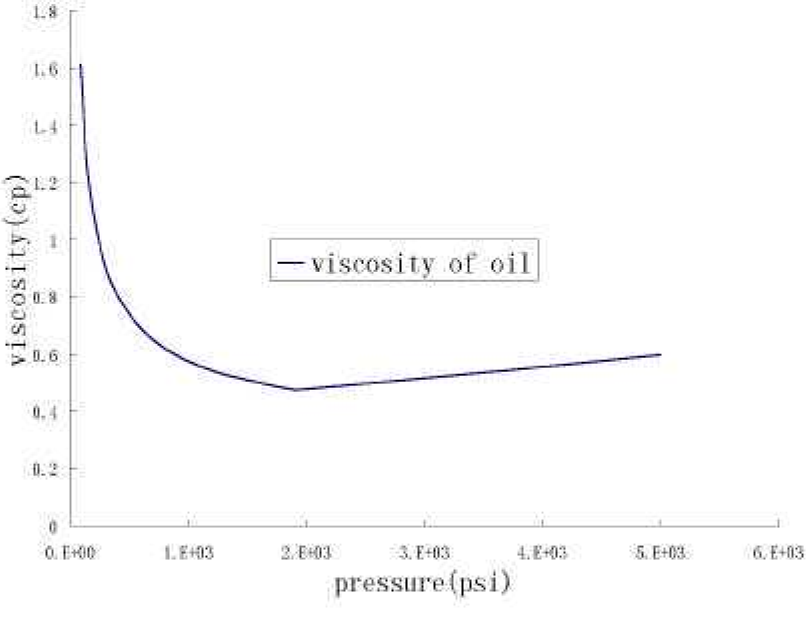

Figure 4-145. Oil viscosity as a function of pressure

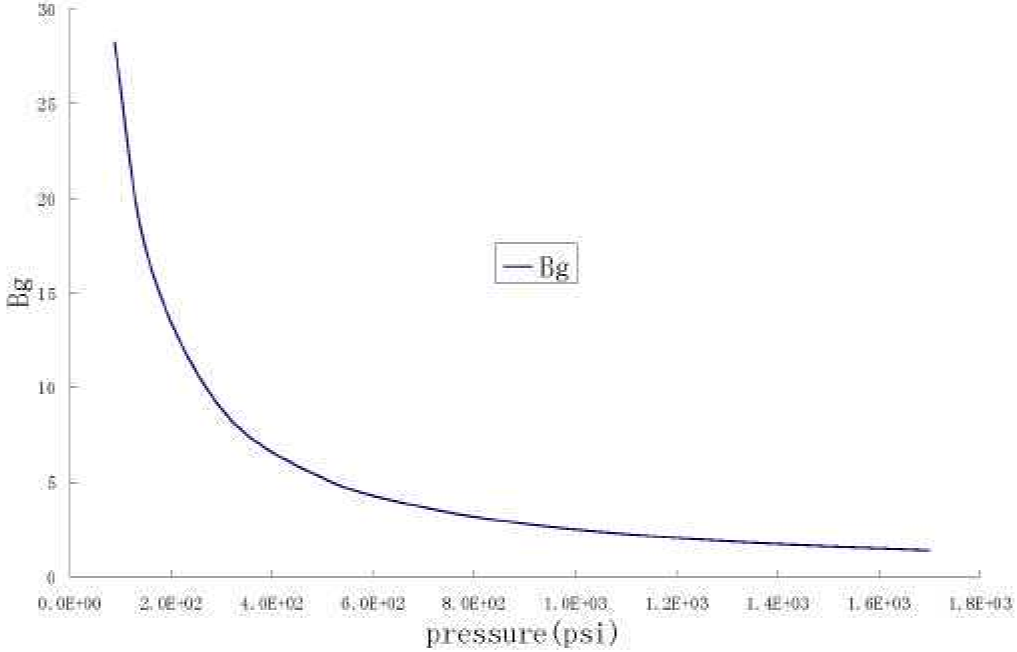

Figure 4-146. Gas formation volume factor as a function of pressure

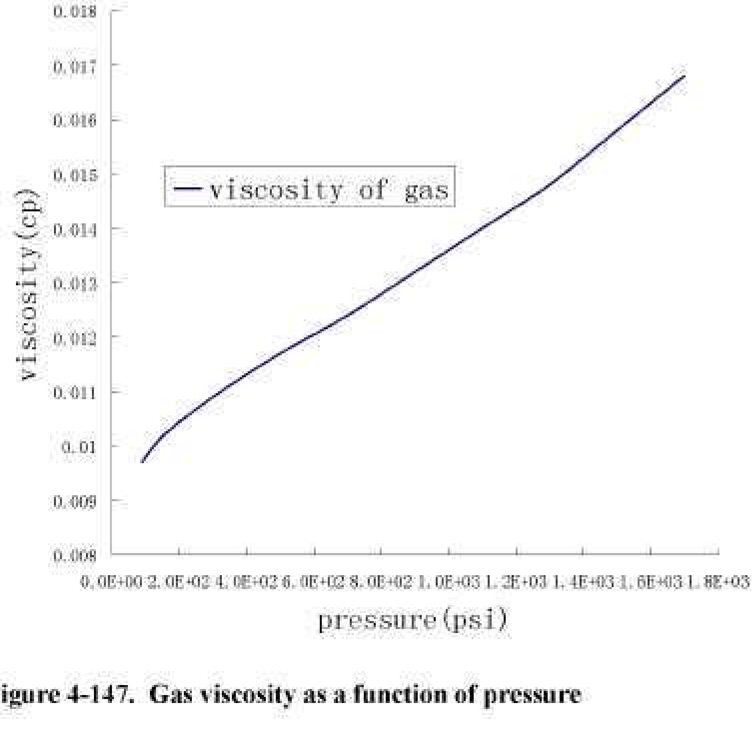

Figure 4-147. Gas viscosity as a function of pressure

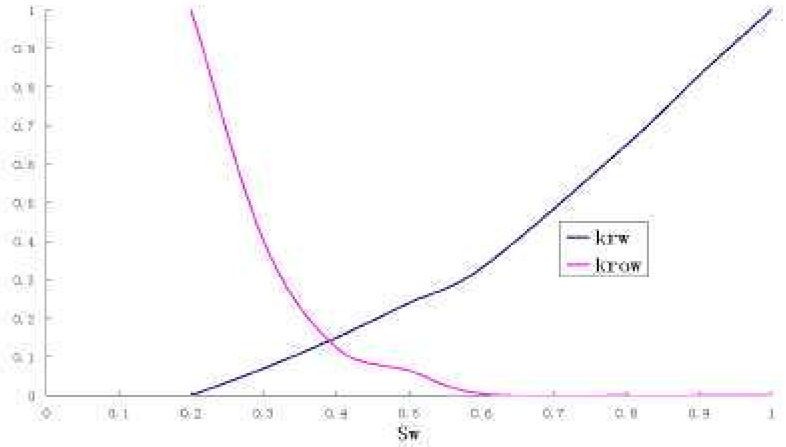

Figure 4-148. Relative permeability curve used in the simulations

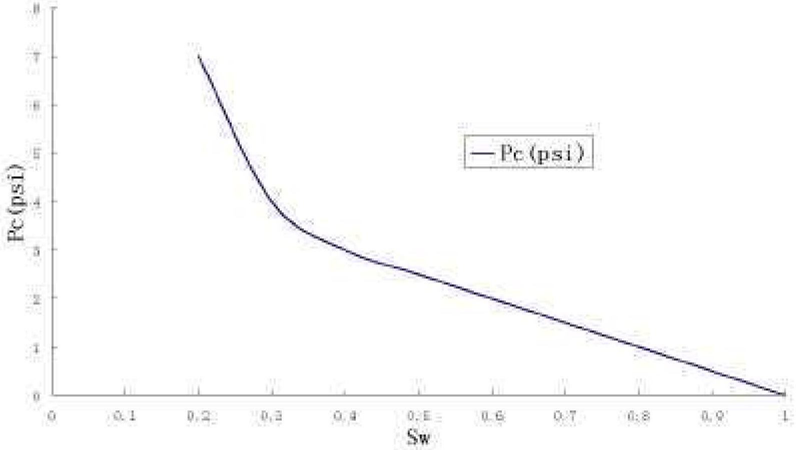

Figure 4-149. Capillary pressure curve used in the simulations

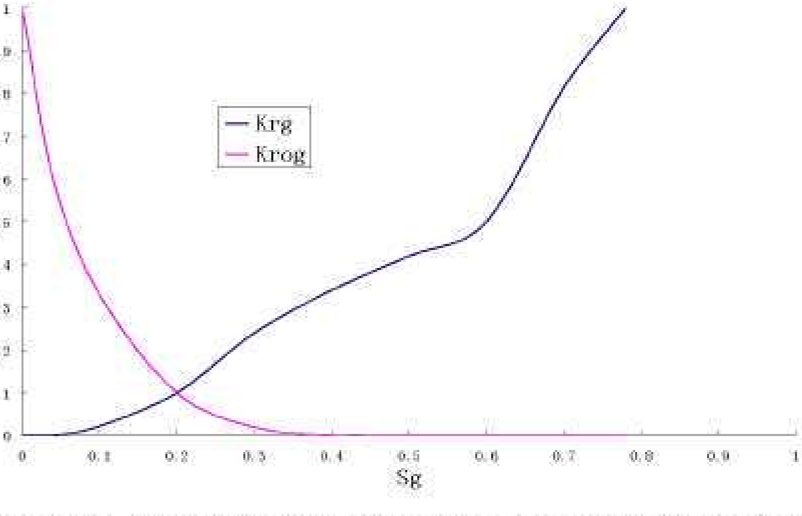

Figure 4-150. Gas-liquid relative permeability curve used in the simulations

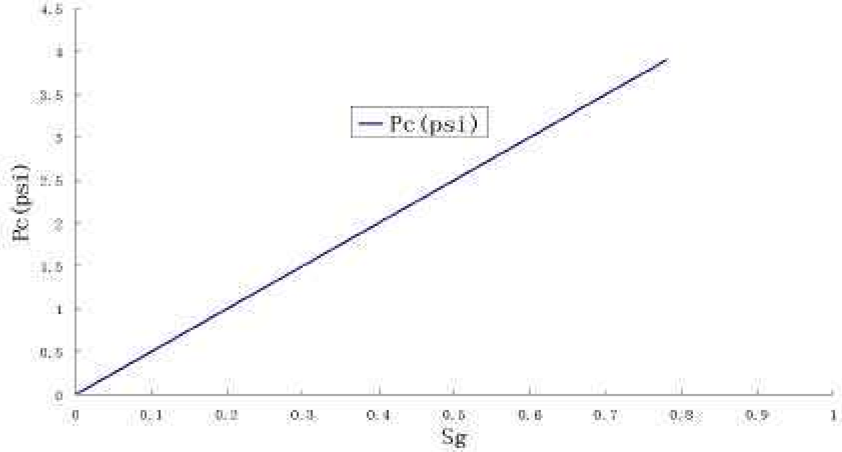

Figure 4-151. Capillary pressure curve for gas-liquid

The wells modeled are shown in Table 4-13:

Well NO.	*Well name*	*Grid cell*
1	UTE_#16-22	(94.2)
2	UTE_#15-22	(81,8)
3	UTE_TRIBAL_#11-15	(73,72)
4	UTE_TRIBAL_#6-15	(72,83)
5	ROADRUNNER_#15-44	(100,53)
6	ROADRUNNER_#15-33	(88,73)
7	ROADRUNNER_#15-34	(88,63)
8	TOWAOC_#1-22	(56,6)
9	UTE_MOUNTAIN_TRIBAL_#2	(44,19)
10	SENTINEL_PEAK_#17-42	(111,67)

Table 4-13. Wells used for history matching.

All production rates are based on annual production reports provided by Gerry Simon who serves as the Ute Mountain Ute tribe's reservoir engineering consultant. Simulation covered the time period January 1, 1991 through December 31, 2006. The location of these wells is shown in Figure 4-152.

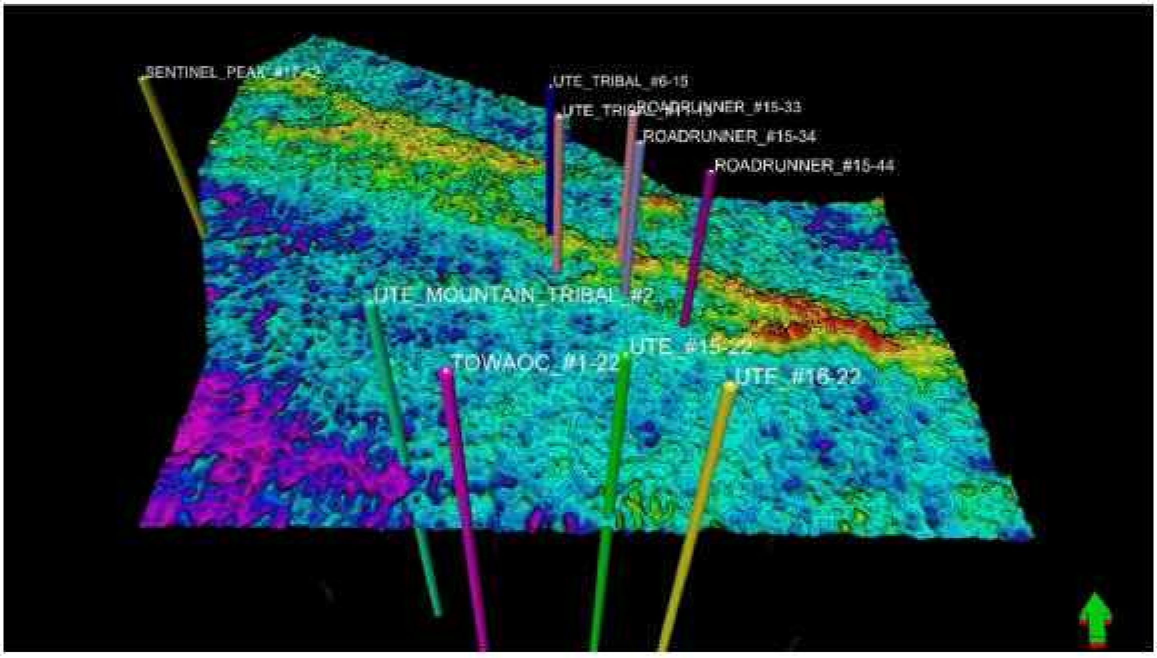

Figure 4-152. Location of wells used for history matching. The colors and contours correspond to the Ismay – Desert Creek isochron.

The oil production rates in the simulation were reproduced exactly. The gas production and water rates (averages) over the production of the reservoir are provided in Table 4-14.

Well	Simulation Oil Rate	Simulation Water Rate	Simulation Gas Rate	Field Water Rate	Field Gas Rate
	(STB/day)	(STB/day)	(Mscf/day)	(STB/day)	(MSCF/day)
UTE_#16-22					
1999	9.2	3.7	5.6	9.4	19.6
2000	10.6	5.5	6.5	12.7	21.9
2001	9.3	5.3	5.7	12.9	23.2
2002	9.6	6	5.9	11.4	21.6
2003	1.7	0.8	1	0.0	8.0
2004	2.4	1.2	1.4	0.0	10.7
2005	2.2	1.1	1.3	3.7	11.1
2006	1.6	0.8	1	22.6	6.7
UTE_#15-22					
1999	3.8	0.9	2.4	7.8	11.6
2000	4.2	0.9	2.6	9.4	14.0
2001	4.1	0.9	2.6	8.5	14.6
2002	3.6	0.8	2.2	12.4	14.6

2003	2	0 4	1 3	12 8	12 8
UTE_TRIBAL_#11-15					
1991	27 3	3	17 1	174 9	93 3
1992	26 9	2 8	16 7	242 0	84 3
1993	21 5	2 2	13 2	213 5	84 9
1994	15 2	1 5	9 4	77 4	60 9
1995	12 7	1 3	7 8	39 4	34 8
1996	14 3	1 4	8 7	131 9	37 7
1997	8 7	0 8	5 3	82 3	44 3
1998	11 8	1 2	7 1	104 9	26 6
1999	10 2	1	6 1	121 4	30 7
2000	10 3	1	6 2	115 5	31 6
2001	8 1	0 7	4 8	151 5	33 7
2002	5 1	0 4	3	152 8	27 1
2003	4	0 3	2 4	107 0	17 9
2004	5 6	0 4	3 4	128 3	25 3
2005	4 3	0 3	2 6	80 8	19 6
2006	4	0 3	2 4	97 6	7 3
UTE_TRIBAL_#6-15					
1991	24 9	2 6	15 6	265 9	69 6
1992	23 7	2 1	14 7	229 8	65 9
1993	23	1 9	14 1	220 6	65 3
1994	17 8	1 3	10 9	178 9	72 8
1995	17 1	1 2	10 4	188 3	64 3
1996	19 2	1 3	11 7	255 1	63 9
1997	16 1	1	9 8	221 0	60 1
1998	16 2	1	9 9	204 1	42 5
ROADRUNNER_#15-44					
1991	7 4	2 5	4 7	15 5	56 1
1992	6 4	4	3 9	14 7	57 4
1993	3 9	2 5	2 4	11 8	45 1
1994					
1995	2	1	1 2	8 4	8 4
1996	4 4	2 6	2 6	7 6	31 1
1997	3 7	2 3	2 2	11 5	28 8
1998	1 9	1 1	1 1	8 0	18 1
1999	1 6	0 9	1	6 5	14 2
2000	2 1	1 2	1 2	14 1	29 0
2001	0 3	0 1	0 2	2 2	10 3
2002	1 8	1	1 1	10 9	20 1
ROADRUNNER_#15-33					

1991	19 9	1 5	12 5	101 2	78 3
1992	14 7	0 8	9 1	77 6	91 6
1993	15 1	0 6	9 3	114 6	109 0
1994	7 7	0 2	4 7	55 8	62 4
1995	7 3	0 1	4 4	50 2	35 0
1996	9 7	0 2	5 9	131 0	45 4
1997	7	0 1	4 3	83 3	40 7
1998	0 8	0	0 5	10 6	7 3
1999	4 4	0 1	2 7	21 4	16 4
2000	9 9	0 3	6 3	162 0	31 4
2001	6 3	0 1	3 9	154 0	6 4
2002	1 9	0	1 1	98 5	4 6
ROADRUNNER_#15-34					
1991	16 9	2 2	10 6	11 1	48 0
1992	13 5	1 8	8 3	10 3	34 0
1993	11 1	1 6	6 8	10 3	24 4
1994	8 9	1 3	5 4	9 1	32 9
1995	10 3	1 5	6 2	9 1	30 1
1996	8 9	1 2	5 3	6 7	26 5
1997	7 9	1	4 8	9 4	22 3
1998	7 4	0 9	4 4	12 7	18 7
1999	7 4	0 8	4 4	11 3	14 5
2000	8 3	0 8	5	13 5	20 7
2001	8	0 7	4 8	8 4	22 0
2002	7 2	0 6	4 3	9 2	30 2
2003	5 2	0 4	3 1	9 1	18 4
2004	6 7	0 5	4	17 8	25 6
2005	4 6	0 3	2 8	0 0	14 9
2006	0 1	0	0 1	0 0	0 7
UTE_MOUNTAIN_TRIBAL_#2					
1991	5	6 3	3 2	16 6	5 2
1992	4 8	6 1	3	18 4	0 2
1993	5 1	6 3	3 2	19 4	0 0
1994	3 6	4 1	2 2	18 0	0 0
1995	3 5	3 8	2 2	15 2	0 0
1996	4 5	4 8	2 8	20 2	0 0
1997	1 9	1 8	1 2	9 9	0 0
1998	3 7	3 7	2 3	19 8	0 0
1999	3 6	3 6	2 3	15 1	0 0
2000	3 4	3 4	2 1	20 5	0 0
2001	3 1	3 1	1 9	19 2	0 0

2002	1.8	1.9	1.1	15.6	0.0
2003					
2004	1.5	1.8	0.9	4.6	0.0
SENTINEL_PEAK_#17-42					
1991	103.2	35.8	113.8	86.5	275.8
1992	121.2	52.5	193.1	83.9	218.8
1993	93.7	34	67.8	73.7	224.2
1994	48.6	13.4	26.7	72.7	155.0
1995	39.9	11.2	21.8	68.8	140.7
1996	30.3	8.7	16.2	78.9	99.3
1997	23.3	6.8	12.3	84.5	79.6
1998	24.4	7	13.4	98.3	177.8

Table 4-14. Comparison of field production data with simulation results

Both the water rates and gas rates are underestimated in the model. There are several possible reasons for this. One possible explanation is that the initial water and gas saturations are not well accurately predicted by the regressions used to populate the geologic model. There may be some uncertainty in the PVT data, but that is likely to have lesser impact on production. Initial and final water saturations, final gas saturation and pressure are shown in Figure 4-157 through Figure 4-162.

The regression plots illustrate the uncertainty in predicting water saturation at an unknown location using the regressions, and the possible reason for the underprediction of water rates. Figure 4-153 shows the regression (solid blue line), 95% regression limits (dashed blue lines) and 95% prediction limits (outermost black curves) for the net water saturation regression for one of the upper Ismay intervals. The prediction bands describe the expected range of for the measured data and the predicted values. This plot shows that the uncertainty is on the order of ± 0.1. More importantly, extension of the regression line (Figure 4-154) to measured saturations of 1.0 produce a y-intercept of about 0.75. The regressions for the other intervals also underpredict the measured water saturations on average.

There are several ways to compensate for this underprediction at higher water saturation values, from forcing the regression to go through the (1.0, 1.0) point to adding a linear compensation function to the regression line that re-adjusts it to a slope of 1.0. However, these possible improvements have not been implemented at this time.

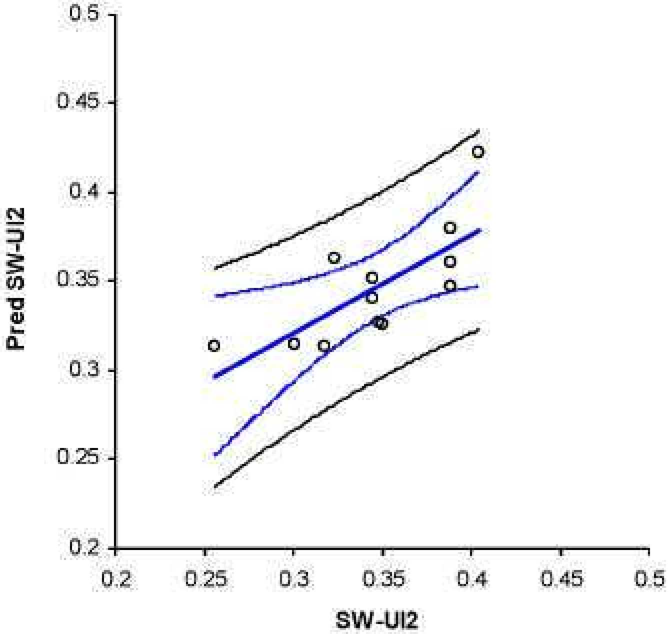

Figure 4-153. Regression and confidence bands for water saturation regression for Upper Ismay interval. Outer bands are the 95% prediction bands.

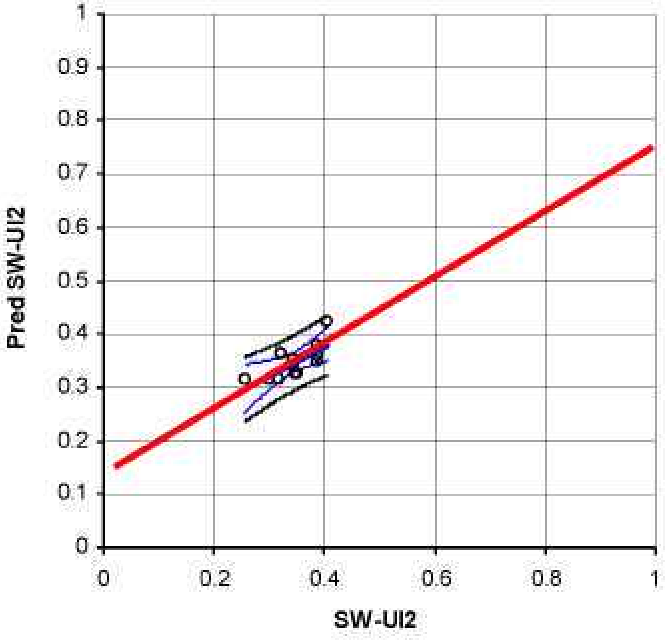

Figure 4-154. Regression line (red solid line) extended to measured saturation of 1.0.

	Measured Median	Predicted Median	Measured Mean	Predicted Mean
LI1	7.30%	7.83%	6.42%	8.34%
LI2	0.00%	0.00%	4.46%	0.00%
UI1	8.90%	10.32%	8.23%	10.51%
UI2	0.00%	7.37%	4.62%	7.73%
Upper Ismay	0.00%	0.00%	0.33%	0.00%

Table 4-15. Comparison of predicted versus measured net porosity.

Further examination of the regression results gives additional confidence in the calculated OOIP. Table 4-15 compares the predicted and measured net porosity values broken out by the five major reservoir divisions. The predicted and measured data is in good agreement; the LI2 and UI2 intervals where the differences are greater are likely due to the problem of calculating a robust regression when most of the measured data is 0.0. This can be seen by comparing the regression results for the LI1 interval (Figure 4-155) to the UI2 interval (Figure 4-156). There is a possibility that the net porosity assigned to the dynamic simulation could be slightly higher than the actual porosity, particularly in the UI2 interval. Nonetheless, the agreement is quite close so that the calculated OOIP is probably not too much less than the value reported.

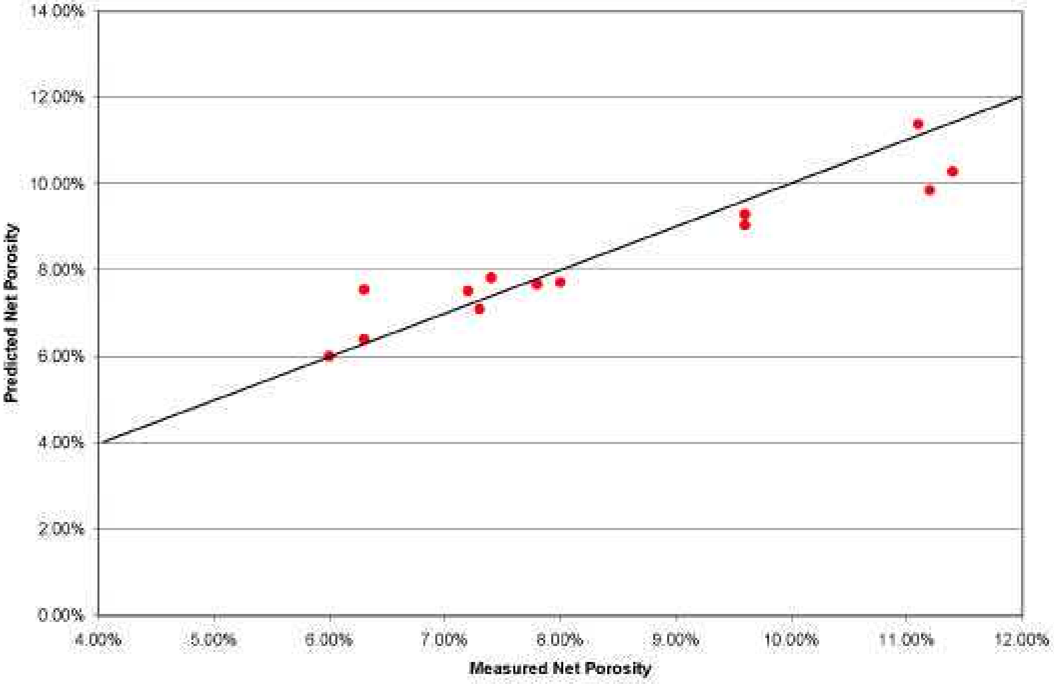

Figure 4-155. Predicted versus measured net porosity for LI1 interval.

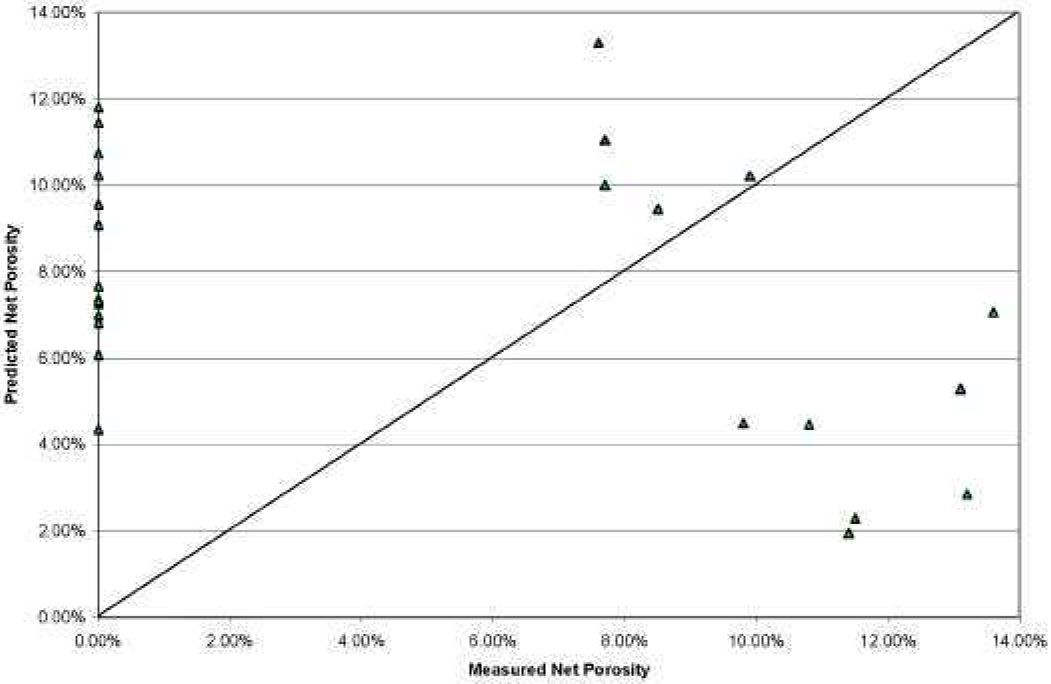

Figure 4-156. Predicted versus measured net porosity for the UI2 interval.

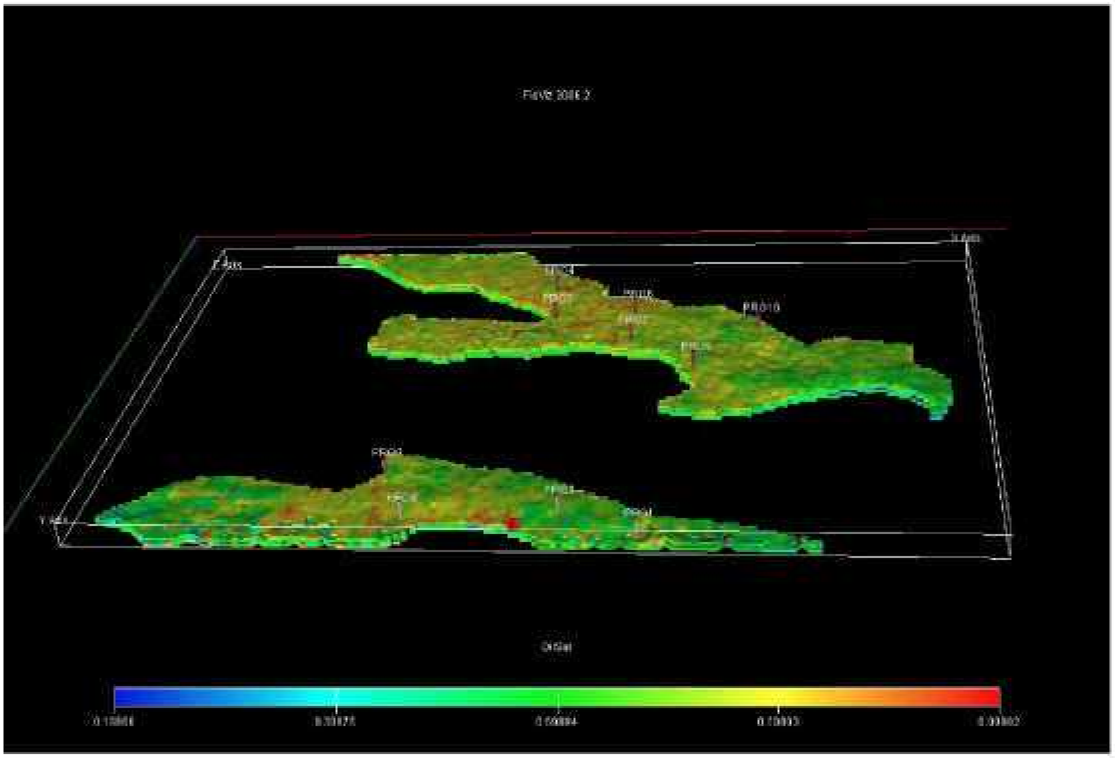

Figure 4-157. Initial oil saturation distribution in the reservoir

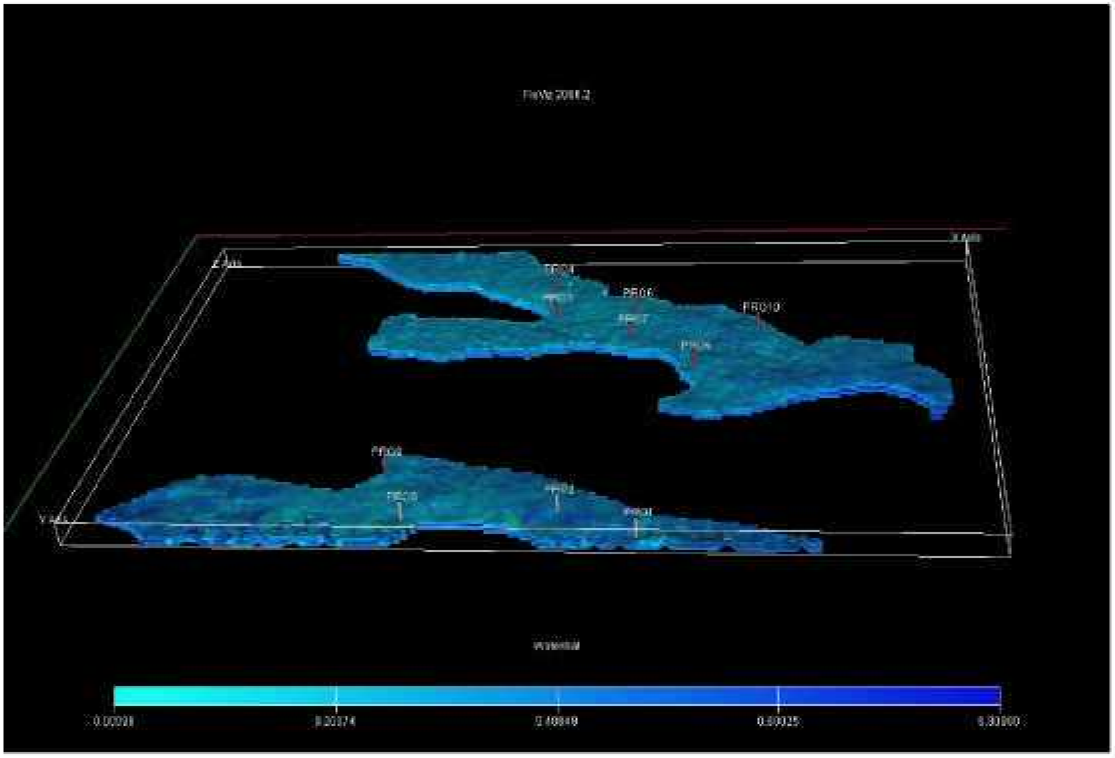

Figure 4-158. Initial water saturation distribution in the reservoir Final oil saturation

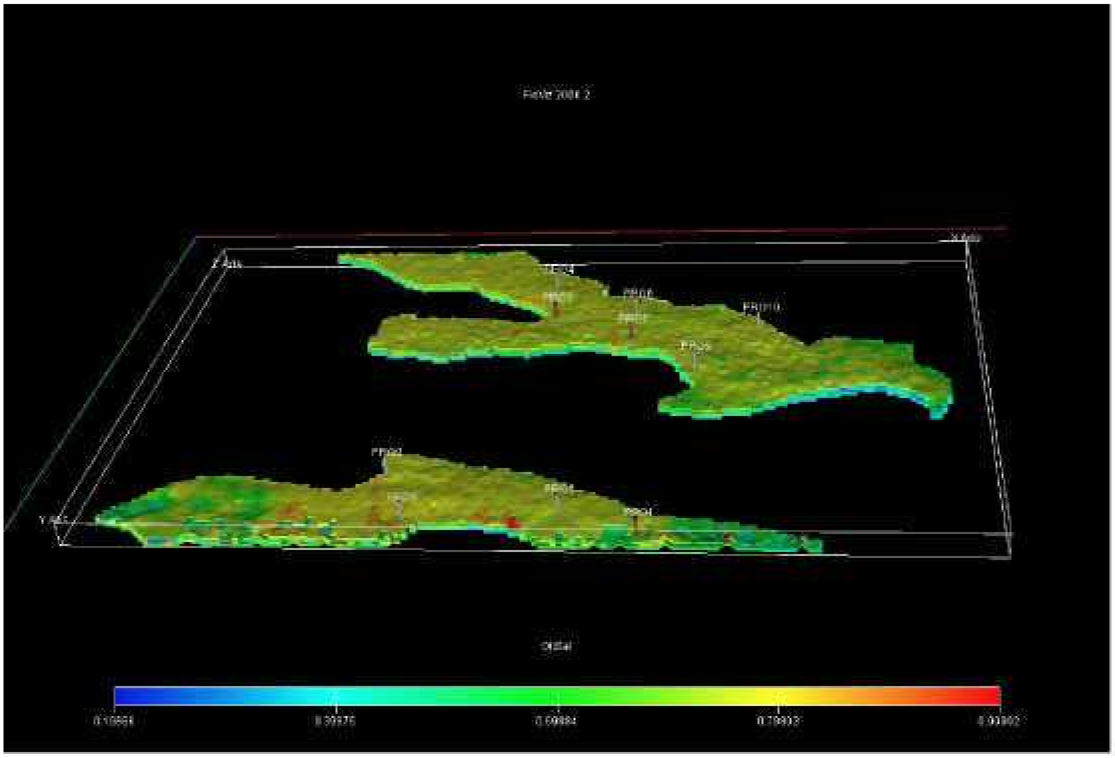

Figure 4-159. Final oil saturation distribution in the reservoir

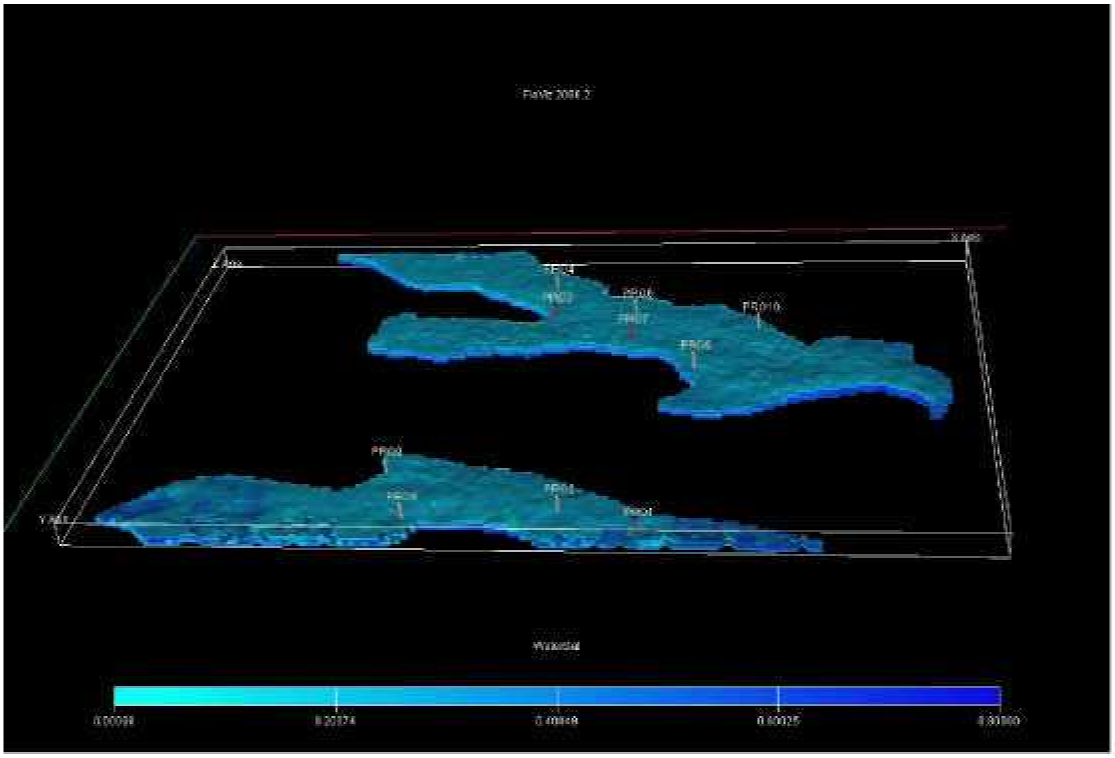

Figure 4-160. Final water saturation distribution in the reservoir

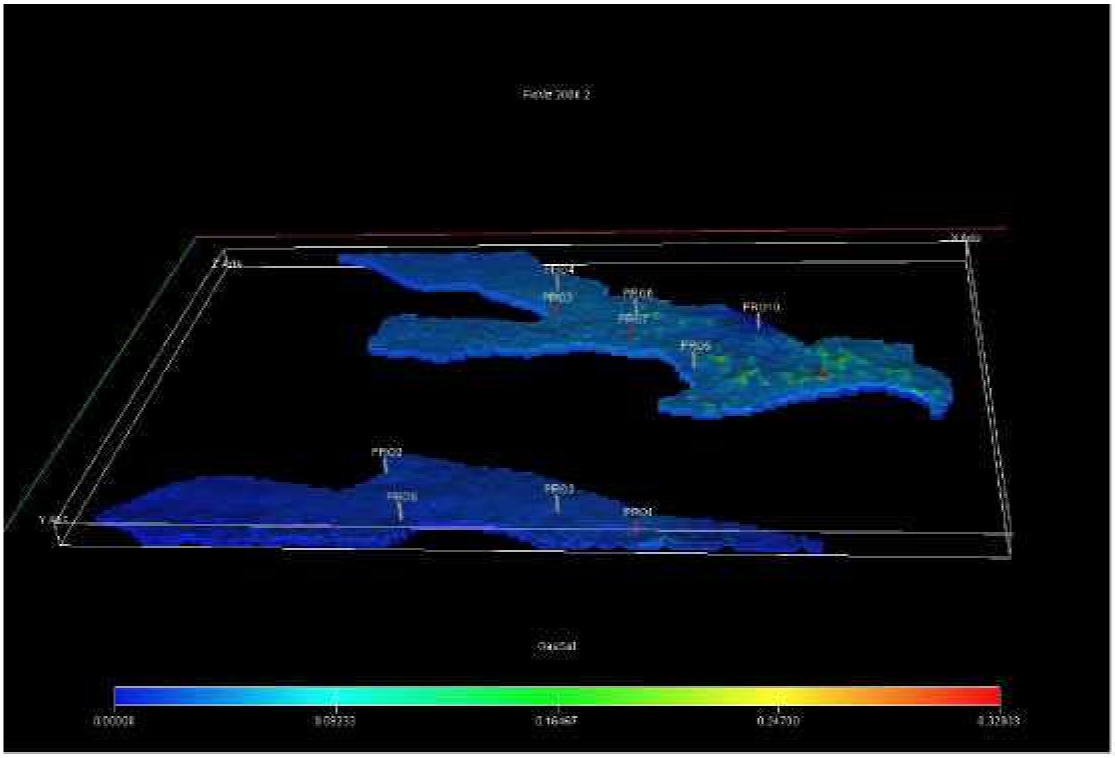

Figure 4-161. Final gas saturation distribution in the reservoir

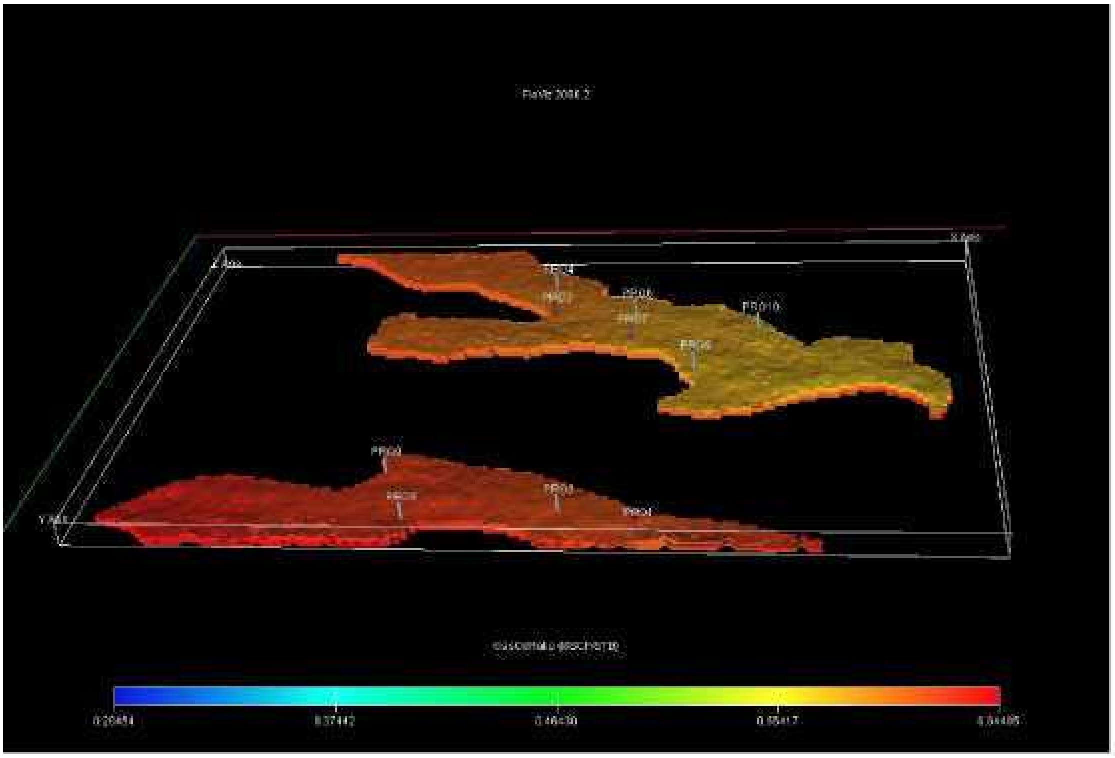

Figure 4-162. Final gas oil ratio distribution in the reservoir

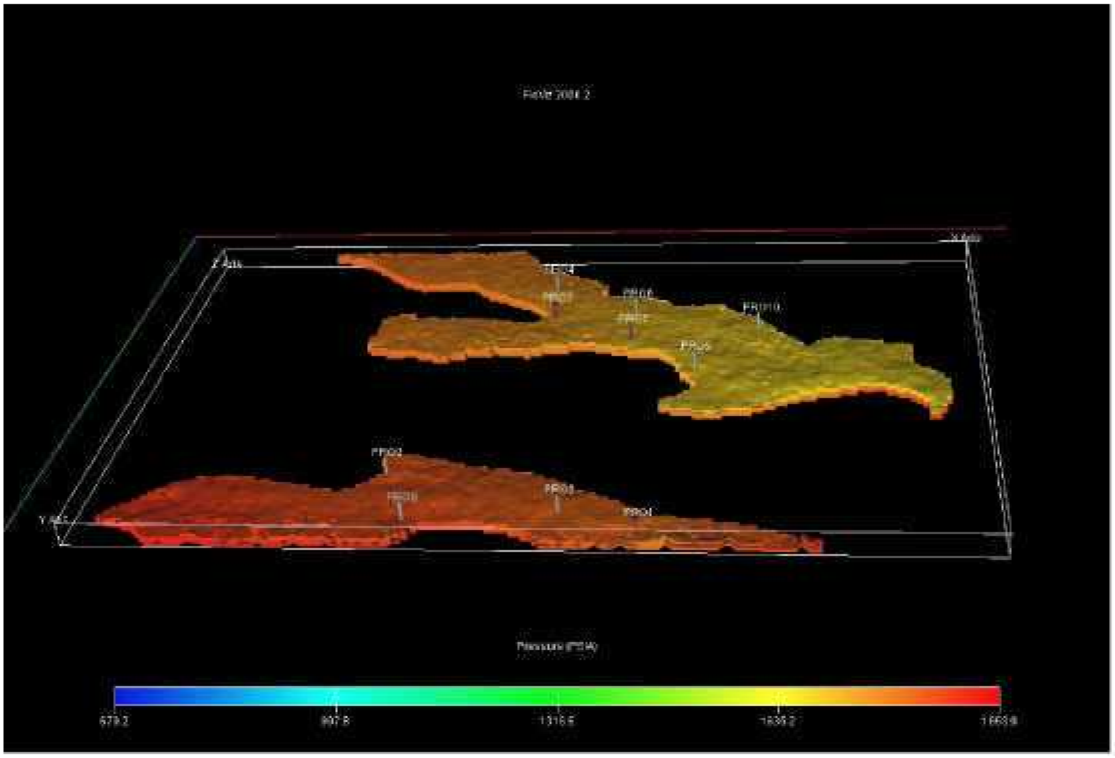

Figure 4-163. Final reservoir pressure

4.7.5 SUMMARY AND CONCLUSIONS REGARDING THE DYAMIC MODELING

Multicomponent seismic data was transformed to the required petrophysical simulation data using correlations that were provided by the geophysical team. PVT properties of the oil were brought into the simulator, along with "best-estimate" relative permeabilities. Constant rate reservoir simulations were performed using Eclipse. The production rates of all the producers were matched exactly in the simulator. The simulation creates reasonable pressure histories. Also, the calculated OOIP and oil EUR is consistent with the recovery factors of 15%-20% reported elsewhere in the Paradox Basin, and the pore volumes predicted by the regressions are consistent with measured porosities. However, the water and gas production rates from the simulator are two to ten times lower than the actual rates. The main reason for this discrepancy is the underestimation of initial water and gas saturation in the reservoir. The initial dissolved gas value (from the PVT data) may also be erroneous. As modeled, the reservoir contains a significant amount of oil, which is essentially locked due to lack of reservoir energy. Providing this reservoir energy in the form of water or gas drive could reenergize the reservoir and reactivate production. Indeed, analysis of secondary and tertiary recovery strategies in other algal mound fields in the Paradox Basin (Chidsey, 2003) indicates that the use of CO_2 might boost recoveries to as much as 70%. If the 4 million barrels EUR represents about a 17% primary recovery, that would suggest that an additional 12 million barrels might be recoverable through secondary or tertiary recovery.

4.8 Technology transfer

4.8.1 PROJECT WEBSITE

A project website has been initiated for the project. The homepage for this project is at: http://utemountain.golder.com/. Figure 4-164 shows the homepage (with a view of Ute Mountain), along with some of the basic structure of the web site. On the homepage, there is a navigation bar that takes the visitor to Background, Gallery, Documents Feedback and Links subpages. Also shown in the figure is the Documents subpage and one of its subpages, "Other". There is also a scrolling window on the right that lists the latest project news.

Documents contains the written record of the project, including Progress Reports, informal and professional society presentations, and others, such as the bibliography (see Section 6 of this report) prepared by team member Claudia Rebne of Legacy Energy.

Figure 4-165 shows some of the content being assembled for the subpages. For example, in the Background section, there is a description of the project Task by Task; project data available for download as it becomes available); the project schedule and the project team. It is here that the visitor can learn about the technical workflow of the project, why the project was done, who the principal participants were, and download selected data.

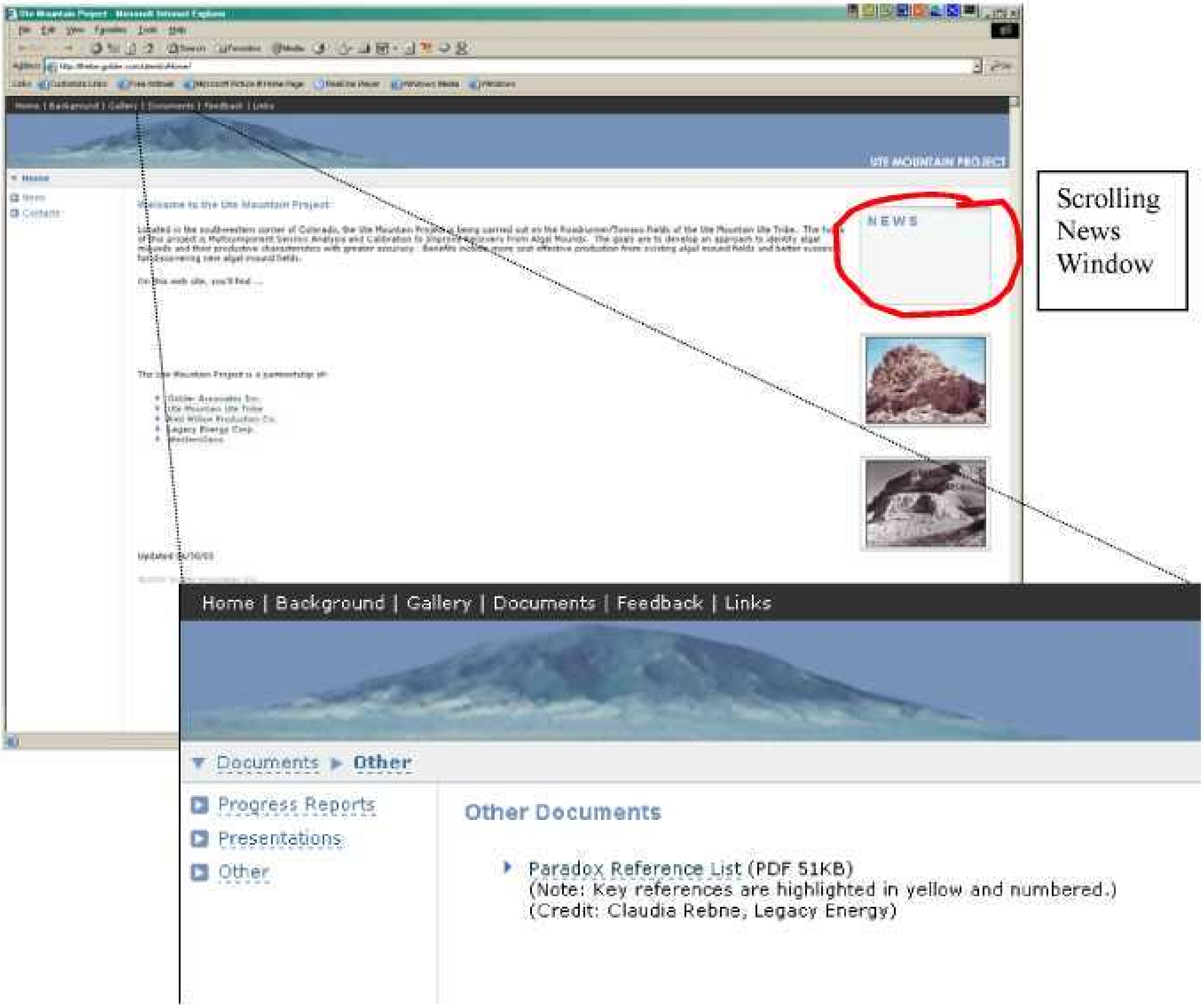

Scrolling News Window

Other Documents

- Paradox Reference List (PDF 51KB)
  (Note: Key references are highlighted in yellow and numbered.)
  (Credit: Claudia Rebne, Legacy Energy)

Figure 4-164. Homepage and example of "Documents" subpage reached from navigation bar.

The Gallery contains photos, drawings and other graphic material related to the project. There are three subdivisions in this page for showing the project location, with particular reference to the seismic grid, and contains photos of the seismic shoot and other photos having to do with the Paradox Basin, the geological data obtained that is of a graphic nature, and other project-related photos.

Documents contains the written record of the project, including Progress Reports, informal and professional society presentations, and other, such as the bibliography prepared by team member Claudia Rebne of Legacy Energy, and listed also in this report.

The Feedback subpage allows visitors to email questions, comments or requests to the project team members, to assist in communicating the technical achievements and findings of the project to others.

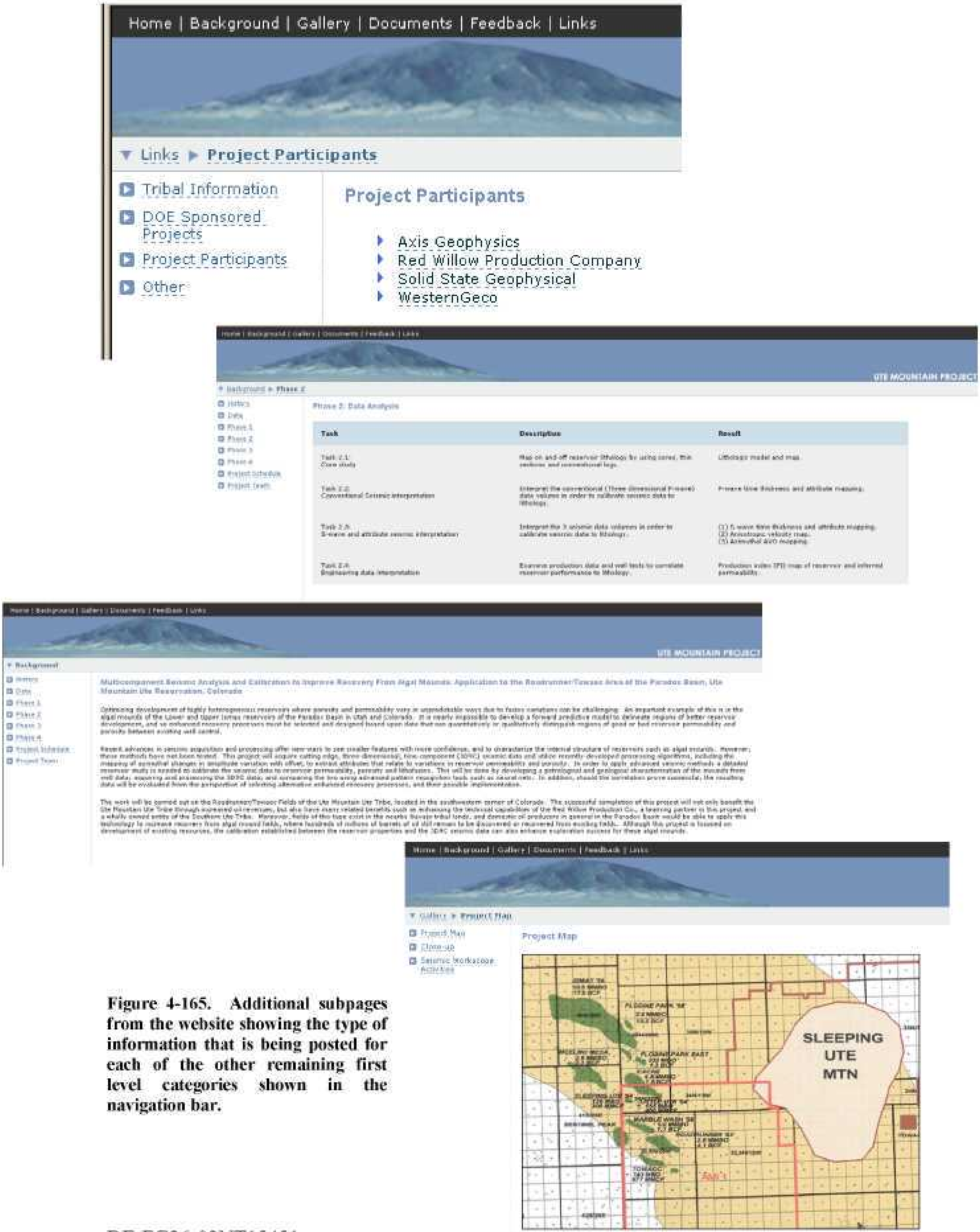

Project Participants

- Axis Geophysics
- Red Willow Production Company
- Solid State Geophysical
- WesternGeco

Phase 2: Data Analysis

Task	Description	Result
Task 2.1: Core study	Map on and off reservoir lithology by using cores, thin sections and conventional logs.	Lithologic model and map.
Task 2.2: Conventional Seismic interpretation	Interpret the conventional (Three Dimensional P-wave) data volumes in order to calibrate seismic data to lithology.	P-wave time thickness and attribute mapping.
Task 2.3: S-wave and attribute seismic interpretation	Interpret the 3 seismic data volumes in order to calibrate seismic data to lithology.	(1) S-wave time thickness and attribute mapping. (2) Anisotropic velocity map. (3) Azimuthal AVO mapping.
Task 2.4: Engineering data interpretation	Examine production data and well tests to correlate reservoir performance to lithology.	Production index (PI) map of reservoir and inferred permeability.

Multicomponent Seismic Analysis and Calibration to Improve Recovery From Algal Mounds: Application to the Roadrunner/Towaoc Area of the Paradox Basin, Ute Mountain Ute Reservation, Colorado

Project Map

Figure 4-165. Additional subpages from the website showing the type of information that is being posted for each of the other remaining first level categories shown in the navigation bar.

The Links section provides links to project member web pages, to the DOE's Fossil Energy sites of interest, to the Ute Mountain and Southern Ute Tribes' homepages, and to other websites that might be of general interest. New content is added on a regular basis.

4.8.2 PRESENTATIONS

During the project period, a number of presentations have been made on different aspects of the project, and more are in preparation. All presentations can be downloaded from the project webpage (http://utemountain.golder.com). Thus far, the following presentations have been made:

- Reservoir Characterization Conference, Colorado School of Mines:
    - *P-wave interpretation (presented by P. La Pointe)*
    - *Processing Update (present by R. Van Dok, WesternGeco*)
- EAGE/SEG Summer Research Workshop on Multicomponent Seismic (Pau, France, Sept. 5-7, 2005)
- 2006 Annual meeting of the American Association of Petroleum Geologists in Houston, TX.
- Rocky Mountain Section of the AAPG, 6-9 October, 2007, at Snowbird Utah

The citations, papers and abstracts for the EAGE/SEG and AAPG presentations follow.

4.8.2.1 EAGE/SEG

R. Van Dok, J. Gaiser, P. La Pointe and R. Benson (2005). Multicomponent processing and analysis of a 3D/9C survey over an algal mound carbonate reservoir in the Paradox Basin: Roadrunner Field, Colorado. *EAGE/SEG Summer Research Workshop on Multicomponent Seismic (Pau, France, Sept. 5-7, 2005)*. Paper Z-99.

Z-99

Multicomponent processing and analysis of a 3D/9C survey over an algal mound carbonate reservoir in the Paradox Basin: Roadrunner Field, Colorado

R VAN DOK[1], J GAISER[1], P LA POINTE[2] AND R BENSON[3]

4.9

[1] *WesternGeco, 1625 Broadway, Suite 1300, Denver, Colorado, 80202, USA*
[2] *Golder Associates, Inc*
[3] *Colorado School of Mines, Department of Geophysics*

Summary

The Paradox Basin in southwestern Colorado contains several isolated carbonate reservoirs created by algal limestone buildups. These algal mounds are relatively straightforward to locate on conventional P-wave seismic data. The reservoirs, however, are generally not internally homogeneous and ultimate recovery depends on locating zones of increased porosity and permeability. In 2003, a nine-component (9-C) 3D survey was acquired over the Roadrunner Field in the Paradox Basin northwest of the town of Towaoc (Figure 1) in order to investigate a porous carbonate oil reservoir of Pennsylvanian age. This survey was part of a U.S. Department of Energy study (DE-FG26-02NT15451) on the Ute Mountain Ute Tribal Lands. In addition to the surface seismic, a 9-C, zero offset and P-wave, offset VSP were acquired. Initial analysis of the P-wave volume shows good delineation of the algal mound structure but no obvious indications of internal variations in lithology. The PS-wave data is relatively good quality as well and has potentially better vertical resolution within the reservoir zone. The PS-wave data also shows the algal mound structure and possibly offers a glimpse into the internal lithology of the algal mound.

Introduction

The reservoirs in this region are typically mounds of algal (Ivanovia) limestone associated with organic-rich black dolomitic shale and mudstone rimming evaporite sequences of the Paradox Formation of the Hermosa Group (Ismay zone). Net pay is on the order of 3 m – 15 m but occasionally reaches a net thickness of 30 m. Porosities typically vary from 5% to 20%. The goal of this project is to detect reliably stratigraphic features that are on the order of 200 to 1000 acres. These features have little structural expression. The mounds are surrounded and overlain by massive anhydrite. The reservoir properties of these mounds are not homogeneous throughout. From the standpoint of reservoir development of an existing algal mound field, the critical factors lie in predicting the porosity, permeability, internal mound geometries and fluid content of the mounds. While well information and production data are useful to understand some of these variations, they cannot alone be used to make more accurate descriptions of the salient reservoir parameters between well control.

Data Acquisition

Acquisition of these data utilized both P-wave and S-wave vibrators into three-component geophones. Four AHV-IV vibrators were used for the P-wave source effort while a single Mertz M18 was used for the S-wave portion. Two orthogonally oriented S-wave sources were used at each source location oriented approximately N315°E and N225°E (or N045°E). The change in source orientation for one of the S-wave sources was due to the direction of travel of the vibrator with respect to the source line direction. The horizontal geophones were oriented N180°E and N270°E for the x and y components respectively. Polarity convention and S-wave source orientation were carefully checked for each location to ensure consistency in the final products.

The geophone spacing was 220 feet with line spacing of 660 feet. Source points were 220 feet apart along diagonal lines spaced every 1,320 feet. The entire record spread was fixed and live for all sources.

Data Processing

Processing and analysis for this study was done to obtain additional information about the lithologic variations within the reservoir. The P-wave source and vertical geophone data were processed using conventional time processing techniques that included surface-consistent deconvolution, refraction and reflection statics, DMO and FK time migration. The horizontal geophone data for the same P-wave sources were processed using a similar flow with the significant addition of a receiver rotation to a radial and transverse orientation, S-wave detector statics estimation and CCP binning. Limited-azimuth PS-wave volumes were produced for both the radial and transverse components and evaluated for azimuthal anisotropy using a 2C x 2C Alford rotation and layer stripping methodology. The S-wave source and horizontal geophone data were processed in the principal S1/S2 orientations as determined from the PS-wave data. Again, a similar flow to the P-wave data was utilized.

Data Analysis

The primary method used for locating and delineating the algal mound structures involves the interpretation of key events above and below the reservoir and mapping the time thickness between the two. These events are known as the lower Ismay and Desert Creek formations. Figure 2(a) shows the interpretation of these events on the P-wave and PS-wave data. Figure 4 shows a map of the isochron thickness from the P-wave, clearly outlining the algal mound feature. The internal structure, however, is not apparent

The interpretation of these data also includes comparing isochron thickness maps from the P, PS and SS data volumes between the Ismay and Desert Creek formation picks. The top and base picks for the algal mound structure in Figure 2(b) on the PS-wave data shows an apparent higher resolution than the P-wave data over the same interval. This is probably due to the shorter wavelengths of PS-wave data.

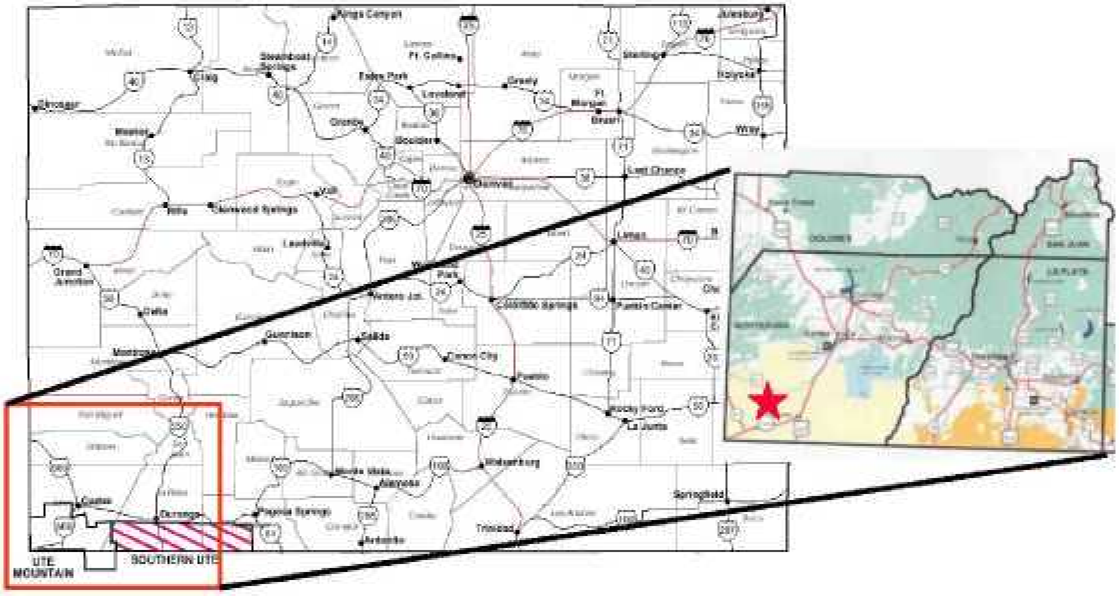

Figure 1. Survey location map in the Paradox Basin in southwestern Colorado.

Azimuthal anisotropy was also measured for the PS-waves over two layers. The first analysis layer included the events above the reservoir zone and is referred to as the overburden layer. The second analysis layer included the zone of interest. The overburden results are shown in Figure 4. The S-wave splitting is very weak over the entire survey area for the overburden as well as over the zone of interest. Peak distribution of percent anisotropy is around 1%, with a maximum of 2% difference in the fast and slow S-waves. While Figure 4 does show a regional NW/SE pattern, there does not appear to be a strong correlation of S-wave splitting attributes with the zone of algal mound buildup.

Conclusions

Preliminary analysis of the P-wave data volume confirms that the geometry of the algal mound buildup can be determined quite clearly. The PS-wave data correlates well with many of the P-wave reflection and the general shape of the algal mound can be identified. While noisier, the PS-wave data shows signs of potentially improved resolution within the reservoir. With this improved resolution it is hoped that a detailed Vp/Vs can be determined leading to a better understanding of the internal lithologic variations in the algal mound. This information combined with the SS-wave surface seismic and VSP data should provide additional confidence in the interpretation.

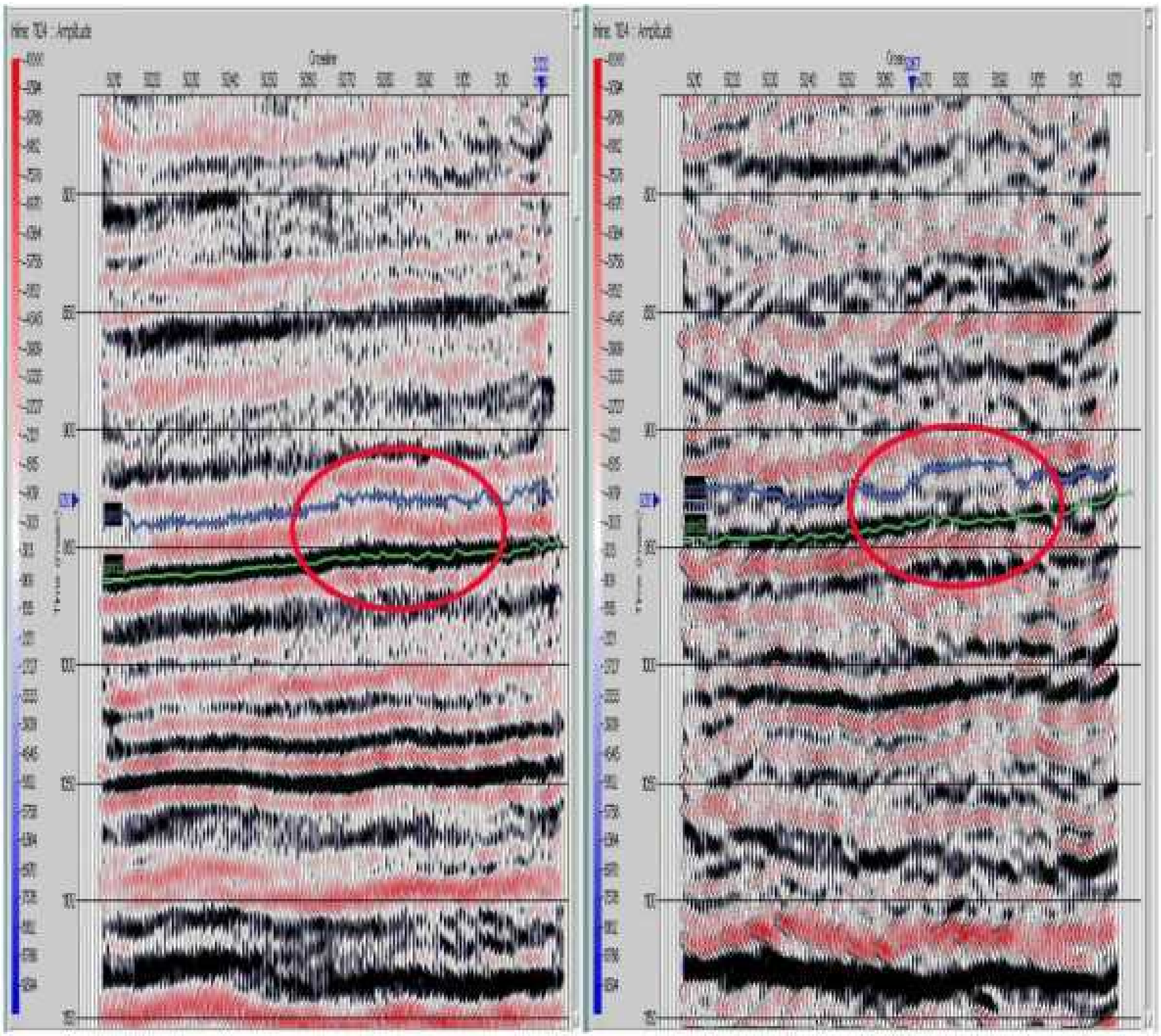

(a) (b)

Figure 2. (a) P-wave line extracted from 3D volume with top and base reservoir horizons. (b) PS-wave line extracted from 3D volume with equivalent top and base horizons. The red ovals indicate the approximate location of the algal mound buildup.

4.9.1.1 2006 AAPG Annual Meeting Oral Presentation

La Pointe, P.R., R. Benson, R. Van Dok, J. Gaiser, C. Rebne (2006). Interpretation of a 3D9C Survey Over Ismay Algal Mounds, Paradox Basin, Colorado [abstr.] AAPG Annual Meeting, 2-5 April 2006, Houston, TX

Abstract

Algal mounds have little structural expression, a small target size (a few hundred acres) and complex internal reservoir geometries. Advances in exploration and development success in these mounds have often occurred through advances in seismic technology. A joint project funded by the US Dept. of Energy and the Southern Ute Tribe's Red Willow Production Co. acquired a 9-component 3D survey, along with 3D Zero-offset VSP, over the Roadrunner Field and surrounding acreage in the Paradox Basin on the Ute Mountain Ute reservation in southwestern Colorado. The goals of the project were to evaluate how well 3D9C data can improve exploration success and the reservoir description of the mounds' internal variations of porosity, permeability and fluid content, and also to develop and refine processing and interpretation strategies.

Several different processing strategies and interpretation methods were applied to the data. The results from the survey show that the P-wave data provides good depiction of the external mound geometry, but little information about the internal structure. The PS- and SS-wave data, however, do reveal aspects of the internal mound structure. Examples of different processing streams, derived attributes and their relation to mound geology are presented. Based on these maps, wells were located and the results of drilling are presented.

The presentation was also posted on AAPG's *Search and Discovery* website at:

http://www.searchanddiscovery.net/documents/2006/06076lapointe/index.htm

4.9.1.2 2007 AAPG Rocky Mountain Sectional Meeting

La Pointe, P., R. D. Benson, C. Rebne. and Z. Gu (2007). Multivariate Modeling of 3D9C Data for Constructing a Static Reservoir Model of Algal Mounds in the Paradox Basin, CO. [poster]. AAPG Rocky Mountain Section Meeting, 7-10 October, Snowbird, UT.

Abstract

Paul La Pointe, FracMan Technology Group, Golder Associates Inc, 18300 NE Union Hill Road, Redmond, WA 98052, phone: 425 883-0777, fax: 425 882-5498, plapointe@golder.com, Robert D. Benson, Colorado School of Mines, Golden, CO 80401, and Claudia Rebne, Legacy Energy, Denver, CO.

A 3D9C survey was carried out over a six square mile portion of the Roadrunner and Towaoc Fields on the Ute Mountain Ute reservation in southwestern CO. This survey was jointly funded by the US DOE and the Southern Ute tribe's Red Willow corporation to promote development of Ismay algal mound plays in the Paradox Basin within the Ute Mountain Tribal lands and elsewhere in the Paradox Basin. Multicomponent data was utilized to better delineate the external mound geometry as well as to estimate internal mound reservoir parameters like matrix permeability, saturation and porosity. Simple cross-plotting of various multicomponent attributes against reservoir properties did not provide the desired predictive accuracy, in part due to sub-optimal frequency content in components derived from the shear wave data. However, a multivariate statistical analysis greatly improved the predictive accuracy. These multivariate regressions were then used to prescribe reservoir properties for a static reservoir model, which in turn formed the basis for a dynamic reservoir simulation model of the project area to assess the usefulness of the multivariate relations developed. This poster illustrates the workflow used to carry out the multivariate modeling, key maps of the reservoir properties that were derived, the static model, and results from the dynamic simulation used to assess the usefulness of the approach. Results from wells drilled based on the seismic data are also presented.

5 CONCLUSIONS

5.1 Seismic Acquisition & Processing

Despite the loss of the original seismic acquisition contractor in the fall of 2002, the project was successful in obtaining a new contractor at an equivalent cost. Despite some of the logistical delays, the project was able to successfully acquire the 3D9C seismic and 3D zero-offset VSP.

The frequency content of the shear wave component was not as high as hoped for, but adequate for the project goals. It is believed that the frequency content could be improved by some changes to the processing workflows. Colorado School of Mines is considering investigating whether the frequency content can be improved, although the work will be done outside the scope of this project using the seismic data volumes acquired for the project.

The project examined three different processing workflows for the P-wave data and two for the shear wave data, using two different processing contractors. The processing workflow that used the Random Noise Attenuation algorithm produced a smoother and more predictive result than other workflows, for example, using spectral whitening.

A number of seismic attributes were successfully extracted from the P-, PS- and S-wave volumes. These included time structure and isochrons maps, amplitude maps, waveform classifications, Vp/Vs ratios, shear-wave birefringence, and derived depth-structure and isopach maps for key horizons.

The four project Decision Points were addressed during the acquisition and processing:

- Field-testing of seismic data acquisition – DP1.

  At the outset of this project, it seemed likely, but not certain, that sufficient energy could be returned from the target depth so that the reservoirs could be imaged. If test arrays were to indicate that acquisition was not possible, then the project would not continue. However, prior seismic acquisition in the Paradox Basins suggested that this would be unlikely.

    - Critical factor: adequate data quality as assessed by field crew,
    - Options: If sufficient energy is returned go forward with acquisition. If sufficient energy is not returned don't go forward with acquisition, which terminates project. During the field acquisition, it was judged that there sufficient energy to complete the acquisition.

- Processing of multi-component seismic data – DP2

Local variation in the subsurface and near surface properties can affect the quality of the resulting data volumes. Further interpretation of the data volumes depends on the final quality of the processing. The Road Runner/Towaoc area is known as a good data area for conventional 3D but it was not known if sufficient shear-wave energy would be returned to the surface to provide shear-wave imaging of the target formations.

- Options: If there was sufficient shear wave energy then processing of the shear wave energy would go forward. If there was not sufficient energy detected then processing of the shear wave data would not go forward, which would also terminate the interpretation of the shear wave data, but would allow correlation of the P-wave, Anisotropic Velocity and Azimuthal AVO data volumes to lithology to continue. Assessment by the project team concluded that although the frequency content of the shear wave data was not as high as hoped for, it was still adequate to proceed with the interpretation and correlation analyses.

- Interpretation of multi-component seismic – DP3

Although sufficient energy might be returned to the multi-component geophones to go forward with the S-wave processing (DP2), it might be that after processing the S-wave data volume, imaging at the reservoir level was not capable of focusing the energy enough to get a clear image of the reservoir level of interest, or that difficulties in resolving the near surface statics or phase of the S-wave section might make it impossible to correlate between the reflection on the S-wave volume and the top of the reservoir formation. Options: If the S-wave section was clearly imaged and could be tied back to the reservoir then the interpretation would go forward. If it were not possible to clearly identify and map the reservoir formation on the S-wave data volume then the S-wave interpretation would be dropped. Conventional interpretation could go forward as can all of the modeling. As shown by the results, the S-wave data could be tied back to the reservoir and to several key internal horizons in the mound stratigraphy. As a result, interpretation was undertaken.

- Interpretation of velocity anisotropy – DP4

After processing of the P-wave velocity anisotropy data volume it needed to be determined if there was sufficient velocity anisotropy to be measured during this process.

- Options: If there were apparent trends in the velocity anisotropy data then interpretation of this data for local strain and modeling of strain would continue. If the results of the velocity anisotropy showed no coherent trends then interpretation of the velocity anisotropy section would be dropped as well as any tasks dependent on it. The results of the shear wave birefringence showed that the amount of anisotropy was very weak and did not seem to have any visual correlation with the mound geometry or properties. As a result, it was dropped from the interpretation and subsequent tasks based on it were also dropped.

5.2 Potential for Multicomponent Seismic Data in Enhancing Exploration and Development in Algal Mounds

The interpretation was made using conventional methods as well as more advanced statistical and pattern recognition methods.

The conventional methods consisted of producing maps of attributes, thicknesses (in time and depth) and structures (in time and depth), and examining simple non-parametric correlations between these seismic variables and stratigraphy in wells. The conventional analyses were designed to provide structural contour and isopach of key reservoir intervals and the overall external geometry of the mounds.

Multivariate statistical techniques and neural nets were used to develop alternative structural contour and isopach maps, as well as to evaluate whether the seismic data could be used to estimate reservoir properties. The alternative structural contour and isopach maps were primarily used in the construction of the layers of the static and dynamic reservoir model where the tops and bottoms of certain reservoir units could not be directly imaged from a single seimic variable or attribute.

5.2.1 EXPLORATION – DELINEATION OF MOUND GEOMETRY AND EXTENT

The P-wave data proved very reliable for delineating the external geometry of algal mounds in the project area. The usefulness of this data for ensuring that future wells intersect the mounds and that the prediction of the key reservoir units in terms of depth and thickness is demonstrated by:

1. The pattern of historical producing wells and dry holes, and the gross thickness of the mounds derived from the seismic acquired in the project; and
2. The predrill predictions of the stratigraphy for the MarbleWash #9-2 well in comparison to the actual drilling results.

With regards to the pattern of historical drilling success and the mound boundaries as imaged from the seismic, Figure 4-117 through Figure 4-120 show that historical dry holes are generally outside of the mounds, while productive wells are largely within the mounds. These images show that many historical dry holes were off of the main mound thicks. These figures also show that most of the wells with the highest oil & gas EUR lie in the thickest parts of the mounds (Figure 4-119).

The accuracy of these maps has been demonstrated by the results of the Marble Wash #9-2 well. As shown in Table 4-3, the gross mound thickness and the gross reservoir thickness were very accurately predicted, especially given the high variability of these two measures in the area surround the #9-2 well.

These maps and the results of the Marble Wash #9-2 well, will form an important resource as future wells are located in the project area. The results will help future exploration by providing reliable outlines of the lound complexes and where mound development has the greatest gross carbonate thickness that may be relatively undrained by existing or historical wells.

As of the and of August, 2007, the Marble Wash #9-2 had produced 11,914 barrels of oil, of which 11,353 of those barrels had been sold (Table 4-4). Over the same period of time, the well had produced 32,132 mcf of gas, of which 6,849 mcf had been sold. At typical oil and gas prices prevalent during this time period, this represents a revenue stream of close to $1,000,000.

5.2.2 RESERVOIR DEVELOPMENT – PREDICTION OF RESERVOIR ENGINEERING PROPERTIES

The multivariate modeling results were used to construct a 3D static model of the mounds in the project area. The static model was then combined with additional production and PVT data to carry out dynamic simulations of the mounds complexes in the project area. The seismic data was used to prescribe the tops of the key mound reservoir and non-reservoir units, as well as to specify the net porosity, water saturation and some additional reservoir engineering parameters.

The results of the history matching suggest tat the seismic data was useful in producing reliable estimate of OOIP and porosity, but that it may have underpredicted initial water saturations. The results were obtained with few changes to the parameter values estimated from the multivariate seismic regression models, which suggests that the multicomponent data can be useful for improving estimates of some reservoir parameters, especially those related to pore volumes. Although the regressions prediction of water saturation needs some improvement, the lesser usefulness is likely due to some of the aspects of the multivariate regression that could be improved or compensated for. Improvement in the frequency content of the shear wave data might also improve the estimation of the water saturations. It is recommended that additional work by interested parties evaluate these aspects with the data produced by this project and now available to researchers and other interested parties.

5.3 Potential for Enhanced Production from Algal Mounds on Ute Mountain Ute Tribal Lands

5.3.1 ADDITIONAL DRILLING TARGETS

Figure 5-1 shows that there may be several attractive undrilled mound thicks in the algal mound complexes in the project area. During the project, two additional wells were permitted, although they were not drilled. Inspection of this map shows that there are other mound thicks that may have not been adequately tested by existing wells and may have sufficiently extensive undrained volumes adjacent to the wells.

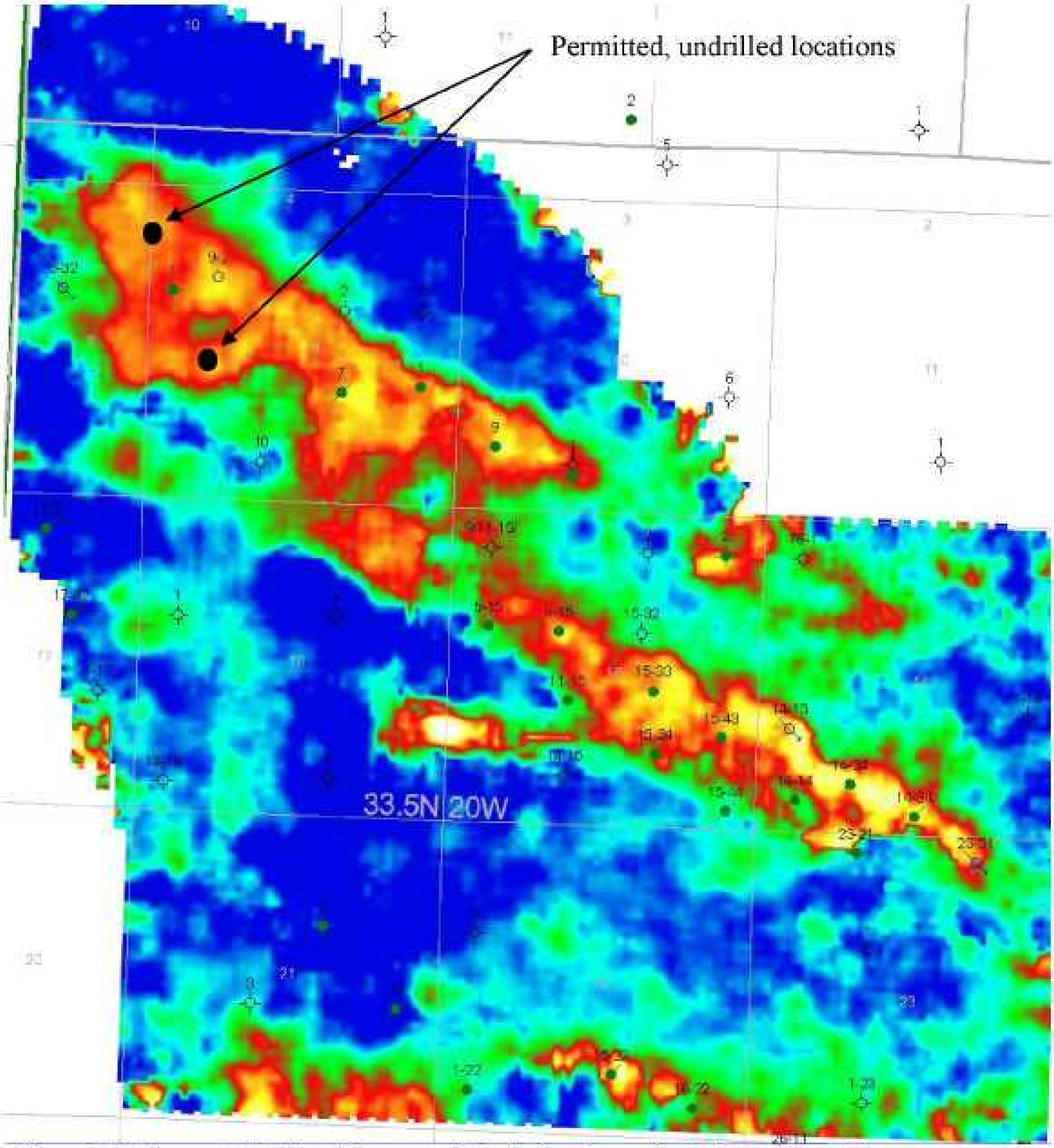

Figure 5-1. Two undrilled locations permitted during the project. Contours are the gross mound thickness isochron. Locations shown are approximate.

5.3.2 POTENTIAL FOR SECONDARY OR TERTIARY RECOVERY

The reservoir simulations indicate that the reservoir, as modeled, contains a significant amount of oil, which is essentially locked due to lack of reservoir energy. Providing this reservoir energy in the form of water or gas drive could re-energize the reservoir and reactivate production. Indeed, analysis of secondary and tertiary recovery strategies for other algal mound fields in the Paradox Basin (Chidsey, 2003) indicate that the use of CO_2 might boost recoveries to as much as 70%. If the 4 million barrels EUR represents about a 17% primary recovery, that would suggest that an additional 12 million barrels might be recoverable through secondary or tertiary recovery.

5.4 Technology Transfer

5.4.1 WEBSITE

The project website has been published, and contains background information on the project, data, reports, presentations and news.

5.4.2 REPORTS & PRESENTATIONS

During the course of the project, a number of presentations have been made at industry group and professional society meetings, and currently a manuscript is in preparation for inclusion in a special volume on the Paradox Basin to be published by the Rocky Mountain Association of Geologists in 2008. Presentations have been made on the seismic acquisition and processing at the RCP Reservoir Conference at the Colorado School of Mines and at the EAGE/SEG workshop on Multicomponent Seismic; on the interpretation of the seismic for mound geometry and internal reservoir properties at the AAPG Annual Meeting in 2006 and at the sectional Rocky Mountain Meeting in 2007; and the construction of the static and dynamic models, as well as the seismic aspects of the project, in the forthcoming RMAG volume on the Paradox Basin.

Nine Technical Progress Reports and this Final Technical Report have also been prepared and submitted. These reports provide substantial technical details, data and workflow descriptions not contained in the presentations. The reports are available on the project website or from the appropriate DOE sources.

5.4.3 TRIBAL INVOLVEMENT

The work in this project was partially funded and staffed by geologists from the Red Willow Energy company, a wholly-owned company of the Southern Ute Tribe. Red Willow staff were significantly involved in all aspects of the acquisition, processing and interpretation, and through this project, this Native American-owned company gained knowledge and understanding of the possible processing workflows that need to be applied to multicomponent data, what multicomponent attributes may prove of greatest or least value for improving exploration and production in algal mounds, and the costs and workflows associated with acquiring and exploiting multicomponent data. For all team members in this project, this effort provided much first-time experience with the advantages and issues of acquiring and applying multicomponent data to algal mounds. A literature and web search suggest that this may be one of the very first, if not the first, applications of nine-component data to algal mounds anywhere in the world, so that this project has provided the Southern Ute Tribe with experience in the use of one of the most cutting-edge emerging seismic technologies that they will have available to them for other areas in Ute Mountain Ute Tribal lands, as well as elsewhere in the Paradox Basin or even to other areas outside of the Paradox Basin in which the companies of the Southern Ute Tribe are currently exploring.

6 REFERENCES

Amaral, L., 2001. Shear wave azimuthal AVO analysis, Vacuum Field, New Mexico. MS Thesis T-5467, Colorado School of Mines

Ambraseys, N. N. and A. J. Hendron (1968). Dynamic Behavior of Rock Masses. In *Rock Mechanics in Engineering Practice*, Stagg, K. G. and Zienkiewicz, O. C. eds., John Wiley & Sons, New York.203-236.

Chidsey, T. 2003. Secondary/Tertiary Recovery Techniques for Small Reservoirs in the Paradox Basin, UT. The Class Act, Vol. 9 No. 1, 7-8.

Chidsey, T. C., C. D. Morgan and K. P. McClure (2004). Outcrop Analogs iin Utah: Templates for Reservoir Characterization and Modeling. Poster presented at the American Association of Petroleum Geologists Rocky Mountain Section Meeting, Denver, Colorado, August 2004.

Core Laboratories, 1991. Reservoir fluid study for the Chuska Energy Company, North Heron No. 35-C Well, Undesignated Field, San Juan County, Utah. Report Number ARFL-910078.

Duranti, L. 2001. Seismic analysis of reservoir dynamics. Ph. D. Thesis, Colorado School of Mines

Gautier, D. L., G. L. Dalton, K. I. Takahashi and K. L. Varnes, 1996. 1995 National Assessment of United States Oil and Gas Resources – Results, Methodology, and Supporting Data. U. S. Geological Survey Digital Data Series DDS-30, Release 2.

Gilbert, R. O. 1987. Statistical Methods for Environmental Pollution Monitoring. Van Nostrand Reinhold, New York, 320 p.

Louden, R.O., D. D. Lehman, W. E. Johnson and D. L. Edwards (2002). 3-D Seismic Data in Delineating Productive Ismay Algal Mounds in Southern Paradox Basin, Utah. American association of Petroleum Geologists, Search and Discovery, #40048.

La Pointe, P. R. C. Rebne, S. Dobbs, C. Van Denberg, R.Van Dok and R. Benson (2005). Multicomponent Seismic Analysis And Calibration To Improve Recovery From Algal Mounds: Application To The Roadrunner/Towaoc Area Of The Paradox Basin, Ute Mountain Ute Reservation, Colorado; Sixth Semi-Annual Technical Report – May. 1, 2005 through October 31, 2005. DOE Award Number: DE-FG26-02NT15451, 45 p.

La Pointe P.R., R. Benson, R. Van Dok, J. Gaiser, C. Rebne (2006). Interpretation of a 3D9C Survey Over Ismay Algal Mounds, Paradox Basin, Colorado [abstr.] 2006 AAPG Annual Meeting, Houston, TX 2-5 April 2006..

Michaid, G. 2001. Time-lapse multicomponent borehole seismic monitoring of a pilot CO_2 flood. Ph. D. Thesis T-5506, Colorado School of Mines.

Petrel, 2005. http://www.slb.com/content/services/software/geo/petrel/index.asp.

Press, W. H.; Flannery, B. P.; Teukolsky, S. A.; and Vetterling, W. T., 1992. Numerical Recipes in FORTRAN: The Art of Scientific Computing, 2nd ed. Cambridge, England: Cambridge University Press, 963 p.

Russo, D. and W. A Jury, 1987. A theoretical study of the estimation of the correlation scale in spatially variable fields: 1. Stationary fields. Water Resources Research, Vol. 23., No. 7, 1257-1268.

Simmons, J and M. Backus, 2001. Shear waves from 3-D-9-C seismic data. The Leading Edge, June 2001, 604-612.

Snedecor, G. W. and W. G. Cochran 1980. Statistical Methods (7th Edition). Iowa State University Press, Ames, Iowa, 507 p.

Spearman, C., 1904. The proof and measurement of association between two things. American Journal of Psychology, 15, 72-101

SPSS, 2004. Version 13.0. SPSS Inc. Headquarters, 233 S. Wacker Drive, 11th floor Chicago, Illinois 60606

Wooldridge, J. M., 2000. Introductory Econometrics: A Modern Approach, South Western College Publishing, a Division of Thomson Learning, Cincinnati, OH. 824 p.
Gilbert, R. O. 1987. Statistical Methods for Environmental Pollution Monitoring. Van Nostrand Reinhold, New York, 320 p

7 LIST OF ACRONYMS & ABBREVIATIONS

3D3C – three dimensional, three component

3D9C – three dimensional, nine component

AVO - amplitude variation with offset

AKAH – Akah Salt

BIA – U. S. Bureau of Indian Affairs

CDP – Common Depth Point

CUTL – Cutler Formation

DOE – U. S. Department of Energy

EUR – Estimated Ultimate Recovery

GTHC – Gothic Shale

IP – Initial Production

KB – Kelly Bushing

LI – Lower Ismay

MD – Measured Depth

ME –Mean Maximum Error

MRE – Mean Reduced Error

MSE – Mean-Square Error

MSL – Mean Sea Level

NMO – Normal Moveout

OOIP – Original Oil in Place

RE – Reduced Error

RMS - Root Mean Square

RW – Red Willow Production

SU – Southern Ute Tribe

UDC – Desert Creek

UI – Upper Ismay

UIC – Upper Ismay Carbonate

UM – Ute Mountain Ute Tribe

VAR - Variance

VIF – Variance Inflation factor

VSP – Vertical Seismic Profiling

National Energy Technology Laboratory

626 Cochrans Mill Road
P.O. Box 10940
Pittsburgh, PA 15236-0940

3610 Collins Ferry Road
P.O. Box 880
Morgantown, WV 26507-0880

One West Third Street, Suite 1400
Tulsa, OK 74103-3519

1450 Queen Avenue SW
Albany, OR 97321-2198

2175 University Ave. South
Suite 201
Fairbanks, AK 99709

Visit the NETL website at:
www.netl.doe.gov

Customer Service:
1-800-553-7681

DEPARTMENT OF ENERGY
UNITED STATES OF AMERICA